V. 122, NO. 5
SEPTEMBER 2025

ACI MATERIALS JOURNAL

A JOURNAL OF THE AMERICAN CONCRETE INSTITUTE

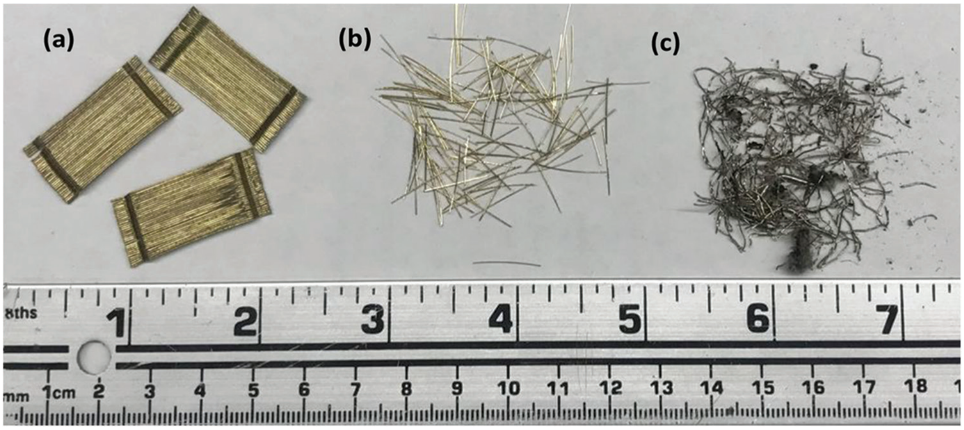

American Concrete Institute

CONTENTS

Editorial Board
Shiho Kawashima, Editor-in-Chief,
Columbia University
Liberato Ferrara,
Polytechnic University of Milan
Raissa Ferron,
The University of Texas at Austin
O. Burkan Isgor,
Oregon State University
Prannoy Suraneni,
University of Miami

Board of Direction

President
Maria Juenger

Vice Presidents
Scott M. Anderson
Matthew R. Sherman

Directors
Michael Ahern
Corina-Maria Aldea
Oscar R. Antommattei
Peter Barlow
Arturo Gaytan Covarrubias
James H. Hanson
Carol Hayek
Werner K. Hellmer
Mary Beth Diesz Hueste
Kimberly Waggle Kramer
Enrique Pasquel
Xiomara Sapón-Roldán

Past President Board Members
Charles K. Nmai
Antonio Nanni
Michael J. Paul

Executive Vice President
Frederick H. Grubbe

Staff
Publisher
John C. Glumb

Senior Managing Director of Technical Operations
Michael L. Tholen

Engineers
Will J. Gold
Matthew R. Senecal
Michael L. Tholen
Gregory M. Zeisler

Managing Editor
Lauren E. Mentz

Associate Editor
Kimberly K. Olesky

Editors
Erin N. Azzopardi
Lauren C. Brown
Kaitlyn J. Dobberteen
Tiesha Elam
Angela R. Noelker
Kelli R. Slayden

PRINTED WITH SOY INK®

ACI MATERIALS JOURNAL

SEPTEMBER 2025, V. 122, NO. 5

A JOURNAL OF THE AMERICAN CONCRETE INSTITUTE
AN INTERNATIONAL TECHNICAL SOCIETY

ACI Materials Journal
© 2025 American Concrete Institute. All rights reserved.

This material may not be reproduced or copied, in whole or in part, in any form or by any means, including making copies by any photo process, or by electronic or mechanical device, printed, written, graphic, or oral, or recording for sound or visual reproduction for use in any knowledge or retrieval system or device, without the written consent of ACI. This material may not be used by data mining, robots, screen scraping, or similar data gathering and extraction tools such as artificial intelligence (“AI”) for purposes of developing or training a machine learning or AI model, conducting computer analysis or creating derivatives of this material, without the written consent of ACI.

American Concrete Institute®, ACI®, Always Advancing®, *ACI Structural Journal*®, and *ACI Materials Journal*® are registered trademarks of American Concrete Institute.

The *ACI Materials Journal* (ISSN 0889-325x) is published bimonthly by the American Concrete Institute. Publication office: 38800 Country Club Drive, Farmington Hills, MI 48331. Periodicals postage paid at Farmington, MI, and at additional mailing offices. Subscription rates: $210 per year, payable in advance. POSTMASTER: Send address changes to: *ACI Materials Journal*, 38800 Country Club Drive, Farmington Hills, MI 48331.

Canadian GST: R 1226213149.

Direct correspondence to 38800 Country Club Drive, Farmington Hills, MI 48331. Telephone: +1.248.848.3700.
Website: http://www.concrete.org.

MEETINGS

OCTOBER 2025

9-11—International Conference on Civil and Structural Engineering (ICCSE 2025), Dubai, UAE, https://www.concrete.org/newsandevents/eventscalendar.aspx?m=CalendarSearchDetails&CurrentID=210910

10-12—NRMCA's ConcreteWorks 2025, Orlando, FL, www.nrmca.org/conferences-events/nrmca-concreteworks

19-21—CMAA2025, Nashville, TN, www.cmaanet.org/CMAA2025

19-22—2025 International Concrete Repair Institute (ICRI) Fall Convention, Chicago, IL, www.icri.org/news-events/2025-icri-fall-convention

20-21—1st RILEM Youth Symposium (RYS2025), Online, www.rilem.net/agenda/1st-rilem-youth-symposiumrys2025-1672

20-21—Advanced Sustainable Structural Systems (AS3), Riyadh, Saudi Arabia, https://advancedstructuresksa.com

20-23—Deep Foundations Institute (DFI) 50th Annual Conference on Deep Foundations, Nashville, TN, https://dfi-events.org/dfi50

22-24—Hardscape North America (HNA), Louisville, KY, www.hardscapena.com

23-25—14th UBT International Conference on Resilience, Innovation, and Sustainability (IC-UBT 2025), Pristina, Kosovo, https://conferences.ubt-uni.net/2025/

26-30—37th Annual American Segmental Bridge Institute (ASBI) Convention and Committee Meetings, Bellevue, WA, https://asbi-assoc.org/events/37th-annual-asbi-convention-and-committee-meetings/

29-30—ICCX North Africa, Casablanca, Morocco, www.iccx.org/exhibition/north-africa/visitors

NOVEMBER 2025

4-7—IIIAE 2025: 27th International Acoustic Emission Symposium (IAES-27) and 11th International Conference on Acoustic Emission (ICAE-11), Nagoya, Japan, https://2025.iiiae.org/

4-7—2025 Greenbuild International Conference and Expo, Los Angeles, CA, https://informaconnect.com/greenbuild/about-greenbuild

4-10—International Symposium on Volume Changes of Hardening Concrete (ISVCHC 2025), Nanjing, China, https://isvchc2025.com/en/index.html#conference

ACI CONCRETE CONVENTION: FUTURE DATES

2025—Oct. 26-29, Hilton Baltimore & Baltimore Marriott Inner Harbor, Baltimore, MD
2026—Mar. 29-Apr. 1, Hyatt Regency O'Hare Chicago, Rosemont/Chicago, IL
2026—Oct. 11-14, Hilton Atlanta, Atlanta, GA
2027—Mar. 21-24, Caesars Palace Las Vegas, Las Vegas, NV

For additional information, contact:
Event Services, ACI
38800 Country Club Drive
Farmington Hills, MI 48331
Telephone: +1.248.848.3795
email: conventions@concrete.org

ON FRONT COVER: 122-M33, p. 45, Fig. 2—Types of steel fibers used in this study: (a) hooked-end manufactured steel fiber (MSF); (b) straight MSF; and (c) recycled steel fiber (RSF).

Papers appearing in the *ACI Materials Journal* are reviewed according to the Institute's Publication Policy by individual experts in the subject area of the papers.

Contributions to *ACI Materials Journal*

The *ACI Materials Journal* is an open forum on concrete technology and papers related to this field are always welcome. All material submitted for possible publication must meet the requirements of the "American Concrete Institute Publication Policy" and "Author Guidelines and Submission Procedures." Prospective authors should request a copy of the Policy and Guidelines from ACI or visit ACI's website at **www.concrete.org** prior to submitting contributions.

Papers reporting research must include a statement indicating the significance of the research.

The Institute reserves the right to return, without review, contributions not meeting the requirements of the Publication Policy.

All materials conforming to the Policy requirements will be reviewed for editorial quality and technical content, and every effort will be made to put all acceptable papers into the information channel. However, potentially good papers may be returned to authors when it is not possible to publish them in a reasonable time.

Discussion

All technical material appearing in the *ACI Materials Journal* may be discussed. If the discussion is received within four months of the paper's print publication, it will appear in the issue dated ten months from this journal's date. Discussion material received after specified dates will be considered individually for publication or private response. ACI Standards published in ACI Journals for public comment have discussion due dates printed with the Standard. Discussion should be complete and ready for publication, including finished, reproducible illustrations. Discussion must be confined to the scope of the paper and meet the ACI Publication Policy.

Follow the style of the current issue. Discussions should not exceed 1800-word equivalents (illustrations and tables count as 300 words each). References should be complete. Do not repeat references cited in original paper; cite them by original number. Numbering of additional references, figures, tables, and equations should follow sequentially from the original manuscript throughout the discussion. The discusser must indicate the month, year, volume number, issue number, authors' names, and manuscript number of the original manuscript. Closures responding to a single discussion should not exceed 1800-word equivalents in length, and to multiple discussions, approximately one half of the combined lengths of all discussions. Closures are published together with the discussions.

Discuss the paper, not some new or outside work on the same subject. Use references wherever possible instead of repeating available information.

Discussion offered for publication should offer some benefit to the general reader. Discussion which does not meet this requirement will be returned or referred to the author for private reply.

Send manuscripts to:
http://mc.manuscriptcentral.com/aci

Send discussions to:
Journals.manuscripts@concrete.org

ACI MATERIALS JOURNAL TECHNICAL PAPER

Title No. 122-M30

Development of Test Method to Detect Soft Grout Formation in Prepackaged Post-Tensioning Grouts

by Alex Piper, Alexander J. Randell, Brett Brunner, and H. R. (Trey) Hamilton

This paper presents research focused on the development of a test method that can be used to gauge the susceptibility of a post-tensioning (PT) grout to form soft grout. Depending on the grout formulation, soft grout may have a lower pH, retain excessive moisture, and be corrosive to the tendon. While relatively rare, it has been documented in bridge construction in the United States and abroad, and in some cases has prompted the replacement of PT tendons.

One of the causes of soft grout is thought to be the use of low-reactivity fillers such as ground limestone. When tendons deviate significantly, these fillers can segregate and then accumulate into a mass of material that does not harden. The modified inclined tube test (MITT) was developed based on the Euronorm inclined tube test. None of the commercially available PT grouts produced soft grout when they were mixed and injected in accordance with manufacturer's recommendations and tested well before their expiration date. Additional mixture water or residual water in the tube, however, produced soft grout consistently in one of the PT grouts.

Keywords: bleed; duct; grout; post-tensioning; segregation; soft grout; tendon.

INTRODUCTION

Prestressed concrete has proven to be an efficient and long-lasting design choice in post-tensioned (PT) bridge construction. In PT concrete, high-strength steel tendons are installed in ducts and tensioned against anchors that are cast into the concrete with the ducts. A portland cement grout mixture, which provides corrosion protection and structurally bonds the tendon to the surrounding concrete, is then injected into the duct.

Problems have been discovered with PT grout in several bridges in Florida.[1-3] These bridges typically suffered from poor detailing, voids in the grout, or both, which eventually led to corrosion of the prestressing steel in the tendon. These bridges were also constructed before prepackaged high-performance grouts were in common use. More recently, however, Lau et al.[4] reported on one particular bridge in which two external tendons failed as a result of severe corrosion of the prestressing steel. During the investigation, it was noted that in most cases, the grout was well-consolidated and hardened in the lower portions of the deviated tendons. In some of the upper portions, though, the grout was either soft and chalky or wet and plastic (soft grout). Measurements indicated that the moisture content of the hardened grout was approximately 20% by mass, while the soft moisture content exceeded 60% by mass. Moisture and low pH in the soft grout appear to have contributed to the severe corrosion of the prestressing strands.

Although there have been no catastrophic structural failures related to grout in the United States, expensive repairs must be made to prevent such failures. This paper presents the results of experimental work aimed at evaluating the cause of soft grout and how to test prepackaged grouts for their susceptibility to such deficiencies.

BACKGROUND

Grout bleed occurs when excess water rises to the top of the grout as cement particles settle to the bottom.[5] If bleeding occurs in sufficient volume, then structural bond is lost, and prestressing steel may be exposed and at risk of corrosion. Excessive bleeding can also lead to segregation of solids, which may result in the formation of soft grout. While bleed water can be reabsorbed by the grout during hydration, soft grout has a lower pH, retains excessive moisture, and can be extremely corrosive to the tendon. Soft grout has been found near corroded tendons and tube sections in both the United States and abroad and has been attributed to grout segregation.[6]

Identifying problems with grout bleed and segregation in high-performance PT grout has customarily been accomplished using the pressure bleed test[7] and the wick-induced bleed test, which is a modified version of ASTM C940-10.[8] In the late 1990s, a method for determining bleed and segregation resistance was developed in Europe.[9,10] The test consists of an inclined tube containing twelve 0.6 in. (15.2 mm) diameter unstressed PT strands placed at a 30-degree incline from horizontal. PT grout is injected into the low point of the inclined tube and discharged at the top of the incline. The exit valve is then shut off and the grout pressure is then maintained at the value and for the duration specified in the method statement. The tube used for the test is transparent, which allows for visual identification of bleed and segregation. Grout segregation is identified visually by a change in color along the length of the tube. The inclined tube test, as described in the Euronorm standards,[11] was incorporated into guideline grouting specifications[12] to help offset problems with soft grout.

RESEARCH SIGNIFICANCE

This paper describes the development of a test method that can be used to identify grouts that are susceptible

---

ACI Materials Journal, V. 122, No. 5, September 2025.

MS No. M-2015-221.R1, doi: 10.14359/51747868, received July 15, 2015, and reviewed under Institute publication policies. Pertinent discussion including author's closure, if any, will be published ten months from this journal's date if the discussion is received within four months of the paper's print publication.

Table 1—Summary of PT grouts tested

Testing ID	Bag weights	Pilot tests	Final tests	Date manufactured	Expiration date
PT1-2		x		11/17/11	05/17/12
PT1-3	x			06/25/12	01/01/13
PT1-4	x		x	04/29/13	11/01/13
PT2-2		x		01/05/12	07/05/12
PT2-3	x			06/26/12	12/01/12
PT2-4	x		x	03/28/13	09/28/13
PT3-1		x		10/19/11	04/19/12
PT3-2	x			06/01/12	12/01/12
PT3-3	x		x	04/10/13	10/07/13
PT4-1		x		08/25/11	02/25/12
PT4-2	x	x		02/02/12	08/02/12
PT4-3	x			03/19/12	09/19/12
PT4-4	x			03/03/12	09/03/12
PT4-5	x			05/24/12	11/24/12
PT4-6	x		x	05/04/13	11/04/13
PT5-1			x	06/10/13	06/10/14
PT6-1			x	06/03/13	06/03/14

to soft grout formation following injection. To this end, a modified version of the EN 445:2007 inclined tube test was developed. The test consisted of using a full-scale colloidal grout plant to mix and inject grout into a 15 ft (4.6 m) long tube containing prestressing strand. Initially, pilot testing was conducted to determine the cause of soft grout formation; to this end, a range of variables were tested using the modified test method to study their effect on the performance of prepackaged PT grouts. The inclined tube test was altered to introduce variations that might occur in the field with respect to the tube geometry and the introduction of unintended water into the grout. In addition, tube constrictions, tubes overfilled with strand, placement of strand in the top of the tube, injecting under pressure, injecting and setting under pressure, and high-temperature injection were evaluated. Once the test method was developed, all the grouts that were then available were tested using this methodology. Piper et al.[13] provide further details on materials, testing procedures, and results.

MATERIALS AND MIXING EQUIPMENT

Testing was conducted primarily on commercially available proprietary prepackaged PT grouts. Table 1 summarizes the PT grouts tested, the individual lots used to conduct both the pilot and final testing, and the expiration date. All grouts were stored at laboratory conditions and tested prior to their respective expiration date. Testing identification PT*x*-*y* is used to distinguish between specific manufacturers (*x*) and their respective lot numbers (*y*). Ordinary portland cement and water were tested for comparison during the pilot testing. C675 and C45 were mixtures with a water-cement ratio (w/c) of 0.675 and 0.45, respectively.

Each of the commercial PT grouts was prepackaged in bags in either 50 or 55 lb (22.7 or 25.0 kg) weights. Prepackaging allows factory control on the proportioning of dry materials, which avoids the potential errors associated with jobsite proportioning. Bags are typically marked with the allowable range of water dosage based on an assumed dry bag weight. This method of water dosage requires that the bag quantities match the weight shown on the bag or that the field personnel weigh the bags and adjust for bags containing more or less material than specified.

After initiation of the research, the issue of varying bag weight was raised. Although some of the testing had been completed, the bag weight measurements were completed on the remaining tests (Table 2). The weights shown in the table include bag and contents, where the weight of the paper bag was generally found to be approximately 0.30 lb (0.14 kg). Materials PT4-3 and PT4-4 arrived on a single pallet. Every bag on this pallet was weighed, and no distinction was made between two lot numbers.

A commercially available, heavy-duty, high-volume colloidal mixing grout plant was used to prepare grout mixtures for testing. The plant was equipped with an 8 ft^3 (220 L) colloidal mixer. The agitator tank was equipped with a variable-speed paddle mixer to prevent freshly mixed grout from building up in the structure before it was pumped. The grout pump was a three-stage progressing cavity, positive displacement, rotor-stator pump capable of a maximum output of 20 g/min (77 L/min). The pump was capable of a maximum pressure of 261 psi (18 bar). Mixtures were typically prepared in three to five bag volumes for injecting a single inclined tube.

MODIFIED INCLINED TUBE TEST (MITT)

Although introduced into Post-Tensioning Institute (PTI) guide specifications[12] (herein referred to as PTI specification) in the United States, the inclined tube test has been

Table 2—Summary of weights of bags of PT grouts

Material	Specified weight, lb	No. of bags	Average weight, lb	CoV[*]	Percentage of bags underweight	Minimum, lb	Maximum, lb
PT1-3	50	40	51.1	1.86%	12.5%	48.3	52.
PT1-4	50	40	48.9	1.04%	100%	46.3	49.
PT2-3	55	58	55.5	0.84%	8.62%	54.1	56.
PT2-4	55	60	55.6	0.97%	15%	54.1	56.
PT3-2	55	60	55.9	0.64%	0%	55.2	56.
PT3-3	55	60	56.1	0.74%	1.67%	54.3	57.
PT4-2	50	3	50.5	3.8%	N/A	48.3	51.8
PT4-3 and PT4-4	50	63	52.1	2.7%	7.94%	49.1	54.6
PT4-5	50	73	50.6	1.84%	24.66%	48.9	53.
PT4-6	50	64	50.1	1.40%	35.94%	48.5	52.

[*] Coefficient of variation.

Note: 1 lb = 0.45 kg.

used for several years in Europe to test grout mixture designs to determine the potential for bleed under simulated field conditions.[11] The test is conducted by injecting a 16.4 ft (5 m) long x 3.1 in. (80 mm) diameter transparent polyvinyl chloride (PVC) pipe filled with twelve 0.59 to 0.63 in. (15 to 16 mm) diameter prestressing strands; grout is injected into the low end and discharged at the top. The tube is placed on a 30-degree slope. In the 24 hours following grout injection, visual observations are made of the tube to determine if bleed water has collected at the top or if overall volume has changed.

In this research, preliminary inclined tube tests were conducted on commercially available prepackaged PT grouts using a 15 ft x 3 in. (4.6 m x 76.2 mm) diameter PVC pipe with twelve 0.6 in. (15.2 mm) diameter seven-wire prestressing strands cut to the same length as the tube (shortened to 14 ft [4.3 m] in subsequent tests, as described in the following). In nearly all cases, if proportioned and mixed in accordance with the manufacturer's instructions, the test revealed no bleed, volume change, or soft grout. However, under some conditions, such as the use of excess water or expired grout, soft grout was discovered at the top of the incline tube upon dissection.

This soft grout is thought to be the result of segregation of particles within the suspension based on their density (Fig. 1). The change in elevation between the top and bottom of the inclined test tube caused bleed water to rise. The rising bleed water carried less-dense particles (non-cementitious) in suspension upward until contact was made with the strand bundle or tube. At this point, particles were carried to the top of the incline, resulting in the accumulation of unreacted material near the free surface of the grout at the exit of the inclined tube. Hardened solid grout, though, was still present along the remainder of the length of the tube. The characteristics of the soft grout tend to vary depending on the characteristics and relative quantity of grout constituents.

EN 445:2007[11] is focused on determining "…the bleed properties and volume stability of grout at full-scale…". The test method, as indicated, is designed to measure the bleed water and volume change of grout after injection and does not specifically address the issue of soft or segregated grout. Bleed water and air are measured at the top of the inclined tube over a period of 24 hours following injection of the grout. These data are then reported as part of the test. No specific measurement or inspection for soft or segregated grout is required in the referenced version of the test. In some cases, identification and distinction between grout and bleed is visually obscure even through the transparent tube. The investigation of soft grout for this research required that the specimen be dissected 24 hours after injection to determine whether soft grout was present at the top of the incline.

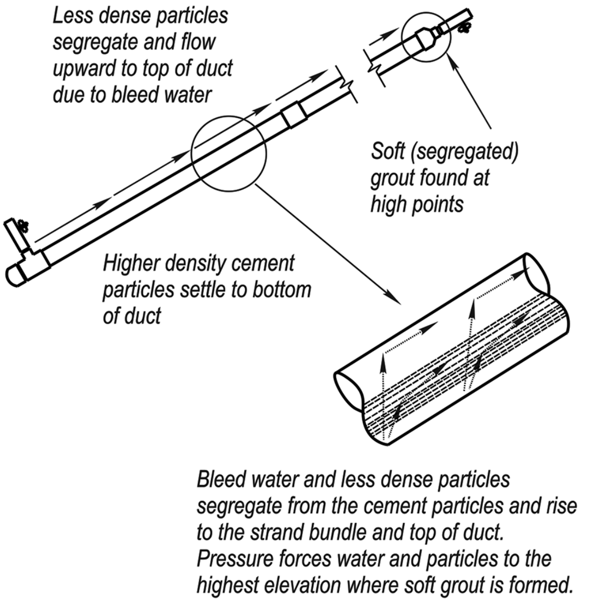

Fig. 1—Bleed and segregation mechanism.

Because EN 445:2007 procedures do not directly address soft grout, the following supplemental measurements were taken to identify grout formulations or grouting conditions that would result in the formation of soft grout:

1. The tube was dissected at the top of the inclined tube and visually inspected for segregated or soft grout (Fig. 2). The mass of the collected sample was measured, and the moisture content of the soft grout was determined using ASTM C566-13.[14]
2. Grout was sampled at selected locations along the length of the tube and at the top and bottom of the cross

section. The samples were tested for moisture content using ASTM C566.[14]

3. The strand bundle was shortened to a 14 ft (4.3 m) length to allow unimpeded sampling of the grout near the top of the inclined tube.

This test is referred to as the modified inclined tube test (MITT). The ideal benchmark to determine the relative quality of hardened grout samples is unit weight. Relative unit weight would show whether the grout is homogenous throughout the tube. A sample containing voids or excessive water would have a lower unit weight than solid, well-consolidated grout. Determining the unit weight of a small, irregular-shaped sample is impractical and probably unnecessary. Instead of unit weight, the moisture content of grout samples collected along the length of the tube was measured. If the grout segregated along the length of the inclined column, then it is expected that the moisture content of the grout at the top of the column would be higher than that at the bottom of the column. Ultimately, moisture content provided a quantitative comparison among grout samples collected from the inclined tubes.

EN 445:2007 requires that bleed measurements be taken at 0 minutes, 30 minutes, 1 hour, 3 hours, and 24 hours after injection. At these intervals, bleed water level, and any other liquid that is visible through the tube near the top of the incline, are recorded. These same observations were used for taking readings during testing of prepackaged PT grouts. In nearly all tests, however, bleed water was not detected at the top of the inclined tubes.

After the grout had been allowed to set for at least 24 hours, samples were collected along the length of the tube. Early in the testing program, each tube was cut to shorter lengths and generally sampled in four to five locations along its length. After cutting the tubes into smaller sections, the PVC casing was removed to provide direct access to the grout. The casing was removed using a handheld rotary tool, which did not disturb the surface of the grout. Typically, a 6 in. (152 mm) window of PVC casing was removed, and a chisel was used to collect at least 50 g (0.11 lb) of grout sample (Fig. 3).

Results from the earlier sampling scheme indicated that the sampling locations could be reduced to those shown in Fig. 2. Furthermore, grout samples were taken from above and below the strand bundle, which obviated the need to cut the strand. At the top of the incline, grout was more easily sampled due to lack of strand near the top. Samples were taken in adjacent locations; one was removed from under the end cap, which was cut off using a band saw. This also allowed bleed water to be collected during the cutting process. Soft grout, if present, was scraped from the top of the grout column and weighed. Samples were also taken over a 6 in. (152 mm) length near the end of the strand bundle. Extensive testing experience had shown that bleed water was typically not found in the prepackaged grouts, and, because the primary focus of the inclined testing was the measurement of soft grout and moisture content, opaque tubes were used to reduce testing costs.

Grout samples of approximately 25 g (0.055 lb) were taken from the top and bottom of the cross section at selected locations for a total sample size at each location of approximately 50 g (0.11 lb). The moisture content of grout samples was determined using ASTM C566.[14]

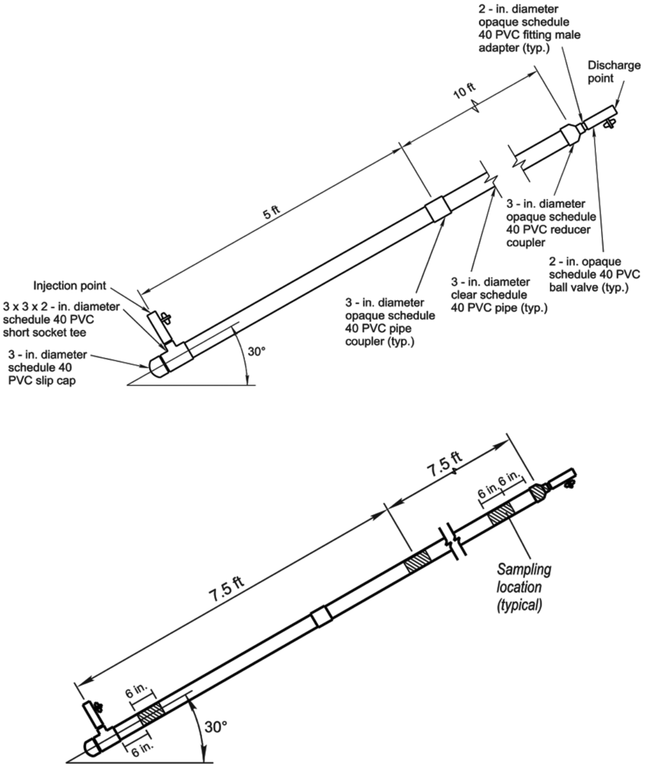

Fig. 2—Schematic of MITT setup. (Note: 1 in. = 25.4 mm; 1 ft = 306 mm.)

Several standard test methods were conducted to evaluate the fresh and hardened properties of the grout for each MITT. Modified flow cone[12] and dynamic viscosity[15] were conducted on the fluid grout immediately following mixing to assess the rheological properties of the grout. Pressure bleed[16] was conducted to evaluate bleed under pressure, and unit weight[17] and mud balance[12] were conducted to evaluate water dosage.

PILOT TESTING

During the initial pilot testing, none of the proprietary prepackaged PT grouts tested using the MITT produced bleed or soft grout when they were fresh and when they were mixed and injected in accordance with the manufacturer's recommendations. For these initial tests, the grouts were mixed at the maximum water dosage (MWD) recommended by the manufacturer. To induce soft grout production, several variations on the test method were introduced, simulating adverse grouting conditions that might occur in the field. Initially, the following variations were imposed on all the PT grouts tested using the MITT:

- 15% above maximum water dosage (1.15 · MWD)
- Residual water in the tube
- Duct constriction

It was discovered in initial tests of some of the grouts that mixtures prepared with a higher water dosage than recommended by the manufacturer might be prone to producing soft grout. Consequently, two series of tests were developed to simulate conditions in which excess water might be introduced into the grout in the field. The first was the addition of too much mixing water, which might occur due to an error in the measurement of the material quantities or to temper or increase the fluidity of the PT grout before injection. For a typical-sized batch of test grout, 2 gal. (7.6 L) of water corresponded to approximately 15% of the manufacturer's maximum recommended water dosage (1.15 · MWD).

The second was to introduce residual water in the inclined tube specimen. This simulated water in the PT duct that had not been adequately cleared to grouting. Each tube was filled with 2 gal. (7.6 L) of water, which occupied approximately half of the volume of the tube.

Post-tensioning ducts may have constrictions due to anchorages or couplings, which forces grout through a tortuous path and perhaps results in mechanical filtering of large particles, causing different behavior in the fluid or hardened grout. To simulate the effect of these constrictions, the inclined tube specimen was redesigned with a series of smaller-diameter sections (Fig. 4). To further enhance the constriction, reduced-diameter sections were packed full with seven-wire strands. Some of the seven-wire strands were separated into individual wires and packed into the constrictions to create the most tortuous path possible for the grout. No strand was placed in the remainder of the specimen.

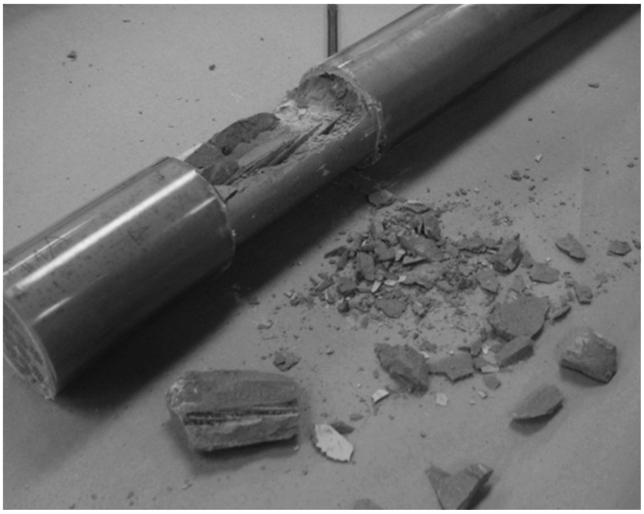

Fig. 3—Collecting grout samples for moisture content measurement.

PT4 was found to consistently produce soft grout when mixed at 1.15 MWD using the standard MITT; although not confirmed by testing, its sensitivity to excess water dosage may be due to a large proportion of nonreactive filler material used in its formulation. To determine potential sensitivity to other conditions, PT4 was further tested using the variations shown in Table 3.

RESULTS AND DISCUSSION

Moisture content

This section presents the moisture content measured in grout samples taken from the inclined tube specimens and evaluates the effect of the variables on this moisture content.

Effect of MWD—Figure 5 shows the maximum moisture content measured in each tube for all grouts mixed at the manufacturer's maximum specified water dosage. Tests on PT4-1 were repeated, as indicated by PT4-1a and PT4-1b, because of the suspected sensitivity of this grout to producing soft grout. No soft grout was detected in any of the prepackaged grouts when mixed at MWD and none of the grouts exhibited a moisture content higher than 25%. This agreed well with results from tests conducted on grouts in the field,[4] where similar measurements indicated a moisture content of approximately 20%.

Figure 6 shows the details of further MITT results when mixed at MWD. The plots show the variation in moisture content between the top and bottom of the tube section and

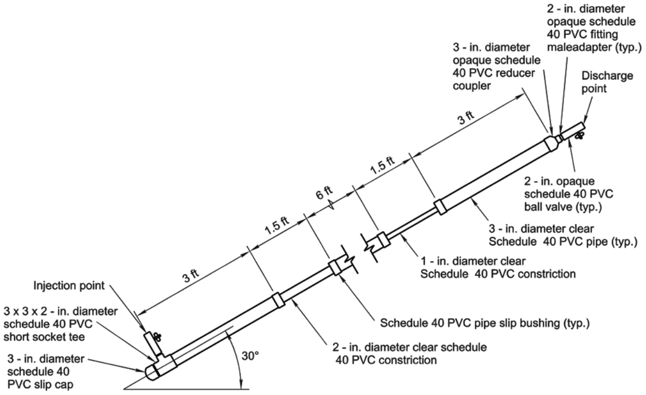

Fig. 4—Inclined tube specimen modified with constrictions. (Note: 1 in. = 25.4 mm; 1 ft = 306 mm.)

Table 3—Summary of additional field conditions tested on PT4

Condition	Description
Tube full of strand	Tube was filled to capacity with strands. Eighteen strands were used instead of the standard 12. Grout was mixed at MWD.
Pressurized injection	The pressure at the injection point was 55 psi (380 kPa). Standard injection pressure was 20 to 30 psi (140 to 207 kPa). Grout was mixed at MWD.
Strand tube top	Tube was filled with 12 strands that were elevated to the top of the tube cross section. The strand in standard tubes was laid flat on the bottom of the tube cross section. Grout was mixed at MWD.
Pressurized set	Tube was sealed at a pressure of 60 psi (414 kPa), and then the grout was allowed to set. Standard tubes were sealed at 0 psi (kPa). Grout was mixed at MWD.
High-temperature injection	The grout material and water were conditioned to 90°F (32°C) in an oven prior to testing. Standard materials were stored at room temperature. Grout was mixed at MWD.
Water in hose	Grout hose was filled with 2 gal. (7.6 L) of water prior to injection. This is similar to the 2 gal. (7.6 L) of water in the tube test, except that the water was in the grout hose instead of the tube. Grout was mixed at MWD.
1.5 · MWD	The grout was mixed with a water dosage 50% greater than MWD.

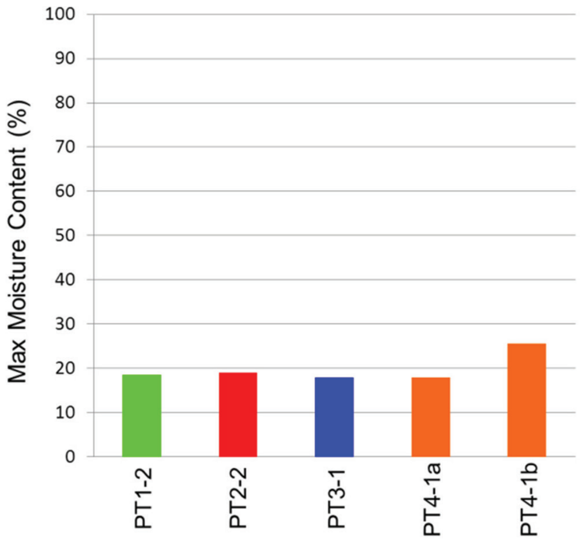

Fig. 5—Maximum moisture content measured in tube for all grouts at maximum water.

along the length of the tube. Generally, the moisture content at the top of the section was either equal to or greater than the moisture content of grout at the bottom of the section. Evaluating the moisture content along the length of the specimen provides a measure of the fresh grout stability. Variations along the length of the specimen would indicate relative movement of moisture or particles and perhaps the beginnings of complete segregation. Based on the relatively minor variation in moisture content shown in these plots, however, it appears that the fresh PT grout, when mixed at MWD, was stable over the length of the tube, with the possible exception of PT4 and PT5, which had higher moisture contents in the upper reaches of the incline. Yet none of the PT grouts exhibited a moisture content measurement above 25%, nor was soft grout found in any of the specimens. Water-to-bagged material ratios for these grouts ranged between 0.232 and 0.318 (by mass), which translates to theoretical pre-hydration moisture contents ranging between 18 and 24%. Measured moisture contents varied between 12 and 20%; the difference accounts for bound water not released when hardened grout samples were heated to determine moisture content.

Effect of excess mixing water (1.15 · MWD)—PT1-2, PT2-2, PT3-1, and PT4-2 were each tested three times at 1.15 · MWD. Figure 7 shows the maximum moisture content measured in each tube for all grouts at 1.15 · MWD. These results are very similar to those seen when 2 gal. (7.6 L) of water was placed in the tube prior to injection. Soft grout was found at the top of all the tubes injected with PT4-2. It was not found in any other case, although porous grout was found in the tubes injected with PT1-2.

Figure 8 shows the details of further MITT results when mixed at 1.15 · MWD. As with those shown in the previous section, the plots show the variation in moisture content between the top and bottom of the tube section and along the length of the tube. With the exception of PT3 and PT6, an increased moisture content is noted at the top of the inclined tube relative to that at the bottom. In the case of PT4, the moisture content is over 70% and the grout was soft, which agrees with results from tests conducted on grouts in the field,[4] where similar measurements indicated that the moisture content of soft grout is approximately 60%.

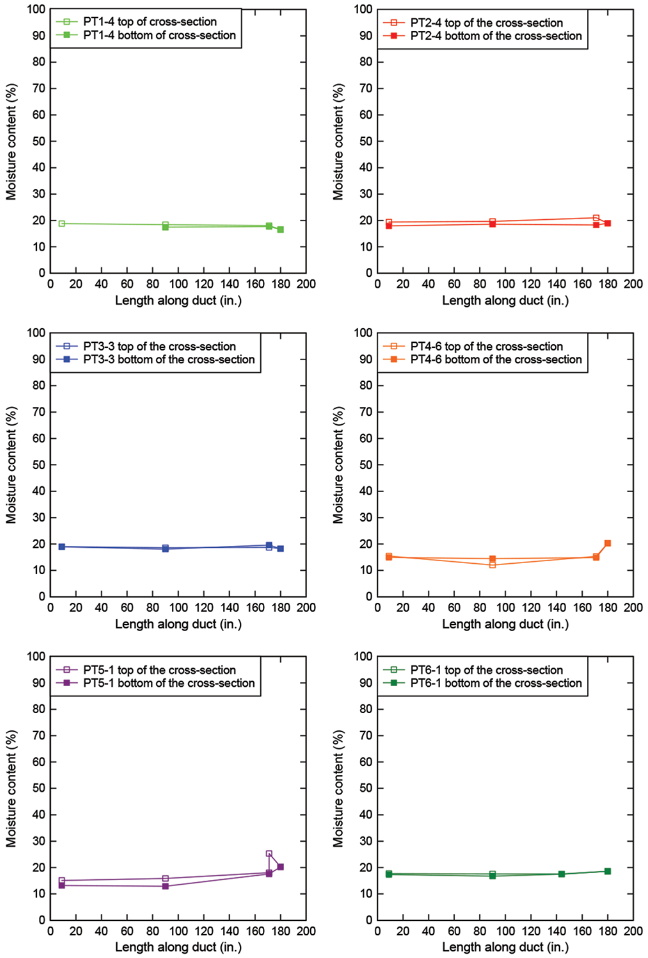

Fig. 6—Variation in moisture content with respect to position along tube for MWD mixtures.

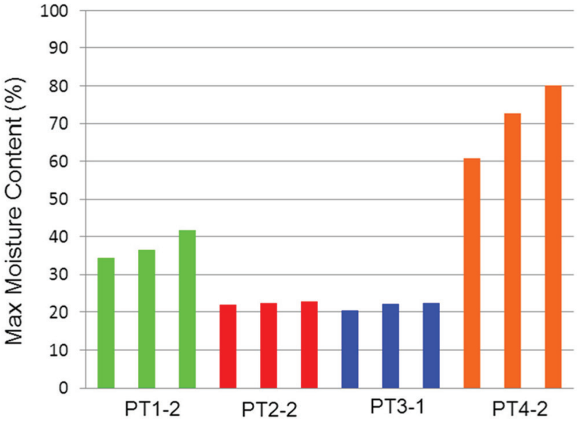

Fig. 7—Maximum moisture content measured in tube for all grouts at 1.15 · MWD.

Differences in moisture content between the top and bottom of the section were relatively small compared to the very large increases noted in PT2 and PT4 near the top of the incline. Based on the consistency noted in these results, grout sampling was limited to the single moisture content readings at each location along the length.

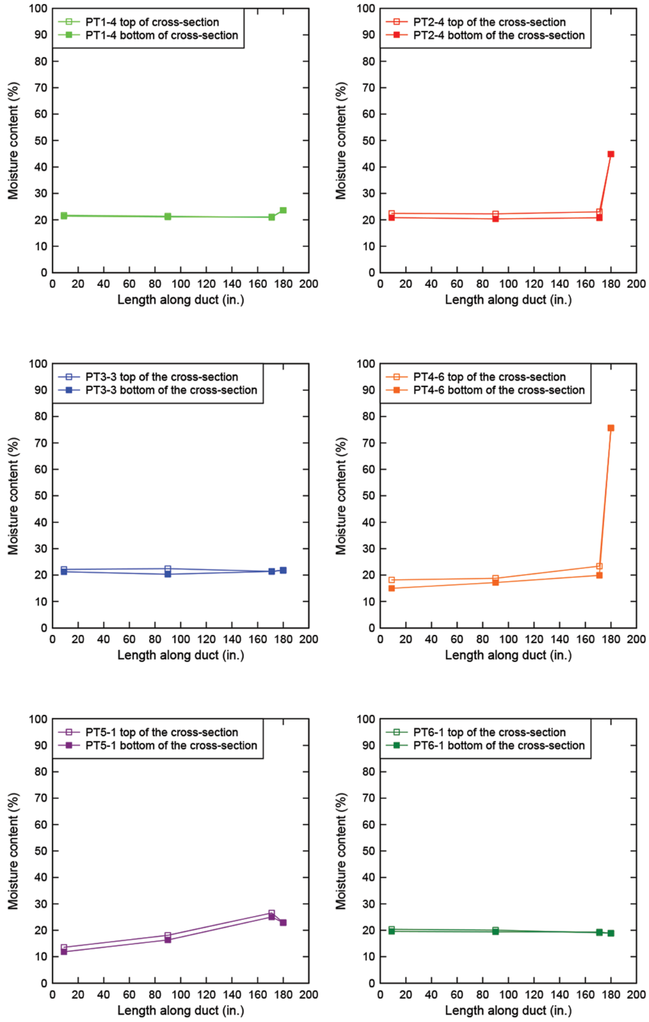

Fig. 8—Variation in moisture content with respect to position along tube for 1.15 · MWD mixtures.

It is desirable to place an upper limit on the moisture content measurements resulting from this test. To ensure a robust formulation of PT grout, the grout must be capable of enduring some level of water overdosage and still produce solid, durable grout. One possibility is to require that the moisture content from MITT tests with 1.15 · MWD be limited to a suitable maximum. The theoretical moisture content of the six tested grouts when mixed at 1.15 · MWD ranges from 21 to 27%. Most of the moisture contents, however, measured below approximately 25%. The upper limit of the water-cementitious materials ratio (*w*/*cm*) given by the PTI specification is 0.45; the theoretical moisture content for a *w*/*cm* of $1.15 \times 0.45 = 0.52$ is approximately 35%. To ensure that other properties are not adversely affected by additional water or that the additional water does not cause serious segregation, it is reasonable to limit the moisture content to 35% as measured at any location along the tube length.

Constricted tube—PT1-2, PT2-2, and PT3-1 were tested once and PT4-2 was tested twice using a constricted tube. In the first test of PT4-2, the grout was injected in the standard manner. In the second test, the grout was recirculated through the constricted tube. During recirculation, one of the fittings failed, which resulted in the tube being partially filled with grout.

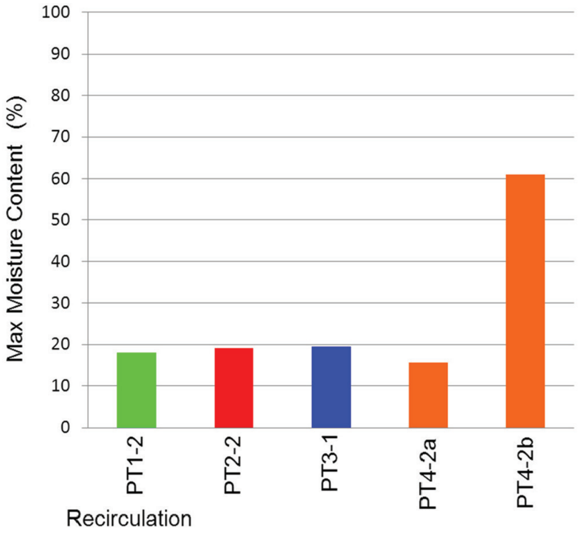

Fig. 9—Maximum moisture content measured for all grouts with constricted tubes.

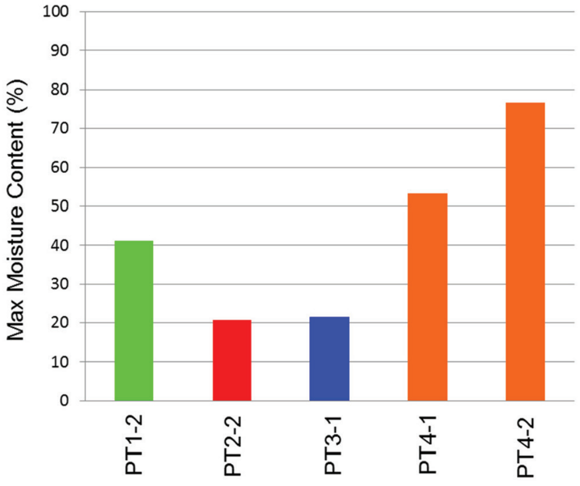

Fig. 10—Maximum moisture content measured in tube for all grouts with 2 gal. (7.6 L) of water in tube prior to injection.

Moisture content samples for the constricted tube were collected on both ends of both constrictions and at the top of the incline. Figure 9 shows the maximum moisture content measured at any of these locations for each test. Results indicate that the PT4-2 had high moisture content relative to the other results, indicating soft grout. The maximum moisture content in the constricted tubes for PT1-2, PT2-2, and PT3-1 was nearly identical to that measured using the standard tubes. PT4-2, however, exhibited a low moisture content at the top of the tube when it was injected through a constriction and recirculated. Furthermore, PT4-2 exhibited a high moisture content at the top of the tube in the other case when it was injected through a constriction in the standard manner.

Water in tube—Figure 10 shows the maximum moisture content measured in each tube filled with 2 gal. (7.6 L) of water prior to injection. Moisture content values varied widely among the various PT grouts from 20 to over 70%. PT2-2 and PT3-1 behaved in a similar manner to a mixture at MWD. PT1-2 exhibited a higher moisture content than it did when mixed at MWD. PT4-1 exhibited a very high moisture

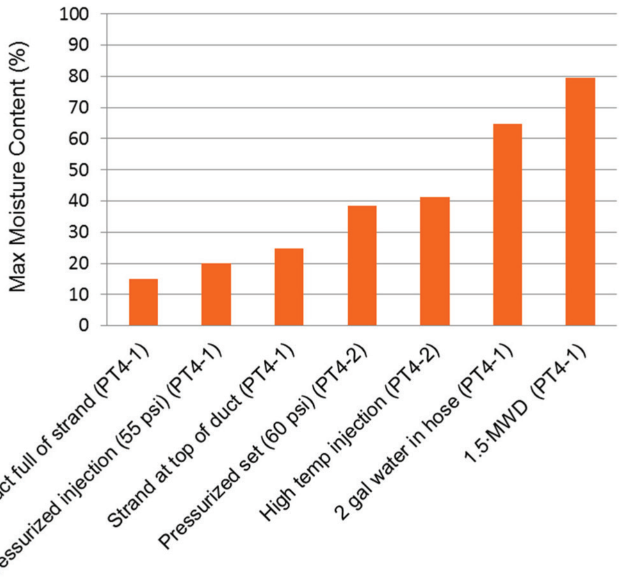

Fig. 11—Maximum moisture content measured in tube for additional tests conducted on PT4-1 and PT4-2. (Note: 1 gal. = 3.78 L; 1 psi = 6.89 kPa.)

content (over 50%) when compared to that measured when the grout was mixed at MWD, while PT4-2 exhibited a higher moisture content (over 70%) than PT4-1. This was the only case in which the same testing condition was conducted on both lots of PT4 (PT4-1 and PT4-2). These results indicate that PT4-2 was more susceptible to high moisture content than PT4-1. In both cases, soft grout was found at the top of the incline during dissection.

Other conditions—Because PT4-1 and PT4-2 were the only materials that produced soft grout, additional tests were conducted to determine if other conditions would produce soft grout. Figure 11 contains a summary of the maximum moisture content measured for the additional tests conducted on PT4-1 and PT4-2. Of the conditions listed in the figure, two resulted in soft grout. One was 1.5 · MWD. The other condition was when 2 gal. (7.6 L) of water was placed in the grout injection hose. Pressurized injection and strand at top of tube tests resulted in similar moisture content values to the MWD mixture.

When grout was mixed for the pressurized set test, it was noted that some solids remained in the mixer. Lower than typical flow cone time and unit weight values in the mixer were measured. No solids were noted in the mixer for the high-temperature injection test; however, similar initial unit weight and flow cone results as were measured in the pressurized set test were noted. It is not clear why this occurred, but it is notable that both mixtures in which solids were noted had higher moisture contents.

Table 4—Summary of conditions that produced soft grout in initial pilot tests

Material	Condition	Maximum moisture content
PT4-1	2 gal. (7.6 L) water in tube	53%
	2 gal. (7.6 L) water in hose	65%
	1.5 · MWD	80%
PT4-2	Constriction	61%
	1.15 · MWD	61%
	1.15 · MWD	73%
	2 gal. (7.6 L) water in tube	77%
	1.15 · MWD	80%

Table 5—Summary of conditions that did not produce soft grout in initial pilot tests

Material	Condition	Maximum MC
C45	Standard tube	23%
C675	Standard tube	54%
PT1-2	Constriction	18%
	MWD	19%
	1.15 · MWD*	35%
	1.15 · MWD*	36%
	2 gal. (7.6 L) water in tube*	41%
	1.15 · MWD*	42%
PT2-2	MWD	19%
	Constriction	19%
	2 gal. (7.6 L) water in tube	21%
	1.15 · MWD	22%
	1.15 · MWD	22%
	1.15 · MWD	23%
PT3-1	MWD	18%
	Constriction	20%
	1.15 · MWD	21%
	2 gal. (7.6 L) water in tube	22%
	1.15 · MWD	22%
	1.15 · MWD	23%
PT4-1	Tube full of strand	15%
	MWD	18%
	Pressurized injection (55 psi [380 kPa])	20%
	Strand at top of tube	25%
	MWD	26%
PT4-2	Recirculate through constriction	16%
	Pressurized set (60 psi [414 kPa])	39%
	High-temperature injection	41%

*Porous grout observed.

Note: MC is moisture content.

Moisture content and soft grout

Table 4 provides a summary of the testing conditions that resulted in the formation of soft grout, and Table 5 summarizes testing conditions that did not. Both tables also indicate the maximum moisture content measured in the tube under each condition. The lowest moisture content measured in any soft grout sample was 53%. This sample was observed to be semi-hard but could be scraped out using the tip of a screwdriver. Conversely, the highest moisture content measured in a hardened sample of PT4 was 41%. This sample could not be collected by scraping with a screwdriver. If plain grout C675 is not considered, then the maximum moisture content found in any hardened sample was 42%. Although the definition of soft grout is not based on measurable mechanical properties, the data indicate that if the moisture content approaches 50%, then the sample is likely to fit the description of soft grout.

While the minimum moisture content of a soft grout is likely to be greater than 50%, it was noted that the plain grout sample exhibited higher moisture content but was not necessarily considered soft. This is likely due to the large amount of bleed water that was not present in PT4 tests.

Pressure bleed results

Visual observations were made on the inclined tubes at the following times after injection: 30 minutes, 1 hour, 2 hours, and 24 hours. Bleed water in the tubes was difficult to visually discern for several reasons. First, although the tubes were constructed of clear PVC, the fittings on either end were opaque and covered several inches of grout at the end of the tube. When the tubes were fully grouted, they were completely filled, and small amounts of bleed water would have been covered by the opaque fittings. In addition to the opaque fittings, the grout generally coated the interior wall of the clear PVC tubes during the injection process, making visual bleed readings difficult.

Despite these obstacles, bleed water was still observed in some of the inclined tubes. It is important to note, however, that bleed water may have been present in some of the other tubes, but not necessarily observed. In most cases, however, observed bleed did not correspond to soft grout.

PT1-2 exhibited bleed for 1.15 · MWD. Bleed water was observed to be yellow in color and was located below a layer of porous grout at the top of the tube. Bleed water was not observed until 24 hours after the tube was injected.

PT2-2 exhibited bleed water when 2 gal. (7.6 L) of water was in the tube prior to injection. This was not observed when the tube was in the inclined position, but instead when the tube was cut open 24 hours after injection. PT2-2 also exhibited bleed three times for 1.15 · MWD. In one case, bleed water was observed 2 hours after injection and again 24 hours after injection. In the next case, bleed water was only observed 24 hours after injection. In the final case, bleed water was not observed when grout was in an inclined position, but instead when it was cut open 24 hours after injection. In each case, bleed water was yellow in color.

PT3-1 exhibited bleed when mixed at 1.15 · MWD. In each case, bleed water was visible between 30 minutes and 2 hours after the tube was injected. Twenty-four hours after the tube was injected, however, bleed water was no longer visible. PT3-1 also exhibited bleed water when there was 2 gal. (7.6 L) of water in the tube prior to injection. However, bleed water was not observed until the tube was cut open 24 hours after injection.

PT4-1 and PT4-2 did not exhibit bleed water but rather formed soft grout when extra mixing water was introduced.

Finally, the two plain cement grouts, C45 and C675, both exhibited bleed. Bleed water was visible 30 minutes after injection in each case and continued to be visible 24 hours after injection. Material C675 exhibited bleed water extending approximately 4 ft (1.22 m) down from the top of the tube.

Overall, the bleed water observed during the MITT does not appear to correlate well to the formation of soft grout. Each of the materials, aside from PT4-1 and PT4-2, exhibited bleed water, but not soft grout. PT4-1 and PT4-2, however, exhibited soft grout several times, but did not exhibit bleed water in any case.

Pressure bleed test results

Pressure bleed testing was conducted on several grout samples prepared for the MITT. Samples for the pressure bleed test were collected in the mixer before injection into the tube. PT3-1 and C675 failed the pressure bleed test, yet none produced soft grout under the MITT. This agrees with the findings regarding bleed readings for the MITT, which is that the propensity to bleed does not necessarily indicate an affinity to produce soft grout.

SUMMARY AND CONCLUSIONS

The objective of this research was to determine and be able to reproduce the cause of soft grout that has been discovered in post-tensioning (PT) ducts in several bridges in the United States. This phenomenon has also been noted abroad. A modified version of the Euronorm inclined tube test, called the modified inclined tube test (MITT), was developed and used to conduct most of the testing. The inclined test tube offered a configuration that could be used in a laboratory setting to simulate grout bleed and segregation during full-scale mixing and injection. The change in elevation between the top and the bottom of the inclined test tube causes bleed at the base of the tube to flow upward along the length of the tube due to the pressure head. This bleed then filters or washes out the less-dense particles present in the suspension, resulting in an unreacted putty near the free surface of the grout at the exit of the inclined tube and normal hardened grout along the remaining length of the tube. Modifications to the inclined test method included using a slightly shorter length of bundled strand to facilitate grout sampling at the top end of the tube, sampling and inspecting for soft grout at the top and bottom of the specimen, and measuring moisture content in the sampled grout.

Other common grout fresh property tests, including flow cone, wet density, unit weight, and pressure bleed, were routinely conducted in parallel with the MITT.

None of the commercially available prepackaged PT grouts tested with the MITT produced bleed or soft grout when the grout was mixed and injected in accordance with the manufacturer's recommendations and tested well before the expiration date printed on the bag.

To induce soft grout production, testing was conducted in which several variations on the MITT were introduced to simulate more closely the variations that occur in field conditions. In this series of testing, the following variations were imposed on all the PT grouts tested:

- 15% additional water beyond the maximum recommended water dosage (1.15 · maximum water dosage [MWD])
- Residual water in the tube
- Tube constriction

Additional mixing water and residual water in the tube produced soft grout consistently in one of the PT grouts, and in one case with the tube constriction (PT4). Further tests were conducted on PT4 that involved tubes that were packed full of strands, high-temperature injection, pressurized set, and strand placed in the top of the tube, among others. None of these conditions produced soft grout consistently.

Conclusions can be summarized as follows:

- High-performance prepackaged PT grouts tested at the MWD recommended by their manufacturers and tested well before the expiration date resulted in no soft grout.
- Soft grout was produced in several lots of PT4 under several conditions, which included the introduction of water beyond that recommended by the manufacturer. When extra water was introduced into the mixing or injection process, PT4 was found to produce soft grout. In addition, in one out of the two cases in which the grout was injected through a constricted path, PT4-2 was found to produce soft grout.
- When PT1-2 was mixed with a water dosage greater than MWD, porous hardened grout was found at the top of the inclined tube.
- Except for PT4-1, PT4-2, and PT4-6, high-performance prepackaged PT grouts were robust when subjected to 1.15 · MWD, resulting in no soft grout. PT2-4 did have a higher moisture content of 45% at the exit region of the inclined tube relative to the other four PT grouts, but did not have any visually identifiable soft grout. PT4-6 had a moisture content of 76% at the exit region, with 55.6 g (0.12 lb) of soft grout.
- Supplemental tests of fresh grout properties, such as flow cone, unit weight, wet density, pressure bleed, sedimentation, and bleed readings on inclined tubes, were conducted. The results of these tests did not provide indications that soft grout would be formed during the MITT.

RECOMMENDATIONS

The MITT should be included in the tests used to qualify PT grout formulations. The following are specific suggestions: Test prepackaged grouts under laboratory conditions using a water dosage of 1.15 · MWD recommended by the manufacturer. Fifty-gram (0.11 lb) samples of grout should be taken at the top, middle, and bottom of the inclined tube for the purposes of testing moisture content (ASTM C566-13), which should be limited to a maximum of 35%. This approach, when used in conjunction with the other PTI specification requirements, will ensure robust grout formulations that can withstand accidental or incidental addition of water to the grout formulation.

AUTHOR BIOS

Alex Piper *is the Founder of Piper SE, LLC, where he provides structural consulting services for industrial clients with a focus on steel and reinforced concrete building design. He is also the Founder of SEsort, a software company that develops data analysis tools for structural engineers. He received his bachelor's in civil engineering from Rose-Hulman Institute of Technology, Terre Haute, IN, and his master's in structural engineering from the University of Florida, Gainesville, FL.*

Alexander J. Randell *is a State Construction Structures Engineer for the Florida Department of Transportation. He previously worked at Finley Engineering Group, Inc., as a Bridge Engineer, where he worked on the design of multiple large-scale segmental post-tensioned concrete bridges, including the Wekiva River Bridge, the Bayonne Bridge Approach structures, and the I-90 Dresbach Bridge. He received his BS in civil engineering and his MS in structural engineering from the University of Florida.*

Brett Brunner *is a Senior Associate at Wiss, Janney, Elstner Associates, Inc. (WJE). He is a practicing forensic structural engineer in San Antonio, TX, where he specializes in assessments and analysis of existing structures. He received his BS in civil engineering from the United States Air Force Academy, Colorado Springs, CO, in 2013, and his MS in structural engineering from the University of Florida in 2014. His research interests include grouting in post-tensioned construction.*

H.R. (Trey) Hamilton, *FACI, is Professor Emeritus at the University of Florida and a Senior Engineer at the American Concrete Institute. He has over 40 years of experience in structural engineering research, practice, and education. He is past Chair of the ACI Technical Activities Committee and Joint ACI-ASCE Committee 423, Prestressed Concrete.*

ACKNOWLEDGMENTS

The authors gratefully acknowledge the Florida Department of Transportation for supporting this research under research contract BDK75 977-59.

REFERENCES

1. Powers, R. G.; Sagues, A. A.; and Virmani, Y. P., "Corrosion of Post-Tensioned Tendons in Florida Bridges," Research Report No. FL/DOT/SMO/04-475, Florida Department of Transportation, Tallahassee, FL, Aug. 2004, 17 pp.

2. Corven Engineering, Inc., "Mid Bay Bridge Post-Tensioning Evaluation," final report, Florida Department of Transportation, Tallahassee, FL, 2001, 2622 pp.

3. Corven Engineering, Inc., "New Directions for Florida Post-Tensioned Bridges," final report, Florida Department of Transportation, Tallahassee, FL, 2002, 68 pp.

4. Lau, K.; Lasa, I.; and Paredes, M., "Bridge Tendon Failures in the Presence of Deficient Grout," *Materials Performance*, V. 52, No. 11, 2013, pp. 64-68.

5. Schokker, A.; Koester, B.; Breen, J.; and Kreger, M., "Development of High Performance Grouts for Bonded Post-Tensioning Structures," Center for Transportation Research, The University of Texas at Austin, Austin, TX, 1999, 69 pp.

6. Bertolini, L., and Carsana, M., "High pH Corrosion of Prestressing Steel in Segregated Grout," *Modelling of Corroding Concrete Structures: Proceedings of the Joint* fib*-RILEM Workshop held in Madrid, Spain, 22–23 November 2010*, C. Andrade and G. Mancini, eds., Springer, Dordrecht, the Netherlands, 2011, pp. 147-158.

7. ASTM C1741-18, "Standard Test Method for Bleed Stability of Cementitious Post-Tensioning Tendon Grout," ASTM International, West Conshohoken, PA, 2018, 4 pp.

8. ASTM C940-10, "Standard Test Method for Expansion and Bleeding of Freshly Mixed Grouts for Preplaced-Aggregate Concrete in the Laboratory," ASTM International, West Conshohoken, PA, 2010, 3 pp.

9. Fuzier, J. P., "Development of Grout and Grouting Techniques," *Durability of Post-Tensioning Tendons*, *fib* Bulletin No. 15, 2001, pp. 173-194.

10. Chaussin, R., and Chabert, A., "Strategies for Improvement - Approach in France," *Durability of Post-Tensioning Tendons*, *fib* Bulletin No. 15, 2001, pp. 235-244.

11. EN 445:2007, "Grout for Prestressing Tendons: Test Methods," European Committee for Standardization, Brussels, Belgium, 2007, 18 pp.

12. PTI Committee M-55, "Specification for Grouting of Post-Tensioned Structures (PTI M55.1-12)," Post-Tensioning Institute, Farmington Hills, MI, 2012.

13. Piper, A.; Randell, A.; Brunner, B.; and Hamilton, H. R., "Simulation of Prepackaged Grout Bleed under Field Conditions," Report No. BDK75 977-59, Florida Department of Transportation, Tallahassee, FL, 2014, 149 pp.

14. ASTM C566-13, "Standard Test Method for Total Evaporable Moisture Content of Aggregate by Drying," ASTM International, West Conshohoken, PA, 2013, 3 pp.

15. Piper, A.; Randell, A.; Brunner, B.; Ferraris, C. F.; and Hamilton, H. R., "Development of Laboratory Test Method to Replace the Simulated High-Temperature Fluidity Test," Report No. BDK75 977-39, Florida Department of Transportation, Tallahassee, FL, June 2014, 126 pp.

16. ASTM C1741-12, "Standard Test Method for Bleed Stability of Cementitious Post-Tensioning Tendon Grout," ASTM International, West Conshohoken, PA, 2012, 4 pp.

17. ASTM C138/C138M-14, "Standard Test Method for Density (Unit Weight), Yield, and Air Content (Gravimetric) of Concrete," ASTM International, West Conshohoken, PA, 2014, 4 pp.

ACI MATERIALS JOURNAL TECHNICAL PAPER

Title No. 122-M31

Predicting Ultrasonic Pulse Velocity for Concrete Health Monitoring

by Mohammad Rahmati and Vahab Toufigh

This study employs machine learning (ML) to predict ultrasonic pulse velocity (UPV) based on the mixture composition and curing conditions of concrete. A data set was compiled using 1495 experimental tests. Extreme gradient boosting (XGBoost) and support vector regression (SVR) were applied to predict UPV in both direct and surface transmissions. The Monte Carlo approach was used to assess model performance under input fluctuations. Feature-importance analyses, including the SHapley Additive exPlanation (SHAP), were conducted to evaluate the influence of input variables on wave propagation velocity in concrete. Based on the results, XGBoost outperformed SVR in predicting both direct and surface UPV. The accuracy of the XGBoost model was reflected in average R^2 *values of 0.8724 and 0.9088 for direct and surface UPV, respectively. For the SVR algorithm,* R^2 *values were 0.8362 and 0.8465 for direct and surface UPV, respectively. In contrast, linear regression exhibited poor performance, with average* R^2 *values of 0.6856 and 0.6801 for direct and surface UPV. Among the input features, curing pressure had the greatest impact on UPV, followed by cement content. Water content and concrete age also demonstrated high importance. In contrast, sulfite in fine aggregates and the type of coarse aggregates were the least influential variables. Overall, the findings indicate that ML approaches can reliably predict UPV in healthy concrete, offering a useful step toward more precise health monitoring through the detection of UPV deviations caused by potential damage.*

Keywords: concrete health monitoring; extreme gradient boosting (XGBoost); feature importance; machine learning (ML); support vector regression (SVR); ultrasonic pulse velocity (UPV).

INTRODUCTION

Concrete is one of the most popular construction materials and has been used in many infrastructures due to its advantages including low cost, high durability, and thermal resistivity.[1-5] However, concrete and other construction materials can experience degradation and deterioration during their lifetime.[6-8] Therefore, it is essential to have highly accurate quality assessment techniques. Nondestructive testing (NDT) methods have been used for decades for quality control. Among the various NDT methods, elastic wave propagation techniques such as ultrasonic testing and acoustic emission monitoring have gained significant popularity due to their low equipment costs, user-friendly operation, and high sensitivity to material defects.[9,10] Ultrasonic pulse velocity (UPV) is one of the most commonly used testing approaches for determining the quality and homogeneity of materials.

Numerous researchers used the UPV technique to evaluate concrete under different environmental conditions.[11,12] Hwang et al.[13] investigated the deterioration of ordinary and ultra-high-strength concrete exposed to high temperatures using the UPV method. It was reported that the UPV method could monitor damage inside the concrete. More specifically, a decrease in the pulse velocity accompanied an increase in crack width. Camara et al.[14] studied the self-healing of concrete using the UPV approach. It was observed that the UPV decreases at the stage in which the specimens are cracked. However, the self-healing process recovered the UPV. Additionally, the studies in the literature reveal that UPV is well-correlated with concrete ingredients and properties. For instance, UPV was effectively used to determine the concrete's water content, porosity, elasticity modulus, Poisson's ratio, compressive strength, water absorption, and aggregate textural properties.[15-17] These findings indicate the robustness of the UPV method in the nondestructive assessment of concrete.

Damage in a material influences the velocity of waves passing through it. The deviations of measured pulse velocities from the velocity at which the wave propagates in the undamaged state of material are used to assess the severity of damage.[18] Whitehurst[19] proposed a classification procedure for evaluating the quality of normal concrete based on UPV test results. More specifically, different ranges of UPV were presented, categorizing concrete conditions as excellent, good, regular, poor, and very poor. Carino[20] asserted that researchers mainly rely on this classification to expound UPV tests. However, it is worth noting that the results of UPV tests on concrete in intact status differ based on the concrete mixture. The deviation is attributed to the different aggregates, binders, chemical and mineral additives, moisture content, curing conditions, age, and so on that affect wave propagation velocity. Therefore, accurately defining the concrete condition solely through a predetermined set of classified velocity ranges is inherently challenging. To enhance the efficacy of UPV-based nondestructive evaluation, the development of robust frameworks is essential.

One effective approach to refine this methodology involves integrating specific concrete characteristics such as mixture design and curing conditions into the UPV assessment process. By creating methods that can precisely determine wave propagation velocity in intact concrete with defined attributes, the accuracy and reliability of damage evaluation

---

ACI Materials Journal, V. 122, No. 5, September 2025.
MS No. M-2023-340.R5, doi: 10.14359/51747869, received April 11, 2025, and reviewed under Institute publication policies. Pertinent discussion including author's closure, if any, will be published ten months from this journal's date if the discussion is received within four months of the paper's print publication.

using the UPV technique can be significantly enhanced. This advancement would not only improve diagnostic capabilities but also facilitate more informed decision-making regarding the structural integrity of concrete materials. However, many variables complicate the relationship between UPV and material properties. Therefore, it is imperative to use robust methods to predict the UPV well. Machine learning (ML) and data-driven modeling as modern methods for estimating materials' characteristics can be used for this purpose.

Construction materials studies demonstrate the remarkable recent interest in using data-driven models and ML techniques to predict and classify tasks regarding concrete properties. In general, data-driven models refer to a set of computationally intelligent methods that predict a certain characteristic of a particular class of data.[21] Nguyen et al.[22] investigated the efficiency of artificial neural network (ANN) and adaptive neuro-fuzzy inference system (ANFIS) in predicting the compressive strength of fiber-reinforced high-strength self-consolidating concrete. It was demonstrated that ANN outperformed ANFIS, showing coefficient of determination (R^2) values equal to 0.9742 for ANN and 0.9584 for ANFIS. Additionally, the potential of data-driven and ML methods can be combined with metaheuristic optimization technology to reach high precisions.[23,24]

In recent years, ML techniques such as extreme gradient boosting (XGBoost) and support vector regression (SVR) have gained significant attention for their effectiveness in predictive modeling tasks. XGBoost, a powerful ensemble learning method based on gradient boosting, has been widely used for its ability to handle complex patterns and large data sets efficiently.[25] On the other hand, SVR, a kernel-based method derived from support vector machines (SVMs), is known for its robustness in modeling complex nonlinear dependencies.[26] Given their success, studies have explored their applications in concrete research. Safhi et al.[27] predicted the rheological properties of self-consolidating concrete using the XGBoost method. Their findings indicated that the XGBoost model effectively captured the relationship between concrete mixture parameters and rheological properties, achieving R^2 values of 0.98 for plastic viscosity and 0.87 for yield stress. Singh and Rajhans[28] developed SVR models to predict the mechanical properties of concrete made with recycled concrete aggregate. It was reported that the model accurately predicted compressive, flexural, and splitting tensile strengths with accuracies of 97%, 95%, and 88%, respectively.

Despite the recent significant interest in using ML methods in materials and engineering, relatively few research studies have been conducted to predict UPV using ML methods.[29,30] Numerous studies have been reported on ML algorithms' capabilities in estimating the compressive strength of various types of concrete. However, the prediction of pulse velocity based on concrete mixture design and preparation method has not been thoroughly studied. It is important to comprehensively investigate the performance of different ML models in predicting wave velocity in various types of concrete. Developing general frameworks for using artificial intelligence approaches in NDT would improve the health monitoring procedure of concrete structures.

The current study employed XGBoost and SVR models to predict direct and surface UPVs. The results of 1495 ultrasonic tests were collected from previous research studies. Data related to several concrete characteristics were used as input features, while UPV values served as the outputs. Hyperparameter tuning was performed using the grid search method to improve the models' accuracy. A Monte Carlo approach was applied to evaluate model performance under input uncertainty. This sensitivity analysis included 100 Monte Carlo simulations for each developed model. The coefficient of determination was used as the primary evaluation metric, and linear regression was implemented as a baseline model for comparison. Finally, feature importance analyses were conducted to identify the most influential parameters affecting UPV.

RESEARCH SIGNIFICANCE

A widely used nondestructive evaluation method involves performing UPV tests on existing concrete and comparing the results to predefined ranges that classify the condition of the concrete. However, these classification ranges are often too general. Given the high variability in concrete mixtures, it is challenging to accurately assess the condition of concrete using a fixed set of velocity thresholds. A potential enhancement to this approach is to employ ML to predict the expected UPV of healthy concrete based on its mixture design. The deviation between the measured UPV of in-place concrete and the ML-predicted value can then serve as an indicator of potential damage severity.

DATA SET DESCRIPTION

The concrete and UPV test data are derived from previously published experiments.[31-38] The experiments from which data were collected used ordinary portland cement and sulfate-resisting cement for making concrete. Different curing conditions were included in the collected data set. Water, air, and pressure steam curing of 2, 4, and 8 bars were considered. Table 1 presents the descriptive statistics of the data set. Table 2 shows a subset of the data used for training the ML models. Two separate data sets were used to develop models, which included a total of 1495 input-output data pairs. Specifically, the first data set comprised 873 samples corresponding to UPV in direct measurement, and the second data set included 622 instances related to UPV in surface measurement. The schematic representation of direct and surface UPV tests is illustrated in Fig. 1.

For illustrative purposes, the statistical distributions of some of the concrete attributes in the data set are presented in Fig. 2. A comprehensive correlation analysis was performed to provide a heatmap demonstrating clear correlation values between all of the components in the data set. Figure 3 presents the correlation heatmap between the concrete attributes and UPVs. As shown in the heatmap, direct UPV was positively correlated with cement, fine aggregates, concrete age, and fiber. In contrast, direct UPV had a negative correlation with the coarse aggregate and water. Surface UPV was positively correlated with cement and concrete age. Moreover, the surface UPV was negatively correlated with the pressure of curing and sulfite content in the fine aggregates.

Table 1—Descriptive statistics of data set

Parameter	Average	Minimum	Maximum	Std
Coarse aggregate content, kg/m^3	1035.06	0	1564.22	255.83
Fine aggregate content, kg/m^3	730.60	0	1567	160.82
Cement content, kg/m^3	397.45	166.54	1803	124.86
Water content, kg/m^3	194.21	130.99	511	29.22
Concrete age, days	38.56	1	365	44.83
Steam curing pressure, bar	3.66	2	8	2.01
Slump, mm	51.90	5	115	30.89
Metakaolin, kg/m^3	0.74	0	47.90	5.38
Silica fume, kg/m^3	1.44	0	180	12.83
Fiber, kg/m^3	2.51	0	1.56	11.94
High-range water-reducing admixture, kg/m^3	0.32	0	21	1.48
SO_3 in fine aggregate, %	0.92	0.34	4.45	1.11
Direct UPV, m/s	4399.35	1320	5190	465.63
Surface UPV, m/s	4332.87	490	5420	821.12

Note: Std is standard deviation.

Table 2—Examples of gathered data set (in part)

ID No.	CA	FA	C	W	SP	SF	Fiber	MT	Age, days	Curing	Fiber type	UPV, m/s
	kg/m^3											
1	1098.9	581.5	471.6	217	2.4	—	—	—	7	Water	—	4230
2	1107.3	586	451.5	218.6	2.4	—	—	23.9	7	Water	—	4280
59	990	618	462	185	2.3	—	—	—	365	Water	—	4700
65	1035	480	648	180	—	72	—	—	7	Water	—	4700
107	862	908	332	192.6	—	—	—	—	90	Water	—	4620
147	735.7	1022.7	521.8	167	—	—	39	—	7	Water	Steel	5100
158	713.3	991.5	505.9	192.2	—	—	13.5	—	7	Water	Glass	5090
161	733.9	1020.1	520.5	166.6	—	—	20.2	—	7	Water	Glass	5230
166	737.6	1025.3	523.11	167.4	—	—	2.27	—	7	Water	Nylon	5350
167	735.7	1022.7	521.8	167	—	—	4.55	—	7	Water	Nylon	5380
211	733.9	1020.1	520.5	166.6	—	—	58.5	—	44	Water	Steel	6100
243	946	772	450	139	10	45	39	—	28	Water	Steel	5137
567	1109	708.2	345.5	207.3	—	—	—	—	28	Air	—	4410
574	1088.1	724.4	313.6	203.8	—	—	—	—	90	Air	—	4580
612	1232.1	753.9	235.6	188.5	—	—	—	—	28	Air	—	4650
827	1015.4	796.6	237.8	190.2	—	—	—	—	2	Pressure (4 bar)	—	3050
871	1092.4	857	255.8	204.7	—	—	—	—	2	Pressure (8 bar)	—	3610

Note: CA is coarse aggregate; FA is fine aggregate; C is cement; W is water; SP is high-range water-reducing admixture; SF is silica fume; and MT is metakaolin.

Generally, the features that have strong correlations with target characteristics can be neglected during model development to reduce computational time and cost. However, all of the mentioned features were considered in this study to have a comprehensive investigation.

MACHINE LEARNING METHODOLOGY

Extreme gradient boosting (XGBoost)

XGBoost is a decision tree-based model that uses gradient boosting to ensemble the outputs of several base predictors as the final result. Thus, over-fitting is prevented.[39] This method is developed to work well with sparse data, which is frequently found in real-world data sets that have frequent

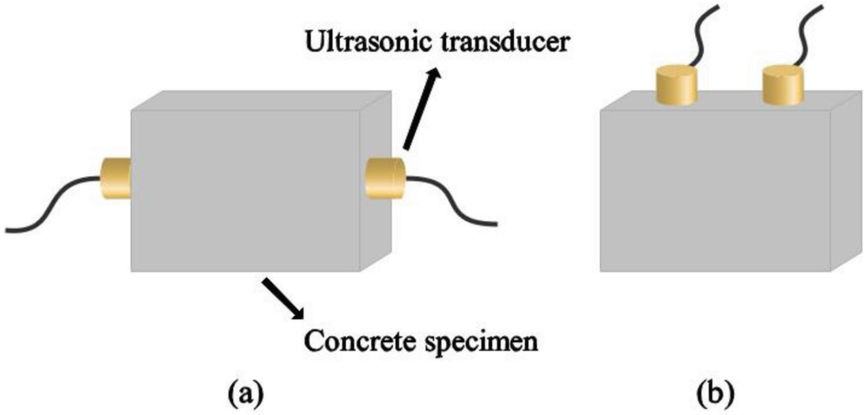

Fig. 1—Schematic representation of UPV measurement: (a) direct UPV; and (b) surface UPV.

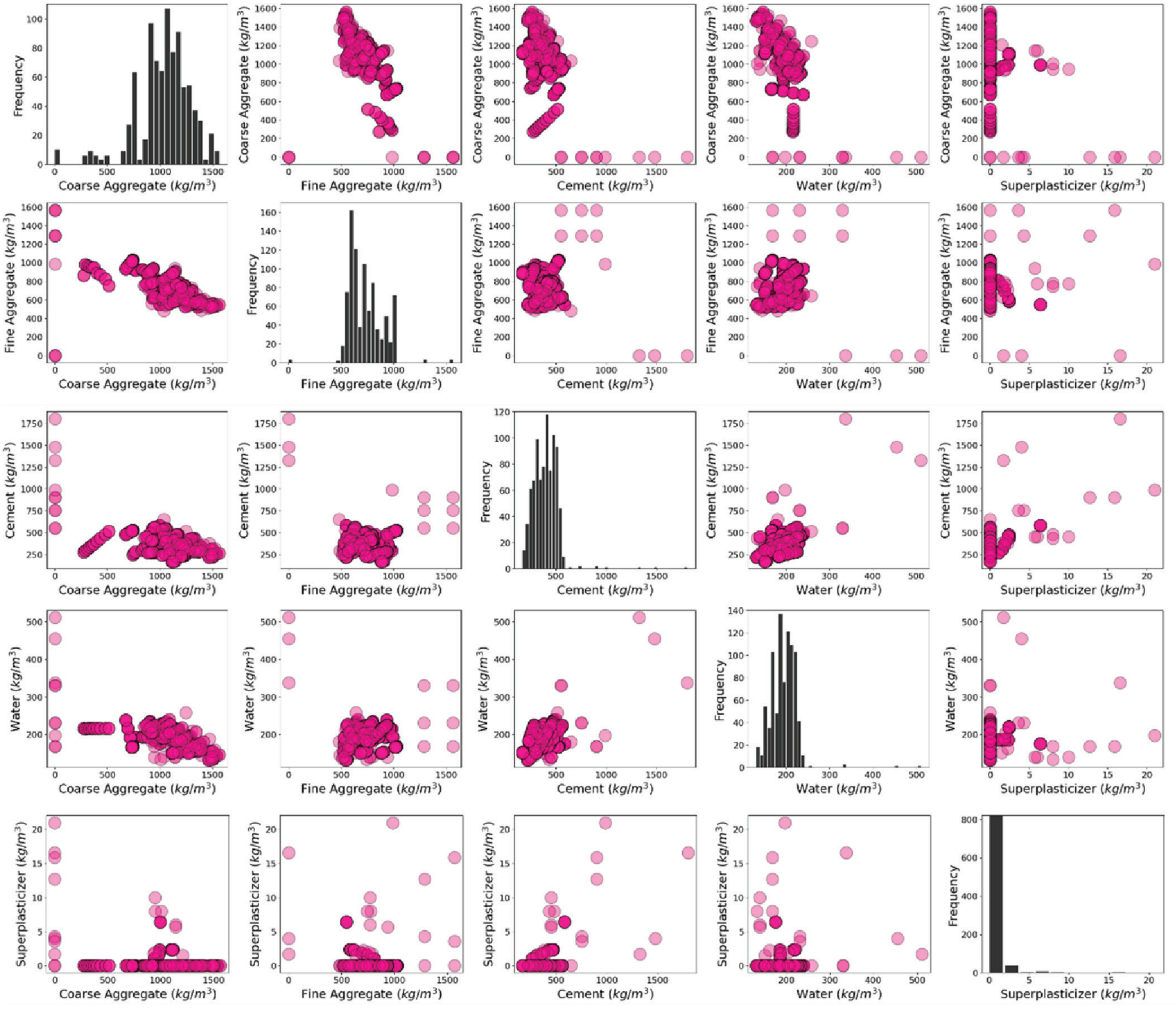

Fig. 2—Statistical distribution of concrete attributes in data set.

zero entries or missing values.[40] The prediction is performed using many additive functions as Eq. (1)[41]

$$\bar{y}_i = y_i^0 + \eta \sum_{k=1}^{N} f_k(X_i) \tag{1}$$

where $\bar{y}_i$ is the predicted result corresponding to the i-th instance with the feature vector X_i; y_i^0 represents the initial hypothesis (commonly the mean of the values in the training set); and η is known as the learning rate or shrinkage parameter. It enhances the efficiency of the model while appending new trees. Therefore, over-fitting is avoided. The process of model training is performed in an additive approach. In

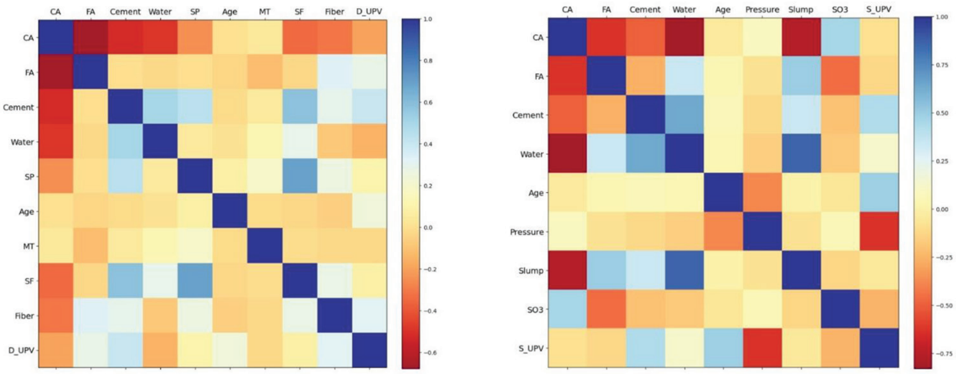

(a) (b)

Fig. 3—Correlation matrix of attributes in data set: (a) direct UPV data set; and (b) surface UPV data set.

other words, the additional *k*-th estimator is connected to the model at the *k*-th iteration. Knowing the value of prediction at the previous iteration, $\bar{y}_i^{-(k-1)}$, and the estimation f_k of the additional estimator, the predicted output $\bar{y}_i^{-k}$ is then calculated as Eq. (2)[42]

$$\bar{y}_i^{-k} = \bar{y}_i^{-(k-1)} + \eta f_k \tag{2}$$

where f_k is the leaves' weights, which are obtained through minimizing an objective function. The regularized objective function can be expressed as Eq. (3)[41]

$$L(\phi) = \sum_i l(\bar{y}_i, y_i) + \sum_k \Omega(f_k) \tag{3}$$

where $l(\bar{y}_i, y_i)$ is the loss function, measuring how much the predicted outputs deviate from actual targets; and $\Omega(f_k)$ is the regularization function inflicting a penalty on the model complexity. This action helps to prevent over-fitting.[43] The regularization is expressed as

$$\Omega(f) = \gamma T + \frac{1}{2}\lambda \|\omega\|^2 \tag{4}$$

where T indicates the number of leaf nodes; ω represents the weights of leaf nodes; and γ and λ are controlling parameters used to prevent over-fitting.[44]

Support vector regression (SVR)

SVM is a powerful method developed by Vapnik et al.[45] to solve classification problems. This kernel-based method also extended to deal with regression tasks using Vapnik's ε-insensitive loss function and was named support vector regression (SVR).[46] The SVR was chosen in this research because of its effective application in simulating engineering processes related to construction materials.[2,43,47,48] The methodology of SVR is concisely introduced in the following.

Consider a data set containing $\{(x_i, y_i)i = 1, \ldots, k\}$, where x_i is the vector of input variables, y_i is the vector of outputs, and k denotes the number of training instances. In the case of nonlinear regression, the function $f(x)$ can be expressed as Eq. (5)[49]

$$f(x, w) = \langle w \cdot \Phi(x) \rangle + b \tag{5}$$

where w represents weights, specifying how the discriminating plane is orientated; $\Phi(x)$ is a nonlinear mapping function; and b is the bias term.

The SVR minimizes the Euclidean norm of the weight vector using non-negative slack variables (ξ_i, ξ_i^*) through an optimization problem formulated as follows

$$\text{Minimize}\left[\frac{1}{2}\|w\|^2 + C\left(\sum_{i=1}^{k}\xi_i + \sum_{i=1}^{k}\xi_i^*\right)\right] \tag{6}$$

which is subjected to

$$\begin{cases} y_i - w \cdot \Phi(x_i) - b \leq \varepsilon + \xi_i^* \\ w \cdot \Phi(x_i) + b - y_i \leq \varepsilon + \xi_i^*, \qquad i = 1, \ldots, k \\ \xi_i^*, \xi_i \geq 0 \end{cases} \tag{7}$$

In Eq. (6), C denotes a constant mediating the model flatness and the empirical error. Next, Lagrange multipliers are involved in solving Eq. (6), and the optimization is transformed into a dual-quadratic programming problem.[49] Finally, the function $f(x)$ can be represented as

$$f(x) = \sum_{i=1}^{k}(\alpha_i^* - \alpha_i)K(x_i \cdot x) + b \tag{8}$$

where $K(x_i \cdot x_j) = \Phi(x_i) \cdot \Phi(x_j)$ indicates the kernel function; and α and α^* are Lagrange multipliers.

MODEL ESTABLISHMENT

The Python programming language was chosen to perform ML-based predictions of direct and surface UPV. Data preprocessing is one of the most important primary steps in ML model development because the variables could possess different scales, missing values, and so on. For instance, in this study, the age of concrete varied between 1 and 365 days, while the cement ranged between 166.54 and 1803 kg/m^3. Normalization can enhance the performance and convergence of ML models by mitigating the scale effect. Moreover, it also improves the model against outliers as it takes the mean and standard deviation of the data into the calculation.[50] Therefore, it is crucial to normalize the data to have a common scale during model development. The normalization was performed according to Eq. (9)

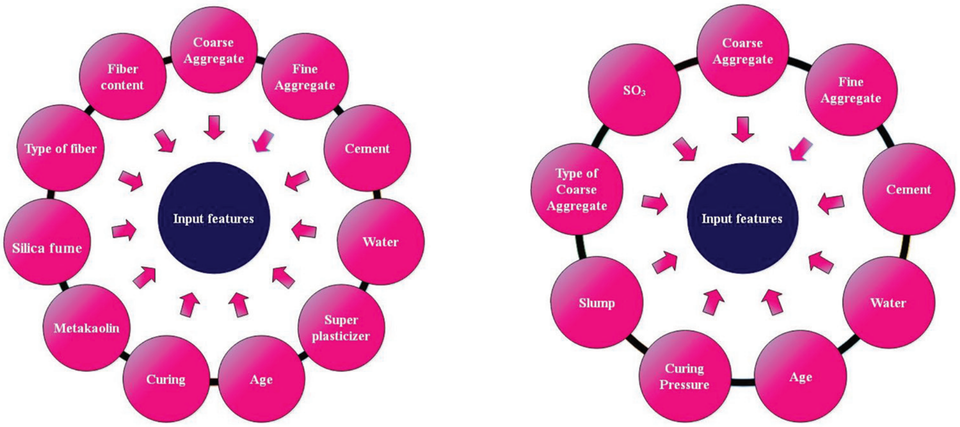

(a) (b)

Fig. 4—Input features used to develop ML models: (a) direct UPV predictors; and (b) surface UPV predictors.

$$Z = \frac{x - \mu}{\sigma} \tag{9}$$

where x denotes the original variable; μ represents the mean of the variable; and σ is the standard deviation.

Next, the data samples were randomly shuffled to avoid biases and enhance generalization. The data set was partitioned into two sections in a 7:3 ratio, where 70% of the data was used to train the model and the remaining 30% was employed in the testing stage. A variety of hyperparameters exist owing to the scalability property, laying the foundation of the XGBoost system.[43] Tuning hyperparameters can significantly improve the model's accuracy. This study selected four hyperparameters of the XGBoost for tuning: colsample_bytree and n_estimators, subsample, and max_depth. The hyperparameter colsample_bytree indicates the subsampling ratio of features in a given tree. The hyperparameter n_estimators represents the number of boosted trees.[51] The hyperparameter subsample handles the ratio of observations used for each tree. The hyperparameter max_depth specifies the maximum depth of a tree. For the SVR model, the radial basis function (RBF) was used as a kernel function. Moreover, the two hyperparameters, C and gamma (γ), were considered for tuning. C specifies a penalty for margin-violated samples and controls the scope of the decision boundary. As previously mentioned, SVR uses a kernel approach to make data linearly separable, and the hyperparameter γ is related to the RBF kernel. It ascertains the influence of individual training instances on hyperplane.[43] The scenario considered to develop ML models using all of the features existing in the data set, as shown in Fig. 4.

An evaluation criterion was employed to measure the accuracy of statistical models. In this research, the coefficient of determination (R^2) was selected to monitor the performance of ML models and is expressed as Eq. (10)[52]

$$R^2 = 1 - \frac{\sum_{i=1}^{n} (y_i - \hat{y}_i)^2}{\sum_{i=1}^{n} (y_i - \bar{y})^2} \tag{10}$$

where y_i represents the target value; $\hat{y}_i$ is defined as the predicted output; $\bar{y}$ denotes the average of the targets; and n expresses the number of samples.

MONTE CARLO SIMULATION

As the first step of developing an ML model, it is common to randomly split data into training and testing parts with a predefined portion. The optimal values of weights are then determined during the training phase based on the feed data. The random process lies in selecting training samples that could undoubtedly influence ML models' performance. Therefore, it is important to investigate the robustness and efficiency of ML models during this random operation. To this aim, the Monte Carlo simulation was adopted. Each ML model was independently run 100 times while the training instances were randomly selected and fed to the model in each run. The evaluation criterion, R^2, was used to investigate the models' precision.

RESULTS AND DISCUSSION

XGBoost

Hybrid grid searches were performed for each model. The colsample_bytree ranged from 0.3 to 1.0, with increments of 0.01. The number of trees varied from 300 to 800, with increments of 20. The subsample ranged from 0 to 0.9, with increments of 0.1. The max_depth ranged from 3 to 9, with increments of 1. Figure 5 illustrates the contours of calculated R^2 during hybrid grid searches for XGBoost models predicting direct and surface UPV. The combination of colsample_bytree equal to 0.9 and the number of trees equal to 360 resulted in an R^2 equal to 0.8902 for the direct UPV predictive model. Also, the subsample equal to 0.9 and the max_depth equal to 6 showed the best combination, resulting in an R^2 equal to 0.9092 for the direct UPV predictive model. For surface UPV predictive models, the combination of colsample_bytree equal to 0.77 and the number of trees equal to 780 resulted in an R^2 equal to 0.9156. Also, the subsample equal to 0.7 and the max_depth equal to 3 showed the best combination, resulting in an R^2 equal to 0.9260 for the direct UPV predictive model.

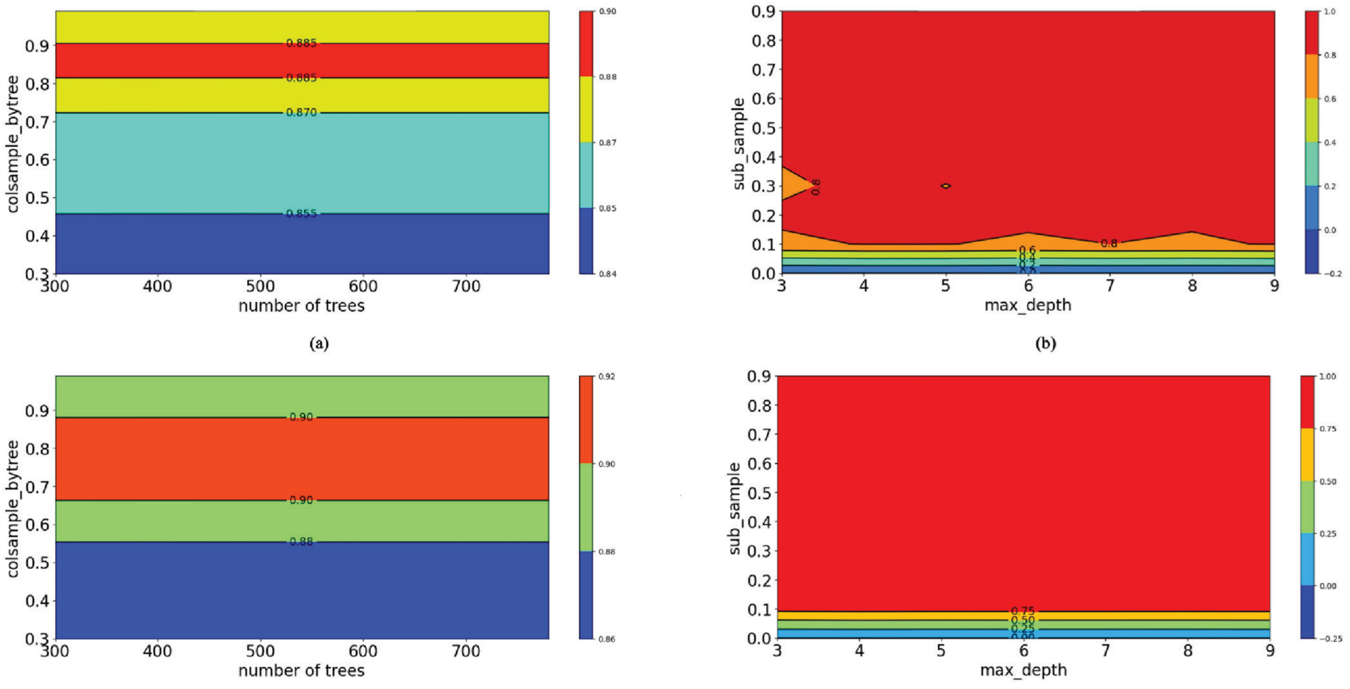

(a) (b)

(c) (d)

Fig. 5—Contours of R^2 *values related to XGBoost models during hybrid grid search for: (a) direct UPV; (b) direct UPV; (c) surface UPV; and (d) surface UPV.*

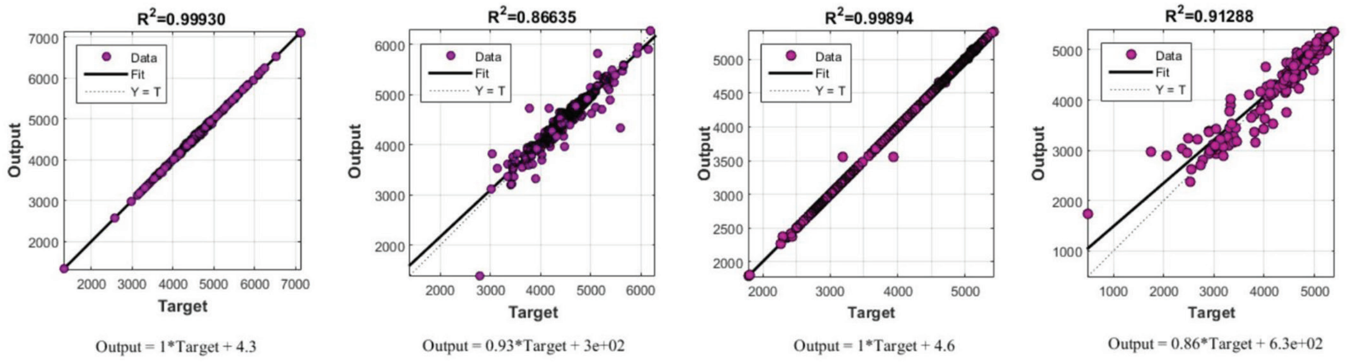

(a) (b) (c) (d)

Fig. 6—Correlation plot of XGBoost model's predicted outputs with experimental targets: (a) training data-direct UPV; (b) testing data-direct UPV; (c) training data-surface UPV; and (d) testing data-surface UPV.

The obtained optimal values of hyperparameters were then set in XGBoost models to perform Monte Carlo simulations. As previously mentioned, 100 different cases for each direct and surface UPV predictive model were run in the Monte Carlo simulation. At the same time, training samples were randomly changed in each run. R^2 was determined in each run, and the average of 100 R^2 values was calculated. Among the 100 developed models, the model with the closest R^2 to that average value of R^2 was selected as the main predictive model. The mentioned approach determines models based on average accuracy. Thus, they could be well representative of the performance of ML algorithms.

Figure 6 illustrates the best-fit lines demonstrating the relationship between the estimated outputs of direct and surface UPV predictive models and experimental targets. The satisfactory coefficients of determination were observed in the testing phase of XGBoost models for direct UPV and surface UPV models as $R^2 = 0.8663$ and 0.9128, respectively. Also, the values of 0.9993 and 0.9989 were perceived in the training procedure for direct and surface UPV predictors, respectively. The test data showed that surface UPV was more accurately predicted than direct UPV using the XGBoost method. This could be attributed to the more sources of data samples in the direct UPV data set. Accordingly, the wave velocity inside concrete can be efficiently predicted using the XGBoost algorithm without the expense of many experiments. It is perceived that the XGBoost algorithm is powerfully applicable in addressing complex problems related to wave propagation in concrete materials. Figure 7 presents the variation of R^2 during the performed Monte Carlo simulations.

SVR

A hybrid grid search was performed for each direct and surface predictive SVR model in which C changed between 16,000 and 20,000 with an increment of 400. At the same time, γ varied between 0.01 and 0.72 with an increment of 0.02. Figure 8 illustrates the results of the hybrid grid search. The highest R^2 value for the direct UPV model was 0.8732. This accuracy was achieved for C = 16,000 and γ = 0.069. The best performance of the surface UPV predictive model was R^2 = 0.8721, in which C = 16,400 and γ = 0.049 were the optimal values of hyperparameters.

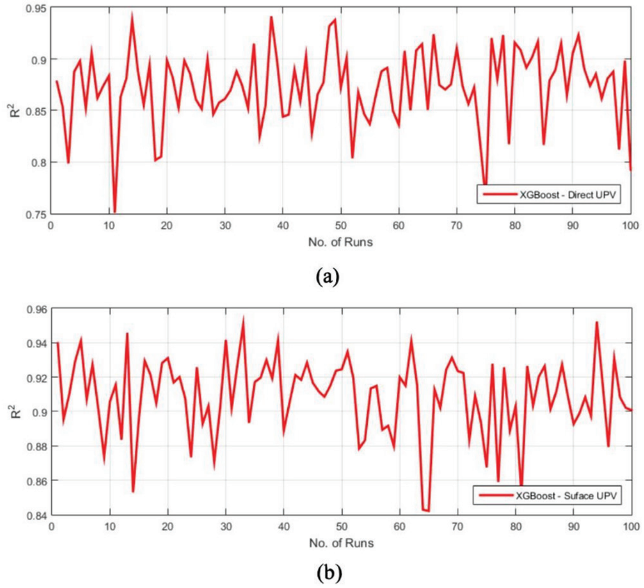

Fig. 7—Variation of R^2 *test data of XGBoost models during Monte Carlo simulation: (a) direct UPV; and (b) surface UPV.*

Next, the perceived optimal values of hyperparameters were set in the SVR models, and a Monte Carlo simulation was performed. The relationship between the predicted outputs and experimental targets of SVR models is presented using best-fitting curves as shown in Fig. 9. The results indicate that the SVR model well estimates the direct UPV with an accuracy of R^2 = 0.9079 and 0.8289 in the training and testing phases, respectively. Additionally, the surface UPV was predicted with high accuracy, showing R^2 = 0.9087 and 0.8545 in the model's training and testing, respectively. The obtained results demonstrate that the SVR algorithm predicts surface UPV more accurately than direct UPV. This could be attributed to the more sources of data instances in the direct UPV data set. Moreover, the performance of SVR during the Monte Carlo simulation was evaluated using the R^2 measure as presented in Fig. 10, demonstrating the influence of input fluctuations.

The measured accuracies of the developed models are presented in Table 3. These values are the average of R^2 scores obtained during 100 runs for each model. In the training step of both direct and surface UPV predictive models, the XGBoost method demonstrated higher precision than the SVR algorithm. However, the superiority of a model should be deduced based on the testing part. According to the test data, it is again perceived that XGBoost outperformed

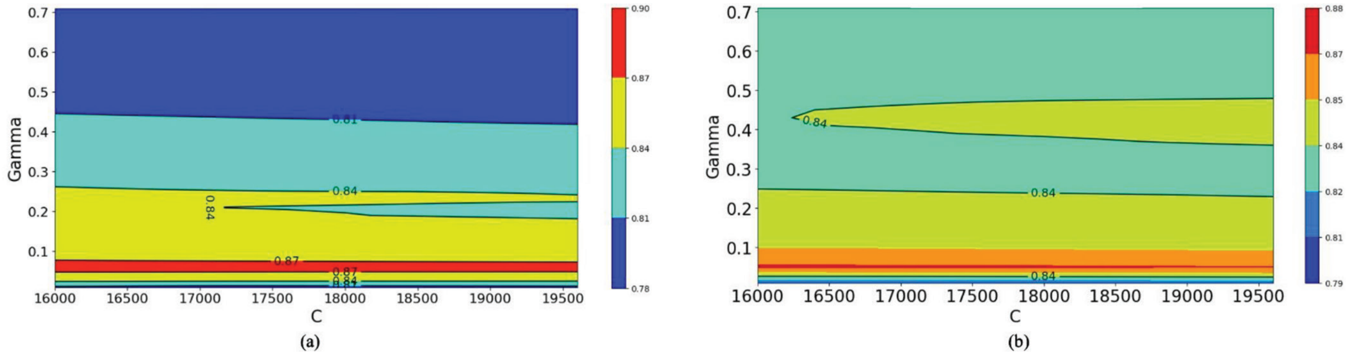

Fig. 8—Contours of R^2 *values related to SVR models during hybrid grid search for: (a) direct UPV; and (b) surface UPV.*

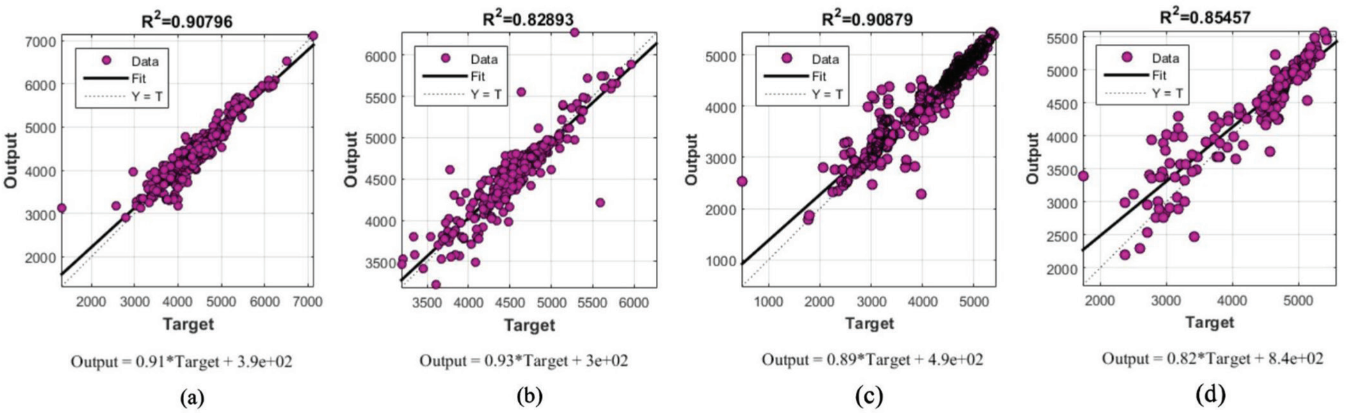

Fig. 9—Correlation plot of SVR model's predicted outputs with experimental targets: (a) training data-direct UPV; (b) testing data-direct UPV; (c) training data-surface UPV; and (d) testing data-surface UPV.

Table 3—Values of evaluation criterion for different ML models

R^2 average	XGBoost-Direct UPV	XGBoost-Surface UPV	SVR-Direct UPV	SVR-Surface UPV
Training data	0.9991	0.9995	0.9096	0.9093
Testing data	0.8724	0.9088	0.8362	0.8465

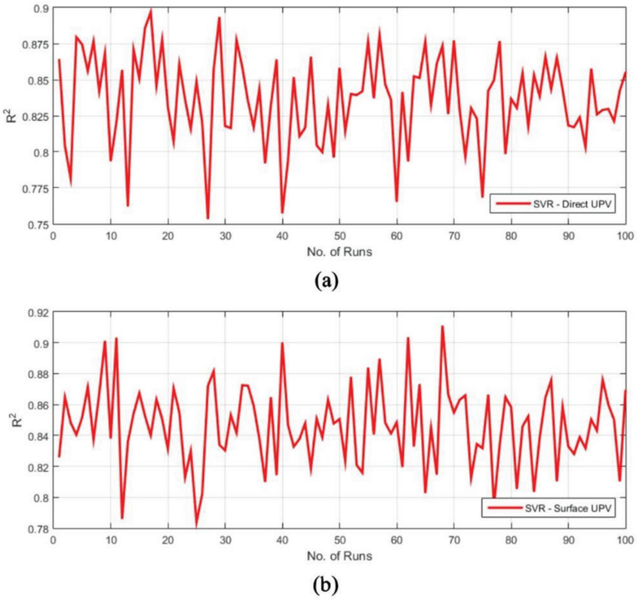

Fig. 10—Variation of R^2 *test data of SVR models during Monte Carlo simulation: (a) direct UPV; and (b) surface UPV.*

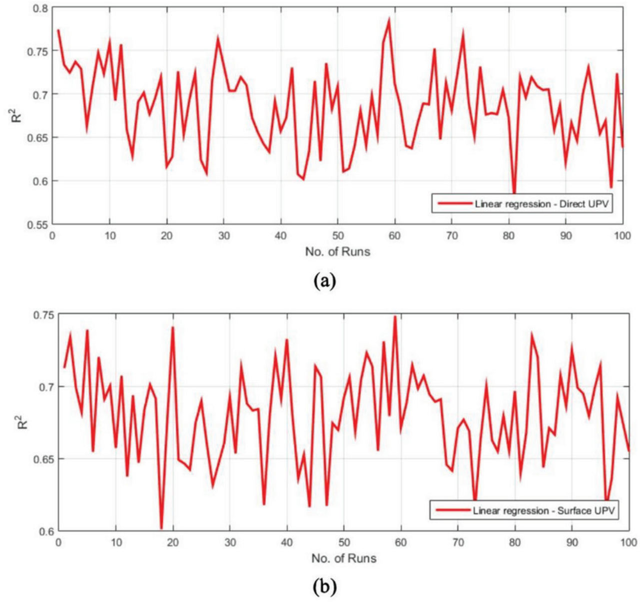

Fig. 11—Variation of R^2 *test data of linear regression models during Monte Carlo simulation: (a) direct UPV; and (b) surface UPV.*

SVR in predicting direct and surface UPV. This superiority could be attributed to the ensemble nature of the XGBoost algorithm. Generally, the two used methods possessed extreme accuracy in predicting the propagating wave velocities inside cementitious materials and have the potential to be successfully adopted in real-world applications—for example, stress wave-based health monitoring.

Linear regression

Linear regression, as a baseline model, was also used to predict the direct and surface UPV. The results of R^2 during the Monte Carlo simulation are illustrated in Fig. 11. The average R^2 values were obtained as 0.6856 and 0.6801 for direct and surface UPV models, respectively. Comparing the ML models with linear regression can better demonstrate the efficiency of the proposed methods. Accordingly, the XGBoost method demonstrated a 27% and 33% improvement compared to linear regression counterpart models for direct and surface UPV, respectively. The SVR precision was approximately 22% and 24% higher than the counterpart linear regression models for direct and surface UPV prediction, respectively.

Feature importance

Feature importance analysis investigated the significance of concrete attributes used as models' inputs on wave propagation velocity for the concrete. The SHapley Additive exPlanation (SHAP) technique introduced by Lundberg was used to explain the employed XGBoost model for direct UPV.[53] Moreover, the SVR permutation feature importance option was adopted to assess the interpretability of the surface UPV predictive model. It is important to note that uncertainties in the inputs and random selection can also affect the significance of the attributes. Thus, a Monte Carlo simulation comprising 100 different runs was again performed, and the average of feature importance degrees was calculated for each attribute. Figures 12 and 13 illustrate the results of SHAP and permutation feature importance analyses. The obtained results show that for both models, curing pressure plays the most important role in determining the UPV values inside the concrete, followed by cement content. Afterward, the water content and concrete age were the parameters that mainly contributed to determining UPV values.

It is important to shed light on the underlying mechanism and investigate the influence of key factors on UPV. Previous experimental research reported that the curing conditions significantly affect the mechanical properties of cementitious materials and UPV. The curing conditions can positively or negatively influence the material's microstructure depending on the curing parameters—for example, temperature, pressure, and duration. Some studies revealed that optimal steam and autoclave curing enhance the compressive strength and reduce concrete's porosity.[54-57] This is attributed to the ameliorated hydration process accomplished in concrete under autoclave curing.[58] Previous experimental research reported that curing time, pressure, and temperature significantly affected the compressive and flexural strength of reactive powder concrete.[59] Moreover, it was indicated that similar compressive strength levels can be obtained in a shorter duration if the pressure level is increased. The

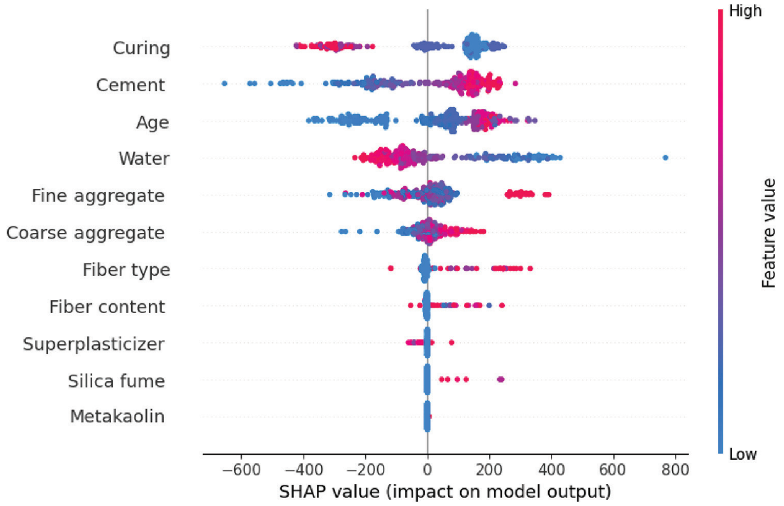

Fig. 12—SHAP violin plot of predictive model for direct UPV.

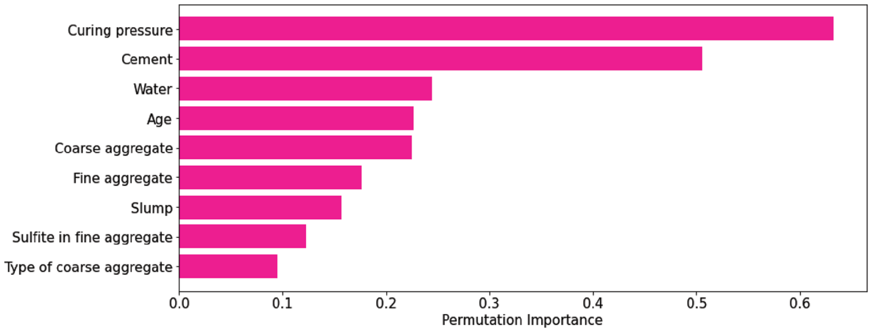

Fig. 13—Permutation feature importance of predictive model for surface UPV.

underlying chemistry of this phenomenon was related to the rate of reaction of the ingredients. Besides, increasing temperature and pressure altered the hydration products. Therefore, the pressure of steam curing can be considered as an important parameter influencing the mechanical properties of concrete.

Another study by Chen et al.[60] demonstrated that greater steam pressure was associated with a shorter curing time, indicating the importance of steam pressure. It was noted that high-pressure steam conditions can accelerate the hydration reactions, which raise the autoclaved aerated concrete's (AAC's) compressive strength. Moreover, a similar study on ultra-high-performance concrete showed that to get the highest strength, concrete with more fly ash requires a higher autoclave pressure.[61] The theory of sound propagation in solids implies that the velocity of sound transmission depends on the elastic modulus and density of the material.[62] UPV increases when cement transforms from a plastic to solid state.[63] It is directly proportional to the strength gain of concrete, and high-pressure steam curing can accelerate hydration and concrete hardening, yielding high pulse velocities.

However, previous experimental studies also revealed that steam and autoclave curing could impede the strength development of concrete and harm its microstructure.[58,64-68] This is due to the transformation of calcium silicate hydrate (C-S-H) gel into crystalline alpha dicalcium silicate hydrate (α-C_2SH) product.[65] The generated phase is accompanied by the strength reduction and high permeability of concrete.[68] As a result, prolonged autoclaving may cause a decrease in UPV. Additionally, the produced phases during hydration need enough time to distribute steadily between cement particles. The increased hydration rate caused by high temperature curing could reduce the time.

Consequently, the nonuniform distribution of hydration products yields high porosity and deterioration. It is worth mentioning that the low thermal conductivity of concrete causes a temperature discrepancy between the surface and the internal parts of the substance during high-pressure steam curing. This discrepancy also leads to a non-uniform rate of cement hydration and thermal expansion, associating concrete with microcracking.[66] These microstructural mechanisms induced by autoclaving influence UPV in a decreasing manner. The reviewed experimental studies ascertain that curing conditions strongly affect concrete properties and wave propagation velocity. Therefore, the significant importance of curing pressure in determining the UPV is justified.

Previous laboratory studies have also verified the significant influence of cement's content and type on UPV.[69,70] However, the curing conditions had a stronger influence on UPV than the type of cement.[71] Generally, cement and water contents play crucial roles in the hydration process. An increased water-cement ratio (w/c) raises capillary pores and microcracks in the cement paste and transition zone. Eventually, the concrete's resistance is augmented by transferring

Table 4—Values of evaluation criterion for different practical ML models

R^2 average	XGBoost-Direct UPV	XGBoost-Surface UPV	SVR-Direct UPV	SVR-Surface UPV
Training data	0.9971	0.9982	0.9442	0.9421
Testing data	0.8715	0.9095	0.8405	0.8450

ultrasonic waves.[72] Therefore, cement and water contents could be the key factors in pulse velocity.

The sulfite content in fine aggregates and the type of coarse aggregates were the two least significant factors affecting surface UPV. It is worth noting that sulfate ions from sand can react with cement products, such as C-S-H gel, to produce gypsum ($CaSO_4 \cdot 2H_2O$). This generated sulfate compound interacts with calcium aluminate in cement, and a secondary ettringite is eventually formed, resulting in stress and mechanical degradation in concrete.[73,74] However, a low degree of importance was observed for sulfite in the feature importance analysis. Considering the prior observation and the high sensitivity of UPV to microcracks, it may be perceived that sulfates did not cause significant damage to concrete. This is due to sulfate-resistant cement in the mixture of concrete specimens whose data set was used in this study. Scholars have investigated the influence of internal sulfite on concrete. The behavior of cement when facing SO_3 in the sand depends on the particular type of cement and different factors—for example, fineness, soundness, and C_3A content.[75] In other words, the effects of high SO_3 content in sand on damaging the concrete microstructure depend on the properties of cement used in concrete.[74,75] Therefore, sulfite emerged as one of the least important features affecting surface UPV in this study.

Silica fume and metakaolin were the two least significant factors affecting direct UPV. It was reported that because of silica fume's large specific surface area, its particles could react with calcium hydroxide (CH) to generate a thick phase of C-S-H. C-S-H gel reinforced the matrix's binding, filled in the pores, and gave the structure more density. It should be noted that the silica fume micro-filling property also contributed to an improvement in the contact surface between the cement and sand particles.[76] Metakaolin also positively affects concrete when used as a partial substitute for cement. Metakaolin combines with $Ca(OH)_2$ to produce more C-S-H gel, thereby increasing the concrete's strength.[77] Therefore, silica fume and metakaolin provide a denser structure, therefore influencing UPV. However, the lower number of concrete samples containing silica fume and metakaolin in the collected data set might have affected its relative importance rate.

Practical applications

The developed models can be potentially used for material assessment of existing concrete structures. However, it is noteworthy that some of the features used as inputs in this study might be difficult to access in real-world scenarios, particularly for older structures.[78] Therefore, a new set of features was selected regarding accessibility for developing more practical models. Moreover, new input data were generated based on the original features to improve the models' performance by extracting relevant features. Variables most likely to be available for older structures were coarse aggregate, fine aggregate to total aggregates ratio, cement, *w*/*c*, age, and curing.

Besides, the mentioned features follow the results of feature importance analyses, demonstrating the greatest contribution to the UPV values. These variables were considered for the practical surface UPV predictive model. The same features were used to develop practical models for predicting direct UPV. However, the data set for direct UPV included fiber-reinforced concrete. Thus, fiber type was also considered as an input because it greatly influences the wave propagation in concrete.[36] The same Monte Carlo methodology was used for practical models. Table 4 shows the result of the practical models' performance. According to the testing phase, the XGBoost models for direct UPV and surface UPV demonstrated an average R^2 of 0.8715 and 0.9095, respectively. The obtained results showed a negligible reduction of approximately 0.0009 for the direct UPV predictor and an improvement of approximately 0.0007 for the surface UPV predictor. It can be perceived that eliminating several features that possessed less importance on the models' outputs did not affect the models' precision. However, incorporating newly generated features based on original data could positively affect the models' performance. Negligible deviations were also observed for the SVR models, indicating the feasibility of developing practical models in real-world applications.

When the literature was surveyed for the prediction of UPV based on the mixture design properties of concrete using ML algorithms, a limited number of studies were found in which R^2 values were obtained from 0.6799 to 0.9331.[29,79] These R^2 values depend on several parameters. However, it is worth noting the substantial differences between the current and the previously mentioned studies. First, the current study used a large data set, enhancing model reliability. As discussed earlier, the data set collected in this study comprised a total of 1495 experiments, 873 samples for direct UPV, and 622 instances for surface UPV. However, the mentioned couple of studies in the literature used less than 150 sample data for modeling. Second, this study incorporated Monte Carlo simulations to obtain the average values of R^2. This is a more reliable approach because a remarkable difference existed between average and best values during the 100 times run for each model. None of the mentioned studies used a similar approach to consider input fluctuation, which might have reduced the model's performance.

SUMMARY AND CONCLUSIONS

This study used machine learning (ML) methods to predict direct and surface ultrasonic pulse velocity (UPV) in cementitious concrete based on the given features. Different hyperparameters were tuned; therefore, the ML models could reach the highest accuracy. Additionally, Monte Carlo simulations were performed to study the influences of uncertainties in input data on the performance of ML algorithms. The following highlights of this research can be stated:

1. The findings reveal that both extreme gradient boosting (XGBoost) and support vector regression (SVR) models can reliably predict the velocity of ultrasonic waves in concrete with diverse mix designs at various curing ages. Notably, the XGBoost model outperformed SVR, achieving R^2 values of 0.8724 for direct UPV and 0.9088 for surface UPV during the testing phases. These results underscore the superior predictive capability of XGBoost.

2. The Monte Carlo simulations demonstrated the significant impact of input data uncertainties on model performance. The fluctuations in input parameters notably influenced the R^2 values, emphasizing the need for a robust probabilistic approach and uncertainty consideration in developing predictive models for concrete health monitoring.

3. Linear regression demonstrated limitation in predicting UPV, with average R^2 values of only 0.6856 and 0.6801 for direct and surface UPV models, respectively, underscoring the necessity of employing advanced ML techniques to achieve more accurate and reliable UPV predictions.

4. Feature importance analysis identified key factors affecting UPV. Curing pressure emerged as the most critical parameter, followed by cement content, underscoring the importance of optimal curing conditions for concrete microstructure and hydration processes. Water content and concrete age also proved influential, highlighting their role in improving prediction accuracy during model development. Conversely, sulfite content in fine aggregates and the type of coarse aggregates were found to have minimal impact on surface UPV, suggesting that these parameters can be deprioritized to reduce computational cost without compromising model precision.

5. The developed models can effectively predict UPV in concrete using a refined set of accessible features, achieving R^2 values of 0.8715 for direct UPV and 0.9095 for surface UPV. This simplification enhances practical application without compromising accuracy, demonstrating the models' potential for assessing aged concrete structures.

FUTURE STUDIES

Future prospects include expanding the scope of this study to incorporate supplementary cementitious materials, ultra-high-performance concrete, and cutting-edge cementless alternatives such as geopolymer and alkali-activated concrete. These advanced materials offer significant advantages, including improved durability, reduced environmental impact, and superior mechanical properties. As the construction industry increasingly shifts toward sustainable practices, understanding the UPV characteristics of these materials will be vital for their widespread adoption.

AUTHOR BIOS

Mohammad Rahmati *is a Graduate Research Assistant at the Nondestructive Testing Laboratory of Sharif University of Technology, Tehran, Iran, where he received his MS. His research interests include structural health monitoring, damage detection, nonlinear ultrasonics, construction materials, and machine learning.*

Vahab Toufigh *is a Professor at the Sharif University of Technology. He received his BS, MS, and PhD in civil engineering from the University of Arizona, Tucson, AZ, in 2007, 2009, and 2012, respectively. His research interests include nondestructive testing, ultrasonics, and concrete and cementitious materials.*

ACKNOWLEDGMENTS

This research did not receive any specific grant from funding agencies in the public, commercial, or not-for-profit sectors.

The authors declare that they have no known competing financial interests or personal relationships that could have appeared to influence the work reported in this paper.

REFERENCES

1. Khoury, G. A., "Passive Fire Protection of Concrete Structures," *Proceedings of the Institution of Civil Engineers. Structures and Buildings*, V. 161, No. 3, 2008, pp. 135-145. doi: 10.1680/stbu.2008.161.3.135

2. Rahmati, M., and Toufigh, V., "Evaluation of Geopolymer Concrete at High Temperatures: An Experimental Study Using Machine Learning," *Journal of Cleaner Production*, V. 372, 2022, p. 133608. doi: 10.1016/j.jclepro.2022.133608

3. Ranjkesh Rashteh Roudi, M.; Hosseini, A.; Ranjkesh, M.; Pan, Z.; and Korayem, A. H., "Dispersion Stability and the Reaction Mechanism of Boron Nitride Nanosheets in a Cementitious Alkaline Environment: An Experimental and Computational Study," *ACS Applied Nano Materials*, V. 7, No. 11, 2024, pp. 12592-12604. doi: 10.1021/acsanm.4c01082

4. Roudi, M. R. R.; Ranjkesh, M.; Korayem, A. H.; and Shahsavary, R., "Review of Boron Nitride Nanosheet-Based Composites for Construction Applications," *ACS Applied Nano Materials*, V. 5, No. 12, 2022, pp. 17356-17372. doi: 10.1021/acsanm.2c03200

5. Rashidi, Y.; Roudi, M. R. R.; Korayem, A. H.; and Shamsaei, E., "Investigation of Ultrasonication Energy Effect on Workability, Mechanical Properties and Pore Structure of Halloysite Nanotube Reinforced Cement Mortars," *Construction and Building Materials*, V. 304, 2021, p. 124610. doi: 10.1016/j.conbuildmat.2021.124610

6. Nazari, A., and Toufigh, V., "Effects of Elevated Temperatures and Re-Curing on Concrete Containing Rice Husk Ash," *Construction and Building Materials*, V. 439, 2024, p. 137277. doi: 10.1016/j.conbuildmat.2024.137277

7. Nematzadeh, M.; Nazari, A.; and Tayebi, M., "Post-Fire Impact Behavior and Durability of Steel Fiber-Reinforced Concrete Containing Blended Cement–Zeolite and Recycled Nylon Granules as Partial Aggregate Replacement," *Archives of Civil and Mechanical Engineering*, V. 22, No. 1, 2021, p. 5. doi: 10.1007/s43452-021-00324-1

8. Yazdani, F.; Sadeghi, H.; AliPanahi, P.; Gholami, M.; and Leung, A. K., "Evaluation of Plant Growth and Spacing Effects on Bioengineered Slopes Subjected to Rainfall," *Biogeotechnics*, V. 2, No. 2, 2024, p. 100080. doi: 10.1016/j.bgtech.2024.100080

9. Rucka, M., and Wilde, K., "Ultrasound Monitoring for Evaluation of Damage in Reinforced Concrete," *Bulletin of the Polish Academy of Sciences. Technical Sciences*, V. 63, No. 1, 2015, pp. 65-75. doi: 10.1515/bpasts-2015-0008

10. Ma, G., and Du, Q., "Structural Health Evaluation of the Prestressed Concrete Using Advanced Acoustic Emission (AE) Parameters," *Construction and Building Materials*, V. 250, 2020, p. 118860. doi: 10.1016/j.conbuildmat.2020.118860

11. Özdal, M.; Karakoç, M. B.; and Özcan, A., "Investigation of the Properties of Two Different Slag-Based Geopolymer Concretes Exposed to Freeze–Thaw Cycles," *Structural Concrete*, V. 22, 2021, pp. E332-E340. doi: 10.1002/suco.201900441

12. Rahmati, M.; Toufigh, V.; and Keyvan, K., "Monitoring of Crack Healing in Geopolymer Concrete Using a Nonlinear Ultrasound Approach in Phase-Space Domain," *Ultrasonics*, V. 134, 2023, p. 107095. doi: 10.1016/j.ultras.2023.107095

13. Hwang, E.; Kim, G.; Choe, G.; Yoon, M.; Gucunski, N.; and Nam, J., "Evaluation of Concrete Degradation Depending on Heating Conditions by Ultrasonic Pulse Velocity," *Construction and Building Materials*, V. 171, 2018, pp. 511-520. doi: 10.1016/j.conbuildmat.2018.03.178

14. Camara, L. A.; Wons, M.; Esteves, I. C. A.; and Medeiros-Junior, R. A., "Monitoring the Self-Healing of Concrete from the Ultrasonic Pulse Velocity," *Journal of Composites Science*, V. 3, No. 1, 2019, p. 16. doi: 10.3390/jcs3010016

15. Güneyli, H.; Karahan, S.; Güneyli, A.; and Yapıcı, N., "Water Content and Temperature Effect on Ultrasonic Pulse Velocity of Concrete," *Russian Journal of Nondestructive Testing*, V. 53, No. 2, 2017, pp. 159-166. doi: 10.1134/S1061830917020024

16. Haddad, K.; Haddad, O.; Aggoun, S.; and Kaci, S., "Correlation between the Porosity and Ultrasonic Pulse Velocity of Recycled Aggregate Concrete at Different Saturation Levels," *Canadian Journal of Civil Engineering*, V. 44, No. 11, 2017, pp. 911-917. doi: 10.1139/cjce-2016-0449

17. Güçlüer, K., "Investigation of the Effects of Aggregate Textural Properties on Compressive Strength (CS) and Ultrasonic Pulse Velocity (UPV) of Concrete," *Journal of Building Engineering*, V. 27, 2020, p. 100949. doi: 10.1016/j.jobe.2019.100949

18. Haach, V. G., and Ramirez, F. C., "Qualitative Assessment of Concrete by Ultrasound Tomography," *Construction and Building Materials*, V. 119, 2016, pp. 61-70. doi: 10.1016/j.conbuildmat.2016.05.056

19. Whitehurst, E. A., *Evaluation of Concrete Properties from Sonic Tests*, American Concrete Institute Monograph No. 2, Farmington Hills, MI, 1966, 27 pp.

20. Carino, N. J., "Nondestructive Test Methods," *Concrete Construction Engineering Handbook*, second edition, 2008, pp. 879-952.

21. Khademi, F.; Akbari, M.; and Nikoo, M., "Displacement Determination of Concrete Reinforcement Building Using Data-Driven Models," *International Journal of Sustainable Built Environment*, V. 6, No. 2, 2017, pp. 400-411. doi: 10.1016/j.ijsbe.2017.07.002

22. Nguyen, T. T.; Pham Duy, H.; Pham Thanh, T.; and Vu, H. H., "Compressive Strength Evaluation of Fiber-Reinforced High-Strength Self-Compacting Concrete with Artificial Intelligence," *Advances in Civil Engineering*, V. 2020, No. 1, 2020, p. 3012139. doi: 10.1155/2020/3012139

23. Houssein, E. H.; Abd Elaziz, M.; Oliva, D.; and Abualigah, L., *Integrating Meta-Heuristics and Machine Learning for Real-World Optimization Problems*, Springer Nature, 2022.

24. Zhang, J.; Huang, Y.; Wang, Y.; and Ma, G., "Multi-Objective Optimization of Concrete Mixture Proportions Using Machine Learning and Metaheuristic Algorithms," *Construction and Building Materials*, V. 253, 2020, p. 119208. doi: 10.1016/j.conbuildmat.2020.119208

25. Mishra, P.; Al Khatib, A. M. G.; Yadav, S.; Ray, S.; Lama, A.; Kumari, B.; Sharma, D.; and Yadav, R., "Modeling and Forecasting Rainfall Patterns in India: A Time Series Analysis with XGBoost Algorithm," *Environmental Earth Sciences*, V. 83, No. 6, 2024, p. 163. doi: 10.1007/s12665-024-11481-w

26. Soegianto, L. M.; Hinandra, A. T.; Suri, P. A.; and Fajar, M., "Comparison of Model Performance on Housing Business Using Linear Regression, Random Forest Regressor, SVR, and Neural Network," *Procedia Computer Science*, V. 245, 2024, pp. 1139-1145. doi: 10.1016/j.procs.2024.10.343

27. el Mahdi Safhi, A.; Dabiri, H.; Soliman, A.; and Khayat, K. H., "Prediction of Self-Consolidating Concrete Properties Using XGBoost Machine Learning Algorithm: Rheological Properties," *Powder Technology*, V. 438, 2024, p. 119623. doi: 10.1016/j.powtec.2024.119623

28. Singh, P. K., and Rajhans, P., "Experimental Investigation and SVR Model to Predict the Mechanical Properties of RAC by Enhancing the Characteristic of RCA Using Surface Treatment Method Along with Modified Mixing Approach," *Construction and Building Materials*, V. 393, 2023, p. 132032. doi: 10.1016/j.conbuildmat.2023.132032

29. Ashrafian, A.; Taheri Amiri, M. J.; Rezaie-Balf, M.; Ozbakkaloglu, T.; and Lotfi-Omran, O., "Prediction of Compressive Strength and Ultrasonic Pulse Velocity of Fiber Reinforced Concrete Incorporating Nano Silica Using Heuristic Regression Methods," *Construction and Building Materials*, V. 190, 2018, pp. 479-494. doi: 10.1016/j.conbuildmat.2018.09.047

30. Yousif, S. T., and Abdullah, S. M., "Artificial Neural Network Model for Predicting Compressive Strength of Concrete," *Tikrit Journal of Engineering Sciences*, V. 16, No. 3, 2009, pp. 55-66. doi: 10.25130/tjes.16.3.05

31. Silva, F. A. N.; Delgado, J. M. P. Q.; Cavalcanti, R. S.; Azevedo, A. C.; Guimarães, A. S.; and Lima, A. G. B., "Use of Nondestructive Testing of Ultrasound and Artificial Neural Networks to Estimate Compressive Strength of Concrete," *Buildings*, V. 11, No. 2, 2021, p. 44. doi: 10.3390/buildings11020044

32. Na, U. J.; Park, T. W.; Feng, M. Q.; and Chung, L., "Neuro-Fuzzy Application for Concrete Strength Prediction Using Combined Non-Destructive Tests," *Magazine of Concrete Research*, V. 61, No. 4, 2009, pp. 245-256. doi: 10.1680/macr.2007.00127

33. Poorarbabi, A.; Ghasemi, M.; and Moghaddam, M. A., "Concrete Compressive Strength Prediction Using Non-Destructive Tests through Response Surface Methodology," *Ain Shams Engineering Journal*, V. 11, No. 4, 2020, pp. 939-949. doi: 10.1016/j.asej.2020.02.009

34. Domingo, R., and Hirose, S., "Correlation between Concrete Strength and Combined Nondestructive Tests for Concrete Using High-Early Strength Cement," *The Sixth Regional Symposium on Infrastructure Development*, 2009, pp. 12-13.

35. Zhang, F.; Pang, K.; Li, J.; Liu, Q.; Du, J.; Xiao, H.; Guo, B.; and Zhang, J., "Ultrasonic Pulse Velocity as a Non-Destructive Measure for the Projectile Impact Resistance of Cementitious Composites Across a Wide Range of Mix Compositions," *Journal of Building Engineering*, V. 94, 2024, p. 109875. doi: 10.1016/j.jobe.2024.109875

36. Hedjazi, S., and Castillo, D., "Relationships among Compressive Strength and UPV of Concrete Reinforced with Different Types of Fibers," *Heliyon*, V. 6, No. 3, 2020, p. e03646. doi: 10.1016/j.heliyon.2020.e03646

37. Said, A. M. I., and Ali, B. A. H., "Assessment of Concrete Compressive Strength by Ultrasonic Non-Destructive Test," *E3S Web of Conferences*, V. 318, 2021, p. 3004. doi: 10.1051/e3sconf/202131803004

38. Ali, B. A. H., "Assessment of Concrete Compressive Strength by Ultrasonic Non-Destructive Test," MSc thesis, University of Baghdad, Baghdad, Iraq, 2008.

39. Li, Y.; Gou, J.; and Fan, Z., "Particle Swarm Optimization-Based Extreme Gradient Boosting for Concrete Strength Prediction," *Proceedings of 2019 IEEE 4th Advanced Information Technology, Electronic and Automation Control Conference, IAEAC 2019*, 2019, pp. 982-986. doi: 10.1109/IAEAC47372.2019.8997825

40. Chen, T., and Guestrin, C., "XGBoost: A Scalable Tree Boosting System," *Proceedings of the ACM SIGKDD International Conference on Knowledge Discovery and Data Mining*, Aug. 13-17, 2016, pp. 785-794. doi: 10.1145/2939672.2939785

41. Friedman, J. H., "Greedy Function Approximation: A Gradient Boosting Machine," *Annals of Statistics*, V. 29, No. 5, 2001, pp. 1189-1232. doi: 10.1214/aos/1013203451

42. Nguyen-Sy, T.; Wakim, J.; To, Q. D.; Vu, M. N.; Nguyen, T. D.; and Nguyen, T. T., "Predicting the Compressive Strength of Concrete from its Compositions and Age Using the Extreme Gradient Boosting Method," *Construction and Building Materials*, V. 260, 2020, p. 119757. doi: 10.1016/j.conbuildmat.2020.119757

43. Wan, Z.; Xu, Y.; and Šavija, B., "On the Use of Machine Learning Models for Prediction of Compressive Strength of Concrete: Influence of Dimensionality Reduction on the Model Performance," *Materials*, V. 14, No. 4, 2021, pp. 1-23. doi: 10.3390/ma14040713

44. Dong, W.; Huang, Y.; Lehane, B.; and Ma, G., "XGBoost Algorithm-Based Prediction of Concrete Electrical Resistivity for Structural Health Monitoring," *Automation in Construction*, V. 114, 2020, p. 103155. doi: 10.1016/j.autcon.2020.103155

45. Vapnik, V.; Golowich, S. E.; and Smola, A., "Support Vector Method for Function Approximation, Regression Estimation, and Signal Processing," *Advances in Neural Information Processing Systems 9 (NIPS 1996)*, 1997, pp. 281-287.

46. Alam, M. S.; Sultana, N.; and Hossain, S. M. Z., "Bayesian Optimization Algorithm Based Support Vector Regression Analysis for Estimation of Shear Capacity of FRP Reinforced Concrete Members," *Applied Soft Computing*, V. 105, 2021, p. 107281. doi: 10.1016/j.asoc.2021.107281

47. Tang, F.; Wu, Y.; and Zhou, Y., "Hybridizing Grid Search and Support Vector Regression to Predict the Compressive Strength of Fly Ash Concrete," *Advances in Civil Engineering*, V. 2022, No. 1, 2022, p. 3601914. doi: 10.1155/2022/3601914

48. Mozumder, R. A.; Roy, B.; and Laskar, A. I., "Support Vector Regression Approach to Predict the Strength of FRP Confined Concrete," *Arabian Journal for Science and Engineering*, V. 42, No. 3, 2017, pp. 1129-1146. doi: 10.1007/s13369-016-2340-y

49. Li, L.; Zheng, W.; and Wang, Y., "Prediction of Moment Redistribution in Statically Indeterminate Reinforced Concrete Structures Using Artificial Neural Network and Support Vector Regression," *Applied Sciences*, V. 9, No. 1, 2018, p. 28. doi: 10.3390/app9010028

50. Singh, D., and Singh, B., "Investigating the Impact of Data Normalization on Classification Performance," *Applied Soft Computing*, V. 97, 2020, p. 105524. doi: 10.1016/j.asoc.2019.105524

51. Laurensia, Y.; Young, J. C.; and Suryadibrata, A., "Early Detection of Diabetic Retinopathy Cases Using Pre-Trained EfficientNet and XGBoost," *International Journal of Advances in Soft Computing & Its Applications*, V. 12, No. 3, 2020, pp. 101-111.

52. Van Dao, D.; Ly, H. B.; Trinh, S. H.; Le, T. T.; and Pham, B. T., "Artificial Intelligence Approaches for Prediction of Compressive Strength of Geopolymer Concrete," *Materials*, V. 12, No. 6, 2019, p. 983. doi: 10.3390/ma12060983

53. Lundberg, S., "A Unified Approach to Interpreting Model Predictions," *Advances in Neural Information Processing Systems 30 (NIPS 2017)*, 2017.

54. Yilmaz, T.; Ercikdi, B.; Karaman, K.; and Külekçi, G., "Assessment of Strength Properties of Cemented Paste Backfill by Ultrasonic Pulse Velocity Test," *Ultrasonics*, V. 54, No. 5, 2014, pp. 1386-1394. doi: 10.1016/j.ultras.2014.02.012

55. Çakir, Ö., and Aköz, F., "Effect of Curing Conditions on the Mortars with and without GGBFS," *Construction and Building Materials*, V. 22, No. 3, 2008, pp. 308-314. doi: 10.1016/j.conbuildmat.2006.08.013

56. Mannan, M. A.; Basri, H. B.; Zain, M. F. M.; and Islam, M. N., "Effect of Curing Conditions on the Properties of OPS-Concrete," *Building and Environment*, V. 37, No. 11, 2002, pp. 1167-1171. doi: 10.1016/S0360-1323(01)00078-6

57. Shen, P.; Lu, L.; He, Y.; Wang, F.; and Hu, S., "The Effect of Curing Regimes on the Mechanical Properties, Nano-Mechanical Properties and Microstructure of Ultra-High Performance Concrete," *Cement and Concrete Research*, V. 118, 2019, pp. 1-13. doi: 10.1016/j.cemconres.2019.01.004

58. Liu, B.; Luo, G.; and Xie, Y., "Effect of Curing Conditions on the Permeability of Concrete with High Volume Mineral Admixtures," *Construction and Building Materials*, V. 167, 2018, pp. 359-371. doi: 10.1016/j.conbuildmat.2018.01.190

59. Yazıcı, H.; Deniz, E.; and Baradan, B., "The Effect of Autoclave Pressure, Temperature and Duration Time on Mechanical Properties of Reactive Powder Concrete," *Construction and Building Materials*, V. 42, 2013, pp. 53-63. doi: 10.1016/j.conbuildmat.2013.01.003

60. Chen, Y.-L.; Chang, J.-E.; Lai, Y.-C.; and Chou, M.-I. M., "A Comprehensive Study on the Production of Autoclaved Aerated Concrete: Effects of Silica-Lime-Cement Composition and Autoclaving Conditions," *Construction and Building Materials*, V. 153, 2017, pp. 622-629. doi: 10.1016/j.conbuildmat.2017.07.116

61. Chen, T.; Gao, X.; and Ren, M., "Effects of Autoclave Curing and Fly Ash on Mechanical Properties of Ultra-High Performance Concrete," *Construction and Building Materials*, V. 158, 2018, pp. 864-872. doi: 10.1016/j.conbuildmat.2017.10.074

62. Solís-Carcaño, R., and Moreno, E. I., "Evaluation of Concrete Made with Crushed Limestone Aggregate Based on Ultrasonic Pulse Velocity," *Construction and Building Materials*, V. 22, No. 6, 2008, pp. 1225-1231. doi: 10.1016/j.conbuildmat.2007.01.014

63. Hwang, C. L., and Shen, D. H., "The Effects of Blast-Furnace Slag and Fly Ash on the Hydration of Portland Cement," *Cement and Concrete Research*, V. 21, No. 4, 1991, pp. 410-425. doi: 10.1016/0008-8846(91)90090-5

64. Bakharev, T.; Sanjayan, J. G.; and Cheng, Y. B., "Effect of Elevated Temperature Curing on Properties of Alkali-Activated Slag Concrete," *Cement and Concrete Research*, V. 29, No. 10, 1999, pp. 1619-1625. doi: 10.1016/S0008-8846(99)00143-X

65. Alawad, O. A.; Alhozaimy, A.; Jaafar, M. S.; Aziz, F. N. A.; and Al-Negheimish, A., "Effect of Autoclave Curing on the Microstructure of Blended Cement Mixture Incorporating Ground Dune Sand and Ground Granulated Blast Furnace Slag," *International Journal of Concrete Structures and Materials*, V. 9, No. 3, 2015, pp. 381-390. doi: 10.1007/s40069-015-0104-9

66. Tan, K., and Zhu, J., "Influences of Steam and Autoclave Curing on the Strength and Chloride Permeability of High Strength Concrete," *Materials and Structures*, V. 50, No. 1, 2017, pp. 1-9. doi: 10.1617/s11527-016-0913-6

67. Ludwig, N. C., and Pence, S. A., "Properties of Portland Cement Pastes Cured at Elevated Temperatures and Pressures," *ACI Journal Proceedings*, V. 52, No. 2, Feb. 1956, pp. 673-687. doi: 10.14359/11624

68. Alhozaimy, A.; Jaafar, M. S.; Al-Negheimish, A.; Abdullah, A.; Taufiq-Yap, Y. H.; Noorzaei, J.; and Alawad, O. A., "Properties of High Strength Concrete Using White and Dune Sands under Normal and Autoclaved Curing," *Construction and Building Materials*, V. 27, No. 1, 2012, pp. 218-222. doi: 10.1016/j.conbuildmat.2011.07.057

69. Hamidian, M.; Shariati, M.; Arabnejad, M. M. K.; and Sinaei, H., "Assessment of High Strength and Light Weight Aggregate Concrete Properties Using Ultrasonic Pulse Velocity Technique," *International Journal of Physical Sciences*, V. 6, No. 22, 2011, pp. 5261-5266.

70. Jain, A.; Kathuria, A.; Kumar, A.; Verma, Y.; and Murari, K., "Combined Use of Non-Destructive Tests for Assessment of Strength of Concrete in Structure," *Procedia Engineering*, V. 54, 2013, pp. 241-251. doi: 10.1016/j.proeng.2013.03.022

71. Estévez, E.; Martín, D. A.; Argiz, C.; and Sanjuán, M. Á., "Ultrasonic Pulse Velocity—Compressive Strength Relationship for Portland Cement Mortars Cured at Different Conditions," *Crystals*, V. 10, No. 2, 2020, p. 133. doi: 10.3390/cryst10020133

72. Abo-Qudais, S. A., "Effect of Concrete Mixing Parameters on Propagation of Ultrasonic Waves," *Construction and Building Materials*, V. 19, No. 4, 2005, pp. 257-263. doi: 10.1016/j.conbuildmat.2004.07.022

73. Neville, A., "The Confused World of Sulfate Attack on Concrete," *Cement and Concrete Research*, V. 34, No. 8, 2004, pp. 1275-1296. doi: 10.1016/j.cemconres.2004.04.004

74. Naser, M. H., and Zainab, J. K., "Studying the Effect of Internal Sulfates on Normal and Lightweight Concrete," *IOP Conference Series. Materials Science and Engineering*, V. 888, No. 1, 2020, p. 012054. doi: 10.1088/1757-899X/888/1/012054

75. Al-Rawi, R. S., and Abdul-Latif, A. M., "Compatibility of Sulphate Contents in Concrete Ingredients," *Fourth Scientific Conference*, College of Engineering, University of Baghdad, Baghdad, Iraq, 1998.

76. Shooshpasha, I.; Hasanzadeh, A.; and Kharun, M., "Effect of Silica Fume on the Ultrasonic Pulse Velocity of Cemented Sand," *Journal of Physics: Conference Series*, V. 1687, No. 1, 2020, p. 012017. doi: 10.1088/1742-6596/1687/1/012017

77. Macfarlane, J., "A Review on Use of Metakaolin in Concrete," *Engineering Science and Technology: An International Journal*, V. 3, 2013, pp. 2250-3498.

78. Selcuk, S., and Tang, P., "A Metaheuristic-Guided Machine Learning Approach for Concrete Strength Prediction with High Mix Design Variability Using Ultrasonic Pulse Velocity Data," *Developments in the Built Environment*, V. 15, 2023, p. 100220. doi: 10.1016/j.dibe.2023.100220

79. Singh, T.; Singh, B.; Bansal, S.; and Saggu, K., "Prediction of Ultrasonic Pulse Velocity of Concrete," *Applications of Computational Intelligence in Concrete Technology*, CRC Press, Boca Raton, FL, 2022, pp. 235-251.

ACI MATERIALS JOURNAL TECHNICAL PAPER

Title No. 122-M32

Enhancing Fracture Properties in Cementitious Composites through Hybrid Fiber Reinforcement

by Qi Cao, Liujingyuan Su, Changjun Zhou, Kaiming Pan, Jun Wu, and Xiaoyan Han

Adding fibers, especially steel fibers, to cementitious composites is one of the most commonly used methods to improve the mechanical properties of cementitious composites. The high price is the most concerning factor in the use of steel fibers. This study aims to investigate the influence of the content of multiscale fibers, including nanocellulose, sisal fibers, and steel fibers, on the fracture properties of cementitious composites. The fracture properties will be evaluated using the initial fracture toughness, unstable fracture toughness, and fracture energy through notched-beam bending tests. The results demonstrate that replacing steel fiber with an appropriate amount of sisal fiber effectively improves fracture properties, indicating a balancing point between fracture-impeding properties and price/environment. Specifically, under total macrofiber volume fractions of 1 and 1.5%, the 0.2% sisal fiber replacement for the steel fibers exhibits the best fracture-impeding properties. Additionally, the incorporation of nanocellulose (2% optimal in the research) enables the formation of a multiscale crack resistance system at the nano-micro level, further enhancing the fracture-impeding properties of cementitious composites. Moreover, the research found that adding the fibers collaboratively can cultivate a better enhancement in fracture-impeding properties than adding them separately.

Keywords: fracture properties; multiscale fiber reinforcement; nanocellulose; sisal fiber; steel fiber.

INTRODUCTION

Cementitious materials, as one of the most important building materials in the construction industry, have a wide range of applications and increasing consumption. Their widespread availability, low cost, and simple production process make cementitious materials a popular choice that can meet various structural design requirements. Despite these advantages, cementitious composites have structural limitations such as low tensile strength, poor toughness, and vulnerability to cracking, which directly impact the safety, durability, and stability of buildings.[1] The addition of fibers is one of the commonly used methods to address these structural shortcomings and enhance the performance of cementitious composites. Fibers can transfer stress and effectively alleviate stress concentration, thereby improving the tensile strength and crack resistance of the composite material.[2] Fiber-reinforced cementitious composites (FRCC) are widely used in bridge and tunnel engineering, hydraulic engineering, highway pavement and airport runways, shotcrete, and seismic engineering due to their excellent mechanical performance and durability.[3,4] Yang et al.[5] studied the influence of a hybrid of sepiolite and basalt fibers on the mechanical properties of cementitious composites. It revealed that the hybrid fibers further enhanced the ultimate stress and strain capacity of the cementitious composites under uniaxial compression conditions compared to adding one of them separately, due to the different elastic moduli and dimensions of the fibers. Additionally, it effectively improved fracture toughness and restrained the initiation and propagation of cracks of different sizes. Alrekabi et al.[6] found that the nanocellulose fibers enhanced the mechanical performance of the cementitious composites both with and without steel fibers. Scanning electron microscope (SEM) observations indicated that nanoscale fibers can impede the propagation of microcracks within the composite material. Smarzewski[7] investigated the influence of the addition of polypropylene fibers and basalt fibers on the fracture properties of high-performance concrete. It was demonstrated that the combined addition of high-modulus basalt fibers and low-modulus polypropylene fibers had a positive effect on fracture toughness in high-performance concrete. Hybrid fibers were found to be more effective than single fibers in improving flexural strength, flexural toughness, and fracture energy. Nanocellulose, also known as nanofibrillated cellulose (NFC), nanocrystalline cellulose (NCC), or cellulose nanocrystal (CNC),[8] has been extensively studied for its effect on the hydration reactions and basic mechanical properties. Kamasamudram et al.[9] found that the addition of cellulose nanofibers (CNF) promoted cement hydration, with the compressive strength of specimens increased by 24% when 0.05% CNF was added at a water-cement ratio of 0.35. Similarly, the flexural strength of cement paste increased with increasing CNF content, with a 75% increase observed when 0.5% CNF was added. In a study by Barnat-Hunek et al.,[10] nanocellulose was found to improve the compressive and flexural strengths of cement mortar by 27.6% and 10.9%, respectively. Goncalves et al.[11] found that the addition of CNF to cement systems reduces the permeability of sulfate ions in the binder system. It indicated that CNF significantly reduces the formation of ettringite and associated expansion, while improving pore size. Onuaguluchi and Banthia[12] investigated the influence of NFC-reinforced repair mortar (with a volume fraction of 0.1% NFC) on the corrosion behavior of reinforcing steel, exploring the possibility of enhancing the durability of repair

---

ACI Materials Journal, V. 122, No. 5, September 2025.
MS No. M-2024-063.R2, doi: 10.14359/51747870, received January 11, 2025, and reviewed under Institute publication policies. Pertinent discussion including author's closure, if any, will be published ten months from this journal's date if the discussion is received within four months of the paper's print publication.

Table 1—Chemical compositions of cement, wt. %

Composition	CaO	SiO_2	Al_2O_3	SO_3	Fe_2O_3	MgO	K_2O	TiO_2	SrO	ZnO
Wt. %	58.51	21.52	6.01	4.51	4.10	3.52	1.08	0.42	0.24	0.09

composite materials. Natural and accelerated corrosion test results indicate that the inclusion of NFC inhibits corrosion of the steel reinforcement, reducing the extent of corrosion and delaying delamination of the repair layer.

Plant fibers, such as sisal fiber, are renewable natural fibers that offer various advantages, including excellent mechanical properties,[13,14] low cost,[15] less energy consumption in production,[16,17] strong water absorption,[18] and similar strength and stiffness to synthetic fibers. They can be used as a green improvement material to substitute mineral and synthetic fibers. Moreover, this approach has no negative impacts on human health or the environmental ecosystem,[19-22] contributing to the sustainable development of construction engineering. Ruano et al.[23] incorporated sugarcane fibers and hemp fibers into cementitious composites and evaluated their flexural performance through notched-beam three-point bending tests. Both fibers exhibited high tensile strength and effectively reinforced the mortar. Sugarcane bagasse fiber increased the flexural strength of cementitious composites, while hemp fiber improved their toughness. Kriker et al.[24] concluded that, by increasing the volume dosage and length of jujube fiber, the post-cracking flexural strength and toughness coefficient of concrete could be improved, but the initial cracking strength and compressive strength would decrease. Kundu et al.[25] used chemically modified jute fiber as a concrete reinforcement and found significantly enhanced compressive and flexural strengths in jute fiber-reinforced concrete. It showed that replacing part of the traditional steel reinforcement with jute fiber would effectively reduce the negative effects of steel corrosion, make concrete products lighter, and improve their mechanical properties.

As a type of natural plant fiber, sisal fiber possesses various advantages, such as being pollution-free, easily available, and highly tough, and having high tensile strength and good corrosion resistance. Moreover, compared with other plant fibers, sisal fiber is more resistant to abrasion,[26] acid and alkaline attacks,[27] corrosion from seawater,[28] and low temperatures. In the marine environment, sisal fiber can effectively enhance the strength of concrete under corrosion.[28] Studies have shown that sisal fiber can undergo expansion in seawater, which can reduce the cracks caused by concrete shrinkage and slow down the corrosion rate of concrete in marine environments, thus extending its lifespan.[28] Ramakrishna and Sundararajan[29] investigated the impact resistance of cement mortar boards reinforced with four types of natural fibers—coconut shell, sisal, jute, and hibiscus—by considering different fiber dosages and fiber lengths. The results revealed that the impact resistance of mortar boards with these plant fibers increased by three to 18 times compared to ordinary mortar boards. Moreover, the addition of any type of fiber showed an increasing trend concerning impact resistance with increasing dosage and length. Zhou et al.[30] investigated the influence of incorporating short discrete sisal fibers on the fracture properties and impact resistance of cementitious composites. The results revealed that, compared with ordinary cement mortar, the jointed fiber-reinforced cementitious composites (JFRCC) exhibited higher tensile strength, compressive strength, and fracture toughness.

RESEARCH SIGNIFICANCE

Fibers are often used to obtain high-performance concrete by increasing its tensile strength and toughness. Although much research exists on natural plant fibers and multiscale fiber reinforcement, barely any research has shed light on multiscale reinforcement considering the differences in stiffness and scales using natural plant fibers. The purpose of this study is to investigate the influence of combinations of hybrid steel fibers, sisal fibers, and nanocellulose (NFC) on enhancing the fracture properties of cementitious composites through experimentation. By conducting experiments on 22 groups of cement mortar specimens, the effects of fiber content on the fundamental mechanical properties and fracture properties of concrete specimens can be understood. Research findings will assist engineers in designing and implementing multiscale-fiber-reinforced cementitious composites in engineering fields while yielding a decent environmental and financial cost.

EXPERIMENTAL PROGRAM

Raw materials

The ordinary portland cement in this research was produced by a cement plant in Dalian, Liaoning, China. Its chemical composition is shown in Table 1. The fine aggregate used in this study was quartz sand with a density of 2.65 g/cm^3 (1.53 oz./in.^{3}) and a fineness modulus of 1.9. The 13 mm (0.51 in.) long non-hooked copper-plated steel fibers were used, as shown in Fig. 1(a). The physical properties of the steel fibers are shown in Table 2. The sisal fibers used in this study are shown in Fig. 1(b), and their physical properties can be found in Table 3. A polycarboxylate-based high-efficiency water-reducing agent (WRA) was used to ensure good workability of cement mortar. The properties of the WRA are as follows: density of 1.060 kg/L (8.85 lb/gal.), solid content of 28.2%, and pH value of 4.5. Class F fly ash was used, and its performance parameters are shown in Table 4. The NFC used in this study was obtained from bleached softwood sulfate pulp. The appearance and transmission electron microscope (TEM) images of the NFC are shown in Fig. 1(c), and its performance parameters are listed in Table 5.

Mixing ratios and procedures

Twenty-two test groups were designed for the fracture properties test of cement mortar to study the influence of steel fibers, sisal fibers, and nanocellulose (NFC) on the fracture properties of cement mortar under single and multiscale interactions. The mixture ratios used in this experiment are shown in Table 6. The control groups with no sisal fiber, steel fiber, or NFC are labeled as N0. Sisal fibers were added to the cement mortar in proportions of 0.1%, 0.2%, and 0.4% by volume of the cement mortar, labeled as FF0.1, FF0.2, and FF0.4, respectively. Steel fibers were added to the concrete in proportions of 1%, 1.5%, and 2% by volume of the cement mortar, labeled as SF1, SF1.5, and SF2, respectively. NFC was incorporated into the cement mortar by mass based on the percentage of cementitious materials, namely 0.05%, 0.1%, 0.15%, and 0.2%, labeled as NFC0.05, NFC0.1, NFC0.15, and NFC0.2, respectively. To enhance the environmental friendliness and cost-effectiveness of the material, steel fibers were replaced by 0.1%, 0.2%, and 0.4% of sisal fibers by volume of the cement mortar, denoted as SF0.9FF0.1, SF0.8FF0.2, SF0.6FF0.4, SF1.4FF0.1, SF1.3FF0.2, and SF1.1FF0.4. The combinations where steel fibers, sisal fibers, and NFC were jointly incorporated are labeled as FF0.1NFC0.2, FF0.2NFC0.2, FF0.4NFC0.2, SF0.8FF0.2NFC0.2, and SF1.3FF0.2NFC0.2. The WRA was added at 0.1% by mass of cement.

Table 2—General properties of steel fibers

Diameter *d*, mm	Length *L*, mm	Aspect ratio *L*/*d*	Tensile strength, MPa
0.21	13	62	2750

Note: 1 mm = 0.0394 in.; 1 MPa = 145.14 psi.

Table 3—General properties of sisal fibers (provided by manufacturer)

Density, g/cm^3	Diameter, mm	Tensile strength, MPa	Elastic modulus, GPa	Water absorption rate, %
1.4	0.4	470	25	65

Note: 1 mm = 0.0394 in.; 1 MPa = 145.14 psi; 1 GPa = 145.14 ksi; 1 g/cm^3 = 0.5787 oz./in.^{3}

The required amounts of steel fibers, sisal fibers, and nanocellulose were measured for different experimental mixture proportions. A 50 L (13.21 gal.) horizontal shaft forced mixer was used in the test. First, cement and fly ash were added to the mixer and stirred for 60 seconds. Quartz sand was then added and stirred for 3 minutes. The steel and sisal fibers were uniformly added to the mixer and stirred for 2 minutes, ensuring even distribution. Finally, water and high-range water-reducing admixture were added to the mixer and stirred for 2 minutes to obtain the desired mortar mixture for the experiment. The cementitious composites

Table 4—Properties of fly ash (provided by manufacturer)

Density, g/cm^3	Sieve residue of 45 μm square-hole sieve, %	Water demand ratio, %	Loss on ignition, %	Water content, %	SO$_3$, %
2.3	8.9	84	4.8	0.3	1

Note: 1 g/cm^3 = 0.5787 oz./in.^{3}

(a) Appearance of steel fibers

(b) Appearance of sisal fibers

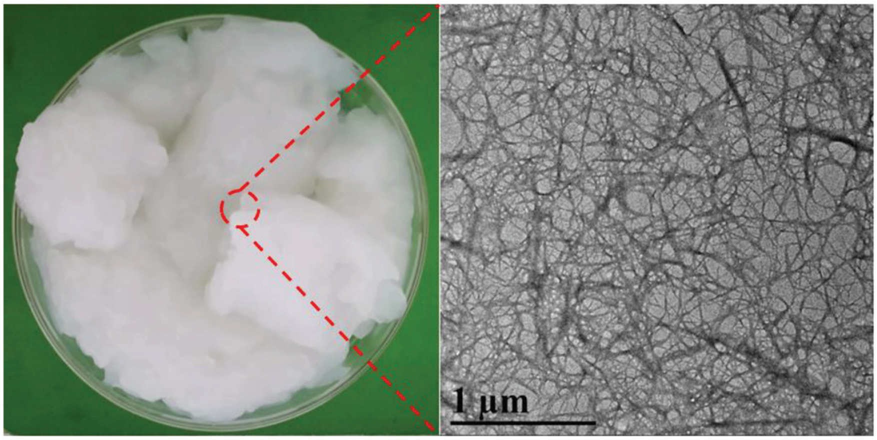

(c) Appearance of NFC under naked eye and TEM

Fig. 1—Appearance of steel fibers, sisal fibers, and NFC.

were mixed under ambient temperature at approximately 20°C (68°F).

Specimen preparation and testing method

The compression tests for the FRCC were carried out after curing for 7 and 28 days. The compression tests adopted cubic specimens with dimensions of 150 x 150 x 150 mm (5.91 x 5.91 x 5.91 in.). The loading speed was 0.8 MPa/s (0.12 ksi/s) for the compression tests. The fracture parameters (initial fracture toughness, unstable fracture toughness, and fracture energy) of FRCC were determined through notched-beam three-point bending tests in accordance with ASTM C78/C78M-22[31] and ASTM E399-24,[32] as depicted in Fig. 2(a). To conduct the experiment, notched-beam specimens with dimensions of 100 x 100 x 400 mm (3.94 x 3.94 x 15.7 in.) were prepared, as depicted in Fig. 2(b). A total of 22 sets of specimens with different mixing ratios were cast. Three parallel specimens were made for each set. Specimens were cured for 24 hours under ambient temperature and then demolded and cured in water until the 28th day. One day prior to the experiment, a midspan notch with 2 mm (0.078 in.) width and 30 mm (1.18 in.) height was created using a diamond saw. During sawing, the diamond saw was moved quite slowly and was cooled using tap water. After sawing, the specimens were placed with the notches facing upward. A universal testing machine was used for the experiment, with a loading rate set at 0.1 mm/min (0.0039 in./min), controlled by deflection collected by the linear variable displacement transducer (LVDT). During the experiment, load sensors, the LVDT, and a clip-on extensometer captured the load (P), deflection (δ), and crack mouth opening displacement (CMOD). Additionally, four resistive strain gauges with an effective length of 5 mm (0.2 in.) were symmetrically attached to the two sides of the notch tip of the experimental specimen, as depicted in Fig. 2(c).

Table 5—Properties of NFC (provided by manufacturer)

Density, g/cm^3	Length, nm	Width, nm	Tensile strength, MPa	Shear viscosity, MPa·s
1.05	>1000	5 to 100	222 to 233	30 to 5000

Note: 1 nm = 0.0394 × 10^{-6} in.; 1 MPa = 145.14 psi; 1 g/cm^3 = 0.5787 oz./in.^{3}.

The double-*K* fracture model was used in this paper to describe the fracture process of FRCC. The double-*K* fracture model uses two critical stress intensity factor parameters—initial fracture toughness K_{Ic}^{ini} and unstable fracture toughness K_{Ic}^{un}—to distinguish concrete fracture states of initiation and instability.[33] The double-*K* model can better reflect the fracture of the quasi-brittle materials, such as FRCC. In the double-*K* fracture model, the whole process of

Table 6—Mixture proportions of cement mortar

Number	Amount of components, kg/m^3							
	Cement	Fly ash	Silica sand	Water	Steel fiber	Sisal fiber	NFC	WRA
N0	1123	125	624	375	—	—	—	1.12
FF0.1	1123	125	624	375	—	1.4	—	1.12
FF0.2	1123	125	624	375	—	2.8	—	1.12
FF0.4	1123	125	624	375	—	5.6	—	1.12
SF1	1123	125	624	375	78	—	—	1.12
SF1.5	1123	125	624	375	117	—	—	1.12
SF2	1123	125	624	375	156	—	—	1.12
NFC0.05	1123	125	624	375	—	—	0.62	1.12
NFC0.1	1123	125	624	375	—	—	1.24	1.12
NFC0.15	1123	125	624	375	—	—	1.86	1.12
NFC0.2	1123	125	624	375	—	—	2.48	1.12
SF0.9FF0.1	1123	125	624	375	70.2	1.4	—	1.12
SF0.8FF0.2	1123	125	624	375	62.4	2.8	—	1.12
SF0.6FF0.4	1123	125	624	375	46.8	5.6	—	1.12
SF1.4FF0.1	1123	125	624	375	109.2	1.4	—	1.12
SF1.3FF0.2	1123	125	624	375	101.4	2.8	—	1.12
SF1.1FF0.4	1123	125	624	375	85.8	5.6	—	1.12
FF0.1NFC0.2	1123	125	624	375	—	1.4	2.48	1.12
FF0.2NFC0.2	1123	125	624	375	—	2.8	2.48	1.12
FF0.4NFC0.2	1123	125	624	375	—	5.6	2.48	1.12
SF0.8FF0.2NFC0.2	1123	125	624	375	62.4	2.8	2.48	1.12
SF1.3FF0.2NFC0.2	1123	125	624	375	101.4	2.8	2.48	1.12

Note: 1 kg/m^3 = 0.0624 lb/ft^3.

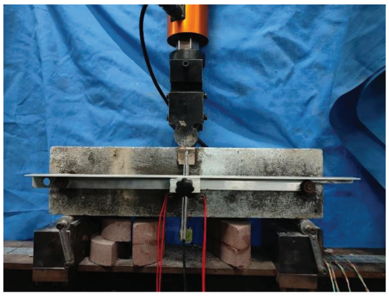

(a) Testing apparatus

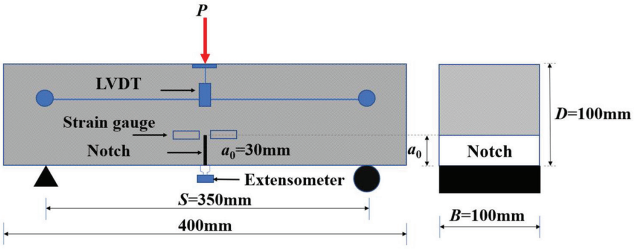

(b) Schematic diagram of the gauges and the section cut view through the notch

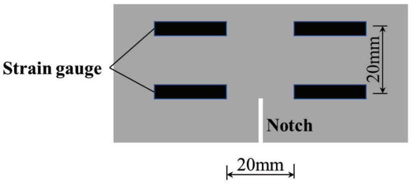

(c) Detailed schematic of the strain gauge near the notch

Fig. 2—Fracture test setup of notched beams. (Note: Dimensions in mm; 1 mm = 0.0394 in.)

concrete fracture damage can be described as follows: when $K < K_{Ic}^{ini}$, the crack does not initiate; when $K = K_{Ic}^{ini}$, the crack initiates; when $K_{Ic}^{ini} < K < K_{Ic}^{un}$, the crack propagates slowly and steadily; when $K = K_{Ic}^{un}$, the unstable crack propagation initiates; and when $K > K_{Ic}^{un}$, the crack propagates rapidly and unsteadily. After the experiment, the initial fracture toughness and unstable fracture toughness were calculated in accordance with Tada et al.[34] using Eq. (1) and (2)

$$K_{Ic}^{ini} = \frac{1.5\left(P_{ini} + \frac{mg}{2} \times 10^{-2}\right) \times 10^{-3} \cdot S \cdot a_0^{1/2}}{th^2} f(a) \quad (1)$$

$$K_{Ic}^{un} = \frac{1.5\left(P_{max} + \frac{mg}{2} \times 10^{-2}\right) \times 10^{-3} \cdot S \cdot a_c^{1/2}}{th^2} f(a) \quad (2)$$

where K_{Ic}^{ini} is the initial fracture toughness, MPa·m$^{1/2}$; K_{Ic}^{un} is the unstable fracture toughness, MPa·m$^{1/2}$; P_{ini} is the initial cracking load, which was determined by the unloading at the strain gauges, as reflected by the sudden drop in strain followed by continuous decrease during the experiment,[35] kN; S is the distance between specimen supports, m; m is the mass of the specimen between supports, kg, which can be calculated using the total mass of the specimen multiplied by a factor of $S/0.4$; g is the acceleration of gravity, m·s^{-2}, which takes the value of 9.81; a_0 is the initial notch depth, m; a_c is the critical effective crack length, m, which can be calculated according to Eq. (3); and t and h are the thickness and the height of the specimen, m.

$$a_c = \frac{2}{\pi}(h + h_0)\arctan\left(\frac{\mathrm{CMOD}_c}{32.6P_{max}}Et - 0.1135\right)^{1/2} - h_0 \quad (3)$$

$$E = \frac{1}{tc_i}\left(3.70 + 32.60\tan^2\left(\frac{\pi}{2}\frac{a_0 + h_0}{h + h_0}\right)\right) \quad (4)$$

where E is the Young's modulus, GPa; h_0 is the thickness of the holder of the clip gauge, m; CMOD$_c$ is the CMOD at the maximum load, μm; and c_i is the CMOD/P at the linear stage of the P-CMOD curve, μm/kN.

$$f(\alpha) = \frac{1.99 - \alpha(1 - \alpha)(2.15 - 3.93\alpha + 2.7\alpha^2)}{(1 + 2\alpha)(1 - \alpha)^{3/2}} \quad (5)$$

$$\alpha = \begin{cases} \dfrac{a_0 + h_0}{h + h_0} & \text{for the calculation of } K_{Ic}^{ini} \\ \dfrac{a_c + h_0}{h + h_0} & \text{for the calculation of } K_{Ic}^{un} \end{cases} \quad (6)$$

Apart from the double-K method, the fracture energy (G_F) was also adopted to assess the energy dissipation ability of the FRCC during fracture. G_F was calculated using the work of fracture method, as shown in Eq. (7), recommended by RILEM Technical Committee 50-FMC[36]

$$G_F = \frac{W_F}{(h - h_0)t} \quad (7)$$

where G_F is the fracture energy, N/m; and W_F is the total fracture energy (equivalent to the area below the P-δ curve), J.

EXPERIMENTAL RESULTS AND DISCUSSION

Compressive strength

The compressive strength of N0 was 59.57 and 80.11 MPa (8.64 and 11.62 ksi) after curing for 7 and 28 days, as shown in Fig. 3(a). The compressive strength of the test groups with steel fibers, SF1, SF1.5, and SF2, increased by 7.55%, 27.38%, and 30.17% (7-day ages), and 12.9%, 25.57%, and 28.44% (28-day ages) compared to N0, respectively. In contrast, the specimens with sisal fibers (FF0.1, FF0.2, and FF0.4) did not show distinct variations in compressive strength compared with N0, as shown in Fig. 3(b), nor did the group with NFC or the group that combined sisal fibers and NFC, as shown in Fig. 3(e) and (f).

From Fig. 3(c), it can be seen that, compared with the test group SF1 with 1% volume dosage of steel fibers, the compressive strengths at 7 and 28 days of the groups replacing steel fibers with 0.1%, 0.2%, and 0.4% volume dosage of sisal fibers with 1% fiber volume dosage in total (SF0.9FF0.1, SF0.8FF0.2, and SF0.6FF0.4) increased by 6.79%, 8.16%, and 0.75% (7-day ages) and 6.51%, 12.08%, and 8.05% (28-day ages). This is because the addition of sisal fibers formed a synergy between the fibers, which impeded the formation and propagation of cracks. However, the group replacing steel fibers with sisal fibers with 1.5% fiber volume dosage in total did not show an obvious increase in compressive strength compared to SF1.5 (Fig. 3(d)), as the sisal fibers in the groups with 1.5% fiber volume dosage in

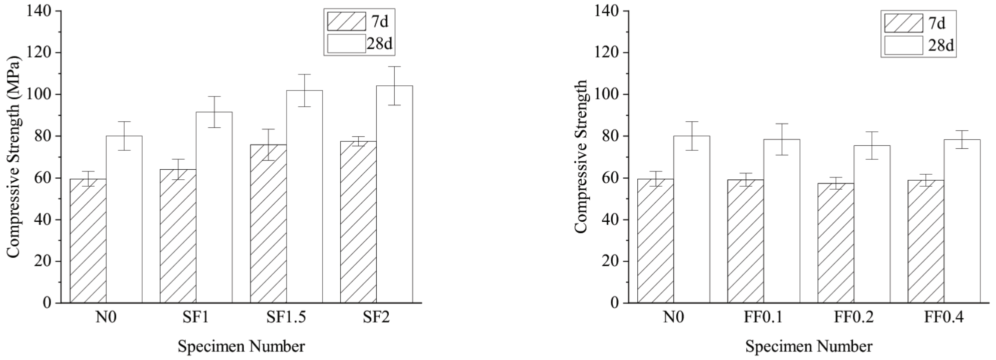

(a) Compressive strength of the mortar with steel fibers

(b) Compressive strength of the mortar with sisal fibers

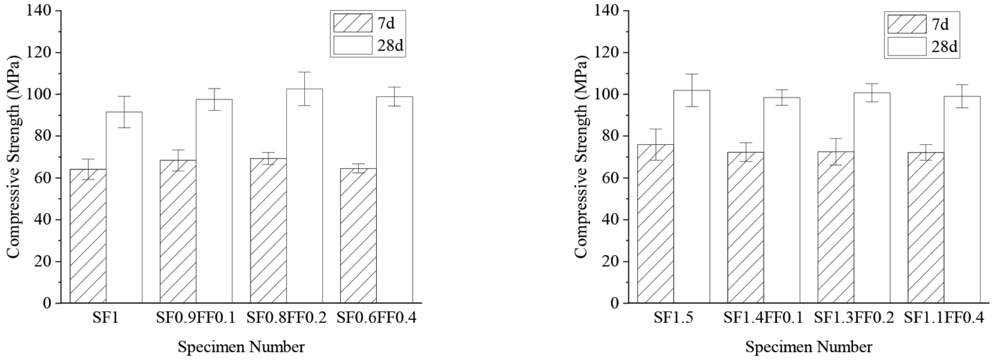

(c) Compressive strength of the mortar with 1% total content of steel fibers and sisal fibers

(d) Compressive strength of the mortar with 1.5% total content of steel fibers and sisal fibers

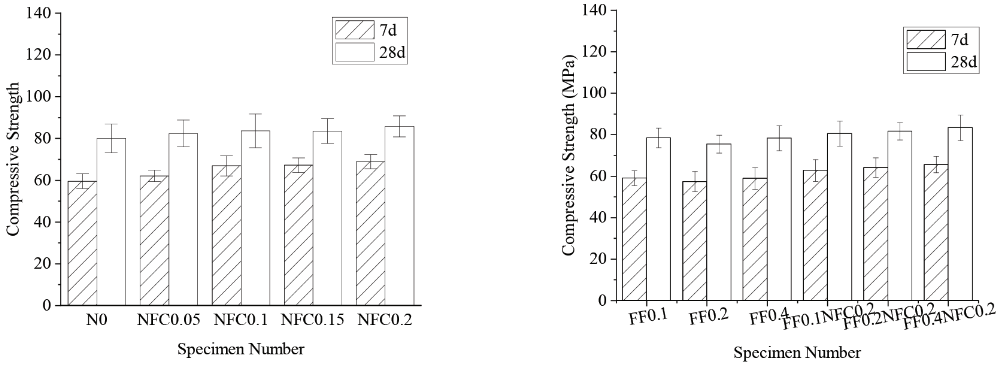

(e) Compressive strength of the mortar after adding NFC

(f) Compressive strength of the mortar with sisal fibers and NFC

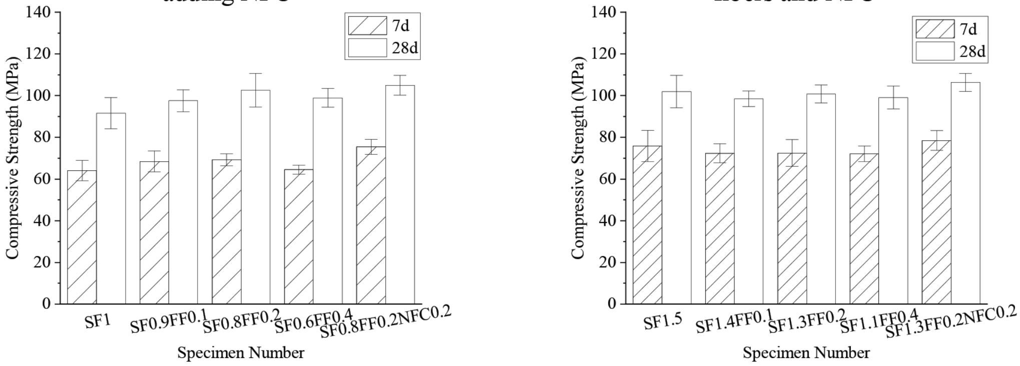

(g) Compressive strength of the mortar with 1.0% total content of steel fibers, sisal fibers, and NFC

(h) Compressive strength of the mortar with 1.5% total content of steel fibers, sisal fibers, and NFC

Fig. 3—Cube compressive strength of mortar at 7 and 28 days. (Note: 1 MPa = 0.145 ksi.)

total cannot adequately reveal the synergy effect in compression with relatively low content.

Moreover, the test group SF0.8FF0.2NFC0.2 showed an increase of 8.89% and 2.23% in compressive strength at 7 and 28 days compared to the test group SF0.8FF0.2, as shown in Fig. 3(g). The group SF1.3FF0.2NFC0.2 showed an increase of 8.22% and 4.66% in compressive strength at 7 and 28 days compared to the test group SF1.3FF0.2, as shown in Fig. 3(h). This is owing to the filling of the voids in the mortar matrix and impeding the initiation of microcracks due to the incorporation of nanofibers.

P-CMOD curves

Figure 4 shows the experimentally measured *P*-CMOD curves. It can be observed that the control group N0 and the experimental group with singly added sisal fibers and nanocellulose exhibited relatively brittle fracture characteristics, as shown in Fig. 4(a), (b), and (e). The *P*-CMOD curves of the FF0.1, FF0.2, and FF0.4 experimental groups did not show a softening segment, as shown in Fig. 4(b), nor did the group combining NFC and sisal fibers, as shown in Fig. 4(f). It can be attributed to the insignificant crack suppression effect of the low dosage of sisal fibers. On the other hand, specimens with singly added steel fiber, as well as a mixture of steel and sisal fibers, exhibited a gradual softening segment after reaching the peak load, as shown in Fig. 4(a), (c), and (d). This demonstrates that the addition of steel fibers and a mixture of steel and sisal fibers can significantly enhance the deformation and bearing capacities of the cementitious composites. The strong bridging effect and load transfer action of the steel fibers effectively suppress the propagation of macrocracks visible to the naked eye.

Moreover, among the specimens with a total dosage of 1% of steel and sisal fibers, when replacing limited volumes of steel fibers with sisal fibers, the *P*-CMOD curve can enclose a larger area than non-replacing specimens. Among them, the *P*-CMOD curve of SF0.8FF0.2 had the highest enclosed area, indicating superior bending performance at a 1% dosage, as shown in Fig. 4(g). Similarly, among the specimens with a total dosage of 1.5% of steel and sisal fibers, the specimens with sisal fibers replacing steel fibers cultivated a better performance in *P*-CMOD curves; the *P*-CMOD curve of SF1.3FF0.2 had the highest enclosed area, indicating superior bending performance at a 1.5% dosage, as shown in Fig. 4(h).

Furthermore, with the addition of nanocellulose, the *P*-CMOD curves of SF0.8FF0.2NFC0.2 and SF1.3FF0.2NFC0.2 had higher enclosed areas than SF0.8FF0.2 and SF1.3FF0.2, respectively. It demonstrated that the addition of NFC to the mixture containing steel and sisal fibers can improve the ductility and bearing capacity. However, when adding NFC to N0 or the mixture just containing sisal fibers, the ductility did not show distinct improvement, as shown in Fig. 4(e) and (f). It indicates that the nanocellulose effectively enhances the interfacial bond strength between steel fibers, sisal fibers, and the cementitious composites.

P-δ curves

Figure 5 shows the experimentally measured *P*-δ curves. The *P*-δ curves showed a similar trend to the *P*-CMOD curves. From Fig. 5(a), it can be observed that specimens containing steel fibers exhibited a distinct ductile fracture mode. However, the individual addition of sisal fiber (Fig. 5(b)) or nanocellulose (Fig. 5(e)) did not significantly improve the fracture mode of the specimens, which may be attributed to the lower content of sisal fibers and poor macroscopic bridging ability of nanocellulose, nor did the group combining NFC and sisal fibers, as shown in Fig. 5(f). Nanocellulose mainly suppresses the occurrence of microcracks in the cementitious matrix and has a negligible effect on the fracture mode of the specimens when added individually. In the case of sisal and steel fiber hybridization, the *P* of the specimens showed a trend of increasing first and then decreasing (Fig. 5(c) and (d)). Furthermore, in the combination of steel-sisal hybrid fibers, specimens further added with nanocellulose exhibited a higher bending capacity with an outstanding toughness (Fig. 5(g) and (h)).

Initial fracture toughness

The initial fracture toughness reflects the ability of cementitious composites to resist the initiation of free cracks. As shown in Fig. 6, whether it is single-doped with steel, sisal, nanocellulose, or hybrid fibers, they can all increase the initial fracture toughness of cement mortar. Compared with the control group N0, the initial fracture toughness of steel fiber-reinforced cement mortar specimens (SF1, SF1.5, and SF2) increased by 94.17%, 159.63%, and 244.41% respectively, as shown in Fig. 6(a). The initial fracture toughness of sisal-fiber-reinforced cement mortar specimens (FF0.1, FF0.2, and FF0.4) increased by 3.24%, 11.58%, and 8.95%, respectively, as shown in Fig. 6(b). The initial fracture toughness of nanocellulose fiber-reinforced cement mortar specimens (NFC0.05, NFC0.1, NFC0.15, and NFC0.2) increased by 18.79%, 11.87%, 10.56%, and 18.48%, respectively, as shown in Fig. 6(e). These trends indicate that steel fibers have the most significant enhancing effect on the initial fracture toughness of cement mortar when added singly.

Under the condition of a total fiber dosage of 1% of steel and sisal fibers (Fig. 6(c)), as sisal fibers gradually replaced steel fibers, the initial fracture toughness of the specimens initially increased and then decreased. Among them, SF0.8FF0.2 was the highest, reaching 0.83 MPa·m$^{1/2}$ (855 psi·in.$^{1/2}$), which was an increase of 148.02% compared to N0. This suggests that a combination of 0.8% steel fibers and 0.2% sisal fibers in the volume fraction is the optimal fiber combination for improving the initial fracture toughness under a 1% total fiber dosage. Additionally, compared to SF0.8FF0.2, the introduction of 0.2% mass fraction of nanocellulose fiber further increased the initial fracture toughness of the specimens by 12.83%, as shown in Fig. 6(g).

Under the condition of a total fiber dosage of 1.5% of steel and sisal fibers (Fig. 5(d)), as sisal fibers gradually replaced steel fibers, the initial fracture toughness of the specimens initially increased and then decreased. Among them, SF1.3FF0.2 was the highest, reaching 1.154 MPa·m$^{1/2}$ (1247 psi·in.$^{1/2}$), which was an increase of 262.11% compared

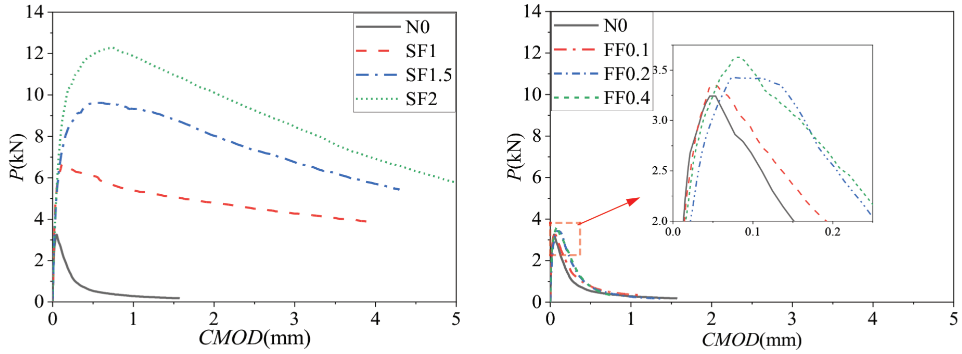

(a)*P-CMOD* curves of the mortar with different steel fiber content

(b)*P-CMOD* curves of the mortar with different sisal fiber content

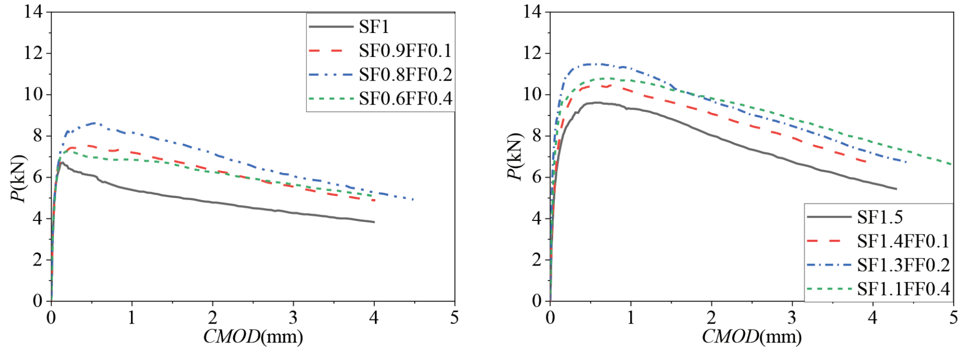

(c) *P-CMOD* curves of the mortar with 1% total content of steel fiber and sisal fiber

(d) *P-CMOD* curves of the mortar with 1.5% total content of steel fiber and sisal fiber

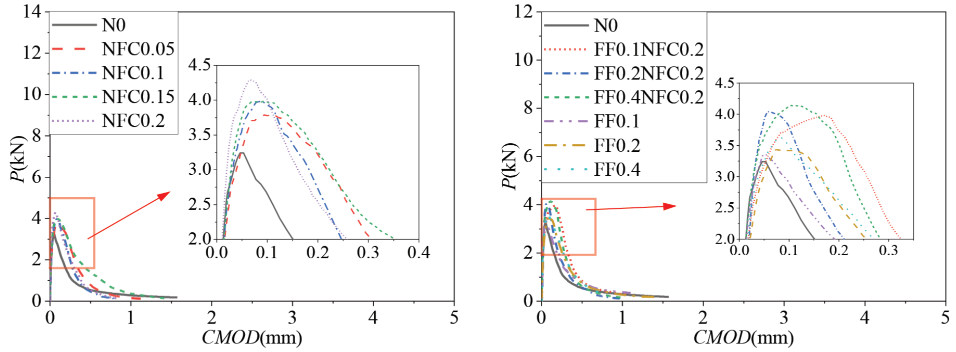

(e)*P-CMOD* curves of the mortar with different NFC content

(f)*P-CMOD* curves of the mortar mixed with combined addition of sisal fiber and NFC

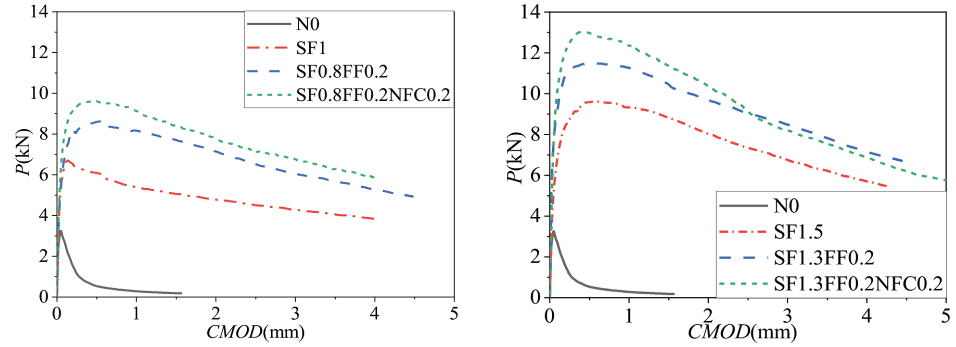

(g)P-CMOD curves of steel fiber and sisal fiber combined with NFC when the total content of steel fiber and sisal fiber is 1%

(h)P-CMOD curves of steel fiber and sisal fiber combined with NFC when the total content of steel fiber and sisal fiber is 1.5%

*Fig. 4—*P-*CMOD curves. (Note: 1 mm = 0.0394 in.; 1 kN = 224.8 lb.)*

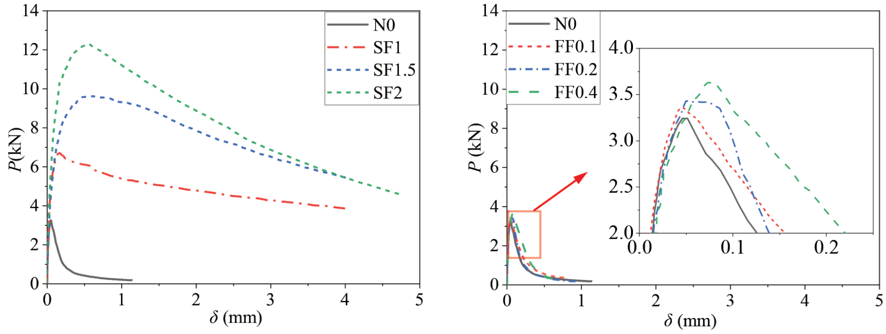

(a) The mortar with different steel fiber content

(b) The mortar with different sisal fiber content

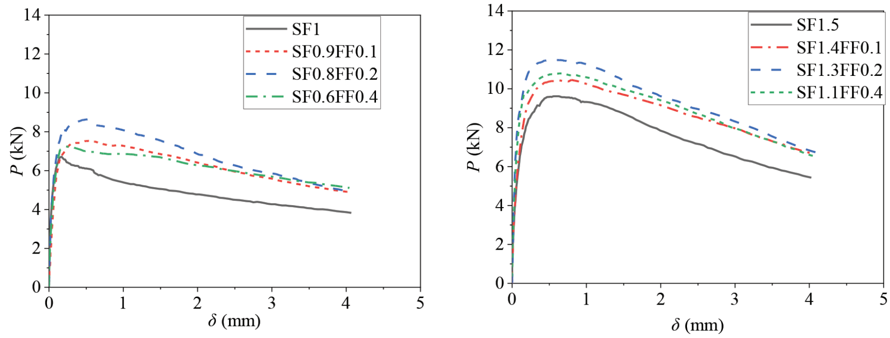

(c) The mortar with 1% total content of steel fiber and sisal fiber

(d) The mortar with 1.5% total content of steel fiber and sisal fiber

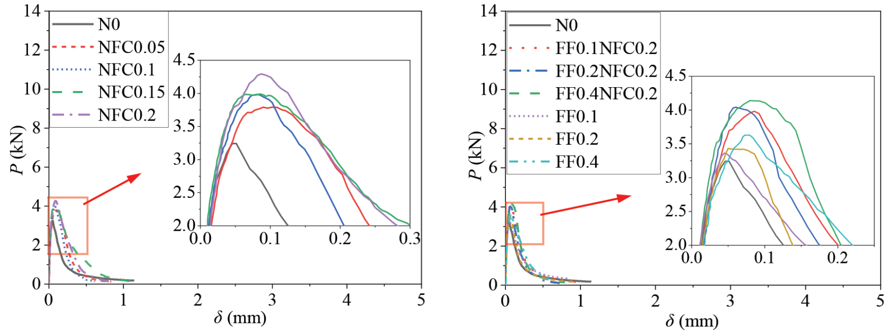

(e) The mortar with different NFC content

(f) The mortar mixed with combined addition of sisal fiber and NFC

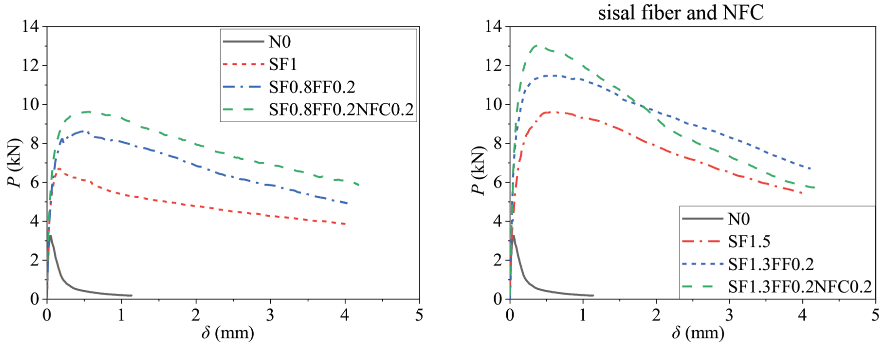

(g) The mortar with steel fiber and sisal fiber combined with NFC when the total content of steel fiber and sisal fiber is 1%

(h) The mortar with steel fiber and sisal fiber combined with NFC when the total content of steel fiber and sisal fiber is 1.5%

*Fig. 5—*P-δ *curves. (Note: 1 mm = 0.0394 in.; 1 kN = 224.8 lb.)*

to N0. This suggests that a combination of 1.3% steel fibers and 0.2% sisal fibers in the volume fraction is the optimal fiber combination for improving the initial fracture toughness under a 1.5% total fiber dosage. Additionally, compared to SF1.3FF0.2, the introduction of 0.2% mass fraction of nanocellulose fiber further increased the initial fracture toughness of the specimens by 18.96%, as shown in Fig. 6(h). This indicates that nanocellulose fiber can be used as a filler in cementitious composites to increase the compactness of the matrix and enhance the ability of specimens to resist external loads when free cracks start to propagate.

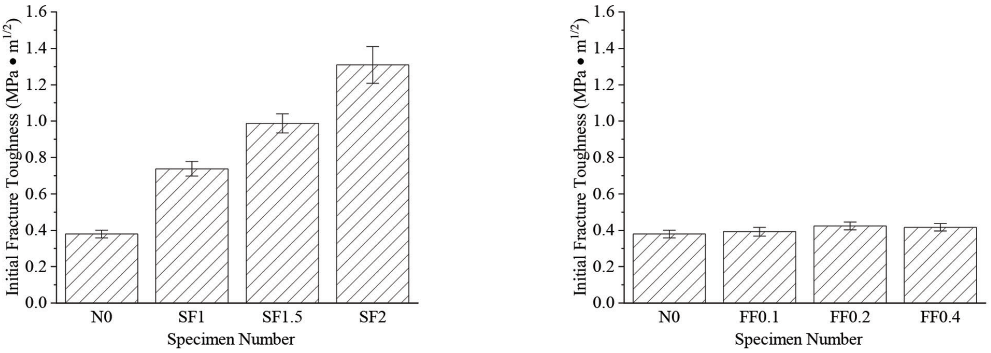

(a) The mortar with different steel fiber content

(b) The mortar with different sisal fiber content

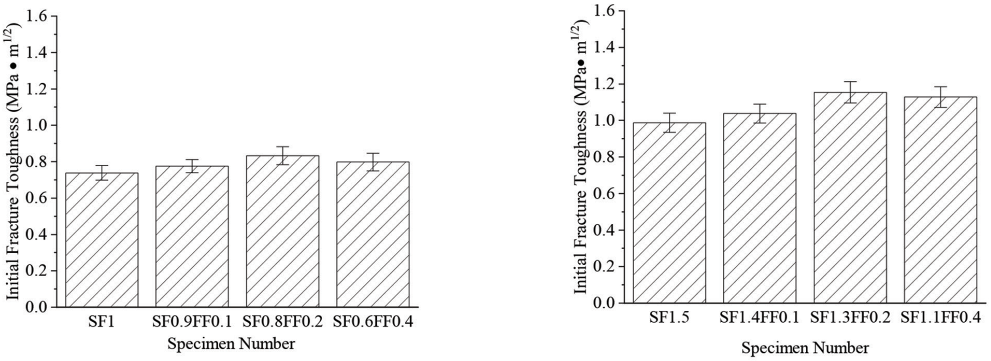

(c) The mortar with 1% total content of steel fiber and sisal fiber

(d) The mortar with 1.5% total content of steel fiber and sisal fiber

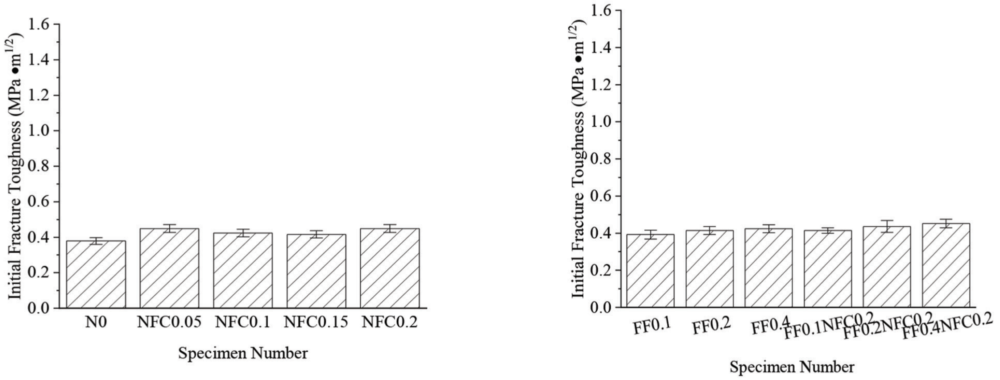

(e) The mortar with different NFC content

(f) The mortar mixed with combined addition of sisal fiber and NFC

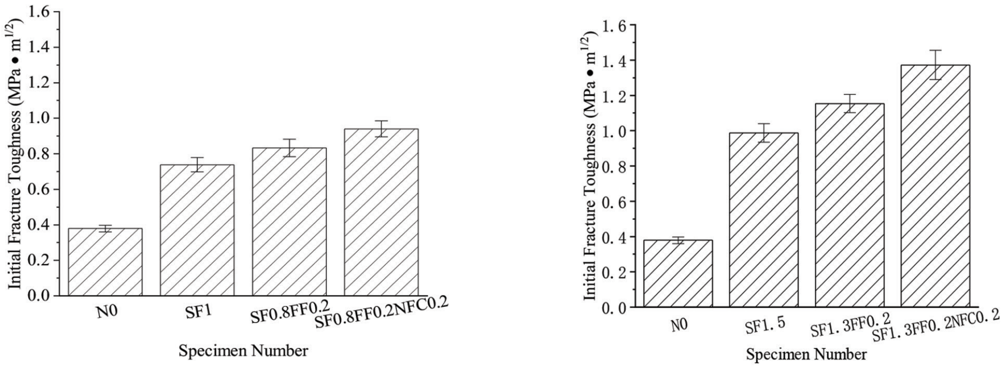

(g) The mortar with steel fiber and sisal fiber combined with NFC when the total content of steel fiber and sisal fiber is 1%

(h) The mortar with steel fiber and sisal fiber combined with NFC when the total content of steel fiber and sisal fiber is 1.5%

Fig. 6—Initial fracture toughness. (Note: 1 m = 39.4 in.; 1 MPa = 145.14 psi.)

Unstable fracture toughness

Unstable fracture toughness reflects the ability of cementitious composites to resist crack instability and expansion under critical conditions. Figure 7 shows the variation of the unstable fracture toughness of cement mortar with steel fibers, sisal fibers, nanocellulose single doping, and sisal fibers in terms of volume fraction of two fibers. It can be seen that the addition of nanocellulose and sisal fibers can both improve the fracture toughness of concrete. Compared to the N0 blank group, the fracture toughness of NFC0.05, NFC0.1, NFC0.15, and NFC0.2 increased by 1.37%, 4.48%, 8.77%, and 14.6%, respectively (Fig. 7(e)). This indicates that as the NFC content increases, the cement mortar continuously shows an increasing trend, indicating that 0.2% of NFC has the best improvement effect on cement mortar. FF0.1, FF0.2, and FF0.4 increased by 2.89%, 5.47%, and 15.01%, respectively, compared to the N0 blank group (Fig. 7(b)). However, compared to steel fibers, their improvement effect was not very significant. SF1, SF1.5, and SF2 reached 5.39 MPa·m$^{1/2}$ (4.9 kip·in.$^{1/2}$), 8.67 MPa·m$^{1/2}$ (7.89 kip·in.$^{1/2}$), and 11.43 MPa·m$^{1/2}$ (10.4 kip·in.$^{1/2}$), respectively, which increased by 278.07%, 509.35%, and 704% compared to N0, as shown in Fig. 7(a). This indicates that steel fibers contribute much more to the improvement of cement mortar than NFC and sisal fibers. Figures 7(c) and (d) illustrate the unstable fracture toughness of cementitious composites with 1% and 1.5% steel fiber content, respectively, when sisal fibers (at volume fractions of 0.1%, 0.2%, and 0.4%) replaced the steel fibers. In the case of a total fiber content of 1%, the cementitious composites, when sisal fibers replaced the steel fibers, exhibited varying degrees of improvement compared to SF1, with increases of 22.52%, 45.52%, and 27.97% for volume fractions of 0.1%, 0.2%, and 0.4%, respectively. Similarly, in the case of a total fiber content of 1.5%, the composite specimens SF1.4FF0.1, SF1.3FF0.2, and SF1.1FF0.4 exhibited different degrees of improvement compared to SF1.5, with increases of 5.15%, 16.35%, and 10.34%, respectively. These results indicate that the ability to resist crack instability and propagation is superior in composites with a combination of steel and sisal fibers compared to those with steel fibers alone.

Figures 7(g) and (h) depict the influence of the combined action of nanocellulose, sisal fibers, and steel fibers on the fracture resistance of cement mortar. When 0.2% nanocellulose was further incorporated into the steel-sisal hybrid fiber system, further improvement was achieved. Compared to SF0.8FF0.2, the addition of nanocellulose resulted in an increase of 16.35% to 9.1 MPa·m$^{1/2}$ (8.28 kip·in.$^{1/2}$). Compared to SF1.3FF0.2, SF1.3FF0.2NFC0.2 reached 11.14 MPa·m$^{1/2}$ (10.1 kip·in.$^{1/2}$), indicating a 10.52% improvement. This enhancement is attributed to the microcrack blocking effect of nanocellulose, which inhibits the formation of microcracks. At the same time, nanoscale NFC acts as a filler to improve the compactness of the cementitious matrix, enhancing crack resistance and preventing crack propagation at critical states in cementitious composites.

Fracture energy

The fracture energy calculation results for each mixture proportion are shown in Fig. 8. It can be observed that steel fibers had the most significant enhancing effect on the G_F of cementitious mortar (Fig. 8(a)). This is because steel fibers at the macroscopic scale can function as a bridge, impeding crack propagation and converting the failure mode of the cementitious mortar toward ductile fracture, thereby increasing the energy absorption capacity of the specimens. However, the inclusion of single sisal fiber does have a significant effect on enhancing the G_F of cementitious mortar, as shown in Fig. 8(b).

Figures 8(c) and (d) illustrate the fracture energy of cementitious composites with 1% and 1.5% steel fiber content, respectively, when sisal fibers were used as a replacement at different volume percentages (0.1%, 0.2%, and 0.4%). For a total fiber content of 1% (including steel and sisal fibers), as the sisal fibers gradually replaced the steel fibers, the fracture energy, G_F, initially increased and then decreased. Among the different combinations, the SF0.8FF0.2 sample exhibited the highest G_F of 3890.04 N/m (265.2 lb/ft). This value was 29.31%, 8.91%, and 7.09% higher than that of SF1, SF0.9FF0.1, and SF0.6FF0.4, respectively. These results indicate that the optimal combination of steel and sisal fibers can improve the energy absorption capacity of cementitious composites, depending on the specific fiber content. Similar trends were observed for a total fiber content of 1.5% as the sisal fibers replaced the steel fibers. The SF1.3FF0.2 sample demonstrated the highest G_F of 5501.92 N/m (375.1 lb/ft), which was 25.97%, 8.79%, and 5.45% higher than that of SF1.5, SF1.4FF0.1, and SF1.1FF0.4, respectively. Therefore, SF1.3FF0.2 represents the optimal fiber combination for achieving the highest energy absorption capacity under a total steel-sisal fiber content of 1.5%.

Figures 8(e) and (f) illustrate the influence of the addition of nanocellulose alone and the combined effect of nanocellulose and sisal fiber on the fracture energy of cement mortar. It can be observed that although the addition of nanocellulose can enhance the fracture properties of cement mortar to some extent, with NFC0.05, NFC0.1, NFC0.15, and NFC0.2 achieving increases of 9.29%, 8.85%, 19.83%, and 27.59%, respectively, in comparison to N0, its effect is far inferior to that of steel fiber. This can be attributed to the structural scale of fiber-reinforced materials, wherein nanocellulose primarily contributes to the nanoscale enhancement of cementitious composites but does not alter the macroscopic brittle fracture characteristics of cement mortar. It is worth noting that, compared to the addition of sisal fiber alone, the inclusion of nanocellulose in FF0.1NFC0.2, FF0.2NFC0.2, and FF0.4NFC0.2 increased the fracture energy by 13.74%, 82.03%, and 48.47%, respectively, highlighting the favorable synergistic effect between nanocellulose and sisal fibers, which enhanced the energy absorption capacity of cement mortar. Figures 8(g) and (h) demonstrate the impact of the combined effect of nanocellulose, sisal fibers, and steel fibers on the fracture energy of cement mortar. Compared to SF0.8FF0.2 and SF1.3FF0.2, the experimental groups SF0.8FF0.2NFC0.2 and SF1.3FF0.2NFC0.2, with the

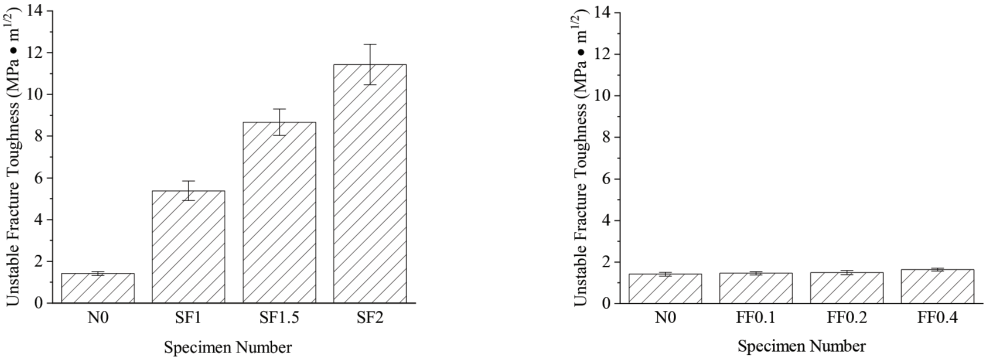

(a) The mortar with different steel fiber content

(b) The mortar with different sisal fiber content

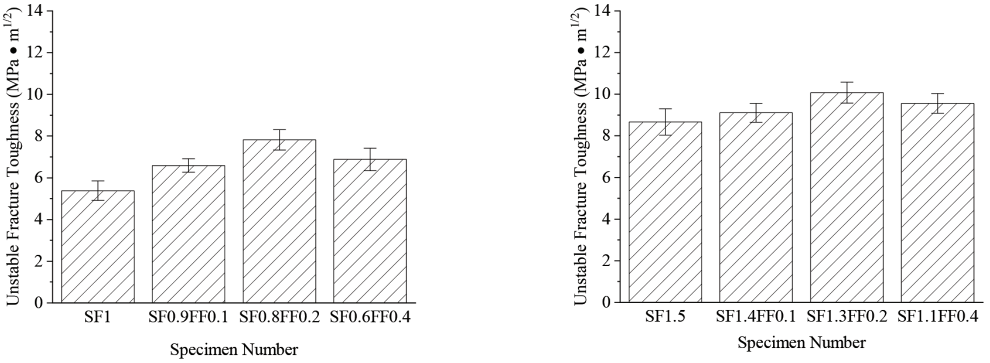

(c) The mortar with 1% total content of steel fiber and sisal fiber

(d) The mortar with 1.5% total content of steel fiber and sisal fiber

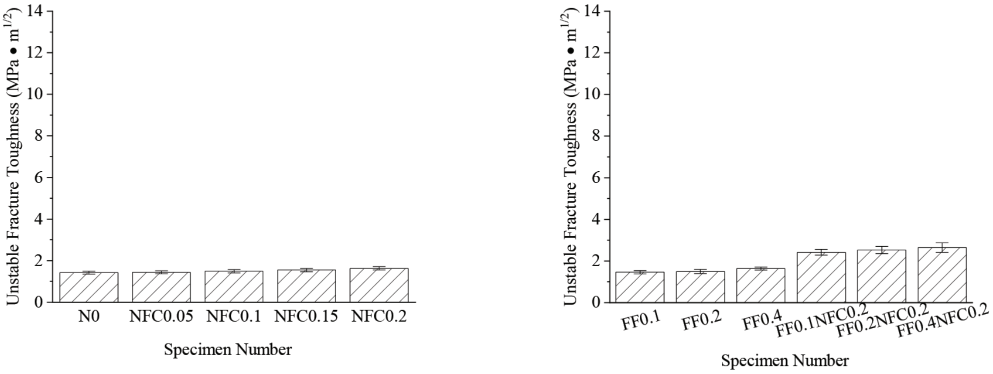

(e) The mortar with different NFC content

(f) The mortar mixed with combined addition of sisal fiber and NFC

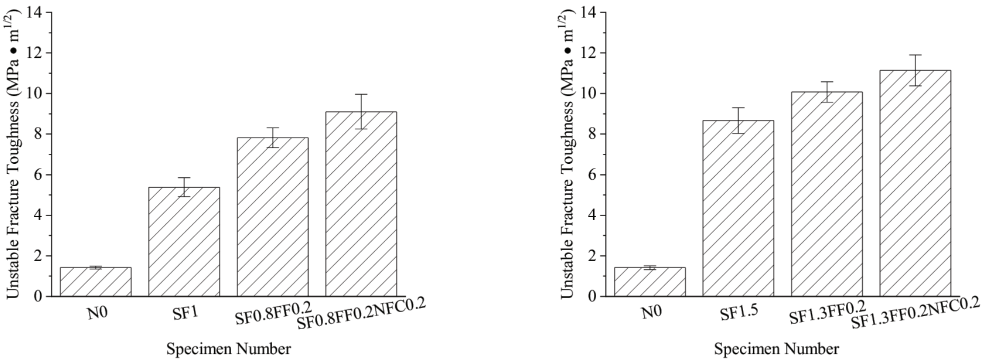

(g) The mortar with steel fiber and sisal fiber combined with NFC when the total content of steel fiber and sisal fiber is 1%

(h) The mortar with steel fiber and sisal fiber combined with NFC when the total content of steel fiber and sisal fiber is 1.5%

Fig. 7—Unstable fracture toughness. (Note: 1 m = 39.4 in.; 1 MPa = 145.14 psi.)

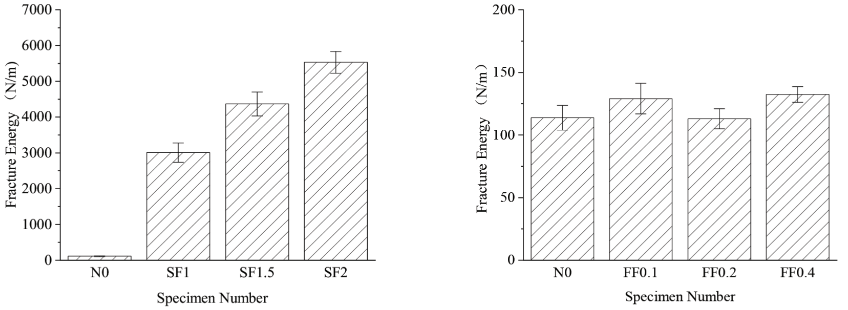

(a) The mortar with different steel fiber content

(b) The mortar with different sisal fiber content

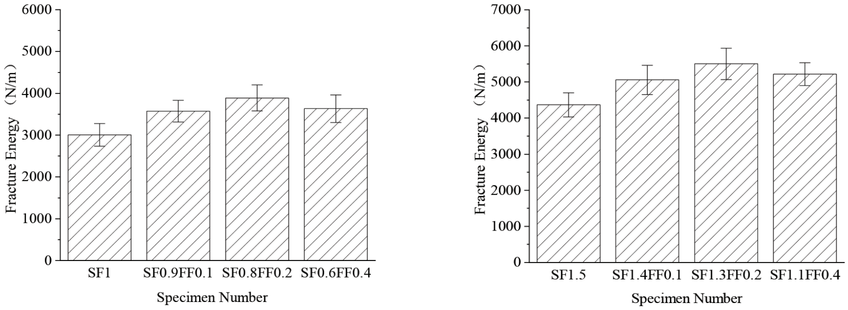

(c) The mortar with 1% total content of steel fiber and sisal fiber

(d) The mortar with 1.5% total content of steel fiber and sisal fiber

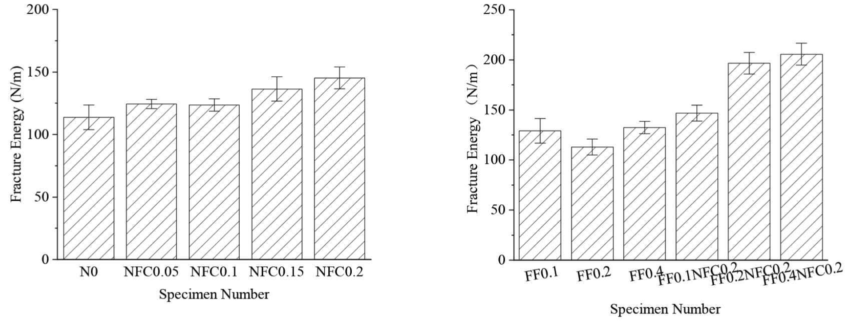

(e) The mortar with different NFC content

(f) The mortar mixed with combined addition of sisal fiber and NFC

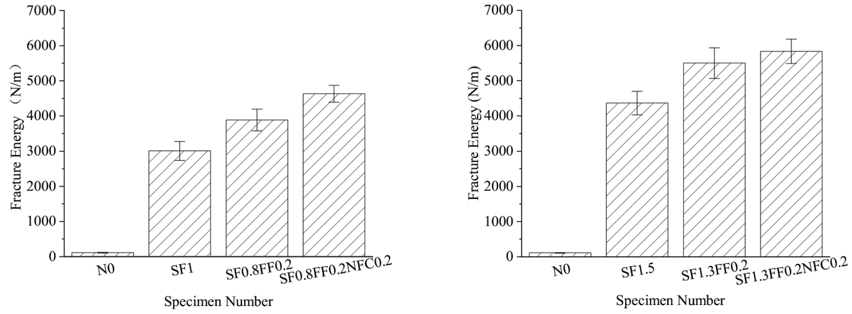

(g) The mortar with steel fiber and sisal fiber combined with NFC when the total content of steel fiber and sisal fiber is 1%

(h) The mortar with steel fiber and sisal fiber combined with NFC when the total content of steel fiber and sisal fiber is 1.5%

Fig. 8—Fracture energy. (Note: 1 m = 3.28 ft; 1 N = 0.225 lb; 1 N/m = 0.068 lb/ft.)

addition of NFC at a mass fraction of 0.2%, exhibited fracture energy increases of 19.12% and 6.03%, respectively.

Synergy of fibers

Three kinds of fibers were used in the research. Among them, the bending capacity and fracture resistance witnessed a surge when more steel fibers were added, while replacing steel fibers with mild volumes of sisal fibers or adding NFC to the system can also enhance the properties. Replacing 0.2% of sisal fibers can increase the load capacity, K_{Ic}^{ini}, K_{Ic}^{un}, and G_F 29.17%, 12.87%, 45.35%, and 29.31% more than that of 1% mono-steel-fiber reinforcement, and 12.01%, 16.91%, 16.26%, and 25.97% more than that of 1.5% mono-steel-fiber reinforcement. In contrast, the load capacity,

K_{Ic}^{ini}, K_{Ic}^{un}, and G_F of the 2% mono-sisal-reinforced mortar was only 5.6%, 11.8%, 5.6%, and –0.75% more than the non-reinforced group N0. That is because monofiber composites with high-stiffness fibers exhibit high ultimate strength, low strain capacity, and small crack widths, whereas those with low-stiffness fibers have low ultimate strength, high strain capacity, and large crack widths. A hybrid composite with an appropriate volume ratio of high- and low-stiffness fibers is anticipated to concurrently enhance ultimate strength, strain capacity, and crack width characteristics.[37]

Furthermore, when adding 2% of NFC to the system containing 1.0% macrofibers, the load capacity, K_{Ic}^{ini}, K_{Ic}^{un}, and G_F could grow 10.34%, 13.25%, 16.37%, and 19.12% more. When adding 2% of NFC to the system containing 1.5% macrofibers, the load capacity, K_{Ic}^{ini}, K_{Ic}^{un}, and G_F could grow by 13.78%, 18.89%, 10.52%, and 6.03%, respectively. When adding NFC singly to the mortar without fibers, the load capacity, K_{Ic}^{ini}, K_{Ic}^{un}, and G_F grew by 34.3%, 18.46%, 14.79%, and 27.59%, but the absolute values were very low due to the relatively poor ability of the no-fiber group. That is because the large macrofibers bridge the big cracks and provide toughness, while microfibers can block the initiation and propagation of cracks by reducing the generation of microcracks and blunting the crack tips.[38] Microfibers also improve the pullout response of macrofibers by improving the properties of the internal zone area between macrofibers and the mortar, thus producing composites with higher strength and toughness.[39] Consequently, the combination of micro and macrofibers can yield a more distinct effect than adding them singly.

CONCLUSIONS

This study investigates the influence of nanocellulose, sisal fibers, and steel fibers on the fracture characteristics (initial fracture toughness, unstable fracture toughness, and fracture energy) of fiber-reinforced cementitious composites (FRCC). Through experimental investigations and analytical study, the following conclusions can be drawn:

1. Compared to cement mortar without fibers, the addition of steel fibers, sisal fibers, and nanocellulose individually enhanced the fracture properties of cementitious composites to some extent. Among them, steel fibers exhibited the best fracture-impeding properties of cement mortar.

2. For both overall volume fractions of 1% and 1.5% of macrofibers, the fracture properties of the cementitious composites increased when the steel fibers were mildly replaced by sisal fibers. An optimum combination ratio exists between the steel and sisal fibers, indicating a balancing point between fracture-impeding properties and price/environment. Under total macrofiber volume fractions of 1% and 1.5%, the 0.2% replacement of steel fibers with sisal fibers (SF0.8FF0.2 and SF1.3FF0.2) exhibited the best fracture-impeding properties.

3. In the hybrid fiber combination containing steel and sisal fibers, the addition of nanocellulose further increased the fracture properties of the cement mortar, with SF0.3FF0.2NFC0.2 exhibiting the best performance. This indicates that nanocellulose synergizes with sisal and steel fibers, achieving a multiscale enhancement effect.

AUTHOR BIOS

Qi Cao *is an Associate Professor in the Department of Civil Engineering, School of Infrastructure Engineering, at Dalian University of Technology, Dalian, Liaoning, China. His research interests include mechanical properties and applications of fiber-reinforced polymer (FRP)-reinforced and strengthened concrete structures, and seismic performance and resilience assessment of concrete structures.*

Liujingyuan Su *is a Doctoral Student in the Department of Civil Engineering, School of Infrastructure Engineering, at Dalian University of Technology, where he received his master's degree. His research interests include mechanical properties of fiber-reinforced concrete.*

Changjun Zhou *is an Associate Professor in the Department of Transportation and Logistics at Dalian University of Technology. He received his PhD from the University of Tennessee, Knoxville, Knoxville, TN. His research interests include the development, characterization, and application of environmentally friendly pavement engineering materials; durability of cement concrete materials; and infrastructure.*

Kaiming Pan *is an Associate Professor at Xinjiang University, Ürümqi, Xinjiang, China. He received his PhD from the Universidad de Castilla-La Mancha, Ciudad Real, Spain. His research interests include fiber-reinforced concrete and fracture mechanics of concrete.*

Jun Wu *is a Graduate Student in the Department of Civil Engineering, School of Infrastructure Engineering at Dalian University of Technology. His research interests include mechanical properties of fiber-reinforced concrete.*

Xiaoyan Han *is a Graduate Student in the Department of Civil Engineering, School of Infrastructure Engineering, at Dalian University of Technology. Her research interests include high-performance concrete materials and fracture mechanics of concrete.*

ACKNOWLEDGMENTS

This work is supported by the National Natural Science Foundation of China (Grant No. 52271264). Some or all data, models, or code that support the findings of this study are available from the corresponding author upon reasonable request.

REFERENCES

1. Pereira, E. B.; Fischer, G.; and Barros, J. A. O., "Effect of Hybrid Fiber Reinforcement on the Cracking Process in Fiber Reinforced Cementitious Composites," *Cement and Concrete Composites*, V. 34, No. 10, Nov. 2012, pp. 1114-1123. doi: 10.1016/j.cemconcomp.2012.08.004

2. Song, H.; Liu, J.; He, K.; and Ahmad, W., "A Comprehensive Overview of Jute Fiber Reinforced Cementitious Composites," *Case Studies in Construction Materials*, V. 15, Dec. 2021, Article No. e00724. doi: 10.1016/j.cscm.2021.e00724

3. Brandt, A. M., "Fibre Reinforced Cement-Based (FRC) Composites After over 40 Years of Development in Building and Civil Engineering," *Composite Structures*, V. 86, No. 1-3, Nov. 2008, pp. 3-9. doi: 10.1016/j.compstruct.2008.03.006

4. Liu, H.; Zhang, Q.; Li, V.; Su, H.; and Gu, C., "Durability Study on Engineered Cementitious Composites (ECC) Under Sulfate and Chloride Environment," *Construction and Building Materials*, V. 133, Feb. 2017, pp. 171-181. doi: 10.1016/j.conbuildmat.2016.12.074

5. Yang, Y.; Zhou, Q.; Li, X.; Lum, G. C.; and Deng, Y., "Uniaxial Compression Mechanical Property and Fracture Behavior of Hybrid Inorganic Short Mineral Fibers Reinforced Cement-Based Material," *Cement and Concrete Composites*, V. 104, Nov. 2019, Article No. 103338. doi: 10.1016/j.cemconcomp.2019.103338

6. Alrekabi, S.; Cundy, A. B.; Lampropoulos, A.; Whitby, R. L. D.; and Savina, I., "Mechanical Performance of Novel Cement-Based Composites Prepared with Nano-Fibres, and Hybrid Nano- and Micro-Fibres," *Composite Structures*, V. 178, Oct. 2017, pp. 145-156. doi: 10.1016/j.compstruct.2017.06.045

7. Smarzewski, P., "Influence of Basalt-Polypropylene Fibres on Fracture Properties of High Performance Concrete," *Composite Structures*, V. 209, Feb. 2019, pp. 23-33. doi: 10.1016/j.compstruct.2018.10.070

8. Guo, A.; Sun, Z.; Sathitsuksanoh, N.; and Feng, H., "A Review on the Application of Nanocellulose in Cementitious Materials," *Nanomaterials*, V. 10, No. 12, Dec. 2020, Article No. 2476. doi: 10.3390/nano10122476

9. Kamasamudram, K. S.; Ashraf, W.; and Landis, E. N., "Cellulose Nanofibrils with and without Nanosilica for the Performance Enhancement

of Portland Cement Systems," *Construction and Building Materials*, V. 285, May 2021, Article No. 121547. doi: 10.1016/j.conbuildmat.2020.121547

10. Barnat-Hunek, D.; Grzegorczyk-Frańczak, M.; Szymańska-Chargot, M.; and Łagód, G., "Effect of Eco-Friendly Cellulose Nanocrystals on Physical Properties of Cement Mortars," *Polymers*, V. 11, No. 12, Dec. 2019, Article No. 2088. doi: 10.3390/polym11122088

11. Goncalves, J.; El-Bakkari, M.; Boluk, Y.; and Bindiganavile, V., "Cellulose Nanofibres (CNF) for Sulphate Resistance in Cement Based Systems," *Cement and Concrete Composites*, V. 99, May 2019, pp. 100-111. doi: 10.1016/j.cemconcomp.2019.03.005

12. Onuaguluchi, O., and Banthia, N., "Plant-Based Natural Fibre Reinforced Cement Composites: A Review," *Cement and Concrete Composites*, V. 68, Apr. 2016, pp. 96-108. doi: 10.1016/j.cemconcomp.2016.02.014

13. Djafari Petroudy, S. R., "Physical and Mechanical Properties of Natural Fibers," *Advanced High Strength Natural Fibre Composites in Construction*, M. Fan and F. Fu, eds., Woodhead Publishing, Sawston, UK, 2017, pp. 59-83.

14. Kurpińska, M.; Pawelska-Mazur, M.; Gu, Y.; and Kurpiński, F., "The Impact of Natural Fibers' Characteristics on Mechanical Properties of the Cement Composites," *Scientific Reports*, V. 12, No. 1, 2022, Article No. 20565. doi: 10.1038/s41598-022-25085-6

15. Rana, S.; Pichandi, S.; Parveen, S.; and Fangueiro, R., "Natural Plant Fibers: Production, Processing, Properties and Their Sustainability Parameters," *Roadmap to Sustainable Textiles and Clothing: Eco-friendly Raw Materials, Technologies, and Processing Methods*, S. S. Muthu, ed., Springer, Singapore, 2014, pp. 1-35.

16. La Rosa, A. D., and Grammatikos, S. A., "Comparative Life Cycle Assessment of Cotton and Other Natural Fibers for Textile Applications," *Fibers*, V. 7, No. 12, Dec. 2019, Article No. 101. doi: 10.3390/fib7120101

17. Munasinghe, P.; Druckman, A.; and Dissanayake, D. G. K., "A Systematic Review of the Life Cycle Inventory of Clothing," *Journal of Cleaner Production*, V. 320, Oct. 2021, Article No. 128852. doi: 10.1016/j.jclepro.2021.128852

18. Bachchan, A. A.; Das, P. P.; and Chaudhary, V., "Effect of Moisture Absorption on the Properties of Natural Fiber Reinforced Polymer Composites: A Review," *Materials Today: Proceedings*, V. 49, Part 8, 2022, pp. 3403-3408. doi: 10.1016/j.matpr.2021.02.812

19. Elfaleh, I.; Abbassi, F.; Habibi, M.; Ahmad, F.; Guedri, M.; Nasri, M.; and Garnier, C., "A Comprehensive Review of Natural Fibers and Their Composites: An Eco-Friendly Alternative to Conventional Materials," *Results in Engineering*, V. 19, Sept. 2023, Article No. 101271. doi: 10.1016/j.rineng.2023.101271

20. John, M. J., and Anandjiwala, R. D., "Recent Developments in Chemical Modification and Characterization of Natural Fiber-Reinforced Composites," *Polymer Composites*, V. 29, No. 2, Feb. 2008, pp. 187-207. doi: 10.1002/pc.20461

21. Gonzalez, V.; Lou, X.; and Chi, T., "Evaluating Environmental Impact of Natural and Synthetic Fibers: A Life Cycle Assessment Approach," *Sustainability*, V. 15, No. 9, May 2023, Article No. 7670. doi: 10.3390/su15097670

22. Mahmud, S.; Hasan, K. M. F.; Jahid, M.; Mohiuddin, K.; Zhang, R.; and Zhu, J., "Comprehensive Review on Plant Fiber-Reinforced Polymeric Biocomposites," *Journal of Materials Science*, V. 56, No. 12, Apr. 2021, pp. 7231-7264. doi: 10.1007/s10853-021-05774-9

23. Ruano, G.; Bellomo, F.; López, G.; Bertuzzi, A.; Nallim, L.; and Oller, S., "Mechanical Behaviour of Cementitious Composites Reinforced with Bagasse and Hemp Fibers," *Construction and Building Materials*, V. 240, Apr. 2020, Article No. 117856. doi: 10.1016/j.conbuildmat.2019.117856

24. Kriker, A.; Debicki, G.; Bali, A.; Khenfer, M. M.; and Chabannet, M., "Mechanical Properties of Date Palm Fibres and Concrete Reinforced with Date Palm Fibres in Hot-Dry Climate," *Cement and Concrete Composites*, V. 27, No. 5, May 2005, pp. 554-564. doi: 10.1016/j.cemconcomp.2004.09.015

25. Kundu, S. P.; Chakraborty, S.; Roy, A.; Adhikari, B.; and Majumder, S. B., "Chemically Modified Jute Fibre Reinforced Non-pressure (NP) Concrete Pipes with Improved Mechanical Properties," *Construction and Building Materials*, V. 37, Dec. 2012, pp. 841-850. doi: 10.1016/j.conbuildmat.2012.07.082

26. Senthilkumar, K.; Saba, N.; Rajini, N.; Chandrasekar, M.; Jawaid, M.; Siengchin, S.; and Alotman, O. Y., "Mechanical Properties Evaluation of Sisal Fibre Reinforced Polymer Composites: A Review," *Construction and Building Materials*, V. 174, June 2018, pp. 713-729. doi: 10.1016/j.conbuildmat.2018.04.143

27. de Souza Castoldi, R.; de Souza, L. M. S.; Souto, F.; Liebscher, M.; Mechtcherine, V.; and de Andrade Silva, F., "Effect of Alkali Treatment on Physical–Chemical Properties of Sisal Fibers and Adhesion Towards Cement-Based Matrices," *Construction and Building Materials*, V. 345, Aug. 2022, Article No. 128363. doi: 10.1016/j.conbuildmat.2022.128363

28. Bao, H.; Meng, H.; You, W.; and Qin, F., "Study on the Corrosion Resistance of Sisal Fiber Concrete in Marine Environment," *SN Applied Sciences*, V. 1, No. 12, Dec. 2019, Article No. 1558. doi: 10.1007/s42452-019-1551-8

29. Ramakrishna, G., and Sundararajan, T., "Impact Strength of a Few Natural Fibre Reinforced Cement Mortar Slabs: A Comparative Study," *Cement and Concrete Composites*, V. 27, No. 5, May 2005, pp. 547-553. doi: 10.1016/j.cemconcomp.2004.09.006

30. Zhou, X.; Ghaffar, S. H.; Dong, W.; Oladiran, O.; and Fan, M., "Fracture and Impact Properties of Short Discrete Jute Fibre-Reinforced Cementitious Composites," *Materials and Design*, V. 49, Aug. 2013, pp. 35-47. doi: 10.1016/j.matdes.2013.01.029

31. ASTM C78/C78M-22, "Standard Test Method for Flexural Strength of Concrete (Using Simple Beam with Third-Point Loading)," ASTM International, West Conshohocken, PA, 2022, 5 pp.

32. ASTM E399-24, "Standard Test Method for Linear-Elastic Plane-Strain Fracture Toughness of Metallic Materials," ASTM International, West Conshohocken, PA, 2024, 40 pp.

33. Xu, S., and Reinhardt, H. W., "Determination of Double-Determination of Double-*K* Criterion for Crack Propagation in Quasi-Brittle Fracture Part I: Experimental Investigation of Crack Propagation," *International Journal of Fracture*, V. 98, No. 2, June 1999, pp. 111-149. doi: 10.1023/A:1018668929989

34. Tada, H.; Paris, P. C.; and Irwin, G. R., *The Stress Analysis of Cracks Handbook*, third edition, ASME Press, New York, 2000, 698 pp.

35. Xu, S.; Li, Q.; Wu, Y.; Dong, L.; Lyu, Y.; Reinhardt, H. W.; Leung, C. K. Y.; Ruiz, G.; Kumar, S.; and Hu, S., "RILEM Standard: Testing Methods for Determination of the Double-K Criterion for Crack Propagation in Concrete Using Wedge-Splitting Tests and Three-Point Bending Beam Tests, Recommendation of RILEM TC265-TDK," *Materials and Structures*, V. 54, No. 6, Dec. 2021, Article No. 220. doi: 10.1617/s11527-021-01786-8

36. RILEM Technical Committee 50-FMC, "Determination of the Fracture Energy of Mortar and Concrete by Means of Three-Point Bend Tests on Notched Beams," *Materials and Structures*, V. 18, No. 4, July 1985, pp. 287-290. doi: 10.1007/BF02472918

37. Bhosale, A.; Rasheed, M. A.; Prakash, S. S.; and Raju, G., "A Study on the Efficiency of Steel vs. Synthetic vs. Hybrid Fibers on Fracture Behavior of Concrete in Flexure Using Acoustic Emission," *Construction and Building Materials*, V. 199, Feb. 2019, pp. 256-268. doi: 10.1016/j.conbuildmat.2018.12.011

38. Chen, Z.; Wang, X.; Ding, L.; Jiang, K.; Huang, H.; Liu, J.; and Wu, Z., "Synergistic Effects of Hybrid Macro Basalt Fibers and Micro Fibers on the Mechanical Properties of UHPC," *Archives of Civil and Mechanical Engineering*, V. 23, No. 4, Nov. 2023, Article No. 264. doi: 10.1007/s43452-023-00807-3

39. Zainal, S. M. I. S.; Hejazi, F.; and Mafaileh, A. M. A., "Strengthening of Reinforced Concrete Slabs Using Macro and Micro Synthetic Fibers," *Structures*, V. 51, May 2023, pp. 1579-1590. doi: 10.1016/j.istruc.2023.03.120

NOTES:

ACI MATERIALS JOURNAL TECHNICAL PAPER

Title No. 122-M33

Hybrid Steel Fiber-Reinforced Concrete for Pavement Overlays

by Pratik Gujar, Beng Wei Chong, Precious Aduwenye, Xijun Shi, and Zachary C. Grasley

This study investigates the feasibility of using a hybrid combination of scrap tire recycled steel fiber (RSF) and manufactured steel fibers (MSF) in concrete pavement overlay applications. A total of five concrete mixtures with different combinations of MSF and RSF, along with a reference concrete mixture, were studied to evaluate fresh and mechanical properties. The experimental findings demonstrate that the concretes incorporating a hybrid combination of RSF with hooked-end MSF exhibit similar or higher splitting tensile strength, flexural strength, and residual flexural strength compared to that of concretes containing only hooked-end MSF, straight MSF, or RSF. This enhanced mechanical performance can be ascribed to the multiscale fiber reinforcement effect that controls different scales (micro to macro) of cracking, thereby providing higher resistance to crack propagation. The concretes containing only RSF show lower splitting tensile strength, flexural strength, and residual flexural strength compared to concrete solely reinforced with straight MSF or other steel fiber-reinforced concrete (SFRC) mixtures due to the presence of various impurities in the RSF such as thick steel wires, residual rubber, and tire textiles. Interestingly, blending RSF with hooked-end MSF overcomes these limitations, enhancing tensile strength, flexural strength, and residual flexural strength, while significantly reducing costs and promoting sustainability. Last, the findings from the pavement overlay design suggest that using a hybrid combination of RSF with hooked-end MSF can reduce the design thickness of bonded concrete overlays by 50% compared to plain concrete without fiber reinforcement, making it a practical and efficient solution.

Keywords: hybrid recycled and manufactured steel fibers; mechanical properties; multiscale fiber reinforcement; overlay design; recycled steel fibers (RSF).

INTRODUCTION

Owing to global population growth and expanding urbanization, a significant amount of tire scrap is generated by vehicles using road networks. This has resulted in various environmental concerns because of the alarming situations regarding the management and disposal of scrap tires. In 2021, approximately 5.03 million tons (4.56 million tonnes) of scrap tires were generated in the United States alone, and 0.73 million tons (0.66 million tonnes) of them were disposed of in landfills.[1] There has been a continuous effort by the U.S. Tire Manufacturers Association (USTMA) and the Texas Commission on Environmental Quality (TCEQ) to ensure a sustainable and circular end-use market for scrap tires.[1,2] In the processing of scrap tires, approximately 15% of the total weight of tire waste can be extracted as steel fibers with irregular shapes and varying dimensions, alongside the production of ground rubber. These recycled steel fibers (RSF) obtained from waste tires have been used as reinforcement in concrete.[3-5] Life cycle assessment studies indicate that processing RSF consumes less energy compared to conventionally manufactured steel fiber (MSF).[6] Interestingly, using all the scrap tire RSF available in the U.S. market to replace conventional steel reinforcement (either reinforcing bar or traditional steel fibers) could lead to a reduction in CO_2 emissions of 245 million tons (222 million tonnes).[7] Moreover, unsorted RSF are significantly cheaper than MSF.[8]

There are several existing studies on the use of steel fibers obtained from waste tires as reinforcement in concrete.[3-6,9-12] However, the majority of the existing studies on RSF-reinforced concrete have been conducted in European nations and the United Kingdom,[3,5,6,11,12] indicating a predominant focus on RSF-reinforced cementitious materials in that region. The mechanical properties of concrete reinforced with RSF—namely, compressive strength, splitting tensile strength, and flexural strength—did not show significant reduction compared to concrete with hooked-end MSF.[4] In another study, RSF-reinforced concrete specimens demonstrated comparable post-cracking behavior to that of MSF-reinforced concrete, exhibiting good energy absorption and residual flexural strength after cracking.[3] However, using a higher volume fraction of RSF in concrete lowered the post-cracking performance of RSF-reinforced concrete.[13] The effectiveness of RSF-reinforced concrete can be attributed to the similar or even higher bond strength between RSF and the cement matrix compared to MSF due to the increased roughness of the RSF surface resulting from adhered residual rubber.[6,14] Recent research conducted by Wang et al.[11] showed that longer fibers significantly improve the flexural strength and residual strength of RSF-reinforced concrete. Therefore, according to the literature, RSF-reinforced concrete appears to be a promising candidate for both structural and nonstructural applications.[4]

With the rapid advancements in tire recycling technology, waste tire processing plants in the United States have adopted better techniques for extracting high-quality RSF, characterized by minimal rubber residue adhering to their surfaces. The increased awareness of sustainability and lack of experimental data to facilitate design warrants the research of using of RSF to reinforce cementitious composites in the

---

ACI Materials Journal, V. 122, No. 5, September 2025.
MS No. M-2024-250.R3, doi: 10.14359/51747871, received March 10, 2025, and reviewed under Institute publication policies. Pertinent discussion including author's closure, if any, will be published ten months from this journal's date if the discussion is received within four months of the paper's print publication.

United States. However, because of the smaller size of the RSF, using RSF alone may only control smaller cracks in concrete. The use of RSF with longer MSF can be of significant potential to effectively mitigate varying levels of crack widths and offer multiscale fiber reinforcement. Additionally, using the larger fiber can help retain mechanical interlocking within the concrete matrix and limit the ingress of various aggressive ions into the concrete.

The mechanical behavior of hybrid manufactured/recycled steel fiber-reinforced concrete (SFRC) was investigated by Martinelli et al.[13] Their experimental results indicate a negligible influence of the addition of fibers in terms of compressive strength, whereas a decrease in the post-cracking performance was observed for specimens with higher fractions of recycled fibers. Nevertheless, an increase in the equivalent fracture energy was observed for fiber-reinforced concrete (FRC) specimens with respect to the plain concrete, even for the case of a total replacement of MSF with RSF. Another research study demonstrated that manufactured fibers can be replaced by an equal amount of recycled fibers without a significant decrease in post-cracking toughness, compared to the MSF-reinforced concrete, provided that the recycled fibers present suitable geometrical characteristics.[15] The enhanced mechanical performance of hybrid fiber systems containing long and short fibers is attributed to their capability to control different scales of cracks—that is, micro- and macroscale cracks.[16-21] Furthermore, there are various studies on hybrid metallic and synthetic FRC systems[17,22-24] reporting a similar trend in the mechanical properties.

The application of concrete overlays is a cost-effective solution for the rehabilitation and maintenance of deteriorated concrete and asphalt pavements. The thickness of a concrete overlay is primarily determined by the concrete material properties, assuming traffic loads, climatic features, and the condition of the existing pavement are the same.[25,26] Thus, it is crucial to design concrete mixtures incorporating a hybrid combination of RSF and longer MSF to achieve maximum flexural strength and residual flexural strength. To the best of the authors' knowledge, there are limited studies on the use of RSF and hybrid RSF/MSF in slab-on-ground and pavement applications,[27,28] and no studies have been conducted specifically focusing on pavement overlay applications in the United States.

This research work aims to investigate the feasibility of using a hybrid combination of RSF and MSF in concrete to achieve multiscale fiber reinforcement for pavement overlay applications. Two types of MSF—that is, hooked-end and straight—and RSF obtained from scrap tires were used in the present investigation. A total of five concrete mixtures with different combinations of MSF and RSF were studied for fresh and mechanical properties, along with a reference concrete mixture without any fiber reinforcement. Subsequently, the full-range load-deflection response for the flexural behavior of SFRC mixtures was evaluated to obtain the residual flexural strength (f_{150}^D), toughness (T_{150}^D), and equivalent flexural strength ratio ($R_{T,150}^D$) using ASTM C1609/C1609M.[29] Finally, based on the flexural and residual flexural strength values obtained for all concrete mixtures, a pavement overlay design was performed to determine the thickness of the bonded SFRC overlay on an existing asphalt pavement, often called whitetopping.

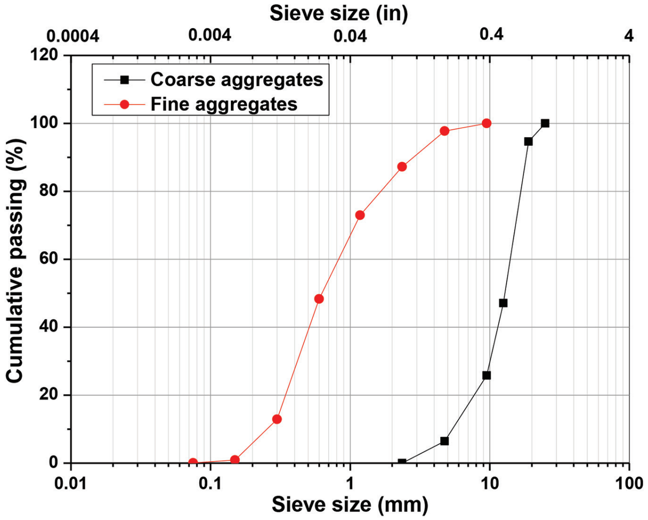

Fig. 1—Particle size distribution of coarse and fine aggregates used in this study.

RESEARCH SIGNIFICANCE

Using FRC in overlays is one of the effective ways to repair and rehabilitate pavements.[30,31] This research explores the synergistic use of RSF obtained from scrap tires with larger-sized manufactured steel fibers. The proposed hybrid fiber combination may effectively mitigate varying levels of crack widths by providing multiscale fiber reinforcement, thereby enhancing resistance to crack opening and propagation. Because the United States is a major source of scrap tire generation, the effective use of RSF in concrete can significantly reduce costs and promote sustainability in construction.

EXPERIMENTAL INVESTIGATION

Materials

First, the physical characteristics of coarse and fine aggregates—that is, particle size distribution, bulk specific gravity, and absorption capacity[32]—were measured. The particle size distribution of both coarse and fine aggregates used in this study is given in Fig. 1. In this work, portland limestone cement (Type IL) and two types of steel fibers—that is, manufactured and recycled—were used. The hooked-end MSF used in this study (refer to Fig. 2) had a circular cross section with an aspect ratio of 64 (l = 1.38 in. [35 mm], d = 0.02 in. [0.55 mm]). The RSF used in this investigation was provided by a tire recycler located in Texas. The RSF had a circular and tortuous cross section with an average aspect ratio of 55 (average l = 0.6 in. [15 mm], average d = 0.012 in. [0.32 mm]) based on a previous study.[33] Most of the RSF had a diameter less than 0.02 in. (0.5 mm), with an average diameter of 0.012 in. (0.32 mm). The length of fiber was within the range of 0.2 to 1 in. (5 to 25 mm), averaging 0.6 in. (15 mm), while aspect ratios of most of the RSF were between 20 and 70 with an average value of 55.[34] As shown in Fig. 3, the RSF is a mixture of steel fibers, steel wires, loose residual rubber, and tire textiles. To compare the mechanical performance of concrete reinforced with a hybrid combination of

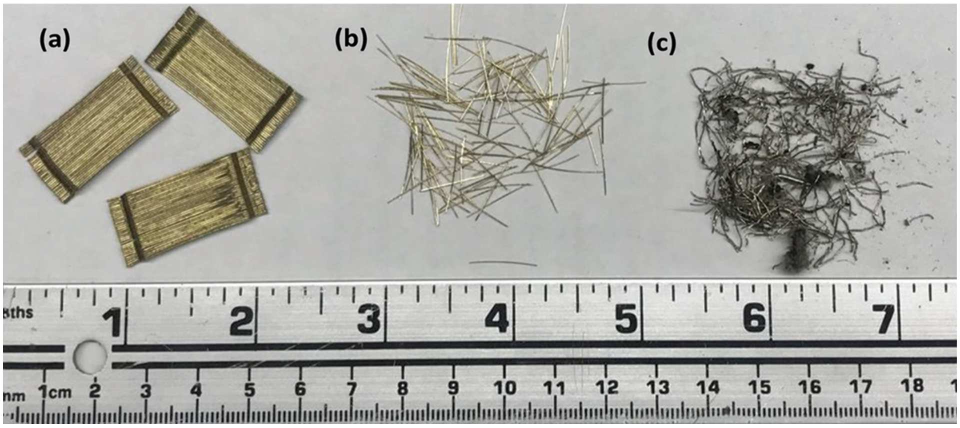

Fig. 2—Types of steel fibers used in this study: (a) hooked-end MSF; (b) straight MSF; and (c) RSF.

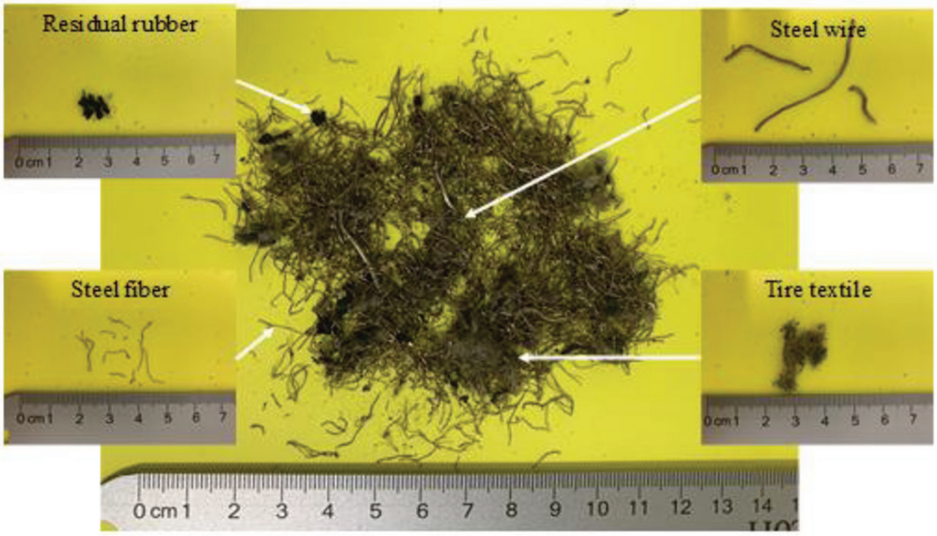

Fig. 3—Various constituents of RSF (reprinted from Shi et al.[33] with permission from Sage Journals). (Note: 1 cm = 2.54 in.)

RSF and hooked-end MSF, concrete incorporating a hybrid combination of hooked-end MSF with similarly sized steel fibers to RSF—that is, straight MSF, was considered. The straight MSF has a circular cross section with an aspect ratio of 65 (l = 0.5 in. [13 mm], d = 0.008 in. [0.2 mm]). Based on a study the authors completed, a steel fiber volume fraction of 1.5% was determined as the optimum fiber dosage[35] for maximizing residual flexural strength. As a result, a steel fiber volume of 1.5% was considered for all SFRC mixtures in the present investigation. A high-range water reducer (HRWR) was used to improve the workability of the reference and SFRC mixtures. The raw material properties are summarized in Table 1.

Mixture design

The concrete mixtures studied in this research work were designed to meet the Class CO requirements specified in the Texas Department of Transportation standard,[36] which are required to have a minimum 56-day compressive strength of 4600 psi (31.72 MPa). All the concrete mixtures used a water-cement mass ratio of 0.40. For the concrete overlay, a design slump value ranging from 3 to 5 in. (75 to 125 mm) was targeted.[36] It is important to note that the volume fraction calculations for SFRC mixtures with RSF were performed using a density of 490 lb/ft^3 (7850 kg/m^3). The mixture proportions for reference concrete and SFRC are detailed in Table 2. In SFRC, a common problem is that both MSF and RSF can easily form fiber clumps in concrete mixtures, thereby reducing the quality of the concrete. To alleviate this issue, the best mixing and casting measures to produce uniform, high-quality SFRC mixtures were examined. The authors explored various mixing approaches to uniformly disperse steel fibers into the concrete mixture, including intermediate mixing and end-stage mixing proposed by different researchers.[35,37] Through experimental trials, the mixing procedure outlined by Shi et al.[35] was found to be more suitable for the author's SFRC mixtures and was therefore adopted for preparing all SFRC mixtures considered in this study. The concrete mixtures were prepared using a stand mixer and the stepwise mixing process is detailed here:

- First, add the coarse and fine aggregates to the Hobart mixer with three-quarters of the water containing HRWR and mix for 1 minute
- Then, add the cement and mix it with other constituents for 1 minute

Table 1—Raw material properties

Material	Specific gravity	Typical size	Other information
Cement	3.15	Not available	Type IL
Coarse aggregate	2.45	0.75 in. (19 mm)	Absorption capacity: 2.51%
Fine aggregate	2.60	0.19 in. (4.75 mm)	Absorption capacity: 0.80%
Hooked-end steel fiber	7.85	*l* = 1.38 in. (35 mm), *d* = 0.02 in. (0.55 mm)	Aspect ratio: *l*/*d* = 64 Tensile strength: 174,045 psi (1200 MPa)
Straight steel fiber	7.85	*l* = 0.51 in. (13 mm), *d* = 0.008 in. (0.2 mm)	Aspect ratio: *l*/*d* = 65 Tensile strength: 385,800 psi (2660 MPa)
Recycled steel fiber	7.65 to 7.85	Average *l* = 0.6 in. (15 mm), Average *d* = 0.012 in. (0.32 mm)	Average aspect ratio: *l*/*d* = 55

Table 2—Mixture proportion of reference and SFRC mixtures, lb/yd^3 (kg/m^3)

	Quantity	
Materials	Reference concrete	SFRC
Cement	565 (335)	565 (335)
Coarse aggregate	1714 (1017)	1714 (1017)
Fine aggregate	1372 (814)	1372 (814)
Water	226 (134)	226 (134)
HRWR	2.83 (1.68)	5.65 (3.35)
Fiber	—	198 (118)

- Add the rest of the water and mix all the constituents for a duration of 2 minutes
- Once the mixture becomes consistent and flowable, manually disperse steel fibers into the concrete mixture and continue mixing for 3 minutes
- Stop the mixer and cover the mixer with a polypropylene (PP) sheet, allowing it to rest for 3 minutes
- Finally, restart the mixer and mix the concrete mixture for 2 minutes

This research work involved a total of six concrete mixtures, as summarized in Table 3. After the concrete mixture was prepared, fresh properties including slump, unit weight, and air content were measured. Subsequently, the specimen casting was completed within 15 to 20 minutes after measuring the fresh properties. A higher than the usual amount of effort was made to consolidate the mixture and screed the surface of the SFRC specimens containing only hooked-end MSF and a hybrid combination of hooked-end and straight MSF. However, the incorporation of RSF in concrete did not show much difficulty in finishing. The prepared specimens were stored in a room with a constant temperature of 73.4°F (23°C) and covered by a plastic sheet to prevent moisture loss. After 24 hours, specimens were demolded and kept for curing in a standard moist room (73.4°F [23°C], 100% relative humidity [RH]) for additional periods of 2, 6, and 27 days.

EXPERIMENTAL METHODS

Fresh properties

The fresh properties of SFRC mixtures including slump, unit weight, and air content were measured according to ASTM C143/C143M[38] and ASTM C138/C138M,[39] respectively.

Fiber dispersion

Ensuring uniform dispersion of steel fibers is a crucial aspect in SFRC mixtures, as the formation of fiber clumps significantly lowers the quality of concrete. In this study, the authors explored intermediate and end-stage mixing techniques to address this issue[35,37] and X-ray computed tomography (CT) was employed to examine the distribution of steel fibers in various SFRC mixtures. The aim was to assess fiber dispersion and compare X-ray CT images between SFRC mixtures containing single fibers and those containing a hybrid combination of longer and shorter fibers.

To examine fiber distribution through CT scans, an industrial 225 kV CT scanner was used. The scanner was operated at voltage and current settings of 115 kV and 95 mA, respectively, with a focal spot size of 120 microns. A series of several thousand images were taken over 360 degrees of rotation on SFRC cylinder, measuring 4 x 8 in. (100 x 200 mm) from the top. It is noteworthy that to eliminate streak artifacts caused by the hybrid fiber system combining RSF and hooked-end MSF, the voltage and current settings were adjusted to 225 kV and 125 mA, respectively. The radiographs were reconstructed using NSI efXct reconstruction software, and the reconstructed volume was imported into Volume Graphics software to obtain complete volume data and image stacks.[40] An example cross section from a typical X-ray CT image of SFRC mixtures containing RSF and a hybrid combination of RSF and hooked-end MSF is presented in Fig. 4. It appeared that the steel fibers were well dispersed in the concrete matrix without the formation of clumps. Further, a greater number of fibers aligned parallel to the filling plane adjacent to the wall of the cylindrical specimen and on the top while undergoing the filling, tamping, and vibrating process. This phenomenon, known as the wall effect, is commonly exhibited in FRCs.[41] During the casting process, fibers tended to align parallel to the mold walls, resulting in a non-uniform fiber distribution. This led to a higher concentration of fibers near the edges of the concrete specimens compared to the center, due to the physical constraints because of the mold boundaries. Additionally, a visual examination of the failure planes of SFRC specimens following the execution of splitting tensile and flexural tests was conducted. It was observed that the fibers were uniformly dispersed without clumping within the concrete matrix, as illustrated in Fig. 5.

Table 3—Summary of various mixtures prepared

Mixture abbreviation	Mixture details	Fiber volume fraction, %
REF	Plain concrete mixture (that is, without fiber reinforcement)	NA
M(H)	SFRC mixture with only hooked MSF	1.5
M(S)	SFRC mixture with only straight MSF	1.5
R	SFRC mixture with only RSF	1.5
M(H)(S)	SFRC mixture with an equal amount of hooked-end and straight MSF (that is, 0.75% each)	0.75 + 0.75 = 1.5
RM(H)	SFRC mixture with an equal amount of hooked-end MSF and RSF (that is, 0.75% each)	0.75 + 0.75 = 1.5

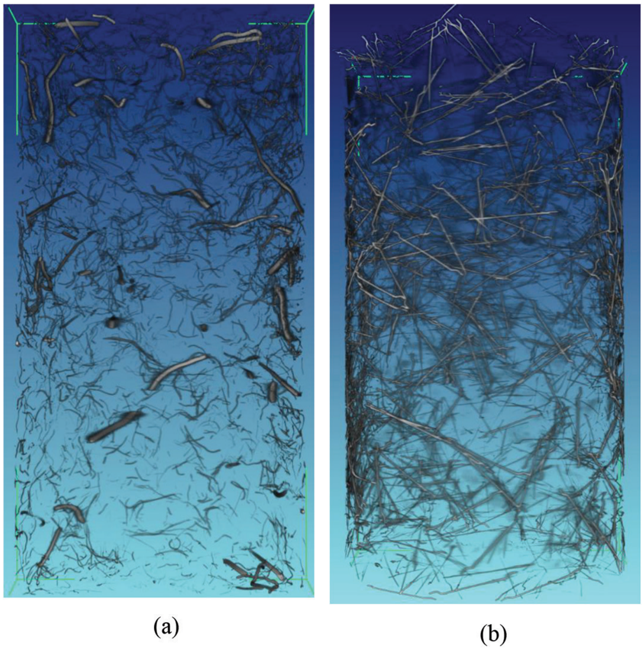

Fig. 4—X-ray CT images of SFRC cylindrical specimen with dimensions of 4 x 8 in. (100 x 200 mm) containing: (a) RSF; and (b) hybrid combination of hooked-end MSF and RSF.

Mechanical properties

The mechanical properties—namely, compressive strength, dynamic modulus of elasticity (MOE), splitting tensile strength, and flexural strength—of all the concrete mixtures at 3, 7, and 28 days were evaluated. The compression test was conducted according to ASTM C39/C39M.[42] Cylindrical specimens with dimensions of 4 x 8 in. (100 x 200 mm) were uniaxially loaded under compression at a loading rate of 35 psi/s (0.25 MPa/s) using a universal testing machine (UTM) with a capacity of 1124 kip (5000 kN) to measure compressive strength. According to ASTM C215,[43] the dynamic MOE of concrete specimens was assessed. A steel ball of diameter of 0.4 in. (10 mm) was used as an impact source for generating incident stress waves in cylindrical concrete specimens with the same dimensions that were used for compressive strength measurements. The longitudinal fundamental resonant frequencies were measured by an accelerometer that was used to calculate the dynamic MOE of the concrete specimens. The splitting tensile strength of the concrete specimens was determined by ASTM C496/C496M[44] using 4 x 8 in. (100 x 200 mm) cylindrical specimens. The test was performed using the UTM at a loading rate of 2.5 psi/s (0.017 MPa/s).

The flexural strength of concrete beams was obtained by performing the third-point loading test in accordance with ASTM C78/C78M.[45] Specimens with dimensions of 4 x 4 x 14 in. (100 x 100 x 350 mm) were loaded at the rate of 2.5 psi/s (0.017 MPa/s) using the UTM to obtain flexural strength. Finally, the full-range (prior-cracking and post-cracking) load-deflection curves for the flexural behavior of SFRC mixtures were studied to obtain ductility and toughness parameters using ASTM C1609[29] at 28 days. The beams with dimensions of 4 x 4 x 14 in. (100 x 100 x 350 mm) tested on a 12 in. (300 mm) span were loaded at their third points with a linear variable differential transformer (LVDT) to measure the midpoint deflection on each side. A metallic frame with screws was fixed to the neutral axis of the concrete beam above the support points, and LVDTs were mounted on each side of the frame as shown in Fig. 6. The load versus deflection was recorded to get ductility and toughness parameters for various SFRC mixtures. It should be noted that all the mechanical tests were performed on a set of three specimens for each mixture at all curing ages considered in this study.

Pavement overlay design

It has been reported that the addition of macrofibers to plain concrete increases the flexural and ultimate capacities of concrete pavement slabs.[25] For FRC, residual flexural strength (f_{150}^{D}) is a representative material property that quantifies the benefits of the addition of macrofibers into plain concrete after it has cracked. Essentially, it is the post-cracking flexural strength of FRC corresponding to the residual load (P_{150}^{D}) at a net deflection of $L/150$. Therefore, for the design of concrete pavement overlay with macrofibers, effective flexural strength (f_{eff}) was used as that of the standard flexural strength (f_1). This effective flexural strength is the sum of residual flexural strength (f_{150}^{D}) and standard flexural strength[25,30] as given in Eq. (1).

$$f_{eff} = f_1 + f_{150}^{D} \tag{1}$$

This design approach was proposed by Altaoubat et al.[30] and validated by small and large-scale testing of FRC slabs in the lab. The approach was then adopted by the American Concrete Pavement Association (ACPA) to design concrete overlay. There are several design procedures and software applications available for bonded and unbonded overlays.[25] In this study, a bonded overlay of concrete over asphalt pavement (located in Texas) was considered and is discussed in detail in the subsequent sections.

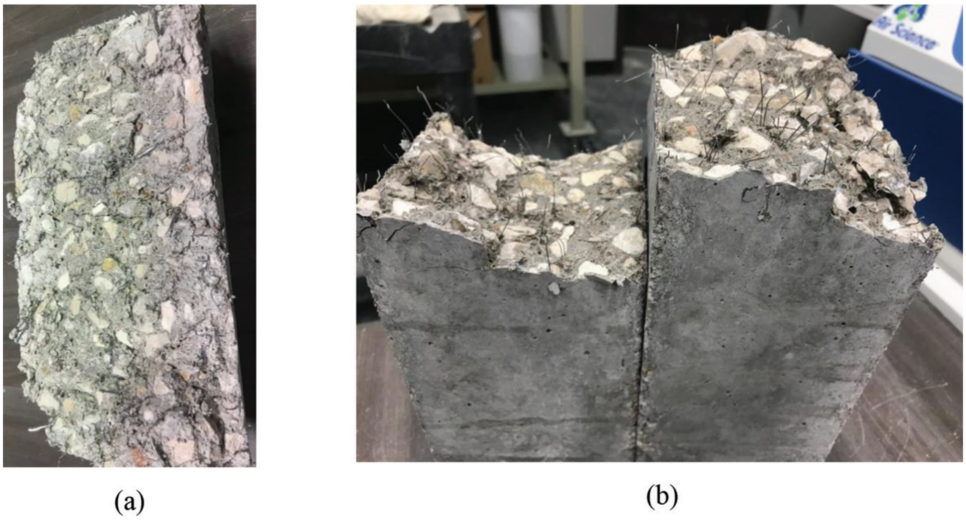
(a) (b)

Fig. 5—Visual inspection of failure plane of SFRC specimens: (a) with RSF after performing splitting tensile; and (b) with hooked-end MSF performing flexural test.

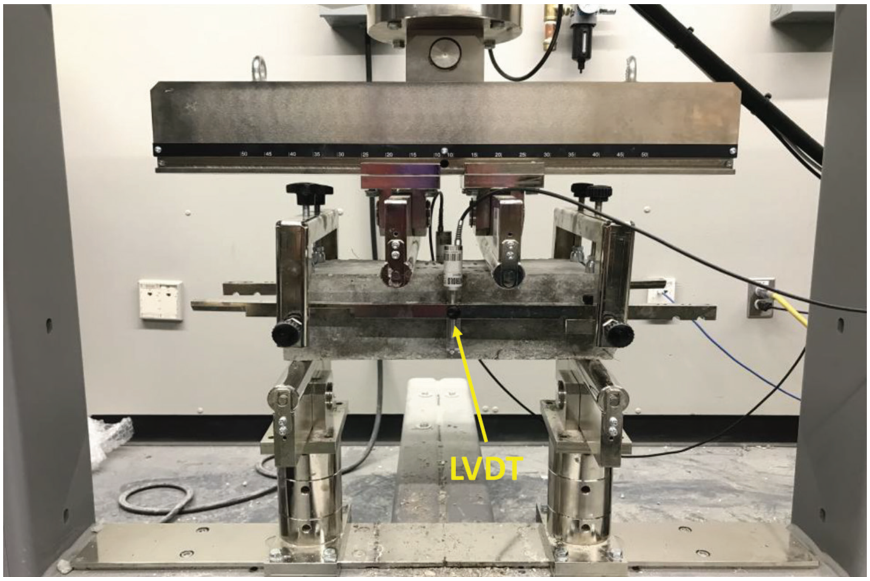

Fig. 6—Experimental setup of flexural test of SFRC beam using third-point loading applying ASTM C1609.

The design procedure adopted in this study was based on the Bonded Concrete Overlay on Asphalt Thickness Designer (BCOA), developed by the ACPA.[46] The overlay design process consists of two steps. The first step requires input of traffic data corresponding to the type of street. In this investigation, a residential street was taken as a case study, and the traffic parameters over the pavement during the design life are outlined in Table 4. The second step entails specifying the properties of existing pavement (in this case, asphalt pavement) and subgrade properties. Table 5 presents the input properties of the existing asphalt pavement and subgrade for the design of the bonded overlay over the asphalt pavement. For all SFRC and reference cases, the same design input parameters such as traffic loading, design life, subgrade properties, and pre-overlay surface preparation were maintained, except for the mechanical properties—that is, flexural strength (or modulus of rupture [MOR]) and residual strength of the SFRC mixtures. The reliability and percentage of slabs cracked at the end of design life were assumed to be 85% and 20%, respectively.

The software specifies a range for the average 28-day flexural strength that spans from 500 to 850 psi (3.45 to 5.86 MPa), disregarding values outside of this range for overlay design purposes. A similar restriction applies to the MOE of concrete. Considering these limitations and ensuring a reasonable comparison between the different concrete mixtures, the MOR and MOE of concrete values were scaled down by a constant scaling factor by establishing higher limit values as a reference. The mechanical properties of various SFRC mixtures examined in this study at 28 days are presented in Table 6.

RESULTS AND DISCUSSION

Concrete fresh properties

From the experiments, the slump value for the reference concrete was observed to be 4 in. (100 mm); whereas, for each of the SFRC mixtures, a slump of 0 in. (0 mm) was

Table 4—Traffic input data for residential street located in Texas

Input	Value
Two-way average daily traffic (ADT)	500
Growth rate, %	2
Design life, years	30
Directional distribution factor, %	50
Design lane distribution factor, %	100
Percent trucks, %	2
Design lane equivalent single axle load (ESAL)	125,862

Table 5—Properties of existing asphalt pavement and subgrade

Input	Value
Remaining asphalt thickness, in.	4 (101.6)
Asphalt modulus of elasticity, psi	350,000 (2413.17)
Modulus of subgrade reaction (*k*-value), psi/in.	150 (40.72)

recorded. The slump results show that adding steel fiber dramatically decreased the concrete slump values. This implies that the addition of steel fibers leads to poorer workability of the concrete mixtures tested in this study. Based on the authors' experiences with high fiber volume fractions with a higher water-cement ratio (*w*/*c*) concrete where the slump was minimally affected, the role of fibers on the slump must be considered on a case-by-case basis. Further, the slump test is not a good indicator of the workability and consistency of FRC, because a mixture can show a low slump while having sufficient workability and consistency.[47] Despite the lower slump, concrete samples were adequately consolidated for hardened property testing. The unit weight and air content of the various concrete mixtures are presented in Fig. 7. The unit weight of all the SFRC mixtures was higher as compared to the reference concrete except the concrete with hooked-end steel fibers (refer to Fig. 7(a)). The lower unit weight of M(H) mixture can be attributed to the increased entrapped air resulting from the larger size and hooked-end geometry of M(H) fibers. The larger hooked-end MSF lower the packing density of concrete, creating larger void spaces which in turn reduces the unit weight. This behavior was reflected in the air content values. The concrete mixtures with higher unit weight show lower air content (refer to Fig. 7(b)). However, the concrete mixture with a hybrid combination of hooked-end and straight MSF shows higher air content despite having higher unit weight. This can be ascribed to the combined effect of increased entrapped air and microvoids because of the higher number of steel fibers (due to the smaller size of straight MSF) and poor aggregate gradation in the concrete mixture, resulting in lower packing density.

Mechanical properties of hardened concrete

In the compression test, the reference concrete specimens experienced a catastrophic brittle failure. Conversely, SFRC specimens failed gradually in a ductile manner (refer to Fig. 8). Similarly, in the splitting tensile test, the reference concrete specimens completely split into two halves after the test, whereas SFRC specimens remained intact with smaller crack widths, as presented in Fig. 9. The flexural test predominantly showed fiber pullout failure (refer to Fig. 5(b)), indicating ductile behavior. The failure patterns observed across all mechanical tests clearly demonstrate the ductile nature of SFRC mixtures.

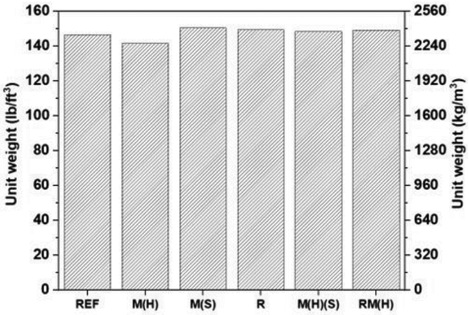

(a) Unit weight

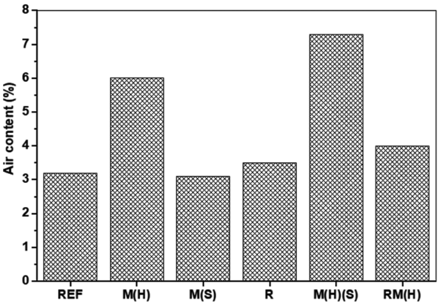

(b) Air content

Fig. 7—Fresh properties of reference and SFRC mixtures; data represent values for single tests.

The compressive strengths of reference and SFRC mixtures at different curing ages are presented in Fig. 10. The compressive strength results indicate that adding steel fibers to plain concrete increases its compressive strength by 15 to 20%. The concrete with straight MSF exhibits the highest compressive strength among all the studied concrete mixtures. This can be explained by the fact that there is a higher number of steel fibers present in the matrix (compared to other fibers at the same fiber volume fraction) because of the smaller dimensions/size of the straight MSF.[48] When compared to straight and hooked-end MSF concrete, the hybrid steel fiber concretes exhibit comparable compressive strength. As expected, compressive strength increases with the curing age of concrete specimens from 3 to 28 days for all concrete mixtures. This is mainly attributed to the strength gained by the concrete matrix because of the cement hydration process.

The MOE of concrete specimens marginally increased with the addition of steel fiber, as displayed in Fig. 11. There is no clear trend found regarding the effect of hybrid steel reinforcement on the MOE of SFRC. As with the compressive strength results, the MOE of concrete mixtures increases with the curing age of concrete.

The splitting tensile strengths for all concrete mixtures at various curing ages are depicted in Fig. 12. From the results, the splitting tensile strength of SFRC is higher in comparison with the reference concrete mixtures (approximately

Table 6—Mechanical properties for SFRC mixtures considered in this study

Mixture	Measured MOR, psi (MPa)	MOR used in simulation, psi (MPa)	Measured MOE, psi (GPa)	MOE used in simulation, psi (GPa)	Residual strength ratio, %
REF	803 (5.54)	558 (3.85)	6,153,950 (42.43)	4,733,800 (32.64)	0
M(H)	982 (6.77)	682 (4.70)	6,507,840 (44.87)	5,000,000 (34.47)	58
M(S)	1054 (7.27)	732 (5.05)	6,507,840 (44.87)	5,000,000 (34.47)	39
R	865 (5.96)	601 (4.14)	6,348,300 (43.77)	4,883,300 (33.67)	24
M(H)(S)	1221 (8.42)	850 (5.86)	6,507,840 (44.87)	5,000,000 (34.47)	47
RM(H)	1022 (7.05)	710 (4.90)	6,251,120 (43.10)	4,797,690 (33.08)	54

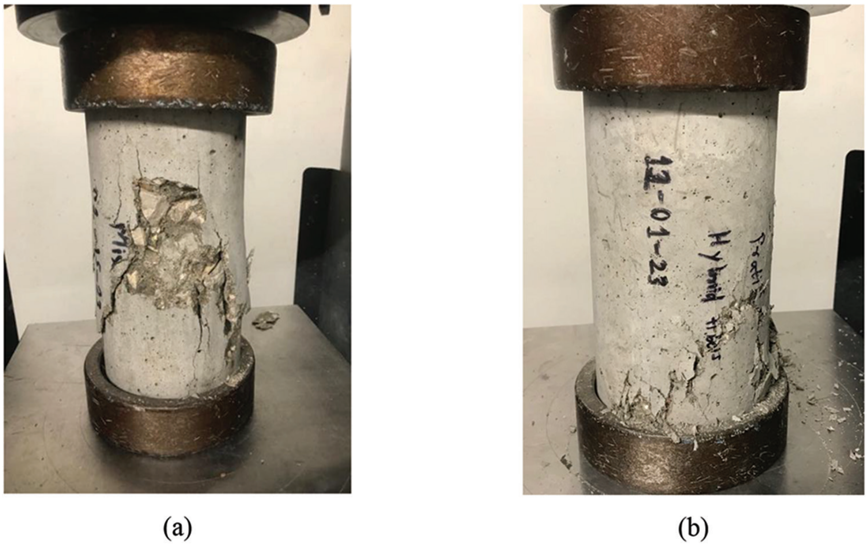

(a) (b)

Fig. 8—Comparison of failure pattern for: (a) reference concrete; and (b) SFRC after compression tests.

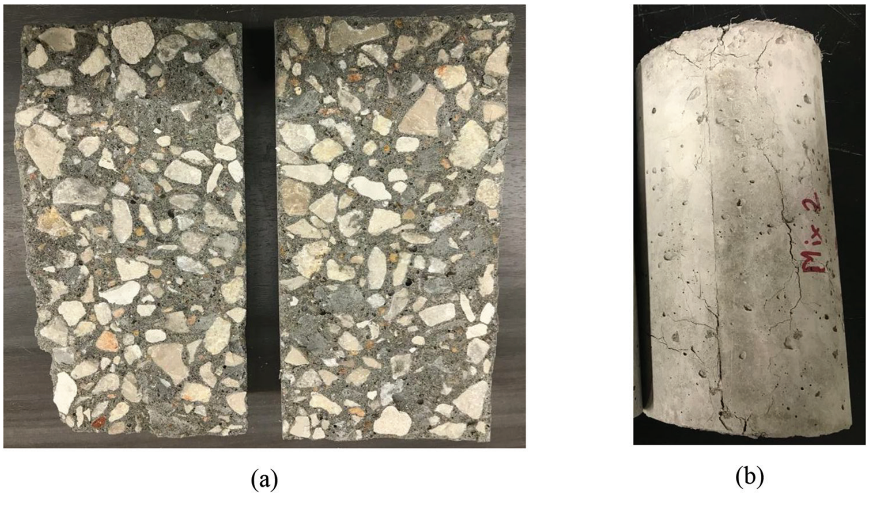

(a) (b)

Fig. 9—Comparison of failure pattern for: (a) reference concrete; and (b) SFRC after splitting tensile tests.

20 to 70%). The concrete containing only hooked-end MSF shows higher splitting tensile strength compared to other SFRC mixtures (refer to Fig. 12(a)). This can be attributed to the geometry of the fiber, specifically the hooked-end. The larger-size hooked-end fiber enhances mechanical interlocking within the concrete matrix, resulting in increased resistance to crack opening and thus higher strength. The concrete mixtures with hybrid steel fibers—that is, M(H)(S) and RM(H)—demonstrate comparable splitting tensile strengths to those comprising only hooked-end and straight MSF. The similar strength performance of hybrid steel fiber concrete mixtures might be due to the multiscale fiber reinforcement provided by the hybrid combination of fibers with varying lengths. The combination of longer and shorter-length fibers can effectively control different scales of cracking (that is, micro- to macrocracks) under tensile or flexural loading, as illustrated in Fig. 13. This observation aligns with findings reported in the previous research studies on hybrid combinations of metallic fibers (hooked-end MSF) and synthetic fibers (polyester), as well as a hybrid

combination of different synthetic fibers such as polyvinyl alcohol (PVA) and PP.[17,19]

Notably, the concrete mixture containing solely RSF exhibits a slightly lower splitting tensile strength compared to other SFRC mixtures, with observed strength reductions of approximately 20 to 25%. This decrease may be attributed to the presence of various impurities in the RSF such as thick steel wires, residual rubber, and tire textiles, as depicted in Fig. 3. These impurities, particularly the steel wires that are longer (in comparison to the specimen size), act as a point of stress concentration, thereby forcing failure to initiate at the perimeter of the steel wire under lower loads. However, they may have a positive effect on full-scale structures with larger cross-sectional areas such as pavements. Despite that, the splitting tensile strength of RSF-reinforced concrete is still approximately 20 to 25% higher than that of the reference concrete. Interestingly, the splitting tensile strength values reveal that blending RSF with hooked-end MSF can compensate for the lower tensile strength observed in concrete mixtures containing RSF alone. An increase of approximately 25% was observed because of this blending. The hybrid combination of straight and hooked-end MSF does not appear to offer additional benefits from the multiscale fiber reinforcement effect.

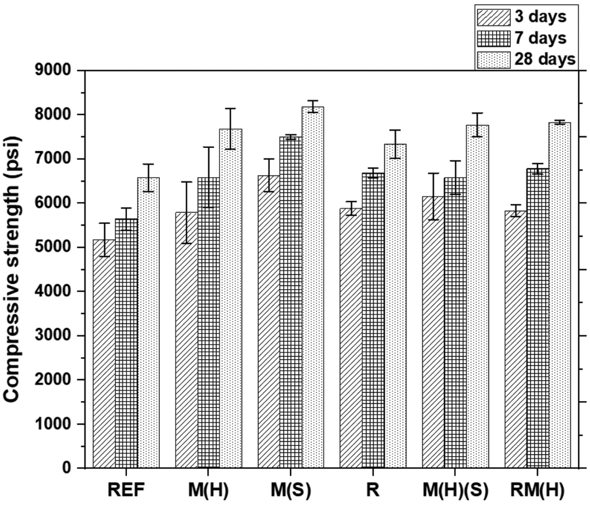

Fig. 10—Comparison of compressive strength for different concrete mixtures at curing ages of 3, 7, and 28 days.

Figure 14 illustrates the flexural strength of both reference and SFRC mixtures at different curing ages. The results indicate that the addition of steel fibers into plain concrete results in a notable enhancement of flexural strength, approximately 30%. A comparable increasing trend was noted for compressive and splitting tensile strengths. Among all SFRC mixtures, the mixture with a hybrid combination of hooked-end and straight MSF shows superior flexural strength compared to others (refer to Fig. 14). This suggests that combining larger and smaller-size fibers might provide a multiscale fiber reinforcement effect. The flexural strength of concrete mixtures containing only RSF is marginally lower compared to those containing solely straight or hooked-end MSF. However, the decrease in flexural strength of the RSF

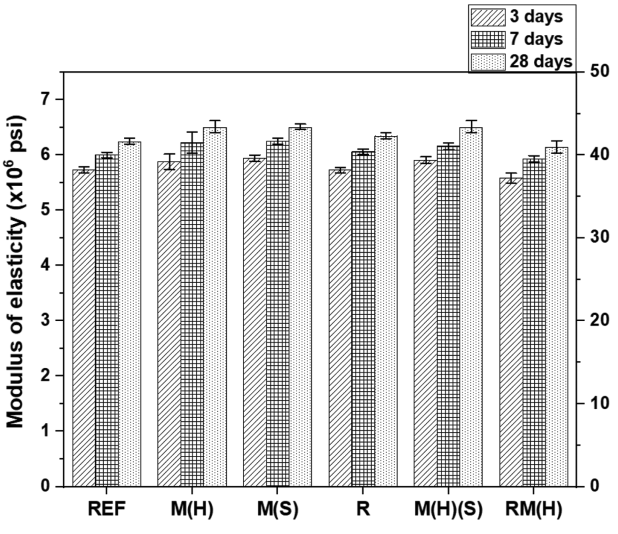

Fig. 11—Comparison of dynamic MOE for different concrete mixtures at curing ages of 3, 7, and 28 days.

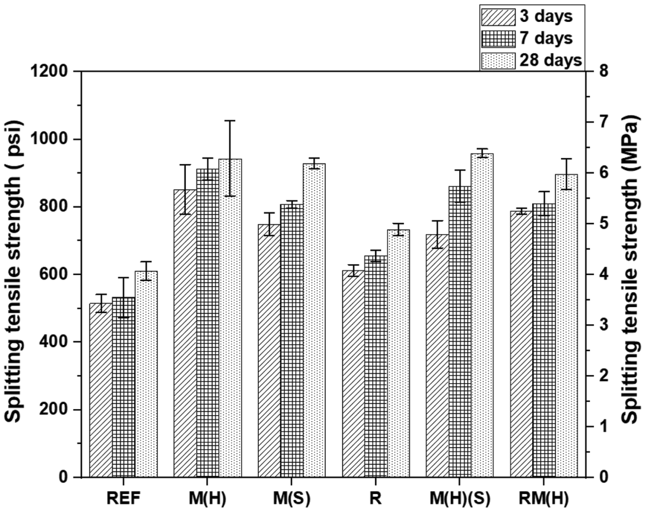

Fig. 12—Variation of splitting tensile strength for different concrete mixtures at curing ages of 3, 7, and 28 days.

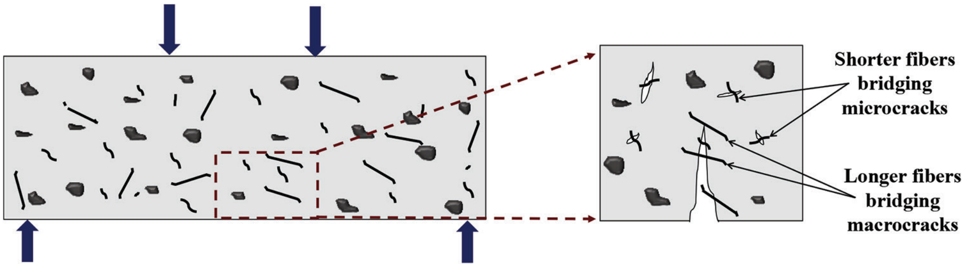

Fig. 13—Schematic showing mechanism of crack bridging in SFRC with hybrid combination of hooked-end MSF and RSF.

reinforced concrete is more pronounced (approximately 15 to 20%) when compared to mixtures with a hybrid combination of fibers. Furthermore, concrete with a hybrid combination of RSF and hooked-end MSF demonstrates flexural strength comparable to that of concretes containing only hooked-end or straight MSF. Thus, the lower tensile capacity of concrete mixtures containing RSF alone can be alleviated by blending them with hooked-end MSF, as evident from Fig. 14. This observation is consistent with the measurements of splitting tensile strengths. Additionally, it is worth emphasizing that all the designed concrete mixtures meet the minimum criteria for average compressive and flexural strength at both 7 and 28 days, as specified for concrete pavement applications.[36] The results of the mechanical properties of concrete containing only RSF and a hybrid combination of RSF and hooked-end MSF are consistent with the values reported in the literature.[4,10,15]

Ductility and toughness measurements

For the design of concrete pavement overlay with macrofibers, effective flexural strength (f_{eff}), which is the sum of residual flexural strength (f_{150}^{D}) and standard flexural strength (f_1), is often used. The standard flexural strength (f_1) corresponds to flexural strength at the first-peak load. On the other hand, toughness (T_{150}^{D}) is the area under the load-deflection curve from 0 to 1/150 of the span that signifies the amount of energy absorbed by the concrete. Additionally, another commonly used parameter for FRC slab design, the equivalent flexural strength ratio ($R_{T,150}^{D}$), is the ratio of the toughness-based equivalent residual flexural strength (from the area under the load-deflection curve up to $L/150$) to the first-peak flexural strength. These values directly signify the post-cracking moment capacity of an FRC slab. Table 7 summarizes the ductility and toughness parameters obtained from the ASTM C1609 tests.

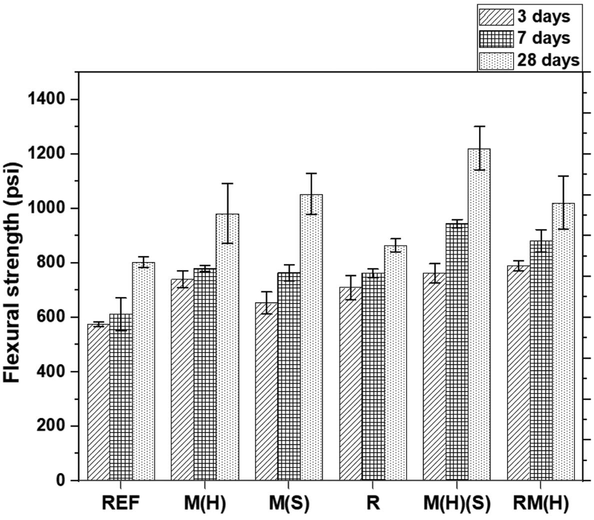

Fig. 14—Comparison of flexural strength for different concrete mixtures at curing ages of 3, 7, and 28 days.

The concrete mixtures with hooked-end MSF and hybrid combinations of fibers—that is, both M(H)(S) and RM(H)—show higher residual flexural strength than other concrete mixtures. The residual strength values obtained for hooked-end MSF are in good agreement with the results reported in the literature.[25] The excellent performance of hybrid steel fiber concrete mixtures can be attributed to the inclusion of longer hooked-end MSF and shorter RSF or straight MSF. The combined use of these fibers may reinforce concrete to effectively control different scales of cracking (refer to Fig. 13) and provide multiscale fiber reinforcement, thereby offering higher resistance to crack opening and propagation. The increase in residual strength resulting from this blending is notably higher (approximately 180%) for the hybrid combination of RSF and hooked-end MSF compared to concrete solely containing RSF. Like other mechanical properties, concrete mixtures with only RSF have slightly lower residual strength compared to other SFRC mixtures (refer to Table 7). Despite that, RSF-reinforced concrete satisfies the 100 to 150 psi (0.69 to 1.03 MPa) residual strength requirements for FRC overlays.[25] Moreover, it meets the requirements specified in Eq. (2) and (3), meaning that RSF can replace (partly or completely) conventional reinforcement in precast applications at the ultimate limit state.[49] From Table 7, blending RSF with hooked-end MSF significantly improves residual strength compared to concrete with RSF only. This significantly reduces limitations associated with the use of RSF as fiber reinforcement in various structural applications.

$$\frac{f_{600}^{D}}{f_1} > 0.4 \tag{2}$$

$$\frac{f_{150}^{D}}{f_{600}^{D}} > 0.5 \tag{3}$$

Similarly, from the toughness (T_{150}^{D}) values, it is inferred that concrete mixtures with a hybrid combination of steel

Table 7—Various ductility and toughness parameters obtained from ASTM C1609 test

Specimen name	f_1, MPa	f_{600}^{D}, MPa	f_{150}^{D}, MPa	T_{150}^{D}, J	$R_{T,150}^{D}$, %
REF	4.44 (2%)	NA	NA	NA	NA
M(H)	5.67 (2%)	5.58 (1%)	4.04 (1%)	33.33 (1%)	76.8 (3%)
M(S)	6.64 (7%)	5.10 (4%)	2.80 (4%)	28.25 (6%)	46.4 (5%)
R	5.48 (5%)	2.97 (4%)	1.43 (5%)	16.34 (1%)	26.1 (10%)
M(H)(S)	6.79 (5%)	6.19 (1%)	3.95 (3%)	36.24 (4%)	67.1 (1%)
RM(H)	5.75 (10%)	5.55 (11%)	3.98 (10%)	31.32 (3%)	67.5 (4%)

Note: Values in parentheses are coefficient of variation (CoV); f_1 is peak flexural strength; f_{600}^{D} is residual strength at net deflection of $L/600$; f_{150}^{D} is residual strength at net deflection of $L/150$; T_{150}^{D} is area under load-versus-net deflection curve from 0 to $L/150$; $R_{T,150}^{D}$ is equivalent flexural strength ratio at net deflection of $L/150$.

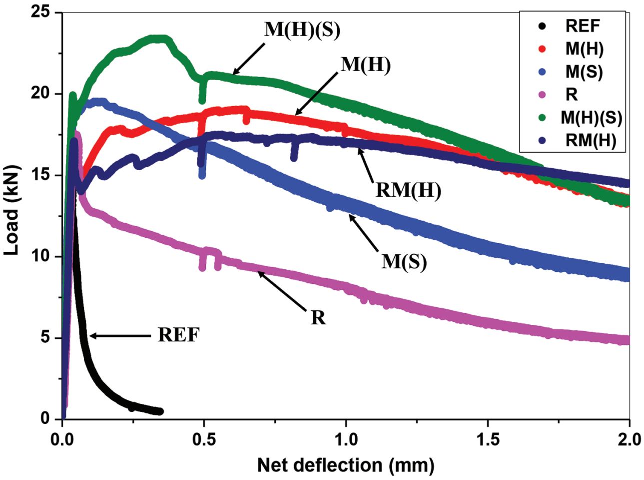

Fig. 15—Typical load-deflection response for reference concrete and SFRC mixtures obtained from ASTM C1609 experiments.

fibers possess higher toughness values among all concrete mixtures. This indicates that concrete with a hybrid combination of fiber can absorb more energy than other concrete mixtures before experiencing complete failure. The equivalent flexural strength ratio ($R_{T,150}^{D}$) demonstrates a similar trend to that of the toughness values. The equivalent flexural strength ratio values for straight and hooked-end MSF are in close agreement with the findings reported in the literature.[25] It is important to highlight that all the designed SFRC mixtures meet a minimum $R_{T,150}^{D}$ of 20% required for FRC overlay applications.[25] The load-versus-deflection response of all concrete mixtures is depicted in Fig. 15. The hybrid steel fiber concrete mixtures show superior performance, followed by those containing hooked-end MSF, as evident from the load-deflection response.

Based on the findings of mechanical tests, it can be inferred that hybrid steel fiber concrete mixtures demonstrate similar or better mechanical performance to concrete using solely hooked or straight MSF. Blending a shorter RSF or straight MSF with a larger hooked-end MSF can reinforce the concrete, effectively controlling various levels of crack widths by providing multiscale fiber reinforcement. However, a hybrid combination of straight and hooked-end MSF is neither cost-effective nor sustainable. Hence, concrete incorporating a hybrid mixture of RSF and hooked-end MSF presents a potentially more environmentally friendly and economic alternative.

Design thickness of overlay

Figure 16 presents the design overlay thicknesses for reference and SFRC cases. It is observed that the addition of steel fiber led to a significant reduction in concrete overlay thickness. The concretes containing hooked-end MSF, straight MSF, and a hybrid combination of fibers reduced overlay thickness from 6 to 3 in. (150 to 75 mm). It should be noted that the overlay thickness calculated using BCOA thickness designer based on the input parameters was less than 3 in. (75 mm). However, the minimum recommended design thickness of 3 in. (75 mm) obtained from the BCOA thickness designer was considered for further analysis. The results of concrete overlay thickness indicate that the design thickness can be potentially reduced by approximately 50% by the addition of steel fibers of 1.5% volume fraction. The overlay thickness yielded for both hybrid fiber systems is very similar as compared to the overlay thickness for concretes with only hooked-end and straight MSF. On the other hand, the addition of RSF into concrete ended up in a 30% reduction of overlay thickness compared to the reference case. A similar range of percentage reduction was obtained for the design thickness of pavement using a 1.25% volume fraction of RSF.[50] The percentage reduction in the thickness of overlay obtained for RSF is even higher in comparison with the percentage thickness reduction reported for concrete containing modified synthetic PP fibers.[51] Furthermore, blending RSF with hooked-end MSF reduces the design thickness of the overlay by 50%. This underscores the significance of replacing carbon and energy-intensive, costly hooked-end MSF with RSF without compromising the mechanical performance.

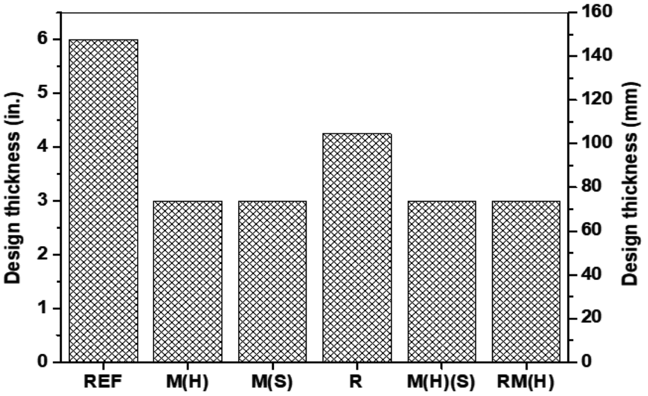

Fig. 16—Design thickness of overlay for reference and SFRC mixtures.

It is worth highlighting that the overlay design approach[30] adopted in this research work based on effective flexural strength can be more suitable for concrete mixtures reinforced with a low volume of macrofibers (producing equivalent flexural strength ratio values between 20 and 50%). In addition to that, the overlay design procedure is sensitive to several factors including properties of the underlying asphalt, the residual strength ratio of the SFRC, joint spacing, and pre-overlay surface preparation. Consequently, the design thickness may vary depending on these factors.

As mentioned earlier, the ACPA software used in this study has certain limitations regarding the input values of flexural strength and MOE for concrete mixtures. This limits its applicability for a wider range of concrete materials with higher flexural strength and MOE. Given these limitations, the design thickness values of the overlay qualitatively provide insight into the effect of incorporating macrofibers into plain concrete mixtures as well as the benefit offered by a hybrid combination of steel fibers. These findings suggest that employing a hybrid combination of RSF with hooked-end MSF is viable for significantly reducing the design thickness of the bonded overlay.

To assess the long-term performance of concretes with a hybrid combination of RSF and hooked-end MSF, it is imperative to conduct durability tests—namely, corrosion resistance, abrasion resistance, freezing-and-thawing resistance, and drying shrinkage. Furthermore, to quantify the economic, social, and environmental benefits of using hybrid fibers in concrete overlays, life-cycle assessment and life-cycle cost analysis are necessary.

CONCLUSIONS

This study investigated the mechanical performance of a hybrid combination of recycled steel fibers (RSF) and manufactured steel fibers (MSF) in concrete designed for pavement overlay applications. Various concrete mixtures incorporating different combinations of RSF and MSF were examined for fresh and mechanical properties. By using flexural strength and residual flexural strength values obtained in this study, the thickness of the bonded steel fiber-reinforced concrete (SFRC) overlay over an existing asphalt pavement was determined. Based on comprehensive experimental and simulation investigation, the following conclusions can be drawn:

1. The use of a hybrid combination of steel fibers, comprising hooked-end MSF and RSF, improves concrete compressive strength by 15 to 20%. However, there is no significant enhancement in the modulus of elasticity (MOE) of the concrete.
2. Concrete mixtures with a hybrid combination of steel fibers demonstrate comparable or higher splitting tensile and flexural strength when compared to those using: (a) only hooked-end; and (b) only straight MSF.
3. The hybrid combination of steel fibers enhances concrete post-cracking behavior in terms of ductility and toughness.
4. RSF-reinforced concrete exhibits lower flexural strength and residual flexural strength; however, blending RSF with hooked-end MSF achieves similar mechanical performance compared to using hooked-end MSF alone. This in turn can notably reduce environmental and economic impacts.
5. The incorporation of hooked-end/straight MSF or a combination of hybrid steel fibers leads to a reduction in the design thickness of the concrete overlay laid over asphalt pavement by approximately 50%.

In summary, the hybrid combination of RSF with hooked-end MSF emerges as a promising solution to pavement overlay applications. It is important to note that this study was only restricted to the mechanical properties of hybrid recycled and manufactured SFRCs. Detailed examination of durability performance remains an area for future investigation.

AUTHOR BIOS

ACI member **Pratik Gujar** *is a Postdoctoral Research Associate and Lecturer in civil engineering at the Ingram School of Engineering, Texas State University, San Marcos, TX. He received his PhD from Indian Institute of Technology Madras, Chennai, Tamil Nadu, India, in 2022. He is a member of ACI Committee 548, Polymers and Adhesives for Concrete. His research interests include developing sustainable construction materials and smart surface coatings for infrastructure applications.*

ACI member **Beng Wei Chong** *is a PhD Student at the Ingram School of Engineering, Texas State University. He received his MS in civil engineering from Universiti Malaysia Pahang, Pekang District, Malaysia, in 2022. His research interests include cement chemistry, sustainable cementitious materials, and alternative cement.*

Precious Aduwenye *is a PhD Student at the Ingram School of Engineering, Texas State University, where he received his MS in civil engineering. His research interests include the development of ultra-high-performance concrete (UHPC) using recycled steel fibers.*

ACI member **Xijun Shi** *is an Assistant Professor of civil engineering at the Ingram School of Engineering, Texas State University. He received his MS and PhD in civil engineering from Texas A&M University, College Station, TX, in 2014 and 2018, respectively. He is a member of ACI Committees 221, Aggregates; 555, Concrete with Recycled Materials; and 565, Lunar Concrete. His research interests include multifunctional construction materials for smart infrastructure, sustainable and high-performance fiber-reinforced construction materials, cement-based materials containing recycled aggregates, and concrete durability.*

Zachary C. Grasley, *FACI, is a Chair Professor and Department Head of the Zachry Department of Civil and Environmental Engineering at Texas A&M University. He received his MS and PhD in civil engineering from University of Illinois Urbana-Champaign, Champaign, IL, in 2003 and 2006, respectively. He received the ACI Young Member Award for Professional Achievement. His research interests include concrete materials, pavement engineering, engineering mechanics, and innovation and commercialization.*

ACKNOWLEDGMENTS

The research presented in this paper is supported by the ACI Foundation (Project No. ACIFP0061). M. Adams, L. Ferrara, and C. Fenger serve on the technical panel, and T. Ladely serves as the project manager. The authors appreciate Circle Concrete Tech for supplying the recycled steel fibers used in this project. The Forensic Anthropology Center at Texas State University is acknowledged for providing access to the X-ray CT facility.

DECLARATION OF INTEREST STATEMENT

Authors Shi and Grasley are co-founders and equity holders of Circle Concrete Tech, a company involved in the commercialization of recycled steel-fiber products. The research presented in this paper was conducted independently at Texas State University and Texas A&M University and was supported by the ACI Foundation under Project No. ACIFP0061.

REFERENCES

1. USTMA, “2021 US Scrap Tire Management Summary,” U.S. Tire Manufacturers Association, Washington, DC, 2022, https://www.ustires.org/resources/2021-scrap-tire-management-report. (last accessed Aug. 26, 2025)

2. AS-213, “Scrap Tire Annual Report Summary,” Texas Commission on Environmental Quality, Austin, TX, 2021, https://www.tceq.texas.gov/downloads/permitting/waste-permits/publications/213-20.pdf. (last accessed Aug. 26, 2025)

3. Centonze, G.; Leone, M.; and Aiello, M. A., “Steel Fibers from Waste Tires as Reinforcement in Concrete: A Mechanical Characterization,” *Construction and Building Materials*, V. 36, 2012, pp. 46-57.

4. Sengul, O., “Mechanical Behavior of Concretes Containing Waste Steel Fibers Recovered from Scrap Tires,” *Construction and Building Materials*, V. 122, 2016, pp. 649-658.

5. Domski, J.; Katzer, J.; Zakrzewski, M.; and Ponikiewski, T., “Comparison of the Mechanical Characteristics of Engineered and Waste Steel Fiber Used as Reinforcement for Concrete,” *Journal of Cleaner Production*, V. 158, 2017, pp. 18-28.

6. Hu, H.; Papastergiou, P.; Angelakopoulos, H.; Guadagnini, M.; and Pilakoutas, K., “Mechanical Properties of SFRC Using Blended Recycled Tyre Steel Cords (RTSC) and Recycled Tyre Steel Fibres (RTSF),” *Construction and Building Materials*, V. 187, 2018, pp. 553-564.

7. Andrew, R. M., “Global CO_2 Emissions from Cement Production,” *Earth System Science Data*, V. 10, No. 1, 2018, pp. 195-217.

8. Bjegovic, D.; Baricevic, A.; Lakusic, S.; Damjanovic, D.; and Duvnjak, I., “Positive Interaction of Industrial and Recycled Steel Fibres in Fibre Reinforced Concrete,” *Journal of Civil Engineering and Management*, V. 19, No. 1, 2013, pp. 50-60.

9. Awolusi, T. F.; Oke, O. L.; Atoyebi, O. D.; Akinkurolere, O. O.; and Sojobi, A. O., “Waste Tires Steel Fiber in Concrete: A Review,” *Innovative Infrastructure Solutions*, V. 6, No. 34, 2021, pp. 1-12.

10. Su, P.; Li, M.; Dai, Q.; and Wang, J., “Mechanical and Durability Performance of Concrete With Recycled Tire Steel Fibers,” *Construction and Building Materials*, V. 394, 2023, p. 132287.

11. Wang, Z.; Hu, H.; Papastergiou, P.; Angelakopoulos, H.; Guadagnini, M.; and Pilakoutas, K., "Effect of Fibre Length on the Mechanical Properties of SFRC Using Recycled Steel Fibres," *Construction and Building Materials*, V. 415, 2024, p. 134890.

12. Zia, A.; Zhang, P.; and Holly, I., "Experimental Investigation of Raw Steel Fibers Derived from Waste Tires for Sustainable Concrete," *Construction and Building Materials*, V. 368, 2023, p. 130410.

13. Martinelli, E.; Caggiano, A.; and Xargay, H., "An Experimental Study on the Post-Cracking Behaviour of Hybrid Industrial/Recycled Steel Fibre-Reinforced Concrete," *Construction and Building Materials*, V. 94, 2015, pp. 290-298.

14. Aiello, M. A.; Leuzzi, F.; Centonze, G.; and Maffezzoli, A., "Use of Steel Fibres Recovered from Waste Tyres as Reinforcement in Concrete: Pull-Out Behaviour, Compressive and Flexural Strength," *Waste Management*, V. 29, No. 6, 2009, pp. 1960-1970.

15. Caggiano, A.; Folino, P.; Lima, C.; Martinelli, E.; and Pepe, M., "On the Mechanical Response of Hybrid Fiber Reinforced Concrete with Recycled and Industrial Steel Fibers," *Construction and Building Materials*, V. 147, 2017, pp. 286-295.

16. Banthia, N., and Nandakumar, N., "Crack Growth Resistance of Hybrid Fiber Reinforced Cement Composites," *Cement and Concrete Composites*, V. 25, No. 1, 2003, pp. 3-9.

17. Sivakumar, A., and Santhanam, M., "Mechanical Properties of High Strength Concrete Reinforced with Metallic and Non-Metallic Fibres," *Cement and Concrete Composites*, V. 29, No. 8, 2007, pp. 603-608.

18. Brandt, A. M., "Fibre Reinforced Cement-Based (FRC) Composites After Over 40 Years of Development in Building and Civil Engineering," *Composite Structures*, V. 86, No. 1, 2008, pp. 3-9.

19. Pereira, E. B.; Fischer, G.; and Barros, J., "Effect of Hybrid Fiber Reinforcement on the Cracking Process in Fiber Reinforced Cementitious Composites," *Cement and Concrete Composites*, V. 34, No. 10, 2012, pp. 1114-1123.

20. Dawood, E. T., and Ramli, M., "High Strength Characteristics of Cement Mortar Reinforced with Hybrid Fibres," *Construction and Building Materials*, V. 25, No. 5, 2011, pp. 2240-2247.

21. Vantadori, S.; Carpinteri, A.; Guo, L. P.; Ronchei, C.; and Zanichelli, A., "Synergy Assessment of Hybrid Reinforcements in Concrete," *Composites Part B: Engineering*, V. 147, 2018, pp. 197-206.

22. Bhosale, A.; Rasheed, M. A.; Prakash, S. S.; and Raju, G., "A Study on the Efficiency of Steel vs. Synthetic vs. Hybrid Fibers on Fracture Behavior of Concrete in Flexure Using Acoustic Emission," *Construction and Building Materials*, V. 199, 2019, pp. 256-268.

23. Zhong, H., and Zhang, M., "Experimental Study on Engineering Properties of Concrete Reinforced with Hybrid Recycled Tyre Steel and Polypropylene Fibres," *Journal of Cleaner Production*, V. 259, 2020, p. 120914.

24. Karim, R., and Shafei, B., "Investigation of Five Synthetic Fibers as Potential Replacements of Steel Fibers in Ultrahigh-Performance Concrete," *Journal of Materials in Civil Engineering*, ASCE, V. 34, No. 7, 2022, p. 04022126.

25. Roesler, J.; Bordelon, A.; Brand, A. S.; and Amirkhanian, A., "Fiber-Reinforced Concrete for Pavement Overlays: Technical Overview," InTrans Project 15-532, National Concrete Pavement Technology Center, Iowa State University, Ames, IA, 2019.

26. Fick, G.; Gross, J.; Snyder, M. B.; Harrington, D.; Roesler, J.; and Cackler, T., *Guide to Concrete Overlays*, fourth edition, National Concrete Pavement Technology Center, Iowa State University, Ames, IA, 2021.

27. Ana Baricevic, M. G.; Paar, R.; Papastergiou, P.; Pilakoutas, K.; and Guadagnini, M., "Long-Term Monitoring of a Hybrid SFRC Slab on Grade Using Recycled Tyre Steel Fibres," *Advances in Concrete Construction*, V. 10, No. 6, 2020, pp. 547-557.

28. Graeff, A. G., "Long-Term Performance of Recycled Steel Fibre Reinforced Concrete for Pavement Applications," PhD thesis, The University of Sheffield, Sheffield, UK, 2011.

29. ASTM C1609/C1609M-19, "Standard Test Method for Flexural Performance of Fiber-Reinforced Concrete (Using Beam with Third-Point Loading)," ASTM International, West Conshohocken, PA, 2019.

30. Altoubat, S. A.; Roesler, J. R.; Lange, D. A.; and Rieder, K. A., "Simplified Method for Concrete Pavement Design with Discrete Structural Fibers," *Construction and Building Materials*, V. 22, No. 3, 2008, pp. 384-393.

31. Bordelon, A., and Roesler, J., "Design with Fiber Reinforcement for Thin Concrete Overlays Bonded to Asphalt," *Journal of Transportation Engineering*, V. 138, No. 4, 2012, pp. 430-435.

32. ASTM C127-15, "Standard Test Method for Relative Density (Specific Gravity) and Absorption of Coarse Aggregate," ASTM International, West Conshohocken, PA, 2015.

33. Shi, X.; Brescia-Norambuena, L.; Grasley, Z.; and Hogancamp, J., "Fracture Properties and Restrained Shrinkage Cracking Resistance of Cement Mortar Reinforced by Recycled Steel Fiber from Scrap Tires," *Transportation Research Record: Journal of the Transportation Research Board*, V. 2674, No. 8, 2020, pp. 581-590.

34. Shi, X.; Brescia-Norambuena, L.; Tavares, C.; and Grasley, Z., "Semicircular Bending Fracture Test to Evaluate Fracture Properties and Ductility of Cement Mortar Reinforced by Scrap Tire Recycled Steel Fiber," *Engineering Fracture Mechanics*, V. 236, 2020, p. 107228.

35. Shi, X.; Park, P.; Rew, Y.; Huang, K.; and Sim, C., "Constitutive Behaviors of Steel Fiber Reinforced Concrete under Uniaxial Compression and Tension," *Construction and Building Materials*, V. 233, 2020, p. 117316.

36. TxDOT, "Standard Specifications for Construction and Maintenance of Highways, Streets, and Bridges," Texas Department of Transportation, Austin, TX, 2014.

37. Khute, S.; Singh, S.; Zerbino, R.; and Gettu, R., "Fresh-State Behavior of Paving Concrete Reinforced with Discarded Coconut Coir Fibres," *Indian Concrete Journal*, V. 96, No. 12, 2022, pp. 5-13.

38. ASTM C143/C143M-15, "Standard Test Method for Slump of Hydraulic-Cement Concrete," ASTM International, West Conshohocken, PA, 2015.

39. ASTM C138/C138M-17, "Standard Test Method for Density (Unit Weight), Yield, and Air Content (Gravimetric) of Concrete," ASTM International, West Conshohocken, PA, 2017.

40. Rowan, A.; Ghebreyesus, F. G.; Zamen, S.; Willis, L. J.; Halliday, H. S.; and Dehghan-Niri, E., "X-Ray Computed Tomography Analysis of Magnetically Oriented Short Steel Fibers and their Effect on Uniaxial Tensile Strength of Cement Mortar," *Journal of Materials in Civil Engineering*, ASCE, V. 34, No. 2, 2022, p. 04021455.

41. Huang, H.; Su, A.; Gao, X.; and Yang, Y., "Influence of Formwork Wall Effect on Fiber Orientation of UHPC with Two Casting Methods," *Construction and Building Materials*, V. 215, 2019, pp. 310-320.

42. ASTM C39/C39M-21, "Standard Test Method for Compressive Strength of Cylindrical Concrete Specimens," ASTM International, West Conshohocken, PA, 2021.

43. ASTM C215-19, "Standard Test Method for Fundamental Transverse, Longitudinal, and Torsional Resonant Frequencies of Concrete Specimen," ASTM International, West Conshohocken, PA, 2019.

44. ASTM C496/C496M-17, "Standard Test Method for Splitting Tensile Strength of Cylindrical Concrete Specimens," ASTM International, West Conshohocken, PA, 2017.

45. ASTM C78/C78M-22, "Standard Test Method for Flexural Strength of Concrete (Using Simple Beam with Third-Point Loading)," ASTM International, West Conshohocken, PA, 2022.

46. ACPA, "Bonded Concrete Overlay on Asphalt (BCOA) Thickness Designer," American Concrete Pavement Association, Rosemont, IL, http://apps.acpa.org/applibrary/BCOA/. (last accessed Aug. 26, 2025)

47. Sassani, A.; Ceylan, H.; Kim, S.; Arabzadeh, A.; Taylor, P.C.; and Gopalakrishnan, K., "Development of Carbon Fiber-Modified Electrically Conductive Concrete for Implementation in Des Moines International Airport," *Case Studies in Construction Materials*, V. 8, 2018, pp. 277-291.

48. Kaźmierowski, M.; Jaskulski, R.; Drzazga, M.; Nalepka, M.; and Kordasz, M., "Effects of the Addition of Short Straight Steel Fibers on the Strength and Strains of High-Strength Concrete During Compression," *Scientific Reports*, V. 14, No. 1, 2024, pp. 1-13.

49. ACI Committee 544, "Design and Construction of Fiber-Reinforced Precast Concrete Tunnel Segments (ACI 544.7R-16)," American Concrete Institute, Farmington Hills, MI, 2016, 36 pp.

50. Zia, A.; Zhang, P.; Holly, I.; and Prokop, J., "Sustainability Enhancement through High-Dose Recycled Tire Steel Fibers in Concrete: Experimental Insights and Practical Applications," *Sustainability*, V. 15, No. 22, 2023, p. 15760.

51. Hasani, M.; Nejad, F. M.; Sobhani, J.; and Chini, M., "Mechanical and Durability Properties of Fiber Reinforced Concrete Overlay: Experimental Results and Numerical Simulation," *Construction and Building Materials*, V. 268, 2021, p. 121083.

NOTES:

ACI MATERIALS JOURNAL TECHNICAL PAPER

Title No. 122-M34

Hardened and Durability Properties of Concrete Made with Washed Waste Fines

by T. U. Mohammed, M. Z. B. Harun, C. Z. B. Zahid, and R. U. Islam

This research investigates the impact of using washed waste fines (WWF), a by-product from ready mixed concrete (RMC) plants, as a partial replacement for natural sand in concrete. Cylindrical (100 x 200 mm) and cubic (50 x 50 x 50 mm) mortar specimens were created with 20% WWF substitution. Hardened properties, such as compressive strength, tensile strength, and ultrasonic pulse velocity (UPV), and durability parameters, such as chloride migration coefficient and carbonation coefficient, were evaluated. The study also examined the microstructure of concrete using a scanning electron microscope (SEM). Results showed that incorporating WWF enhanced both the hardened and durability properties of concrete, increasing compressive strength by 25% compared to the control case. Additionally, WWF decreased the non-steady-state chloride migration and carbonation coefficients, indicating improved durability. SEM analysis revealed a denser microstructure, and WWF incorporation reduced the permeable porosity and absorption capacity of concrete.

Keywords: carbonation; rapid chloride migration test; ready mixed concrete (RMC); returned concrete; washed waste fine (WWF).

INTRODUCTION

Given the current global emphasis on sustainable construction, there has been significant international interest in the recycling and reusing of hardened concrete generated from construction and demolition (C&D) waste.[1,2] Numerous principles and techniques have been established to facilitate the recycling of hardened concrete through cutting-edge research. While significant interest has been shown in the recycling of hardened concrete waste, comparatively little attention has been given to the potential recycling or reusing of waste generated while manufacturing fresh concrete in ready mixed concrete (RMC) plants.

One form of fresh concrete waste commonly generated in RMC plants is referred to as returned concrete. Based on existing calculations, it has been observed that a truck with a volume of 9 m^3 typically transports approximately 300 kg of returned concrete daily.[3] Based on estimations, the proportion of returned concrete amounts to approximately 0.2 to 0.4% of the total daily output. However, in periods of high demand, this range has the potential to expand considerably, reaching approximately 5 to 9%.[4] From a global standpoint, annually, approximately 125 million tonnes of unhardened returned concrete is disposed of as waste at RMC plants.[4] These wastes are in fresh, unhardened to early hardened states within a few hours of production. In most cases, these waste components are often transported, either before or during solidification, to temporary disposal sites in RMC plants. Subsequently, they are disposed of in public landfills or dumping grounds as inert materials. Nevertheless, it is worth noting that many nations have a scarcity of land for waste disposal,[5] thereby indicating that the conventional landfill method used for waste management may not be a viable solution. In addition, landfill taxes exist in some countries, such as Japan, where the cost of disposal of returned concrete in urban areas is estimated to range between 3600 and 4500 yen per m^3 of returned concrete.[6] Using recycled concrete for landfill purposes is also not an environmentally responsible practice. In some countries, returned concrete is classified as hazardous material. Some possible reasons behind this action may include the high pH ($\leq$11.5) of the material and the possibility of it containing heavy metals.[7] In the United Kingdom, for instance, if the pH value of waste exceeds 11.5, it is classified as category H8 hazardous waste under Technical Guidance WM2, Hazardous Waste: Interpretation of the definition and classification of hazardous waste.

As a consequence of the drawbacks mentioned previously of the conventional landfill method for managing returned concrete, it is necessary to look for economically viable and environmentally friendly alternatives. According to Xuan et al., "the composition of returned concrete waste normally includes 70% or more recoverable aggregates, and 30% or less potentially unrecoverable paste."[8] By washing, sedimentation, dewatering, and filtering, returned concrete can be separated as aggregates and slurry composed of sand, hydrated cement particles, unhydrated cement particles, and water.[9] Researchers have named slurry in many ways, such as concrete slurry waste (CSW),[8] fresh concrete waste (FCW),[9] and sludge.[7,10] There are records of previous research where CSW has been used to produce clinker. However, its high chemical variation and high alkalinity, SO$_3$, and MgO contents made it inconvenient to do so.[11] In another investigation, CSW was used as a substitute for sand or cement for concrete production, decreasing the compressive strength of concrete.[12] Audo et al.[7] investigated the effect of sludge as a complete alternative to limestone filler for producing mortar. They concluded that "28 days compressive strength is between 30% lower to 17% higher when the dry sludge is used instead of limestone filler." Kou et al.[9] used FCW as a replacement for sand to produce wall partition blocks without a reduction in compressive strength or an increase in drying shrinkage of blocks. Correia et al.[13] also investigated the recycling potential of FCW and gave similar conclusions regarding the compressive strength of concrete. Zervaki et al.[10] replaced cement with dry sludge

---

ACI Materials Journal, V. 122, No. 5, September 2025.
MS No. M-2024-303.R2, doi: 10.14359/51747872, received February 26, 2025, and reviewed under Institute publication policies. Pertinent discussion including author's closure, if any, will be published ten months from this journal's date if the discussion is received within four months of the paper's print publication.

to produce mortar and assessed the hardened properties of mortar. The results indicated that a small replacement of cement (≤2%) can improve the compressive strength of mortar. However, excess replacements can negatively affect compressive strength and workability.[10]

In Bangladesh, in RMC plants, coarse aggregate is separated from the returned concrete in a washing plant. After washing, the water with sand, fine aggregate, hydrated cement, and unhydrated cement is stored in a sedimentation tank. The deposit of the sedimentation tanks is called washed waste fines (WWF). This study focused on assessing the feasibility of using dried WWF as a partial sand substitute for producing concrete. To achieve the objective, an extensive investigation was conducted on mortar specimens made with different amounts of sand replaced by WWF.[14] It was found that up to 20% replacement of natural sand with WWF increased the compressive strength of mortar. Therefore, a further study was conducted on concrete samples made with natural sand replaced by 20% of WWF with different types of binder, such as ordinary portland cement (OPC) and blended cement. The concrete specimens were tested for compressive strength, ultrasonic pulse velocity (UPV), and splitting tensile strength at different curing ages to evaluate the effect of WWF as a sand replacement on the mechanical properties of concrete. To understand its effect on durability properties, a rapid chloride migration test (RCMT) and accelerated carbonation test were conducted. Furthermore, microstructural investigation of concrete was conducted using a scanning electron microscope (SEM).

RESEARCH SIGNIFICANCE

The research investigates the use of WWF from RMC plants as a partial replacement for natural sand in concrete production. The significance of this research lies in its potential to enhance the sustainability of concrete production by recycling or reusing waste materials, thus reducing landfill use and environmental impact. The study demonstrates that incorporating WWF improves the compressive strength and durability of concrete, decreases permeability and absorption, and results in a denser microstructure. These findings suggest a viable, eco-friendly alternative for managing concrete waste while improving concrete properties.

EXPERIMENTAL INVESTIGATION

Materials

For the production of concrete specimens, granite stone was used as coarse aggregate (CA), and river sand was used as fine aggregate (FA). The gradation of the CA and the river sand were controlled in accordance with ASTM C33/C33M-18.[15]

Mortar specimens were produced using natural sand, the gradation of which was controlled in accordance with ASTM C778-21.[16]

WWF was collected from the different depths of the sedimentation basin of a local RMC facility, as depicted in Fig. 1. Considering the heterogeneity of the material, the sample was collected from the different layers of the sedimentation basin and then mixed to make a representative sample. In this study, the variation in WWF's composition from plant to plant was not considered. In Bangladesh, cement is produced as per BDS EN 197-1: 2003.[17] CEM Type I, CEM Type II/A-M, and CEM Type II/B-M are the most commonly used binders for RMC production across most plants. While some variations in composition of WWF might exist, it is likely not significantly different across plants. However, in future studies, the variation in composition of material from plant to plant will be considered. After collection, WWF was oven-dried at 110 ± 5°C for 24 hours. It was then crushed by using an abrasion machine and sieved through a 4.75 mm sieve to remove larger particulates to meet the sand grading specifications. The surface morphology, microstructure, and phase composition of the WWF particles were evaluated using the SEM and X-ray diffraction (XRD), respectively. The findings from these tests are thoroughly discussed in the "Experimental Results and Discussion" section.

Figure 2 depicts the grading curves of CA, FA, WWF particles, and the natural sand used for mortar production. The grading curve reveals that the WWF adheres to the gradation for FA specified in ASTM C33/C33M.[15] It is also apparent that WWF contributes a substantial amount of

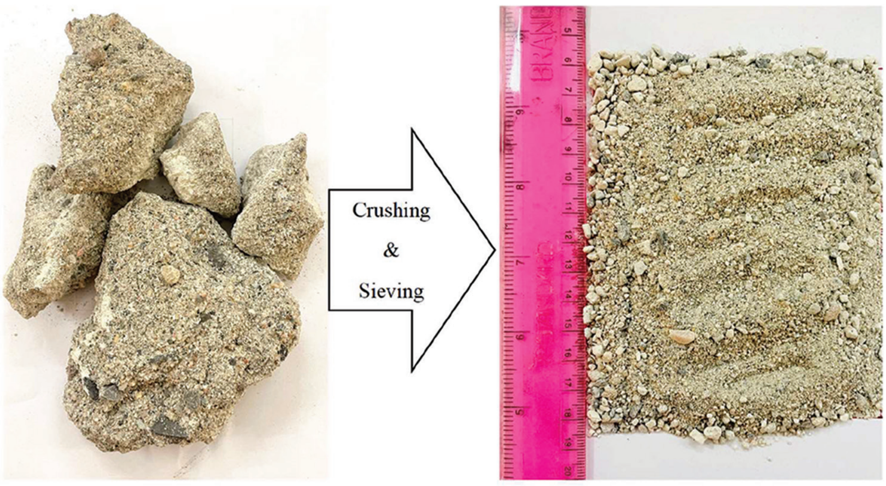

(a) WWF collected from RMC Plant

(b) Crushed WWF

Fig. 1—WWF.

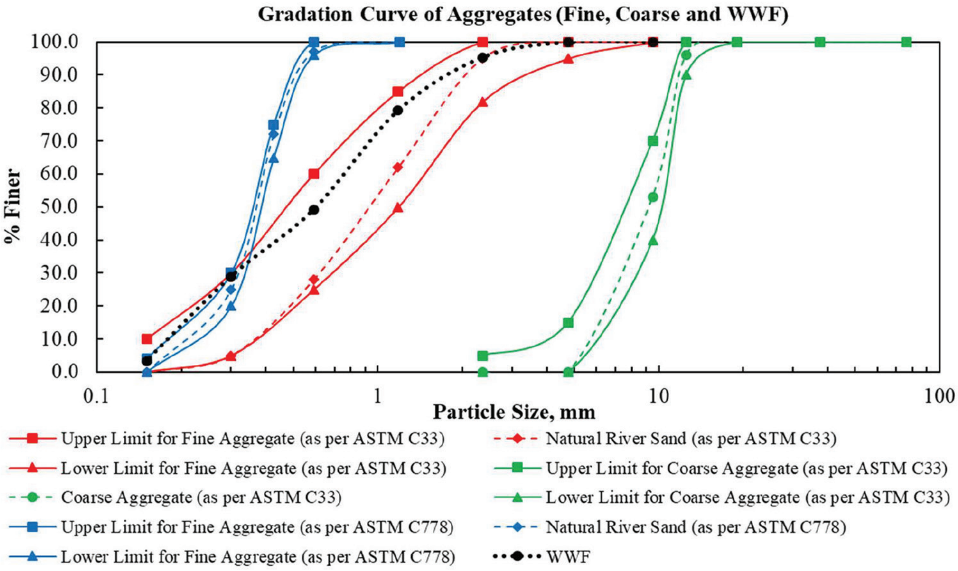

Fig. 2—Grading curve of aggregates.

Table 1—Physical properties of aggregates

	Coarse aggregate	Fine aggregate	WWF	Test method
Bulk SSD specific gravity	2.75	2.56	2.36	ASTM C127-15 (CA)[18] ASTM C128-15 (FA)[19]
Absorption	1.80%	1.98%	3.96%	ASTM C127-15 (CA)[18] ASTM C128-15 (FA)[19]
Unit weight (oven dry), kg/m^3	1544	1509	1489	ASTM C29/C29M-23[20]
Unit weight (SSD), kg/m^3	1572	1539	1432	ASTM C29/C29M-23[20]
Abrasion	22.7%	—	—	ASTM C131-06[21]
Fineness modulus (FM)	Coarse aggregate		6.5	ASTM C136-06[22]
	Fine aggregate used for concrete production		3.1	
	Fine aggregate used for mortar production		1.8	
	WWF		2.44	

finer particles to the mixture. The physical properties of the different aggregate and WWF are summarized in Table 1.

Eight distinct kinds of cement were used in this study. These included CEM Type I (OPC), CEM Type II/A-M,[17] and six different blends of slag and fly ash cement. The binary blends were: 65% OPC + 35% slag, 50% OPC + 50% slag, 35% OPC + 65% slag, 65% OPC + 35% fly ash, 50% OPC + 50% fly ash, and 35% OPC + 65% fly ash. The mineral contents were fixed at 35 to 65% for both slag and fly ash cement to make it a similar composition as per CEM Type III/A and high-volume fly ash cement CEM Type IV.[17] To assess the relative reactivity of slag and fly ash in the presence of WWF, the replacement percentages of these materials were maintained equally for both types of cement. The replacements were done on an absolute volume basis. The CEM Type II/A-M cement was sourced from a local manufacturer and is named PCC (portland composite cement) as per BDS EN 197-1: 2003.[17]

Potable water was used to mix both mortar and concrete.

Mixture and preparation of specimens

Tables 2 and 3 present a summary of the concrete and mortar mixture proportions, respectively. Sixteen concrete and 16 mortar cases were investigated in total. Different WWF contents (0 and 20%) and cement types (CEM Type I [OPC], CEM Type II/A-M, 65% OPC + 35% slag, 50% OPC + 50% slag, 35% OPC + 65% slag, 65% OPC + 35% fly ash, 50% OPC + 50% fly ash, and 35% OPC + 65% fly ash) were used to formulate multiple mixture proportions. The replacement percentage was limited to 20% to examine the influence of WWF on the hardened and durability parameters of concrete. The aggregates used for both the concrete and mortar cases were in saturated surface-dry (SSD) condition, whereas the WWF was in a dry condition. The amount of mixing water was adjusted during the mixing process with due consideration of water absorption by WWF.

Concrete cylinders—According to the mixture proportions summarized in Table 2, a total of 288 cylindrical concrete specimens (100 mm in diameter x 200 mm in height) for 16 independent cases (18 cylinders per case) were produced in accordance with ASTM C192/C192M-15.[23] After placing concrete into cylindrical steel molds, the specimens were

Table 2—Mixture proportions of concrete mixtures

Cement type	CEM Type I (OPC)		CEM Type II/A-M (PCC)		65% OPC + 35% slag		50% OPC + 50% slag		35% OPC + 65% slag		65% OPC + 35% fly ash		50% OPC + 50% fly ash		35% OPC + 65% fly ash	
Cement, kg/m^3	450		360 (80%)		293		225		158		293		225		158	
Slag, kg/m^3	—		90 (20%)		108		154		201		—		—		—	
Fly ash, kg/m^3	—				—		—		—		95		136		176	
Coarse aggregate, kg/m^3	958		939		958		958		958		958		958		958	
Water, kg/m^3	225		225		225		225		225		225		225		225	
WWF content, volume %	0	20	0	20	0	20	0	20	0	20	0	20	0	20	0	20
Sand, kg/m^3	701	561	687	550	701	561	701	561	701	561	701	561	701	561	701	561
WWF, kg/m^3	0	129	0	127	0	129	0	129	0	129	0	129	0	129	0	129

Table 3—Mixture proportions of mortar mixtures

Cement type	CEM Type I (OPC)		CEM Type II/A-M		65% OPC + 35% slag		50% OPC + 50% slag		35% OPC + 65% slag		65% OPC + 35% fly ash		50% OPC + 50% fly ash		35% OPC + 65% fly ash	
Cement, kg/m^3	626		493 (80%)		406		313		219		406		313		219	
Slag, kg/m^3	—		123 (20%)		185		264		343		—		—		—	
Fly ash, kg/m^3	—				—		—		—		136		194		253	
Water, kg/m^3	297		297		297		297		297		297		297		297	
WWF content, volume %	0	20	0	20	0	20	0	20	0	20	0	20	0	20	0	20
Sand, kg/m^3	1251	1001	1229	983	1251	1001	1251	1001	1251	1001	1251	1001	1251	1001	1251	1001
WWF, kg/m^3	0	229	0	225	0	229	0	229	0	229	0	229	0	229	0	229

covered with plastic to prevent water loss by evaporation. After 24 hours from the placement of the concrete, the specimens were demolded and cured underwater in accordance with ASTM C192/C192M[23] until the testing age.

Mortar cubes—A total of 48 mortar cubes (50 x 50 x 50 mm) for 16 distinct cases (three cubes per case) were produced following the mixture proportions summarized in Table 3. The procedure for making mortar cubes adhered to ASTM C109/C109M-20.[24] After placing mortar into the mold, the molds were covered with a polyethylene sheet and demolded after 24 hours. The mortar samples were cured under water until the age of testing. These mortar cubes were used solely for the accelerated carbonation test, and the reason for using them can be attributed to the fact that smaller specimens allow for a more uniform CO_2 exposure, reducing the variability in carbonation depth measurements. Also, they are easy to handle and store in carbonation chambers. In previous studies, cube specimens of the same dimensions have been used for carbonation depth measurement.[25,26]

Test procedures

Compressive strength and UPV—A total of 192 cylindrical concrete specimens were made and tested for compressive strength of concrete as per ASTM C39/C39M-23[27] at the ages of 7, 14, 28, and 90 days (three cylinders per day per case). Additionally, the UPV of the cylinder specimens was measured using a portable ultrasonic nondestructive digital indicating tester (PUNDIT), following the procedures outlined in ASTM C597-22.[28] A total of 48 cylinders were employed to assess the splitting tensile strength at the age of 28 days (three cylinders per case). The experimental protocol adhered to the guidelines outlined in ASTM C496-96.[29]

Rapid chloride migration test (RCMT)—Three concrete discs with diameters of 100 and thickness of 50 ± 2 mm were used in the test as per the standard NT Build 492.[30] The discs were cut from the middle of the cylindrical specimen. Initially, the discs were conditioned by placing them in a vacuum container, sealing it, and subjecting them to a 5 kPa vacuum for 3 hours before being submerged in lime water while maintaining the vacuum for another hour. The discs were kept in the chamber for an additional 18 hours before being exposed to an electrical voltage. The conditioned discs were then placed in rubber sleeves, positioned in the catholyte (10% NaCl solution) reservoir, and filled with anolyte (0.3N NaOH) solution. Electrodes were connected, and the applied voltage was determined based on the initial current at 30 V. After the electrical exposure for the specified time, the specimens were split, sprayed with 0.1N $AgNO_3$ solution, and the chloride penetration depth was measured at 10 mm intervals, excluding the outer 10 mm on both sides. The average depth was used in the following equation to measure the migration coefficient

$$D_{nssm} = \frac{RT}{zFE} \times \frac{x_d - \alpha\sqrt{x_d}}{t} \tag{1}$$

$$E = \frac{U-2}{L} \tag{2}$$

$$\alpha = 2\sqrt{\frac{RT}{zFE}}\mathrm{erf}^{-1}\left(1-\frac{2c_d}{c_0}\right) \tag{3}$$

where D_{nssm} is non-steady-state migration coefficient, mm^2/s; x_d is average penetration depth, mm; z is absolute value of ion valence, for chloride $z = 1$; R is gas constant, $R = 8.314$ J/(K·mol); T is average value of the initial and final temperature in the anolyte solution, K; F is the Faraday constant, $F = 9.648 \times 10^4$ J/(V·mol); U is absolute value of the applied voltage, V; c_d is chloride concentration at which the color change changes, mol/L; c_0 is chloride concentration in the catholyte solution, mol/L; L is thickness of the sample, m; and t is time duration, seconds.

Accelerated carbonation test of mortar—Following a curing period of 28 days, three mortar cube specimens were used from each case that were made with and without WWF. These specimens were subsequently placed in an accelerated carbonation chamber. The concentration of carbon dioxide (CO_2) in the carbonation chamber was maintained at 3%, while the relative humidity was set at 70% and the temperature was maintained at 40°C. Researchers used different concentrations of CO_2 for accelerated carbonation testing, ranging from 1 to 10% of CO_2.[31-40] In this investigation, the concentration of CO_2 was regulated at a level of 3%. The relative humidity was set at 70%, as another study concluded that at this relative humidity, the carbonation depth would be the highest.[41] The temperature was set at 40°C, as some previous studies have used the same temperature for accelerated carbonation of concrete, considering a hot and humid environment similar to their laboratory's terrestrial conditions.[42,43] The carbonation depths of the mortar were assessed at intervals of 15, 30, and 45 days in the accelerated carbonation chamber. This was accomplished by applying a 1% phenolphthalein indicator solution, which consisted of 1 g phenolphthalein mixed with 50 mL 95% ethanol and 50 mL distilled water, onto the recently fractured surface. The measurement of depth of the colorless portion, which refers to the carbonated portion of concrete, was measured using a digital slide caliper. The accelerated carbonation coefficient of mortar was obtained by analyzing the depth of carbonation versus time curve. This was achieved by performing a linear regression analysis on the data, specifically by examining the relationship between the carbonation depths and the square root of the corresponding time in years. The following equation provides the necessary information to calculate the accelerated carbonation coefficient.

$$X_A = K_A\sqrt{t} \rightarrow K_A = \frac{X_A}{\sqrt{t}} \tag{4}$$

where X_A is accelerated carbonation depth, mm; K_A is accelerated carbonation coefficient, mm/$\sqrt{\text{years}}$; and t is time, years.

Density, absorption, and voids in hardened concrete—In accordance with ASTM C642-21,[44] the density, absorption, and void percentage (permeable porosity) of concrete were determined. To conduct the experiments, three specimens measuring 50 mm in thickness and 100 mm in diameter were cut using a diamond cutter. As per the previously referenced standard (ASTM C642), several weight measurements were performed on the discs, including apparent weight, saturated weight, oven-dried weight, and boiled weight. Following that, using the equations mentioned in the standard, the density, absorption, and voids in hardened concrete were measured.

Microstructural investigation—The freshly fractured fragments of concrete were immediately gathered following the crushing of the specimens during the evaluation of their compressive strength at 90 days. The specimens were subjected to a drying process for 120 minutes at a temperature of 60°C. Subsequently, the specimens were submerged in a solution of acetone to eliminate any particulate matter present on the surface. Prior to conducting SEM analysis, the specimens underwent a gold sputtering process to mitigate the occurrence of charge surges that may arise during SEM research conducted at high voltage. The microstructure of the materials was examined by capturing pictures using an SEM.

Research flow diagram—Figure 3 presents the research flow diagram of this investigation.

EXPERIMENTAL RESULTS AND DISCUSSION

Microstructure, surface morphology, and phase composition of WWF particles

The SEM images of WWF are presented in Fig. 4. The examination results revealed that the particles possess a porous calcium-silicate-hydrate (C-S-H) microstructure and exhibit an irregular shape. In addition, WWF particles have a rough surface texture. The XRD pattern in Fig. 5 indicates the presence of $Ca(OH)_2$ and SiO_2. $Ca(OH)_2$ may have originated from prior hydration of cement, and the presence of SiO_2 in WWF also indicates the presence of sand. The peaks of SiO_2 may also correlate with the presence of fly ash and slag. The pH of WWF was found to be 9.52, indicating its high alkalinity, which can be attributed to the presence of $Ca(OH)_2$ crystals. $CaCO_3$ crystals were also found in WWF, likely originating from limestone powder mixed with clinker during the cement production.

Compressive strength and UPV

The 28-day compressive strength and UPV data are plotted against the 0 and 20% WWF contents for various types of cement in Fig. 6. According to Fig. 6(a), the use of WWF as a natural sand substitute increases the compressive strength of concrete compared to the control case with 0% WWF. The concrete mixture using CEM Type I cement and WWF-20% as a sand replacement had the greatest compressive strength (37.01 MPa). The compressive strength increased by over 25% compared to the matching control case of 100% natural sand. However, the rate of increase in compressive strength for other cement types was lower compared to CEM Type I, ranging from 1 to 17%. The strength increased by only 1% for CEM Type II/A-M. When the fly ash content was 65%, the compressive strength was increased by 17% compared to the control case. For 50% slag content, the

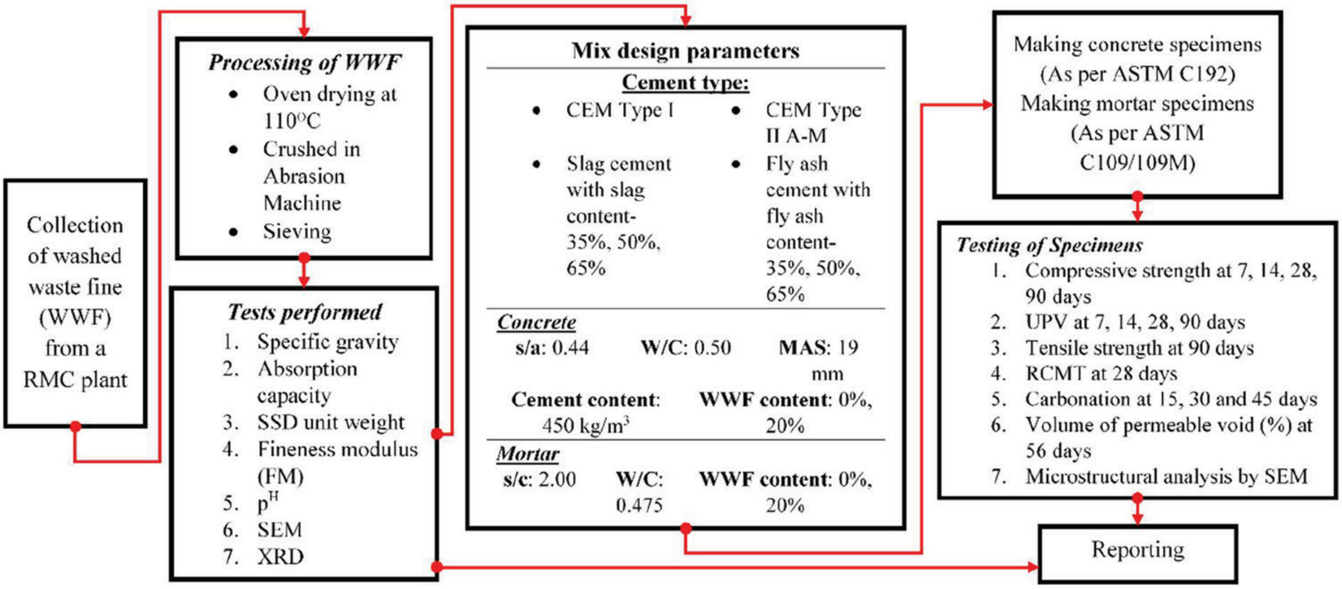

Fig. 3—Research flow diagram.

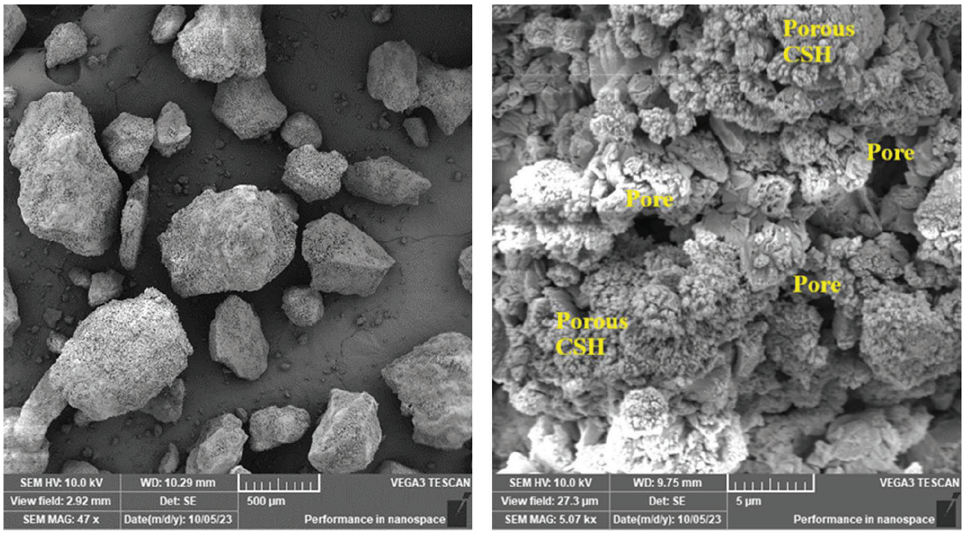

(a) WWF Particles

(b) Microstructure of WWF particles

Fig. 4—SEM images of WWF.

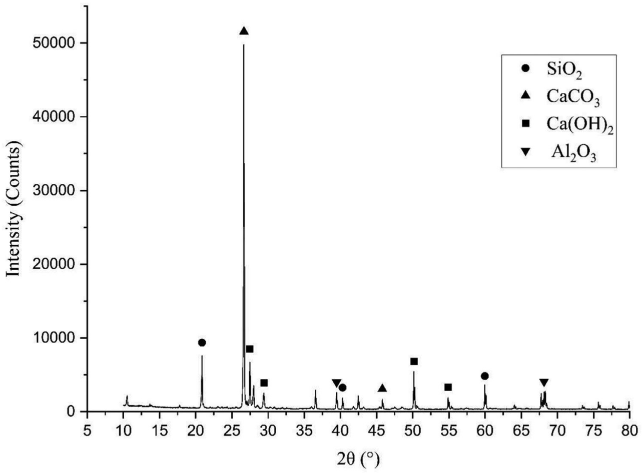

Fig. 5—XRD pattern of WWF.

compressive strength was increased by 13% compared to the corresponding control case. The finer particles in WWF, high alkalinity, presence of anhydrous cement, and higher absorption capacity contribute to an increase in strength by filling voids, accelerating hydration reactions, and helping the hydration of cement particles through internal curing. Kou et al.[9] reported a similar finding when using FCW as a replacement for natural sand in the production of partition blocks. They attributed the increase in compressive strength to the presence of unhydrated cement in FCW, as well as its finer particle size, which helps fill voids more effectively compared to natural sand. Nevertheless, the percentage of strength improvement due to the inclusion of WWF varies among different concrete mixtures. This observation can be explained by the variation in cement composition. The pure clinker-based cement (CEM Type I) experienced a spike in strength increase due to the internal curing effect caused by the inclusion of WWF. For the cases with a significant amount

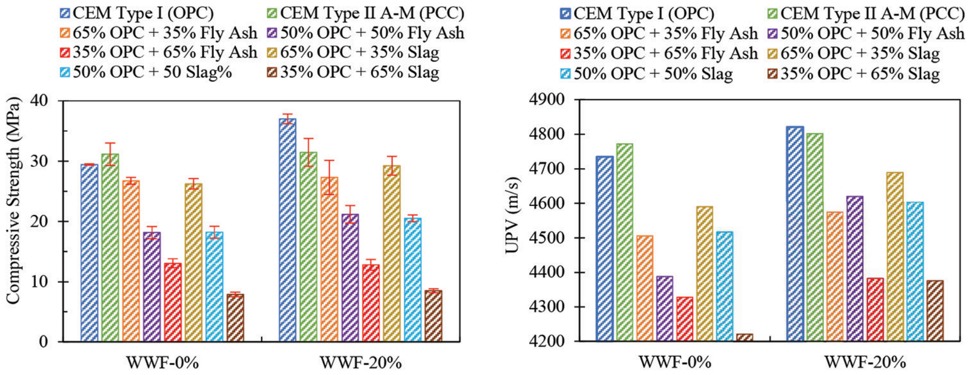

(a)

(b)

Fig. 6—Twenty-eight days: (a) compressive strength; and (b) UPV.

of pozzolans, the strength development was not as significant as the pure clinker-based cement. Uddin et al.[45] studied the strength development of composite concrete incorporating supplementary cementitious materials (SCMs) and reported that its early-age strength gain was slower compared to OPC concrete. They attributed this slower strength development to the delayed pozzolanic reaction of SCMs at early ages. The volume of permeable voids was investigated to see if the porosity had improved due to the addition of WWF, and the results are presented in the later sections of this study. The results of the UPV tests showed a similar trend to that of compressive strength, which can be observed from Fig. 6(b).

Relationship between compressive strength and UPV with variation in cement type and WWF content

The compressive strength and UPV data are plotted and presented in Fig. 7. The results demonstrate that regardless of the type of cement, the concrete specimens including WWF in their mixture exhibit higher levels of compressive strength compared to their respective control instances when considering the same value of UPV. For example, the compressive strength of concrete containing WWF as a partial sand replacement was greater than that of concrete without WWF at a UPV of 4700 m/s. The improvement of concrete compressive strength by incorporation of WWF can be attributed to the improvement of the microstructure of the concrete. The finer particles of WWF might have refined the microstructure to make it denser, which resulted in higher values of UPV.

Based on these data, the following exponential relationship (Eq. (5)) can be developed between compressive strength (f_c') and UPV in concrete for various cement types with varying WWF concentrations

$$f_c' = \alpha \times e^{\beta \times \mathrm{UPV}} \tag{5}$$

where α and β are the coefficients; their values are presented in Table 4. The greater the value of α, the more the graphs deviate from the compressive strength axis. According to the exponential relationships, the value of α varies for different types of cement, with the greatest value observed for CEM Type I cement. In addition, the value of α increased due to the incorporation of WWF compared to cases with no WWF in their mixture. When examining the impact of mineral content in cement, it was seen that the exponential lines shifted toward the right as the mineral content in the cement increased. The β coefficient represented the rate of change in compressive strength with UPV. For most cases, the value of β was high for concretes with WWF compared to their corresponding control cases.

Some of the R^2 values in Table 4 are moderately low. The low R^2 values may also be attributed to the presence of outliers within the data. It is important to consider the inherent heterogeneity of concrete materials, which arises from variations in hydration kinetics, differences in aggregate distribution, and microstructural inconsistencies. These factors introduce natural variability, occasionally leading to data points that appear as outliers in statistical analysis. The outliers have been identified within Fig. 7 using red circles. Despite the moderately low R^2 values, the Pearson correlation coefficient (r) was calculated for all cases, revealing a strong positive correlation between compressive strength and UPV, with statistical significance (p-value < 0.05) in all cases (Table 4). This confirms that the relationship between these two parameters remains valid, even in the presence of natural material variability.

Similar trends have been reported in previous studies, where researchers observed relatively low R^2 values when modeling concrete properties due to its complex and heterogeneous nature.[46,47] However, the strong and statistically significant Pearson correlation values reinforce that UPV remains a reliable indicator of compressive strength, aligning with prior findings.

Variation in compressive strength with time

Figure 8 depicts the strength development with time for concrete specimens made with and without WWF for different binders. The compressive strengths at 7, 14, and 28 days were normalized by the compressive strength at 90 days. It can be observed that for half of the investigated cases, the incorporation of WWF accelerates the strength development process at an early age. The trend of strength development can be explained in a manner that the early-age strength, such as the 7-day strength development, was boosted for mixtures composed of CEM Type I, fly ash cement having a moderate to high level of fly ash content

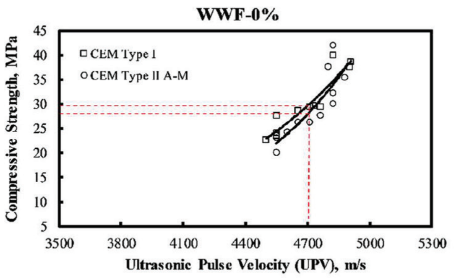

(a) CEM Type I, CEM Type II A-M cement (WWF 0%) (b) CEM Type I, CEM Type II A-M cement (WWF 20%)

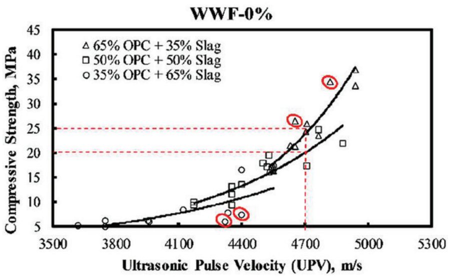

(c) Slag-based cement (WWF 0%) (d) Slag-based cement (WWF 20%)

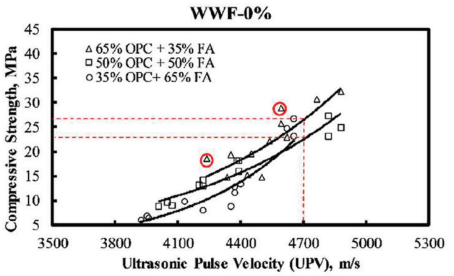

(e) Fly Ash-based cement (WWF 0%) (e) Fly Ash-based cement (WWF 20%)

Fig. 7—Compressive strength versus UPV.

Table 4—Relationships between compressive strength and UPV for different cement types with varying WWF content

Cement type	WWF content	Pearson correlation coefficient, *r*	*p*-value	Relationship between f_c' and UPV	R^2	α	β	Equation No.
OPC	0%	0.932	9.9×10^{-6}	$f_c' = 0.0703 \times e^{0.0013 \times \text{UPV}}$	0.885	0.0703	0.0013	(6)
	20%	0.854	4.0×10^{-4}	$f_c' = 0.3808 \times e^{0.0009 \times \text{UPV}}$	0.745	0.3808	.0009	(7)
PCC	0%	0.850	4.6×10^{-4}	$f_c' = 0.0165 \times e^{0.0016 \times \text{UPV}}$	0.783	0.0165	0.0016	(8)
	20%	0.874	1.9×10^{-4}	$f_c' = 0.0599 \times e^{0.0013 \times \text{UPV}}$	0.808	0.0599	0.0013	(9)
65% OPC + 35% fly ash	0%	0.838	6.6×10^{-4}	$f_c' = 0.0809 \times e^{0.0012 \times \text{UPV}}$	0.655	0.0809	0.0012	(10)
	20%	0.779	2.8×10^{-3}	$f_c' = 0.0004 \times e^{0.0025 \times \text{UPV}}$	0.644	.0004	0.0025	(11)
50% OPC + 50% fly ash	0%	0.977	4.9×10^{-8}	$f_c' = 0.0825 \times e^{0.0012 \times \text{UPV}}$	0.913	0.0825	0.0012	(12)
	20%	0.899	6.8×10^{-5}	$f_c' = 0.0728 \times e^{0.0013 \times \text{UPV}}$	0.825	0.0728	0.0013	(13)
35% OPC + 65% fly ash	0%	0.902	5.9×10^{-5}	$f_c' = 0.0037 \times e^{0.0019 \times \text{UPV}}$	0.900	0.0037	0.0019	(14)
	20%	0.947	2.7×10^{-6}	$f_c' = 0.0046 \times e^{0.0018 \times \text{UPV}}$	0.928	0.0046	0.0018	(15)
65% OPC + 35% slag	0%	0.943	4.1×10^{-6}	$f_c' = 0.0032 \times e^{0.0019 \times \text{UPV}}$	0.878	0.0032	0.0019	(16)
	20%	0.817	1.1×10^{-3}	$f_c' = 0.2902 \times e^{0.0010 \times \text{UPV}}$	0.658	0.2902	0.0010	(17)
50% OPC + 50% slag	0%	0.907	4.6×10^{-5}	$f_c' = 0.0332 \times e^{0.0014 \times \text{UPV}}$	0.815	0.0332	0.0014	(18)
	20%	0.912	3.5×10^{-5}	$f_c' = 0.0355 \times e^{0.0014 \times \text{UPV}}$	0.878	0.0355	0.0014	(19)
35% OPC + 65% slag	0%	0.751	4.8×10^{-3}	$f_c' = 0.0079 \times e^{0.0011 \times \text{UPV}}$	0.631	0.0079	0.0011	(20)
	20%	0.807	1.4×10^{-3}	$f_c' = 0.0308 \times e^{0.0013 \times \text{UPV}}$	0.785	0.0308	0.0013	(21)

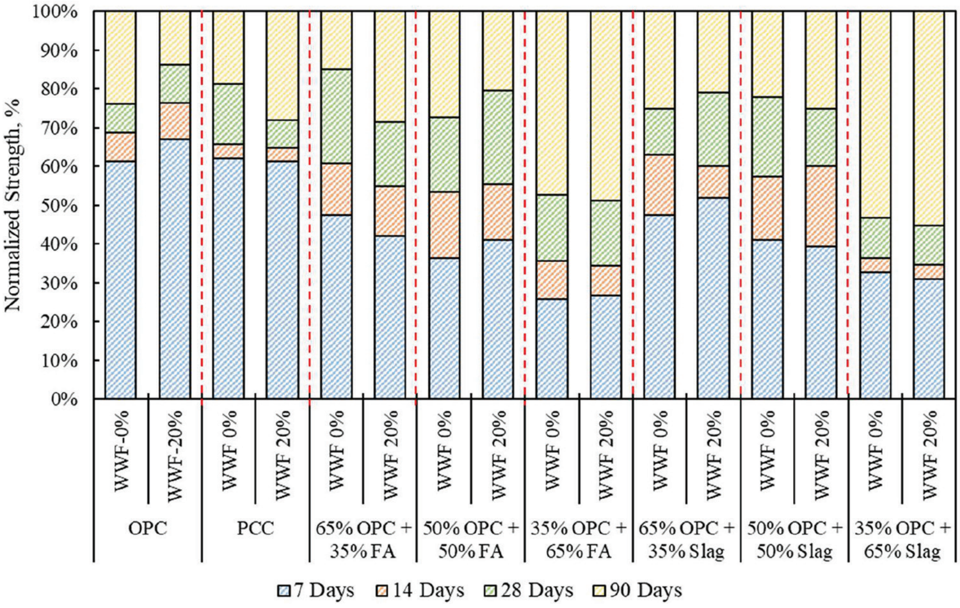

Fig. 8—Strength development for concrete.

(50%), and slag cement having a small slag content (35%) when WWF was incorporated into their mixtures, and at the later curing ages (28 to 90 days), the development rate slowed down. This can be attributed to the fact that WWF may have aided the hydration process for these cases by supplying water internally, as the absorption rate of WWF was high compared to natural sand. Due to this, the majority of the clinker and pozzolans reacted fast at the early age and the strength developed, and in the later ages, a very low amount of clinker and pozzolans remained; that is why, at later curing ages, the development rate slowed down. It is also possible that WWF might have created new nucleation sites within the concrete matrix where the hydrates precipitated and the strength gain was accelerated. Additionally, the elevated alkalinity caused by the presence of WWF, which contains $Ca(OH)_2$, may have facilitated the early-age hydration of pozzolans. Juenger and Jennings[48] also reported that increasing alkalinity by adding hydroxide ions accelerates the initial rate of hydration, thereby enhancing early strength development. However, in some cases, the developing trend is almost identical to their control cases, such as the cases composed of cements that had high amounts of mineral admixtures in their mixture, such as fly ash 65% and slag 50 and 65%. The possible reason for this can be the fact that for the high amount of mineral admixtures, the internal water supplied by WWF at early ages was not adequate to boost the hydration process. In a similar investigation on the use of sludge from returned concrete, Audo et al.[7] examined the heat of hydration in mortar and found that it was higher at early ages in mixtures containing sludge. They attributed this increase to the creation of new nucleation sites for hydrate precipitation due to sludge incorporation, as well as the potential contribution of anhydrous cement, which may have facilitated higher exothermic ion dissolution. It is also a sign that in cases containing WWF, the reaction rates are high at young ages, indicating that the rate of strength development is also high. Kou et al.[9] similarly hypothesized that anhydrous cement particles might be present in these types of materials, contributing to the rapid strength gain at an early age.

Tensile strength

The 90-day tensile strength data are plotted for the different mixtures with and without WWF in Fig. 9. Same as the compressive strength of concrete, the case with OPC and 20% WWF shows the highest tensile strength (4.19 MPa). The results also indicate that partial substitution (20%) of sand with WWF had no significant influence on the tensile strength of concrete. When compared to their corresponding control cases, irrespective of the cement types, the tensile strength of concrete with and without WWF was nearly identical. However, in previous studies where recycled fine aggregates (RFA) were used to produce concrete, the splitting tensile strength of concrete was decreased,[49,50] and the researchers hypothesized that it could decrease even further with a high replacement amount of sand with RFA, attributing this phenomenon to the porous nature of RFA.[51] WWF is also a porous material compared to natural sand; however, no reduction in tensile strength of concrete was found for 20% replacement of sand. Based on Fig. 10(a) and (b), two relationships between compressive strength and tensile strength for concrete made with 0% and 20% WWF are presented in Eq. (6) and (7), respectively. The equations were comparatively similar.

For concrete with 0% WWF

$$f_t = 0.530\sqrt{f_c'} \tag{6}$$

For concrete with 20% WWF as natural sand replacing material

$$f_t = 0.512\sqrt{f_c'} \tag{7}$$

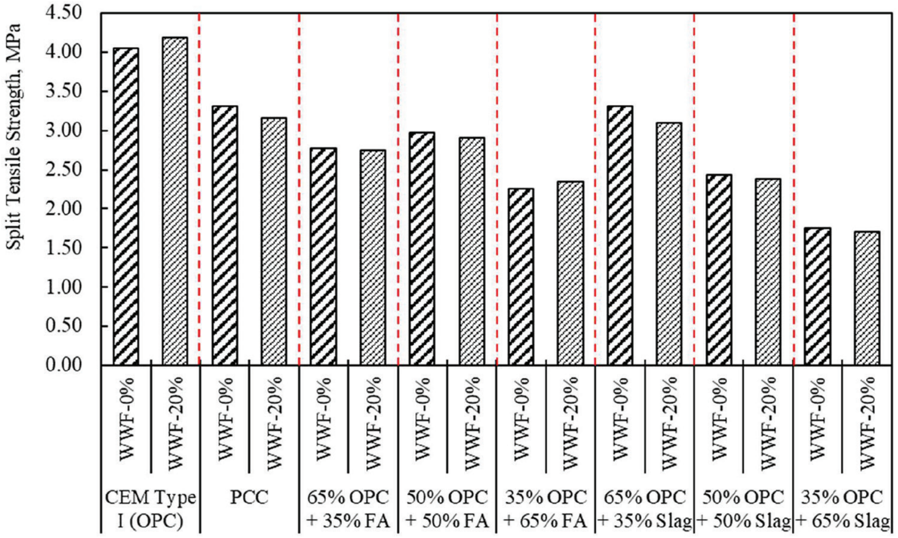

Fig. 9—Ninety-day tensile strength for various cement types and WWF content (0 and 20%).

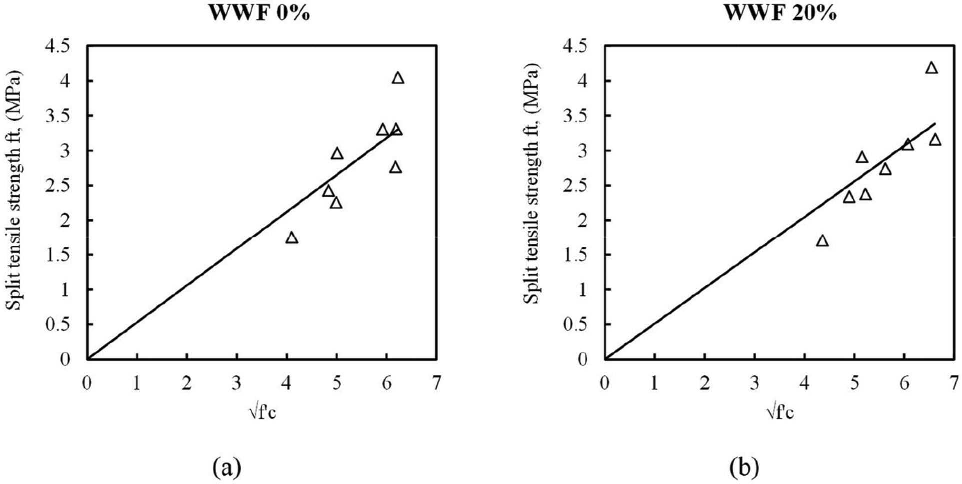

Fig. 10—Relationship between splitting tensile strength and compressive strength: (a) WWF 0%; and (b) WWF 20%.

Volume of permeable voids (%) and absorption capacity (%) of concrete

The volume of permeable voids and absorption capacity of concrete at the age of 56 days for different types of cement with and without WWF are shown in Fig. 11. The volume of permeable voids (VPV) in concrete is reduced with the incorporation of WWF irrespective of the types of cement; however, the maximum reduction in permeable pores is found for OPC. Similar to the volume of permeable pores, the absorption capacity is reduced with the incorporation of WWF; it is clearly understood that WWF improves the microstructure of concrete by filling out the voids. Chen et al. provided a similar explanation in which they substituted fine granite polishing waste (GPW) for sand.[52,53] They attributed this decrease to the filling effect of GPW, which is similar to the filling effect of WWF. Even though the VPV is reduced due to the incorporation of WWF, it is possible that the pore-size distribution shifts toward larger, more continuous pores, which might increase the sorptivity coefficient and enhance ion mobility. The authors previously observed an increased sorptivity coefficient for mortar mixtures containing WWF in an earlier study.[14]

Non-steady-state migration coefficient (D_{nssm})

The non-steady-state migration coefficient (D_{nssm}) values for different mixtures, with and without WWF, are plotted in Fig. 12. It is evident that concrete specimens incorporating blended cement exhibit greater resistance to chloride migration compared to those made with OPC. Among the different mixtures, the lowest migration coefficient is observed for specimens containing 65% slag.

According to prior studies, the incorporation of slag in concrete leads to microstructural refinement, which increases the tortuosity of the chloride-ion transport pathway.[51] Additionally, research has shown that the chloride-binding capacity of slag concrete is influenced by the slag content in blended cement—higher levels of slag replacement enhance binding capacity and reduce the diffusion coefficient.[52] Other studies have also demonstrated that concrete with a high slag content exhibits the lowest chloride ingress in both short-term laboratory tests and long-term exposure to seawater.[51,52] Furthermore, chloride ions can be chemically absorbed by alumina phases, contributing to improved resistance against chloride penetration.[54]

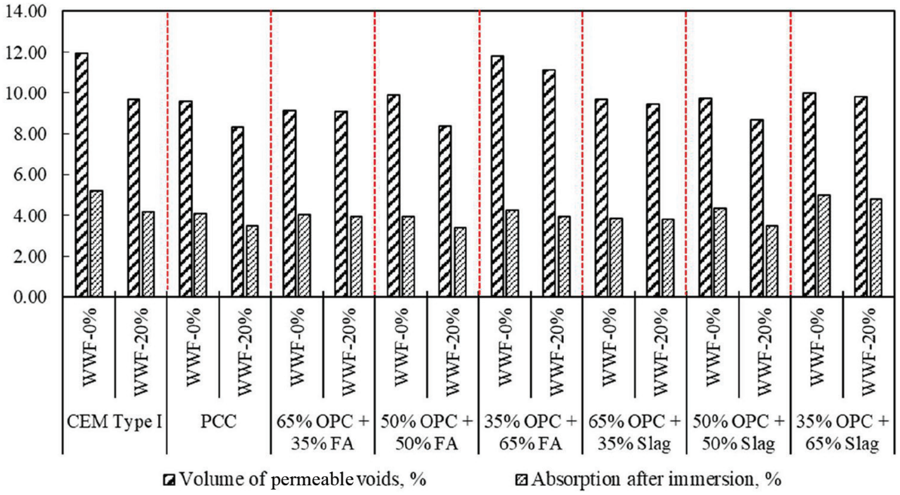

Fig. 11—Volume of permeable voids (%) and absorption capacity (%).

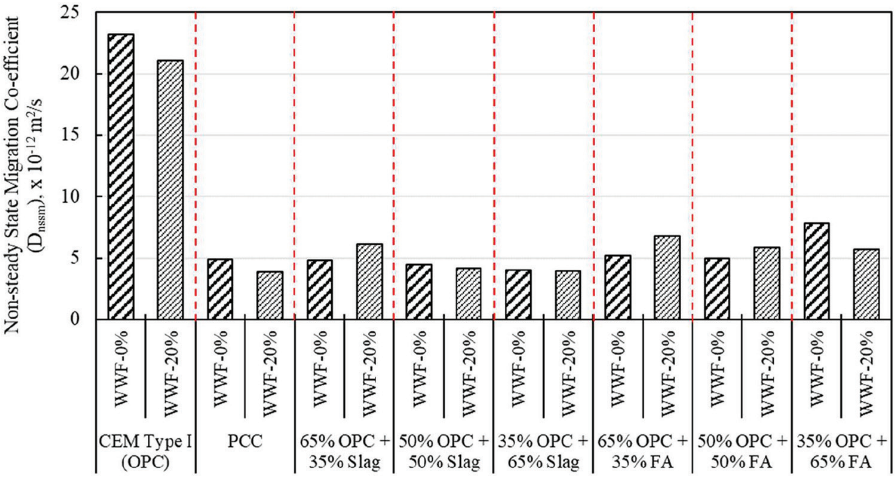

Fig. 12—Non-steady-state migration coefficient (D_{nssm}*) of different concrete mixtures.*

However, the effect of incorporating WWF does not follow the same trend as the use of SCMs. For mixtures with low to moderate SCM content (≤50%), the addition of WWF appears to increase the D_{nssm} value. A noticeable reduction in D_{nssm} is observed only when the SCM content reaches 65%. The XRD pattern of WWF (Fig. 5) reveals the presence of $Ca(OH)_2$ and crystalline SiO_2 (quartz). It is possible that WWF supplies excess $Ca(OH)_2$ to the concrete mixture. When SCM content is low to moderate, unreacted $Ca(OH)_2$ remains after pozzolanic reactions, leading to an increased pH in the concrete pore solution. The excess $Ca(OH)_2$ does not even react with the crystalline SiO_2 present in WWF. As a result, the presence of OH^- ions competes with Cl^- ions, destabilizing the formation of Friedel's salt and subsequently increasing chloride-ion diffusion.

However, when SCM content reaches 65%, the hydration mechanism shifts toward pozzolanic and latent hydraulic reactions, leading to the consumption of excess $Ca(OH)_2$ supplied by WWF. Consequently, the negative impact of excess portlandite is mitigated, and the D_{nssm} decreases as the concrete microstructure becomes denser; chemical binding of Cl^- was not affected. Additionally, based on the XRD pattern (Fig. 5), WWF contains Al_2O_3 crystals, which may contribute to chloride binding.

Carbonation coefficient of mortar

Figure 13 shows the fractured surface of mortar samples that have been sprayed with phenolphthalein solution. These samples were exposed to an accelerated carbonation chamber for 15 days. Figure 14 depicts the depths of carbonation in mortar samples with and without WWF at different phases of exposure in an accelerated carbonation chamber. Figure 15 shows the corresponding carbonation coefficients. As expected, the specimens made with OPC showed the least carbonation depth as well as carbonation coefficient, similar to the conclusions drawn in previous literature.[42] The whole section of the specimens was carbonated for specimens containing 50% or greater fly ash content. The cases made with 65% slag exhibited greater depths of carbonation as well. The alkalinity of the concrete mixture determines the resistance to carbonation, and mixtures with high alkalinity exhibit the highest resistance. During hydration reactions, the quantity of $Ca(OH)_2$ produced influences alkalinity.[54] Compared to the control case, the cases with WWF showed decreased carbonation depths. This reduction in depth was particularly noticeable in cases using PCC and slag-based blended cement with low slag content. When the SCM content is low to moderate, some $Ca(OH)_2$ remains unreacted after pozzolanic reactions, leading to a higher pH in the concrete pore solution. Given that the XRD pattern of WWF reveals the presence of $Ca(OH)_2$ crystals and its measured pH is 9.52, it is reasonable to suggest that the additional alkalinity supplied by WWF may contribute to improving concrete's carbonation resistance.

The effect of incorporating WWF on the improvement of concrete carbonation resistance was further validated using a *t*-test statistical analysis. The critical *t*-value for the explained data to indicate a 95% confidence interval was found to be 2.015. However, after analysis, the calculated *t*-value for the given data was 2.462, indicating a significant and positive effect of WWF on concrete's carbonation resistance.

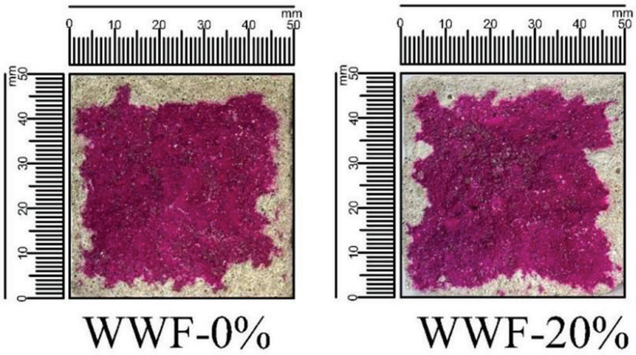

Fig. 13—Fractured mortar surface after spraying phenolphthalein solution (50% OPC + 50% slag).

Microstructural investigation

Figure 16 shows SEM pictures of concrete made with WWF. The SEM photos were taken in and around the WWF particles. In the pores of WWF, the deposits of ettringites (Fig. 16(a)), CH plates (Fig. 16(c)), and fly ash particles (Fig. 16(b) and (d)) are observed. The deposits of ettringite and CH will reduce the porosity of WWF. The fly ash particle of Fig. 16(d) can be attributed to the WWF added to the mixture. The fibrous regions of WWF in Fig. 16(c) and (e) can be linked with the hydration of cement particles at a high water-cement ratio (*w*/*c*) during washing and sedimentation in the tank.

The finer particles of WWF are expected to reduce the permeable pore channels. Also, the higher absorption of WWF will help the hydration of cement particles around the WWF, thereby forming a dense layer of C-S-H around the WWF. Although WWF is porous in nature, the overall permeability of concrete will not increase due to the improvement of the microstructure of concrete around the WWF.

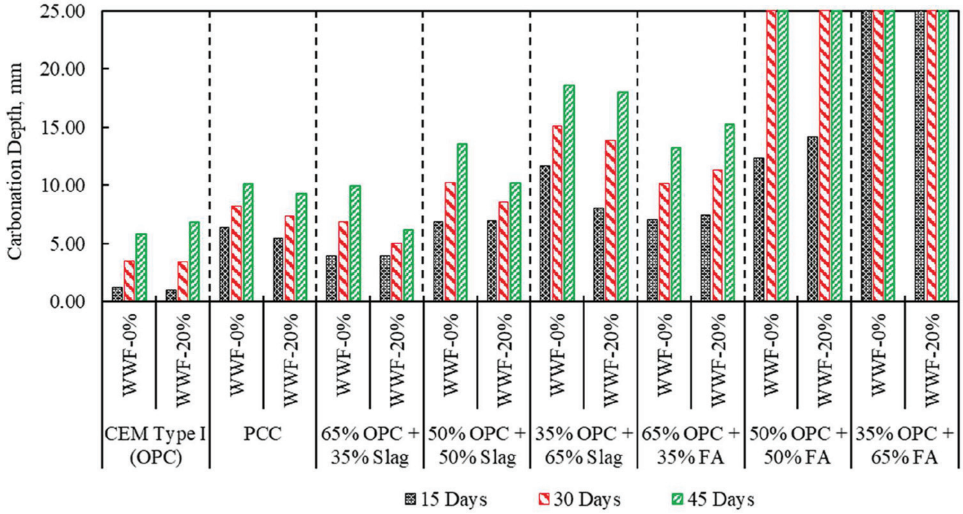

Fig. 14—Carbonation depth for mortar.

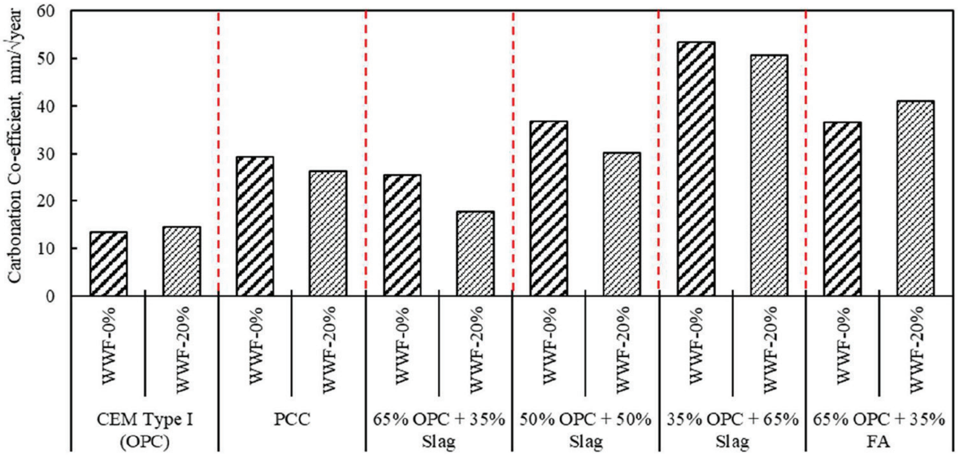

Fig. 15—Carbonation coefficient of mortar.

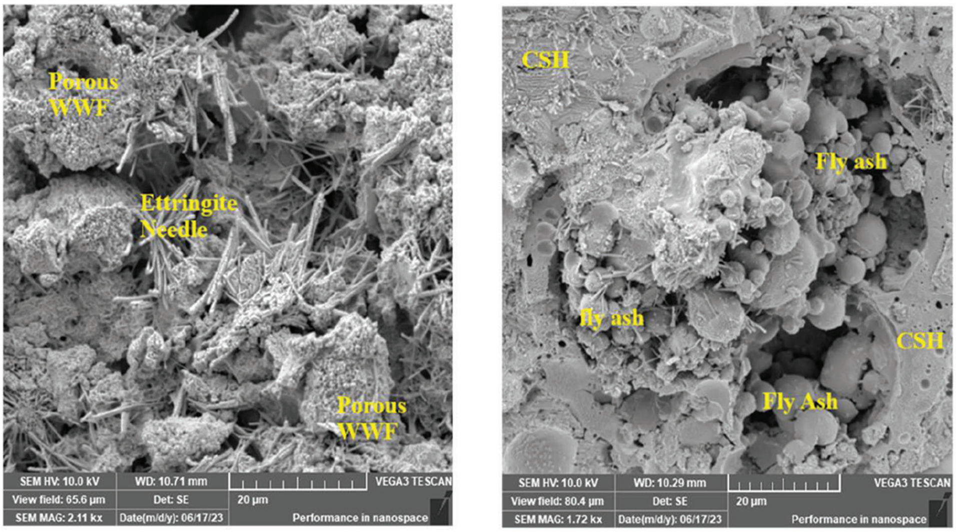

(a) 50 % OPC + 50% FA
WWF 20%

(b) 50% OPC + 50% FA
WWF 20%

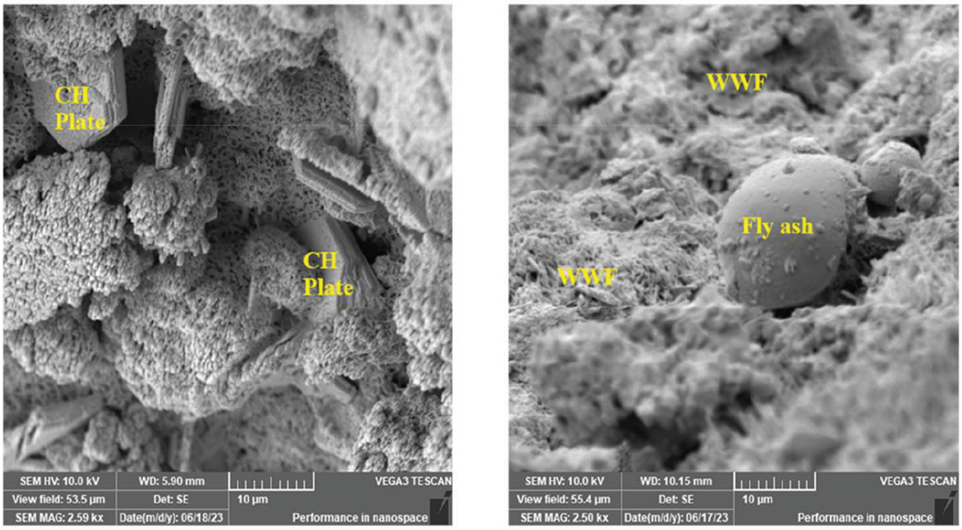

(c) 65% OPC + 35% Slag
WWF 20%

(d) 50% OPC + 50% Slag
WWF 20%

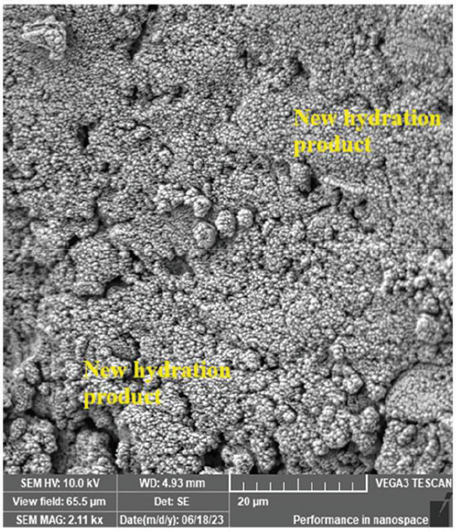

(e) 35% OPC + 65% Slag
WWF 20%

Fig. 16—SEM images of hardened concrete.

CONCLUSIONS

This research was conducted to determine the impact of using washed waste fines (WWF) as a partial replacement of sand in the production of concrete. The following conclusions are drawn from the scope of this investigation:

1. The incorporation of WWF improved the compressive strength of concrete. In the case of CEM Type I, a 25% increase in compressive strength was observed compared to the control, while for other cases, the increase ranged between 1 and 17%. This improvement can be attributed to WWF by filling voids, accelerating hydration reactions, and aiding cement particle hydration through internal curing. Additionally, the hydration of anhydrous cement present in WWF may have contributed to strength gain by participating in later hydration reactions.

2. The incorporation of WWF accelerates the early-age strength development of concrete made with CEM Type I, fly ash cement with moderate fly ash content (50%), and slag cement with low slag content (35%). In the case of CEM Type I, the inclusion of WWF increased the 7-day strength gain from 61.3 to 67%, representing a nearly 6%-point improvement. For the other cases mentioned, this increase was approximately 5% points. WWF may have enhanced the hydration process through internal curing due to its high absorption capacity. Additionally, the higher alkalinity of WWF contributed to early strength development by accelerating hydration. WWF may have also created new nucleation sites for hydrates to precipitate, further aiding early strength gain.

3. The inclusion of WWF improves the microstructure of concrete around WWF particles, leading to a reduction in the volume of permeable voids (VPV). Consequently, the absorption capacity of concrete is also reduced. The filling effect of WWF particles plays a significant role in decreasing both VPV and absorption capacity.

4. Slag significantly enhances resistance to chloride migration by refining concrete's microstructure and increasing chloride binding. The lowest migration coefficient was observed at 65% slag content. WWF's impact on chloride resistance varies with supplementary cementitious material (SCM) content. At low to moderate SCM levels (≤50%), incorporation of WWF increases chloride diffusion due to excess $Ca(OH)_2$ supplied by WWF, which disrupts chloride-binding phases. However, at high SCM contents, pozzolanic and latent hydraulic reactions consume excess $Ca(OH)_2$, leading to a denser microstructure and improved chloride resistance. The Al_2O_3 in WWF may further aid chloride binding at high SCM levels.

5. The carbonation resistance is highest in ordinary portland cement (OPC)-based mixtures and lowest in mixtures with high fly ash (≤50%) or slag (65%) content due to reduced alkalinity. Incorporating WWF reduces carbonation depth, especially in portland composite cement (PCC) and low-slag blended cement mixtures, likely due to the additional alkalinity supplied by WWF. Statistical analysis (*t*-test) further validates WWF's significant positive effect on carbonation resistance at a 95% confidence level.

6. Microstructural analysis indicates that the high absorption capacity of WWF may have facilitated the hydration of surrounding cement particles, leading to the formation of a dense layer of calcium-silicate-hydrate (C-S-H) around the WWF.

7. From both a functional and environmental perspective, the concrete mixture containing 35% slag as CEM Type I replacement and 20% WWF as a replacement for natural sand emerged as the best among all the mixtures studied in this research. This mixture achieved compressive strength comparable to the ultimate control mixture made with CEM Type I cement and 100% natural sand. In terms of durability, its chloride migration coefficient was lower than that of the CEM Type I mixture without WWF, and its carbonation coefficient was close to that of the mixture with the highest carbonation resistance. These findings suggest that replacing both clinker and natural sand in moderate amounts can enhance sustainability while maintaining the structural integrity of concrete, making it both environmentally friendly and suitable for structural applications.

AUTHOR BIOS

ACI member **Tarek Uddin Mohammed** *is a Professor in the Department of Civil and Environmental Engineering, Islamic University of Technology (IUT), Gazipur, Bangladesh. He is currently President of the ACI Bangladesh Chapter. He is a member of ACI Committees S803, Faculty Network Coordinating Committee; 201, Durability of Concrete; 222, Corrosion of Metals in Concrete; and 555, Concrete with Recycled Materials. His research interests include durability, recycling, and sustainability of construction materials.*

Mohammad Zunaied Bin Harun *is an Assistant Professor in the Department of Civil and Environmental Engineering, IUT. His research interests include durability, recycling, and sustainability of construction materials.*

ACI member **Chowdhury Zubayer Bin Zahid** *is a Master's Student in the Department of Civil Engineering, University of Malaya, Kuala Lumpur, Malaysia. He is a member of ACI Committee 130, Sustainability of Concrete, and is Past President of the ACI IUT Student Chapter. His research interests include sustainable construction materials and self-healing of cementitious composites through biomineralization.*

Redwan Ul Islam *is a Master's Student in the Department of Civil and Environmental Engineering, King Fahd University of Petroleum and Minerals, Dhahran, Saudi Arabia. His research interests include self-sensing and sustainable cementitious composites.*

ACKNOWLEDGMENTS

The authors wish to acknowledge the financial as well as laboratory support provided by the Islamic University of Technology, Gazipur, Bangladesh, to conduct this extensive investigation, including the untiring efforts of laboratory staff members to conduct this study. The authors would also like to express their sincere gratitude to Crown Cement Concrete and Building Products Limited (CCC&BPL) for sponsoring the materials (cement, admixture, washed waste fines) used in this research.

REFERENCES

1. Paranhos, R. S.; Cazacliu, B. G.; and Sampaio, C. H., "A Sorting Method to Value Recycled Concrete," *Journal of Cleaner Production*, V. 112, 2016, pp. 2249-2258.
2. Shi, C.; Li, Y.; and Zhang, J., "Performance Enhancement of Recycled Concrete Aggregate–A Review," *Journal of Cleaner Production*, V. 112, 2016, pp. 466-472.
3. Sandrolini, F., and Franzoni, E., "Waste Wash Water Recycling in Ready-Mixed Concrete Plants," *Cement and Concrete Research*, V. 31, 2001, pp. 485-489.
4. Kazaz, A., and Ulubeyli, S., "Current Methods for the Utilization of the Fresh Concrete Waste Returned to Batching Plants," *Procedia Engineering*, V. 161, 2016, pp. 42-46.
5. Kuranchie, F. A.; Attiogbe, F.; and Quarshie, J. T., "Land Scarcity as a Site Selection Challenge for the Management of Municipal Solid Wastes in Accra, Ghana," *International Journal of Environment and Waste Management*, V. 26, 2020, pp. 423-437.

6. Ferrari, G.; Miyamoto, M.; and Ferrari, A., “New Sustainable Technology for Recycling Returned Concrete,” *Construction and Building Materials*, V. 67, 2014, pp. 353-359.

7. Audo, M.; Mahieux, P.-Y.; and Turcry, P., “Utilization of Sludge from Ready-Mixed Concrete Plants as a Substitute for Limestone Fillers,” *Construction and Building Materials*, V. 112, 2016, pp. 790-799.

8. Xuan, D.; Poon, C. S.; and Zheng, W., “Management and Sustainable Utilization of Processing Wastes from Ready-Mixed Concrete Plants in Construction: A Review,” *Resources, Conservation and Recycling*, V. 136, 2018, pp. 238-247.

9. Kou, S.-C.; Zhan, B.-J.; and Poon, C.-S., “Properties of Partition Wall Blocks Prepared with Fresh Concrete Wastes,” *Construction and Building Materials*, V. 36, 2012, pp. 566-571.

10. Zervaki, M.; Leptokaridis, C; and Tsimas, S., “Reuse of By-Products from Ready-Mixed Concrete Plants for the Production of Cement Mortars,” *Journal of Sustainable Development of Energy, Water and Environment Systems*, V. 1, No. 2, 2013, pp. 152-162.

11. Schoon, J.; De Buysser, K.; Van Driessche, I.; and De Belie, N., “Feasibility Study of the Use of Concrete Sludge as Alternative Raw Material for Portland Clinker Production,” *Journal of Materials in Civil Engineering*, ASCE, V. 27, No. 10, 2015, p. 04014272.

12. Pistilli, M.; Peterson, C.; and Shah, S., “Properties and Possible Recycling of Solid Waste from Ready-Mix Concrete,” *Cement and Concrete Research*, V. 5, 1975, pp. 249-259.

13. Correia, S.; Souza, F.; and Dienstmann, G., “Assessment of the Recycling Potential of Fresh Concrete Waste Using a Factorial Design of Experiments,” *Waste Management*, V. 29, No. 11, 2009, pp. 2886-2891.

14. Mohammed, T. U.; Harun, M. Z. B.; and Masud, M. M. U., “Reuse of Washed Fines from Ready-Mixed Concrete Plants in Mortar,” *European Journal of Environmental and Civil Engineering*, V. 29, No. 6, 2024, pp. 1-19.

15. ASTM C33/C33M-18, “Standard Specification for Concrete Aggregates,” ASTM International, West Conshohocken, PA, 2018.

16. ASTM C778-21, “Standard Specification for Standard Sand,” ASTM International, West Conshohocken, PA, 2021.

17. BDS EN 197-1: 2003, “Bangladesh Standard Cement - Part 1: Composition, Specifications and Conformity Criteria for Common Cements,” Bangladesh Standards and Testing Institution, Dhaka, Bangladesh, 2005.

18. ASTM C127-15, “Standard Test Method for Density, Relative Density (Specific Gravity), and Absorption of Coarse Aggregate,” ASTM International, West Conshohocken, PA, 2015.

19. ASTM C128-15, “Standard Test Method for Relative Density (Specific Gravity) and Absorption of Fine Aggregate,” ASTM International, West Conshohocken, PA, 2015.

20. ASTM C29/C29M-23, “Standard Test Method for Bulk Density (“Unit Weight”) and Voids in Aggregate,” ASTM International, West Conshohocken, PA, 2023.

21. ASTM C131-06, “Standard Test Method for Resistance to Degradation of Small-Size Coarse Aggregate by Abrasion and Impact in the Los Angeles Machine,” ASTM International, West Conshohocken, PA, 2006.

22. ASTM C136-06, “Standard Test Method for Sieve Analysis of Fine and Coarse Aggregates,” ASTM International, West Conshohocken, PA, 2006.

23. ASTM C192/C192M-15, “Standard Practice for Making and Curing Concrete Test Specimens in the Laboratory,” ASTM International, West Conshohocken, PA, 2015.

24. ASTM C109/C109M-20, “Standard Test Method for Compressive Strength of Hydraulic Cement Mortars (Using 2-in. or [50-mm] Cube Specimens),” ASTM International, West Conshohocken, PA, 2020.

25. Vu, T. H.; Gowripalan, N.; and De Silva, P., “Assessing Carbonation in One-Part Fly Ash/Slag Geopolymer Mortar: Change in Pore Characteristics Using the State-of-the-Art Technique Neutron Tomography,” *Cement and Concrete Composites*, V. 114, 2020, p. 103759.

26. Shanmugavel, D., “Experimental Analysis on the Performance of Egg Albumen as a Sustainable Bio Admixture in Natural Hydraulic Lime Mortars,” *Journal of Cleaner Production*, V. 320, 2021, p. 128736.

27. ASTM C39/C39M-23, “Standard Test Method for Compressive Strength of Cylindrical Concrete Specimens,” ASTM International, West Conshohocken, PA, 2023.

28. ASTM C597-22, “Standard Test Method for Ultrasonic Pulse Velocity Through Concrete,” ASTM International, West Conshohocken, PA, 2022.

29. ASTM C496-96, “Standard Test Method for Splitting Tensile Strength of Cylindrical Concrete Specimens,” ASTM International, West Conshohocken, PA, 1996.

30. NT Build 492, “Concrete, Mortar and Cement-Based Repair Materials: Chloride Migration Coefficient from Non-Steady-State Migration Experiments,” NORDTEST, Espoo, Finland, 1999.

31. Leemann, A., and Moro, F., “Carbonation of Concrete: The Role of CO_2 Concentration, Relative Humidity and CO_2 Buffer Capacity,” *Materials and Structures*, V. 50, 2017, pp. 1-14.

32. Leemann, A.; Nygaard, P.; and Kaufmann, J.; and Loser, R., “Relation Between Carbonation Resistance, Mix Design and Exposure of Mortar and Concrete,” *Cement and Concrete Composites*, V. 62, 2015, pp. 33-43.

33. Yoon, I.-S.; Çopuroğlu, O.; and Park, K.-B., “Effect of Global Climatic Change on Carbonation Progress of Concrete,” *Atmospheric Environment*, V. 41, 2007, pp. 7274-7285.

34. Castellote, M.; Fernandez, L.; and Andrade, C., “Chemical Changes and Phase Analysis of OPC Pastes Carbonated at Different CO_2 Concentrations,” *Materials and Structures*, V. 42, 2009, pp. 515-525.

35. Dhir, R.; Hewlett, P.; and Chan, Y., “Near-Surface Characteristics of Concrete: Prediction of Carbonation Resistance,” *Magazine of Concrete Research*, V. 41, No. 148, 1989, pp. 137-143.

36. Neves, R.; Branco, F.; and De Brito, J., “Field Assessment of the Relationship Between Natural and Accelerated Concrete Carbonation Resistance,” *Cement and Concrete Composites*, V. 41, 2013, pp. 9-15.

37. Khunthongkeaw, J.; Tangtermsirikul, S.; and Leelawat, T., “A Study on Carbonation Depth Prediction for Fly Ash Concrete,” *Construction and Building Materials*, V. 20, 2006, pp. 744-753.

38. Sanjuán, M.; Andrade, C.; and Cheyrezy, M., “Concrete Carbonation Tests in Natural and Accelerated Conditions,” *Advances in Cement Research*, V. 15, 2003, pp. 171-180.

39. Atiş, C. D., “Accelerated Carbonation and Testing of Concrete Made with Fly Ash,” *Construction and Building Materials*, V. 17, 2003, pp. 147-152.

40. Zhang, D., and Shao, Y., “Effect of Early Carbonation Curing on Chloride Penetration and Weathering Carbonation in Concrete,” *Construction and Building Materials*, V. 123, 2016, pp. 516-526.

41. Chen, Y.; Liu, P.; and Yu, Z., “Effects of Environmental Factors on Concrete Carbonation Depth and Compressive Strength,” *Materials*, V. 11, 2018, p. 2167.

42. Mohammed, T. U., and Masud, M. M. U., “Effects of Aggregate and Cement Types on Carbonation of Concrete: Accelerated Carbonation Test,” *3rd ACF Symposium on Assessment and Intervention of Existing Structures*, Sapporo, Japan, 2019.

43. Mohammed, T. U.; Bin Harun, M. Z.; and Joy, J. A., “Effect of Sand-To-Aggregate Volume Ratio on Durability of Concrete,” *Innovative Infrastructure Solutions*, V. 7, 2022, p. 318.

44. ASTM C642-21, “Standard Test Method for Density, Absorption, and Voids in Hardened Concrete,” ASTM International, West Conshohocken, PA, 2021.

45. Uddin, M. A.; Jameel, M.; and Sobuz, H. R., “Experimental Study on Strength Gaining Characteristics of Concrete Using Portland Composite Cement,” *KSCE Journal of Civil Engineering*, V. 17, 2013, pp. 789-796.

46. Trtnik, G.; Kavčič, F.; and Turk, G., “Prediction of Concrete Strength Using Ultrasonic Pulse Velocity and Artificial Neural Networks,” *Ultrasonics*, V. 49, 2009, pp. 53-60.

47. Mohammed, T. U.; Mahmood, A. H.; and Zunaied-Bin-Harun, M., “Destructive and Non-Destructive Evaluation of Concrete for Optimum Sand to Aggregate Volume Ratio,” *Frontiers of Structural and Civil Engineering*, V. 15, 2021, pp. 1400-1414.

48. Juenger, M. C. G., and Jennings, H. M., “Effects of High Alkalinity on Cement Pastes,” *ACI Materials Journal*, V. 98, No. 3, May-June 2001, pp. 251-255.

49. Zega, C. J., and Di Maio, Á. A., “Use of Recycled Fine Aggregate in Concretes with Durable Requirements,” *Waste Management*, V. 31, 2011, pp. 2336-2340.

50. Evangelista, L., and De Brito, J., “Mechanical Behaviour of Concrete Made with Fine Recycled Concrete Aggregates,” *Cement and Concrete Composites*, V. 29, 2007, pp. 397-401.

51. Fardoun, H.; Saliba, J.; and Coureau, J.-L., “Long-Term Deformations and Mechanical Properties of Fine Recycled Aggregate Earth Concrete,” *Applied Sciences*, V. 12, 2022, p. 11489.

52. Chen, J. J.; Li, B. H.; and Ng, P. L., “Adding Granite Polishing Waste to Reduce Sand and Cement Contents and Improve Performance of Mortar,” *Journal of Cleaner Production*, V. 279, 2021, p. 123653.

53. Yeau, K. Y., and Kim, E. K., “An Experimental Study on Corrosion Resistance of Concrete with Ground Granulate Blast-Furnace Slag,” *Cement and Concrete Research*, V. 35, 2005, pp. 1391-1399.

54. Shah, V., and Bishnoi, S., “Carbonation Resistance of Cements Containing Supplementary Cementitious Materials and its Relation to Various Parameters of Concrete,” *Construction and Building Materials*, V. 178, 2018, pp. 219-232.

NOTES:

ACI MATERIALS JOURNAL TECHNICAL PAPER

Title No. 122-M35

Thermodynamic Modeling of Chemical Acidification of Cementitious Paste

by Feyza Nur Sahan, W. Jason Weiss, and O. Burkan Isgor

The role of limestone (LS) powder replacement and changes in calcium-silicate-hydrate (C-S-H) due to pozzolanic reactions on the acid resistance of cementitious pastes are studied using thermodynamic modeling. Simulations are performed under equilibrium conditions, while hydration products are exposed to increasing levels of sulfuric acid. LS replacement does not show sacrificial characteristics against sulfuric acid attack, and LS acidification starts only after full consumption of portlandite and most C-S-H. Increased LS replacement causes the dilution of the formed portlandite and C-S-H volumes, which results in their full consumption at lower acid concentrations than mixtures without LS replacement. Pozzolanic reactions of supplementary cementitious materials (SCMs) result in C-S-H phases with lower Ca/Si than their ordinary portland cement (OPC) counterparts, increasing acid resistance. However, highly reactive and/or high-volume SCM replacements might further decrease the available portlandite, reducing the buffer acid resistance capacity. This issue is particularly critical for portland-limestone cement (PLC)-based systems.

Keywords: acid attack; calcium-silicate-hydrate (C-S-H); limestone (LS); portland-limestone cement (PLC); supplementary cementitious materials (SCMs); thermodynamic modeling.

INTRODUCTION

Acid resistance of concrete is critical for wastewater transmission and treatment facilities. The construction industry has been moving toward using ASTM C595 Type IL cement (that is, portland-limestone cement [PLC]) across the United States, and there is a significant drive to reduce the clinker content of concrete using supplementary cementitious materials (SCMs) to reduce the carbon footprint of concrete.[1,2] However, it is not clear how clinker reduction will affect acid resistance. Few studies have examined the impact of replacing clinker with limestone (LS) on the acid resistance of cement paste,[3-11] and the literature shows contradictory findings. Senhadji et al.[4] examined the acid resistance of mortars by replacing 5, 10, and 15% by mass of the clinker with LS and showed a lower mass loss for mortars with a higher LS replacement level. The improvement in acid resistance with LS replacement was attributed to reduced permeability and porosity; consumption of calcium carbonate ($CaCO_3$) as a sacrificial material; reduced calcium hydroxide (portlandite, $Ca(OH)_2$, or CH) content, which is considered to be more susceptible to acidification; and the possible role of LS as a filler material that can affect the transport properties of the system.[5,6] Furthermore, the mixtures with LS aggregates showed a greater resistance to sulfuric acid; Chang et al.[5] attributed this to the LS aggregates acting as a sacrificial material to neutralize the acid and decrease the acid degradation of the paste. Supporting this hypothesis, Fernandes et al.[7] showed through a microscopic study the formation of gypsum crystals along the interface of the LS aggregate and paste, indicating that acid attacks both the cement paste (likely the portlandite-rich region of the paste) and LS aggregate. In addition, finer LS fillers showed greater resistance to sulfuric acid attack, presumably due to the increased surface area of the LS, which resulted in a more rapid neutralization of the acid.[8]

Siad et al.[9] reported contradictory results while studying acid resistance of self-consolidating concrete with mixtures containing LS, natural pozzolan, and fly ash. They reported that the mixtures containing LS filler had the greatest mass loss and significant visual deterioration after 12 weeks of immersion, which the authors correlated to higher neutralization capacity of LS and increased kinetics of the reaction with sulfuric acid due to fineness of LS in the study. House[10] reported that while the use of LS coarse aggregate increased concrete resistance to sulfuric acid attack, replacing a portion of cement with finely ground LS did not have positive effects on concrete resistance to sulfuric acid. The lower acid consumption with ground LS replacement was interpreted as lower neutralization capacity of LS than the cementitious material, even though the mass loss was less with LS replacement. Liu and Wang[11] suggested that when cement is replaced with LS filler, the sulfuric acid is more readily available to react with portlandite, reducing acid resistance. These contradictory results indicate a need for a systematic investigation of the role of LS in the acid resistance of cementitious pastes.

Furthermore, studies examined the influence of pozzolanic reactions on sulfuric acid resistance.[12-15] Pozzolanic reactions consume portlandite. Further, the calcium-silicate-hydrate (C-S-H) produced by pozzolanic reactions of SCMs has a lower calcium-silicate ratio (Ca/Si) than C-S-H produced by ordinary portland cement (OPC) hydration. The properties of C-S-H with different Ca/Si were investigated by several researchers.[16-19] Kunther et al.[18] reported that the compressive strengths improved with decreasing Ca/Si when four different Ca/Si (0.83, 1.0, 1.25, and 1.50) were tested. Another study examining the micro/nanostructure of C-S-H[16] reported that with the increase in Ca/Si (0.83, 1.0,

---

ACI Materials Journal, V. 122, No. 5, September 2025.
MS No. M-2024-335.R1, doi: 10.14359/51749035, received May 28, 2025, and reviewed under Institute publication policies. Pertinent discussion including author's closure, if any, will be published ten months from this journal's date if the discussion is received within four months of the paper's print publication.

Table 1—Oxide composition of OPC, LS, and SF

	Eq. Na_2O^*, %	MgO, %	SO_3, %	CaO, %	SiO_2, %	Fe_2O_3, %	Al_2O_3, %	LOI	SG	DOR*†
OPC	0.57	3.80	2.80	62.00	19.90	3.20	4.60	0.96	3.15	—
LS	0.11	0.47	0.05	55.62	1.83	0.05	0.09	41.68	2.70	—
SF	0.48	0.26	0.15	0.70	95.88	0.12	0.69	4.30	2.20	76%
GS	—	—	—	—	>99.00	—	—	—	2.65	0%

*Eq. $Na_2O = Na_2O + 0.658\ K_2O$.

†Maximum degree of reactivity as per pozzolanic reactivity test.[28]

Note: LOI is loss on ignition; SG is specific gravity.

and 1.50), there was a decrease in the degree of polymerization, resulting in more discrete silica chains. Alizadeh et al.[19] suggested that adsorbed and interlayer water contribute significantly to the dynamic mechanical properties of C-S-H. Wanna et al.[14] examined the effect of low- and high-CaO fly ash on the sulfuric acid resistance and found that the addition of fly ash improved the acid resistance of cement pastes by promoting pozzolanic reactions that consume portlandite and produce C-S-H, which is more resistant to acid attack, in addition to the role of the reaction products in refining pore size and pore connectivity. Low-CaO fly ash was more effective in improving the sulfuric acid resistance of cement pastes than the high-CaO fly ash. Bassuoni and Nehdi[15] investigated the acid resistance of self-consolidating concrete mixtures to sulfuric acid attack. The testing was conducted in two 6-week-long phases: Phase I, with the initial pH (0.9) of the solution controlled at a maximum threshold value of 2.5; and Phase II, with the refreshment of the solution with pH (0.9) controlled at a maximum threshold value of 1.0. They reported that the decalcification of C-S-H became the governing factor for mass loss in Phase II. The authors reported that the decalcification of C-S-H with a high Ca/Si resulted in a surface that is susceptible to direct acid attack. Conversely, the decomposition of C-S-H with a lower Ca/Si generated a protective zone, effectively restricting acid diffusion into the cementitious matrix. This protective mechanism consequently diminished mass loss in specimens derived from blended-binder mixtures. These limited studies indicate a need to study the role of pozzolanic reactions, C-S-H type, and Ca/Si on the acid resistance of cementitious pastes.

The main objective of this study is to systematically investigate the role of LS replacement and Ca/Si of the C-S-H (that is, different types of C-S-H) on the acid resistance of cementitious pastes using thermodynamic modeling. This study aims to simulate chemical acidification of paste samples with varying LS, ground silica (GS), and silica fume (SF) contents using thermodynamic calculations where the concentration of sulfuric acid is gradually increased. It should be noted that unreacted clinker phases were excluded by considering 100% degree of hydration (DOH) for the systems, which simply reduces the extent of unreacted cement (which is highly acid-resistant). The water-cementitious materials ratio (*w*/*cm*) was considered higher than in realistic conditions to enable the availability of pore solution and surrounding solution for the reactions. This assumption allowed the authors to study the role of LS replacement and Ca/Si of the C-S-H at the thermodynamic level, without the complication of unhydrated cement phases or ionic transport.

RESEARCH SIGNIFICANCE

The acid resistance of concrete is important for septic tanks, sewer pipes and risers, and water treatment facilities. Experimental tests can be time-consuming, and it is often difficult to isolate the influence of specific changes in a mixture. This study uses computational models to assess the resistance of the unreacted and reacted phases to acid exposure. The results provide a clear indication of the phases that are most susceptible to damage and the reaction products that form for a given level of acid reaction. This approach can enable the design of binder systems that are more resistant to acid attack.

THERMODYNAMIC MODELING

In this study, thermodynamic simulations were performed using the open-source GEMS3K code[20,21] combined with the default PSI/Nagra Chemical Thermodynamic Database and the Cemdata v18.1 thermodynamic database.[22] GEMS3K uses Gibbs free energy minimization to predict the output phase assemblage of a cementitious system in equilibrium. Following the well-established practice,[22,23] the CSHQ model was used to model OPC and OPC + pozzolanic SCM systems. The CSHQ model can predict the changes in four different C-S-H types: jennite D (JenD) with a Ca/Si of 2.25, jennite H (JenH) with a Ca/Si of 1.33, tobermorite D (TobD) with a Ca/Si of 1.25, and tobermorite H (TobH) with a Ca/Si of 0.67. Based on empirical evidence from the literature, the formation of carbonate-ettringite,[24,25] hydrotalcite,[26] hydrogarnet,[26] and thaumasite[27] was blocked in the GEMS-CEMDATA framework because these phases are not observed to form in substantial quantities in cementitious systems at 25°C—the temperature at which the simulations were conducted.

Thermodynamic calculations were performed for systems at 100% DOH for cement and complete pozzolanic reaction for the reactive phases of the SCM, which was chosen as SF in this study. Table 1 provides the chemical composition of the materials used in the simulations (that is, OPC, LS, SF, and GS) and the degree of reactivity (DOR* as per the pozzolanic reactivity test[28]) of SF, which represents the portion of the SCM that is pozzolanically reactive. Note that OPC does not contain any LS, so the effect of LS replacement can be compared to a control case with no LS. All LS is assumed to be available for reaction. In all simulated mixtures, the *w*/*cm* was 0.70 to ensure the high DOR of the simulated cementitious systems and for sufficient pore solution for acidification.

The first set of thermodynamic simulations investigated the effect of LS replacement. Four mixtures were studied with 0, 5, 10, 15, and 25% (mass) LS replacement, labeled as OPC, 5LS, 10LS, 15LS, and 25LS, respectively. To investigate the dilution effect of LS replacement on the hydration products, the 5, 10, 15, and 25% (mass) nonreactive GS replacements were considered and labeled as 5GS, 10GS, 15GS, and 25GS, respectively. Finally, the effect of C-S-H type (and Ca/Si) was studied by incorporating 15% (mass) SF—this mixture was labeled 15SF. The authors acknowledge that this level of SF replacement is higher than the standard industry designs, which are typically 5 and 9%, but the goal of this simulation was to provide comparative pozzolanic reaction data with the same dilution level to 15% LS replacement. Chemical acidification in the simulations was achieved by incrementally adding H_2SO_4 to the hydrated cementitious systems at 100% DOH. The changes of the hydrated solid-phase volumes, the Ca/Si of C-S-H, and the pH of the system at equilibrium were recorded with H_2SO_4 addition for each simulation. Unhydrated phases were excluded in the sulfuric acid attack simulations to develop a clear understanding of the acid resistance of the hydrated phases.

RESULTS AND DISCUSSION

Effect of LS

Figures 1 and 2 show the results of the thermodynamic calculations in the form of volumetric distribution of phases with increasing sulfuric acid addition for OPC and OPC + LS systems, respectively. It should be noted that this modeling was conducted for 100% DOH. The cementitious system hydration phase volume was 100%; the additional phase volume represents the unreacted volume of H_2SO_4. Realistically, there would be unreacted cementitious phases in the system, which might also react with sulfuric acid.

As shown in Fig. 1, for the 100% OPC mixture, monosulfate depleted first with sulfuric acid addition, producing ettringite, which remained in the system until all portlandite and most C-S-H were consumed. During this time, the pH dropped below 10.7. The degradation of ettringite occurred below 10.7, as reported by Gabrisová et al.,[29] who studied ettringite stability in aqueous solutions. As also expected from the literature,[30-32] portlandite was shown to be highly susceptible to sulfuric acid attack even at low acid concentrations. For the 100% OPC system, C-S-H consumption began with H_2SO_4 addition after monosulfate and portlandite were consumed completely. The reaction of C-S-H phases started with high Ca/Si C-S-H (JenD then JenH), followed by low Ca/Si C-S-H (TobD then TobH), decreasing the overall Ca/Si of C-S-H in the system with increasing acidification. Ettringite, portlandite, and C-S-H converted to gypsum with increasing acidification. When the last form of C-S-H with the lowest Ca/Si (that is, TobH with a Ca/Si of 0.67) was consumed by the acid, quartz was formed with the released Si in the system. It is noted that the pH of the system had no obvious change during the portlandite consumption due to the neutralization of the sulfuric acid. The pH started to decrease at a slow rate, from ~13 to ~10, after portlandite depletion while C-S-H was being consumed. When there was no hydration product left to neutralize the sulfuric acid in the system, a rapid decrease in the pH was observed.

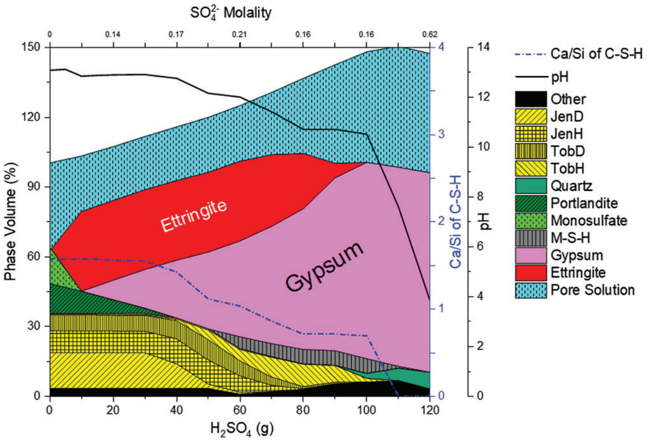

Fig. 1—Phase assemblage of OPC system reacting with H_2SO_4. (Phase volume beyond 100% reflects volume change due to addition of H_2SO_4. Chemical shrinkage is not shown in plot for clarity, but this accounts for why phase volume starts at less than 100%.)

Figure 2 shows that LS replacement causes lower volumes of hydrated phase (for example, portlandite, C-S-H, and so on) formation before acidification, due primarily to dilution. Unlike the OPC mixture, OPC + LS mixtures contained monocarbonate phases instead of monosulfate phases. These monocarbonate phases were the first to acidify to produce ettringite, which remained in the system until all portlandite and most C-S-H were consumed. Other than this difference, 100% OPC and OPC + LS systems showed similar trends under chemical acidification with sulfuric acid. However, a negative effect of increased LS replacement is the dilution of the formed portlandite and C-S-H volumes, which results in their full consumption at lower H_2SO_4 concentrations, as shown in Fig. 2(a) to (d), with progressive increase of LS from 5 to 25%. For example, the mixture with OPC + 15% LS replacement (representing PLC) showed complete portlandite and C-S-H depletion at 25% and 45% lower sulfuric acid concentrations than the 100% OPC mixture, respectively. Note that the OPC used in this study did not contain any LS, and commercial OPC would typically contain up to 5% LS. When this comparison is done with respect to the OPC + 5% LS mixture (Fig. 2(a)), which represents typical commercial OPC, the mixture with OPC + 15% LS replacement (Fig. 2(c)), representing PLC, showed complete portlandite and C-S-H depletion at 20% and 25% lower sulfuric acid concentrations, respectively. Figure 2 also shows that LS (at any replacement level) does not show sacrificial characteristics against sulfuric acid addition. In fact, LS acidification does not start until all portlandite and most C-S-H phases (JenD, JenH, and TobD) are consumed. This observation is supported by an earlier experimental work by Sahan et al.[33] on the acidification of mixed pure phases, which showed when LS was still present after portlandite depletion while other phases were being consumed.

The pH of the pore solution influences the formation of other hydration products in the presence of magnesium oxide

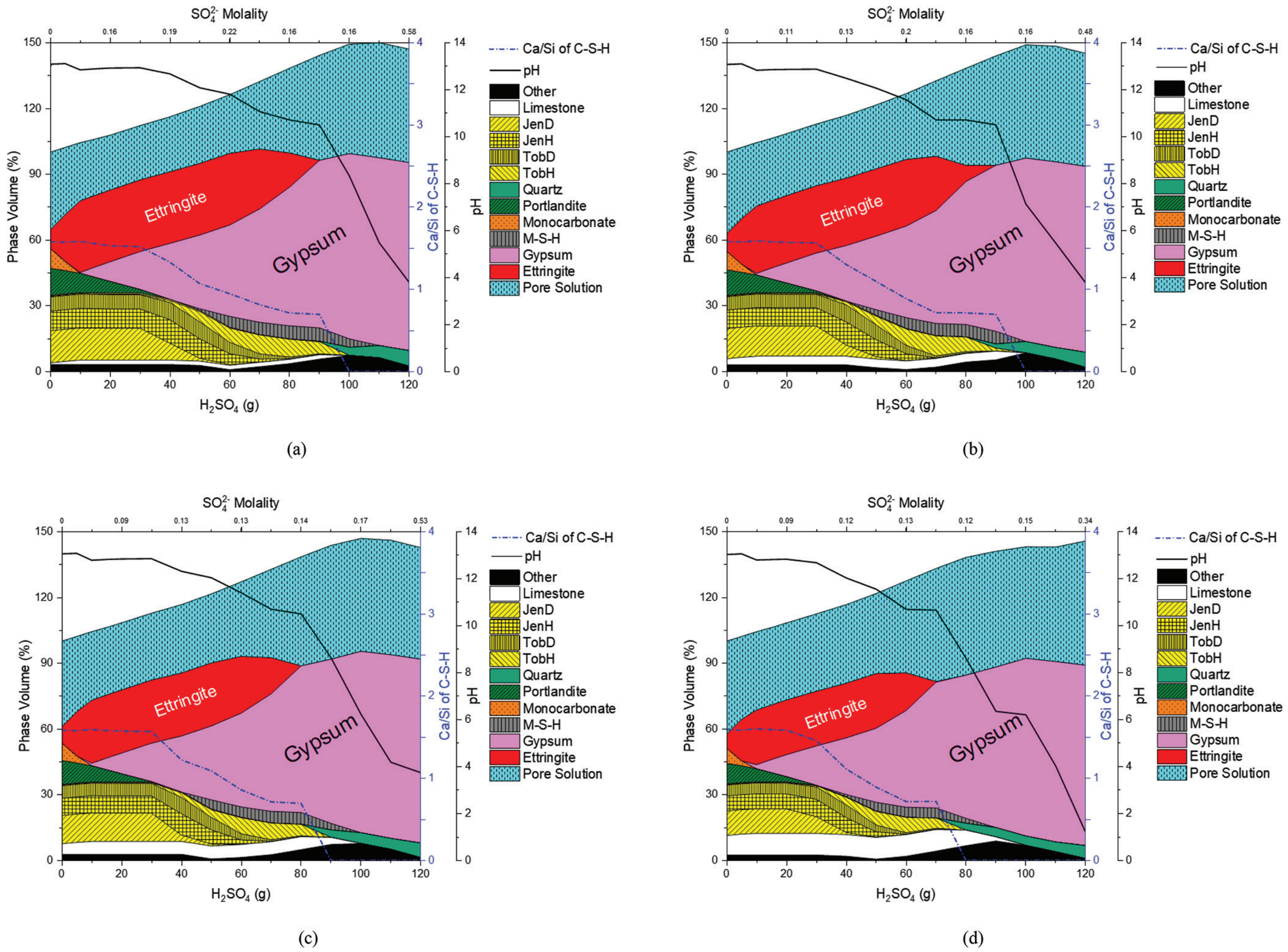

(a)

(b)

(c)

(d)

Fig. 2—Phase assemblage of OPC + LS systems reacting with H_2SO_4: (a) 5LS; (b) 10LS; (c) 15LS; and (d) 25LS. (Phase volume beyond 100% reflects volume change due to addition of H_2SO_4. Chemical shrinkage is not shown in plot for clarity, but this accounts for why phase volume starts at less than 100%.)

(MgO). It is reported in the literature that if the pH exceeds 10.5, brucite will be the primary reaction product.[34] When the pH decreases below 10.5, the progressive formation of magnesium-silicate-hydrate (M-S-H) gel occurs.[34] The formation of M-S-H gels in thermodynamic simulations was attributed to decomposition of brucite at lower pH and an available Si source due to decomposition of C-S-H. With the decomposition of M-S-H, the excess Si source forms quartz.

The changes in portlandite, monosulfate, and monocarbonate phases are clearly shown in Fig. 3 for the OPC and 25LS systems. Although portlandite is traditionally considered to be the most susceptible hydration product to acid attack, the consumption rate of monosulfate and monocarbonate phases is more likely to be higher with the initial sulfuric acid exposure. As the amount of reacted sulfuric acid increases, the phase volume percentage of monosulfate and monocarbonate decreases steadily. The portlandite decreases as the amount of reacted sulfuric acid increases, but at a less rapid rate than monosulfate for both cases.

The observations in Fig. 2 reflect the influence of LS replacement on the acid resistance of OPC pastes; however, they contain both the chemical effects and the effects due to the dilution of the OPC with the LS replacement. To isolate the dilution effect, additional simulations were performed with nonreactive GS replacement at corresponding LS mass replacement levels—that is, 5, 10, 15, and 25%. Figures 4(a), (b), (c), and (d) represent the changes in phase volume (%) as a function of H_2SO_4 addition for 5GS, 10GS, 15GS, and 25GS, respectively. As expected, the reduced hydration phases due to reduced cement hydration with unreactive GS replacement caused these phases to be consumed more readily than the OPC mixture, as shown in Fig. 4. As shown in Fig. 4, with the increase of GS from 5 to 25%, the required H_2SO_4 addition for the depletion of C-S-H decreased from approximately 100 to 80 grams of H_2SO_4. While LS reacted with the H_2SO_4 after C-S-H depletion for the OPC + LS mixtures, unreactive GS did not react in the acidic environment. The further increase in H_2SO_4 caused the conversion of gypsum ($CaSO_4 \cdot 2H_2O$) to anhydrite ($CaSO_4$) and a further decrease in pH. These results confirm earlier simulations on the effect of LS that until the complete consumption of portlandite and C-S-H, LS acts as an inert filler under chemical acidification, similar to inert GS. However, after the consumption of all portlandite and C-S-H, LS provides additional acid resistance and delays the sharp pH decrease to levels below 2.

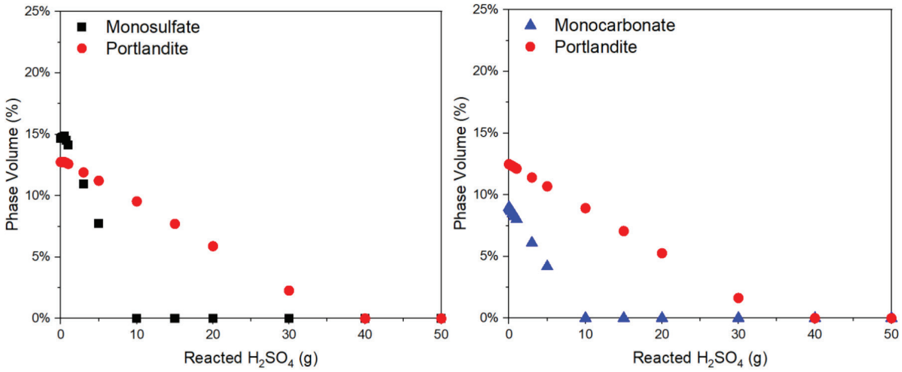

(a) (b)

Fig. 3—Comparison of reaction with sulfuric acid for: (a) monosulfate versus portlandite for OPC system; and (b) monocarbonate versus portlandite for OPC + 25LS system.

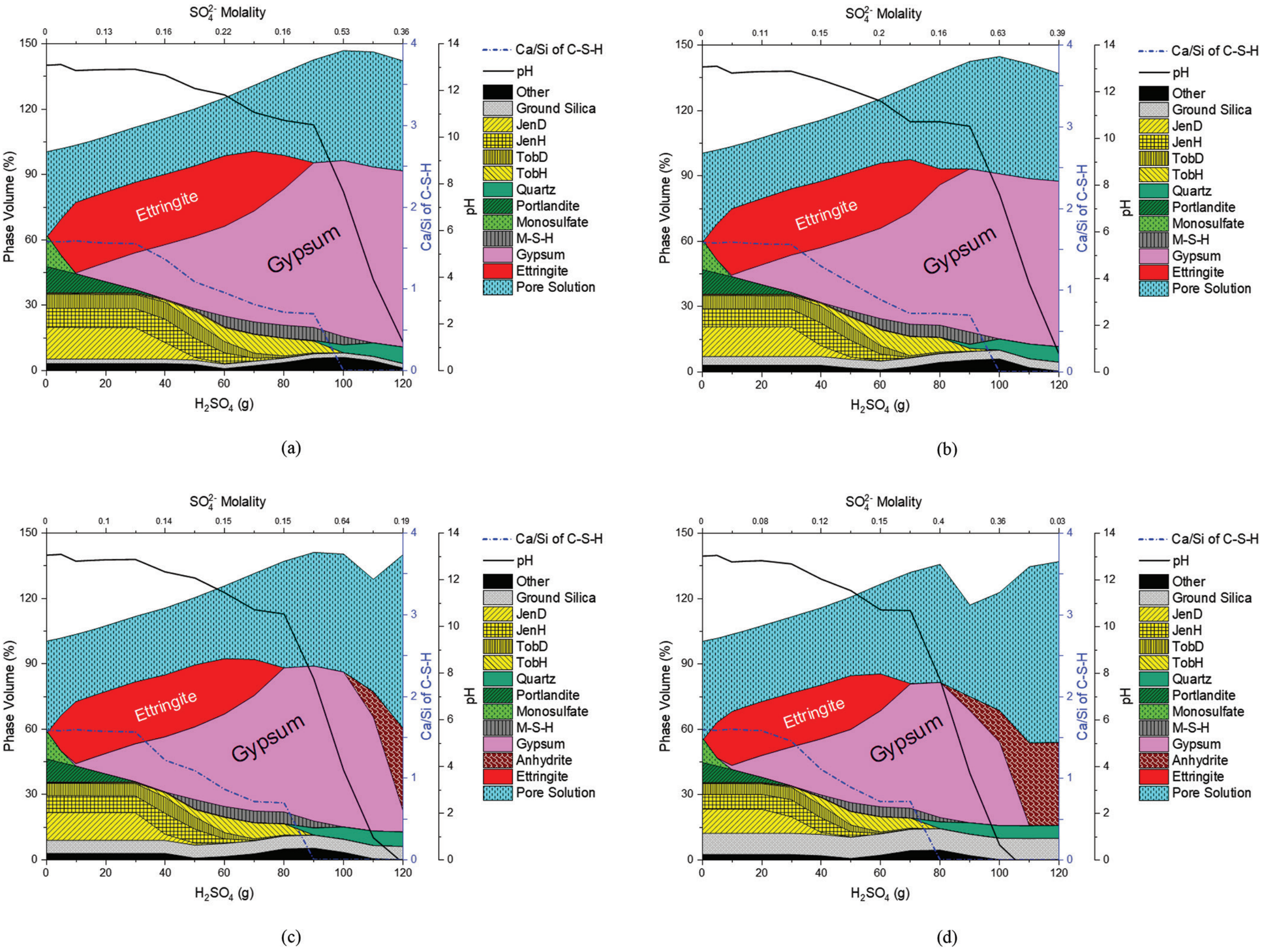

Fig. 4—Phase assemblage of OPC + GS systems reacting with H_2SO_4: (a) 5GS; (b) 10GS; (c) 15GS; and (d) 25GS. (Phase volume beyond 100% reflects volume change due to addition of H_2SO_4. Chemical shrinkage is not shown in plot for clarity, but this accounts for why phase volume starts at less than 100%.)

Effect of C-S-H type

Figure 5 shows the results of the thermodynamic calculations in the form of volumetric distribution of phases with increasing sulfuric acid addition for the OPC + SF system. All simulations (OPC in Fig. 1, OPC + LS in Fig. 2, and OPC + GS in Fig. 4) show that portlandite is highly susceptible to acid attack, as also reported in the literature,[30-32] and decalcification of C-S-H does not occur until the portlandite in the system is mostly consumed.

Figure 5 shows that the pozzolanic reactions consumed all the portlandite in the system. When portlandite is not present in the 15SF system, the initial acid attack promotes the consumption of monosulfate and C-S-H phases. It is shown that the decalcification of C-S-H with acid attack begins with high Ca/Si C-S-H type. The JenD type (high Ca/Si) was followed successively by the lower Ca/Si types, and eventually all converted to the TobH type (the lowest Ca/Si type) with increasing acid volume. Finally, the TobH reacted with sulfuric acid and formed gypsum and quartz by following Eq. (1)

$$CaO_x(SiO_2)_y \cdot H_2O_z + {}_xH_2SO_4 \leftrightarrow {}_xC\overline{S}H2 + {}_ySiO_2 + (z-x)H_2O \qquad (1)$$

The main phases identified in conventional cement paste, following sulfuric acid attack, are gypsum and amorphous silica gels, rather than ettringite.[35]

It is established in the literature that C-S-H generally remains stable at high pH until the pH is reduced to a value of 8.8.[36,37] In the absence of portlandite, the decalcification process of C-S-H starts as soon as acid is introduced and continues until only amorphous silica gel remains. Although the present work only focuses on the chemical aspect of acidification, previous work by Bassuoni and Nehdi[15] and Gu et al.[35] proposed that during sulfuric acid exposure, the decalcification of C-S-H results in the formation of a protective layer composed of silica and aluminosilicate gels. This layer effectively protects the undegraded cement paste from further degradation.

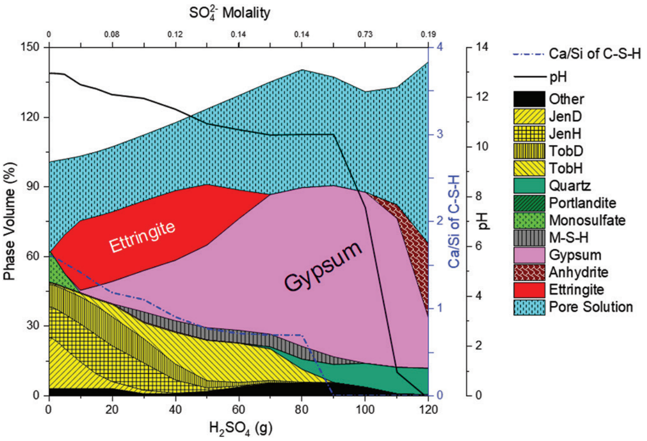

Fig. 5—Phase assemblage of OPC + SF system reacting with H_2SO_4. (Phase volume beyond 100% reflects volume change due to addition of H_2SO_4. Chemical shrinkage is not shown in plot for clarity, but this accounts for why phase volume starts at less than 100%.)

Figures 6(a) and (b) demonstrate the phase volume conversions of different C-S-H types with varying H_2SO_4 amount for the OPC and 15SF mixture, respectively. Figure 6(a) shows a delayed consumption of C-S-H due to consumption of other phases for the OPC system, while the consumption of C-S-H and the decrease in Ca/Si began immediately with H_2SO_4 addition. The comparison of OPC and 15SF systems in Fig. 6 shows an increase in the phase volume of C-S-H due to pozzolanic reaction, which resulted in greater acid consumption by C-S-H in the 15SF system compared to OPC. The degradation of C-S-H began initially with the JenD type, which has a high Ca/Si and deteriorates compared to other types, which were deteriorating and forming from the decalcified material. The temporary increase observed in JenH and TobD types suggests a gradual conversion of C-S-H. TobH is the final product consumed during the acid attack. This study used a CSHQ model incorporating four types of C-S-H with varying Ca/Si, noting the possibility of observing C-S-H structures with different average Ca/Si compositions during the attack.

Figure 7 compares the Ca/Si of the C-S-H in the system for the different mixtures. Figure 7(a) compares OPC with 15% replacement systems, while Fig. 7(b) compares OPC with 25% replacement systems. As can be seen in Fig. 7(a), the decomposition of C-S-H was delayed for the OPC mixture due to the availability of other hydration products, such as portlandite and monosulfate. The LS and GS mixtures followed a nearly identical trend based on the replacement percentages; the higher replacement percentage enabled the decomposition of C-S-H at lower $H_2SO_4(g)$ addition due to dilution of other reaction products. While other hydration products were not available for reaction with sulfuric acid, the decomposition of C-S-H was promoted at lower concentration with the sulfuric acid addition for the 15SF mixture. As can be seen in Fig. 7(a) and (b), the Ca/Si of C-S-H for 25LS and 25GS showed a decrease in Ca/Si at lower H_2SO_4 addition compared to 15LS and 15GS. Besides, the C-S-H was depleted at lower H_2SO_4 addition for 25% replacement systems due to the reduced amount of C-S-H. Although C-S-H was being consumed at a higher rate for 15SF, the higher amount of C-S-H due to pozzolanic reaction led to later depletion compared to 25LS and 25GS mixtures. This provides insight into how the presence of different substitute

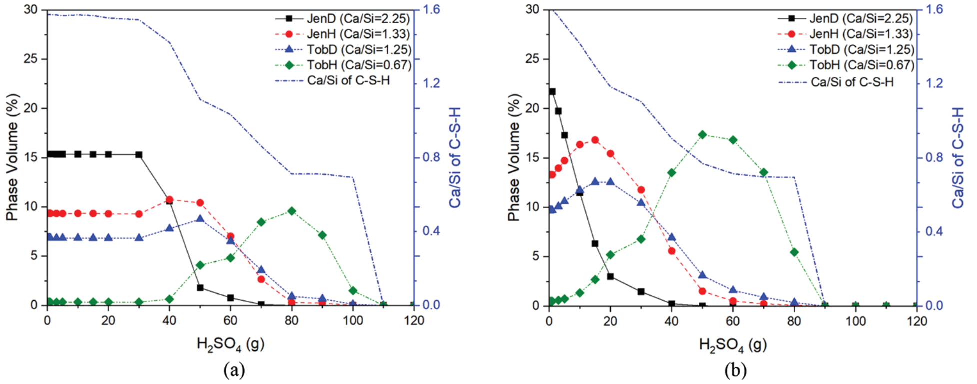

(a)

(b)

Fig. 6—Phase volume alteration of C-S-H types with exposure to H_2SO_4 for: (a) OPC system; and (b) 15SF system.

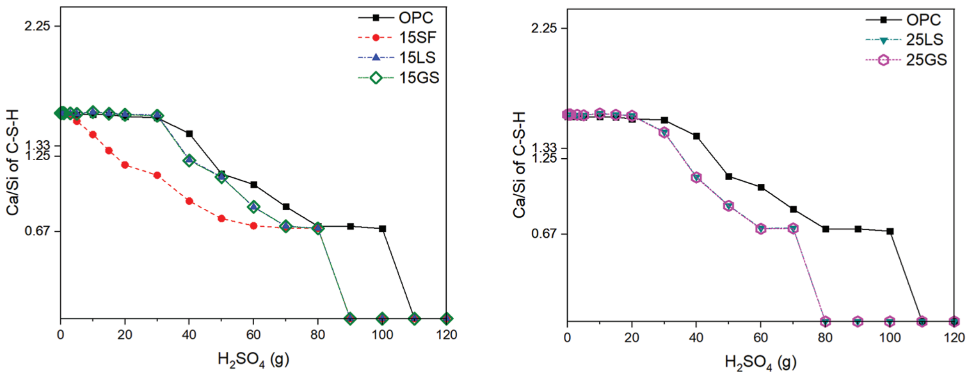

(a)

(b)

Fig. 7—Comparison of average Ca/Si of C-S-H for: (a) OPC and 15% replacement systems exposed to H_2SO_4; and (b) OPC and 25% replacement systems exposed to H_2SO_4.

materials and proportions influences C-S-H's stability and decomposition in the presence of sulfuric acid. The Ca/Si appears to play an important role in the reaction with sulfuric acid.[38] The incorporation of SCMs decreases portlandite in the system with pozzolanic reaction and promotes the formation of C-S-H; however, this also promotes the formation of C-S-H with a lower Ca/Si, which appears more stable when exposed to acid.

Thermodynamic simulations presented in this paper focus on the chemical equilibrium of the phases under increased levels of acidification and do not consider the impact of transport properties. This is one area where the pozzolanic reactions may have additional benefits that are not captured here. Furthermore, the change in pore structure due to acidification reactions plays a significant role in transport properties, which affects the degradation rate.

CONCLUSIONS

This study systematically investigated the influence of limestone (LS) as a replacement of cement in terms of the acid resistance of cementitious pastes. In addition, silica fume (SF) was used to assess the influence of the calcium-silicate ratio (Ca/Si) of the calcium-silicate-hydrate (C-S-H) (that is, different types of C-S-H) on acid resistance. The primary conclusions are based on 100% degree of hydration (DOH) and include:

- LS replacement as a filler material did not show sacrificial characteristics to sulfuric acid attack, contrary to many discussions in the literature. In fact, LS acidification did not start until all portlandite and most C-S-H phases (JenD, JenH, and TobD) were consumed.
- Increased LS replacement caused the dilution of portlandite and C-S-H volumes, which resulted in their complete consumption at lower H_2SO_4 concentrations than mixtures without LS replacement. For example, the mixture with 15% LS replacement (representing a portland-limestone cement [PLC] mixture) showed complete portlandite and C-S-H depletion at 20% and 25% lower sulfuric acid concentrations than corresponding ordinary portland cement (OPC) mixtures, respectively.
- Although portlandite is traditionally considered to be the most susceptible hydration product to acid attack, the consumption rates of monosulfate and monocarbonate phases were higher with sulfuric acid exposure.
- The acidification of C-S-H phases started with high Ca/Si C-S-H (JenD then JenH), followed by low Ca/Si C-S-H (TobD then TobH), decreasing the overall Ca/Si of C-S-H in the system with increasing acidification.
- Pozzolanic reactions resulted in C-S-H phases with lower Ca/Si than the OPC-only counterparts, increasing acid resistance. The level of pozzolanic reaction depends on the reactivity of the pozzolan and the volume of the pozzolan used. However, if pozzolanic reactions consume all portlandite in the mixtures, the buffer acid resistance capacity of the mixtures might decrease. This issue is particularly critical for PLC systems, for which additional LS further dilutes the available portlandite (by approximately 13% for 15% LS mass replacement) and C-S-H in the mixture before acidification.
- Further experimental and/or modeling research is needed to explore the role of changes in transport properties of the hardened systems due to pozzolanic reactions and chemical acidification, particularly for typical degrees of hydration and pozzolanic reactions of PLC-based systems.

AUTHOR BIOS

ACI member **Feyza Nur Sahan** *is a PhD Student at Oregon State University, Corvallis, OR. She received her BS from Özyeğin University, Istanbul, Turkey, and her MS from Oregon State University. Her research interests include microbially induced corrosion of concrete, acid attack, and service life modeling.*

W. Jason Weiss, *FACI, is the Miles Lowell and Margaret Watt Edwards Distinguished Chair in Engineering in the School of Civil and Construction Engineering at Oregon State University. He is the former Editor-in-Chief of the* ACI Materials Journal *and is a member of the ACI Technical Activities Committee.*

O. Burkan Isgor, *FACI, is the Eric H.I. and Janice Hoffman Professor in Civil and Construction Engineering at Oregon State University. He is past Chair and a current member of ACI Committee 222, Corrosion of Metals in Concrete, and a member of ACI Committees 236, Material Science of Concrete, and 365, Service Life Prediction. His research interests include corrosion of steel in concrete, service life modeling of concrete, and thermodynamic modeling of cementitious systems.*

ACKNOWLEDGMENTS

The authors acknowledge the financial support of the University Transportation Center for Durable and Resilient Transportation Infrastructure (DuRe-Transp) for a portion of this work.

REFERENCES

1. Tennis, P. D.; Thomas, M. D. A.; and Weiss, W. J., "State-of-the-Art Report on Use of Limestone in Cements at Levels of up to 15%," PCA R&D SN3148, American Cement Association, Skokie, IL, 2011, 78 pp.

2. Rahla, K. M.; Mateus, R.; and Bragança, L., "Comparative Sustainability Assessment of Binary Blended Concretes Using Supplementary Cementitious Materials (SCMs) and Ordinary Portland Cement (OPC)," *Journal of Cleaner Production*, V. 220, May 2019, pp. 445-459. doi: 10.1016/j.jclepro.2019.02.010

3. Ghrici, M.; Kenai, S.; and Said-Mansour, M., "Mechanical Properties and Durability of Mortar and Concrete Containing Natural Pozzolana and Limestone Blended Cements," *Cement and Concrete Composites*, V. 29, No. 7, Aug. 2007, pp. 542-549. doi: 10.1016/j.cemconcomp.2007.04.009

4. Senhadji, Y.; Escadeillas, G.; Mouli, M.; Khelafi, H.; and Benosman, "Influence of Natural Pozzolan, Silica Fume and Limestone Fine on Strength, Acid Resistance and Microstructure of Mortar," *Powder Technology*, V. 254, Mar. 2014, pp. 314-323. doi: 10.1016/j.powtec.2014.01.046

5. Chang, Z.-T.; Song, X.-J.; Munn, R.; and Marosszeky, M., "Using Limestone Aggregates and Different Cements for Enhancing Resistance of Concrete to Sulphuric Acid Attack," *Cement and Concrete Research*, V. 35, No. 8, Aug. 2005, pp. 1486-1494. doi: 10.1016/j.cemconres.2005.03.006

6. Ramaswamy, K. P., and Santhanam, M., "Influence of Mineralogical Nature of Aggregates on Acid Resistance of Mortar," *Sixth International Conference on Durability of Concrete Structures (ICDCS 2018)*, P. A. M. Basheer, ed., July 2018, Leeds, West Yorkshire, UK, pp. 256-266.

7. Fernandes, I.; Pericão, M.; Hagelia, P.; Noronha, F.; Ribeiro, M. A.; and Maia, J., "Identification of Acid Attack on Concrete of a Sewage System," *Materials and Structures*, V. 45, No. 3, Mar. 2012, pp. 337-350. doi: 10.1617/s11527-011-9769-y

8. Lertwattanaruk, P.; Sua-iam, G.; and Makul, N., "Effects of Calcium Carbonate Powder on the Fresh and Hardened Properties of Self-Consolidating Concrete Incorporating Untreated Rice Husk Ash," *Journal of Cleaner Production*, V. 172, Jan. 2018, pp. 3265-3278. doi: 10.1016/j.jclepro.2017.10.336

9. Siad, H.; Mesbah, H. A.; Kamali-Bernard, S.; Khelafi, H.; and Mouli, M., "Influence of Natural Pozzolan on the Behavior of Self-Compacting Concrete Under Sulphuric and Hydrochloric Acid Attacks, Comparative Study," *Arabian Journal for Science and Engineering*, V. 35, No. 1, 2010, pp. 183-195.

10. House, M. W., "Using Biological and Physico-Chemical Test Methods to Assess the Role of Concrete Mixture Design in Resistance to Microbially Induced Corrosion," MS thesis, Purdue University, West Lafayette, IN, 2013, 172 pp.

11. Liu, S., and Wang, Z., "Effect of Limestone Powder on Acid Attack Characteristics of Cement Pastes," *Materials Science*, V. 20, No. 4, 2014, pp. 503-508.

12. Ramezanianpour, A. A.; Zolfagharnasab, A.; Bahman Zadeh, F.; Estahbanati, S. H.; Boushehri, R.; Pourebrahimi, M. R.; and Ramezanianpour, A. M., "Effect of Supplementary Cementing Materials on Concrete Resistance Against Sulfuric Acid Attack," *High Tech Concrete: Where Technology and Engineering Meet - Proceedings of the 2017* fib *Symposium, held in Maastricht, The Netherlands, June 12-14, 2017*, D. A. Hordijk and M. Luković, eds., Springer, Cham, Switzerland, 2018, pp. 2290-2298.

13. Aydın, S.; Yazıcı, H.; Yiğiter, H.; and Baradan, B., "Sulfuric Acid Resistance of High-Volume Fly Ash Concrete," *Building and Environment*, V. 42, No. 2, Feb. 2007, pp. 717-721. doi: 10.1016/j.buildenv.2005.10.024

14. Wanna, S.; Toochinda, P.; Saengsoy, W.; and Tangtermsirikul, S., "Deterioration in Sulfuric Acid of Cement Pastes Incorporating High CaO and Low CaO Fly Ashes," *Engineering Journal*, V. 25, No. 2, 2021, pp. 71-83.

15. Bassuoni, M. T., and Nehdi, M. L., "Resistance of Self-Consolidating Concrete to Sulfuric Acid Attack with Consecutive pH Reduction," *Cement and Concrete Research*, V. 37, No. 7, July 2007, pp. 1070-1084. doi: 10.1016/j.cemconres.2007.04.014

16. Wang, Z.; Chen, Y.; Xu, L.; Zhu, Z.; Zhou, Y.; Pan, F.; and Wu, K., "Insight into the Local C-S-H Structure and Its Evolution Mechanism Controlled by Curing Regime and Ca/Si Ratio," *Construction and Building Materials*, V. 333, May 2022, Article No. 127388. doi: 10.1016/j.conbuildmat.2022.127388

17. Kunther, W.; Lothenbach, B.; and Skibsted, J., "Influence of the Ca/Si Ratio of the C–S–H Phase on the Interaction with Sulfate Ions and Its Impact on the Ettringite Crystallization Pressure," *Cement and Concrete Research*, V. 69, Mar. 2015, pp. 37-49. doi: 10.1016/j.cemconres.2014.12.002

18. Kunther, W.; Ferreiro, S.; and Skibsted, J., "Influence of the Ca/Si Ratio on the Compressive Strength of Cementitious Calcium-Silicate-Hydrate Binders," *Journal of Materials Chemistry A – Materials for Energy and Sustainability*, V. 5, No. 33, Sept. 2017, pp. 17401-17412. doi: 10.1039/C7TA06104H

19. Alizadeh, R.; Beaudoin, J. J.; and Raki, L., "Mechanical Properties of Calcium Silicate Hydrates," *Materials and Structures*, V. 44, No. 1, Jan. 2011, pp. 13-28. doi: 10.1617/s11527-010-9605-9

20. Kulik, D. A.; Wagner, T.; Dmytrieva, S. V.; Kosakowski, G.; Hingerl, F. F.; Chudnenko, K. V.; and Berner, U. R., "GEM-Selektor Geochemical Modeling Package: Revised Algorithm and GEMS3K Numerical Kernel for Coupled Simulation Codes," *Computational Geosciences*, V. 17, No. 1, Feb. 2013, pp. 1-24.

21. Wagner, T.; Kulik, D. A.; Hingerl, F. F.; and Dmytrieva, S. V., "GEM-Selektor Geochemical Modeling Package: TSolMod Library and Data Interface for Multicomponent Phase Models," *The Canadian Mineralogist*, V. 50, No. 5, Oct. 2012, pp. 1173-1195. doi: 10.3749/canmin.50.5.1173

22. Lothenbach, B.; Kulik, D. A.; Matschei, T.; Balonis, M.; Baquerizo, L.; Dilnesa, B.; Miron, G. D.; and Myers, R. J., "Cemdata18: A Chemical Thermodynamic Database for Hydrated Portland Cements and Alkali-Activated Materials," *Cement and Concrete Research*, V. 115, Jan. 2019, pp. 472-506. doi: 10.1016/j.cemconres.2018.04.018

23. Kulik, D. A., "Improving the Structural Consistency of C-S-H Solid Solution Thermodynamic Models," *Cement and Concrete Research*, V. 41, No. 5, May 2011, pp. 477-495. doi: 10.1016/j.cemconres.2011.01.012

24. Damidot, D.; Barnett, S. J.; Glasser, F. P.; and Macphee, D., "Investigation of the $CaO–Al_2O_3–SiO_2–CaSO_4–CaCO_3–H_2O$ System at 25°C by Thermodynamic Calculation," *Advances in Cement Research*, V. 16, No. 2, Apr. 2004, pp. 69-76. doi: 10.1680/adcr.2004.16.2.69

25. Matschei, T.; Lothenbach, B.; and Glasser, F. P., "Thermodynamic Properties of Portland Cement Hydrates in the System $CaO–Al_2O_3–SiO_2–CaSO_4–CaCO_3–H_2O$," *Cement and Concrete Research*, V. 37, No. 10, Oct. 2007, pp. 1379-1410. doi: 10.1016/j.cemconres.2007.06.002

26. Dilnesa, B. Z.; Lothenbach, B.; Renaudin, G.; Wichser, A.; and Kulik, D., "Synthesis and Characterization of Hydrogarnet $Ca_3(Al_xFe_{1-x})_2(SiO_4)_y(OH)_{4(3-y)}$," *Cement and Concrete Research*, V. 59, May 2014, pp. 96-111. doi: 10.1016/j.cemconres.2014.02.001

27. Schmidt, T.; Lothenbach, B.; Scrivener, K. L.; Romer, M.; Rentsch, D.; and Figi, R., "Conditions for Thaumasite Formation," *Proceedings of the 12th International Congress on the Chemistry of Cement (ICCC 2007)*, J. J. Beaudoin, J. M. Makar, and L. Raki, eds., Montréal, QC, Canada, July 2007, 12 pp.

28. Choudhary, A.; Bharadwaj, K.; Ghantous, R. M.; Isgor, O. B.; and Weiss, W. J., "Pozzolanic Reactivity Test of Supplementary Cementitious Materials," *ACI Materials Journal*, V. 119, No. 2, Mar. 2022, pp. 255-268.

29. Gabrisová, A.; Havlica, J.; and Sahu, S., "Stability of Calcium Sulphoaluminate Hydrates in Water Solutions with Various pH Values," *Cement and Concrete Research*, V. 21, No. 6, Nov. 1991, pp. 1023-1027. doi: 10.1016/0008-8846(91)90062-M

30. Allahverdi, A., and Škvára, F., "Acidic Corrosion of Hydrated Cement Based Materials: Part 2 – Kinetics of the Phenomenon and Mathematical Models," *Ceramics-Silikáty*, V. 44, No. 4, 2000, pp. 152-160.

31. Cizer, Ö.; Elsen, J.; Feys, D.; Heirman, G.; Vandewalle, L.; Van Gemert, D.; Desmet, B.; Vantomme, J.; and De Schutter, G., "Microstructural Changes in Self-Compacting Concrete by Sulphuric Acid Attack," *Proceedings of the 13th International Congress on the Chemistry of Cement (ICCC 2011)*, A. Palomo, ed., Madrid, Spain, July 2011, pp. 436-442.

32. Cao, R.; Yang, J.; Li, G.; Liu, F.; Niu, M.; and Wang, W., "Resistance of the Composite Cementitious System of Ordinary Portland/Calcium Sulfoaluminate Cement to Sulfuric Acid Attack," *Construction and Building Materials*, V. 329, Apr. 2022, Article No. 127171. doi: 10.1016/j.conbuildmat.2022.127171

33. Sahan, F. N.; Isgor, O. B.; and Weiss, W. J., "Acidification in Cement Paste in Which Clinker Is Partially Replaced with Limestone or Silica," *CEMENT*, V. 16, June 2024, Article No. 100103. doi: 10.1016/j.cement.2024.100103

34. Sreenivasan, H.; Bernard, E.; Santos, H. S.; Nguyen, H.; Moukannaa, S.; Adediran, A.; Provis, J. L.; and Kinnunen, P., "A Critical Review of Magnesium Silicate Hydrate (M-S-H) Phases for Binder Applications," *Cement and Concrete Research*, V. 178, Apr. 2024, Article No. 107462. doi: 10.1016/j.cemconres.2024.107462

35. Gu, L.; Visintin, P.; and Bennett, T., "Sulphuric Acid Resistance of Cementitious Materials: Multiscale Approach to Assessing the Degradation," *Journal of Materials in Civil Engineering*, ASCE, V. 32, No. 7, July 2020, p. 04020171. doi: 10.1061/(ASCE)MT.1943-5533.0003261

36. Damion, T.; Cepuritis, R.; and Chaunsali, P., "Sulfuric Acid and Citric Acid Attack of Calcium Sulfoaluminate-Based Binders," *Cement and Concrete Composites*, V. 130, July 2022, Article No. 104524. doi: 10.1016/j.cemconcomp.2022.104524

37. Beddoe, R. E., and Dorner, H. W., "Modelling Acid Attack on Concrete: Part I. The Essential Mechanisms," *Cement and Concrete Research*, V. 35, No. 12, Dec. 2005, pp. 2333-2339. doi: 10.1016/j.cemconres.2005.04.002

38. Yuan, H.; Dangla, P.; Chatellier, P.; and Chaussadent, T., "Degradation Modeling of Concrete Submitted to Biogenic Acid Attack," *Cement and Concrete Research*, V. 70, Apr. 2015, pp. 29-38. doi: 10.1016/j.cemconres.2015.01.002

ACI MATERIALS JOURNAL TECHNICAL PAPER

Title No. 122-M36

Predicting Geopolymer Ultra-High-Performance Concrete Strength Using Machine Learning

by Kamran Aghaee and Kamal H. Khayat

Ultra-high-performance geopolymer concrete (UHP-GPC) can exhibit high to exceptional strength. Given the importance of UHP-GPC's mechanical properties, prediction of its 28-day compressive strength (f_c') remains insufficiently explored. This study predicts UHP-GPC's f_c' based on alkali-activated materials, sand, fiber volume, and water-geopolymer binder and alkali activator ratios. Advanced statistical modeling and a spectrum of ensemble machine learning (ML) algorithms including random forest (RF), gradient boosting (GB), extreme gradient boosting (XGB), and stacking are used to predict UHP-GPC's strength. The derived models reveal the significance of fiber, slag, and sand as the most significant factors influencing the 28-day f_c' of UHP-GPC. All the ML models demonstrate higher precision in forecasting f_c' of UHP-GPC compared to statistical modeling, with R^2 peaking at 0.85. Equations are derived to predict the strength of UHP-GPC. This paper reveals that UHP-GPC with superior mechanical properties can be designed for further sustainability.

Keywords: compressive strength; ensemble machine learning; environment; geopolymer ultra-high-performance concrete; sustainability; ultra-high-performance concrete (UHPC).

INTRODUCTION

Ultra-high-performance concrete (UHPC) represents a significant advancement in the field of concrete technology by offering exceptional characteristics. Its remarkable dense structure, excellent mechanical properties, high ductility, and superior durability make it an attractive construction material for a myriad of applications.[1] However, the use of UHPC can present some challenges given the high cement consumption, high autogenous shrinkage that can lead to cracking, and inadequate fire resistance.[2-4] A low water-binder ratio (*w/b*), high content of fine materials, and high fiber volume adversely affect UHPC's rheology by reducing workability while increasing viscosity and thixotropy.[5] As a result, careful attention to mixture proportioning and selection of admixtures should be taken to facilitate UHPC's mixing, pumping, placement, consolidation, and finishing. The use of supplementary cementitious materials (SCMs) such as silica fume (SF), fly ash (FA), and slag cement can enhance particle packing, reduce water and high-range water-reducing admixture (HRWRA) demand, and provide lubricating effect by reducing friction between particles, thereby improving workability and flow properties.[6,7] Meng et al.[8] proposed cement substitution with 50 wt% slag cement and 5 wt% SF for UHPC with a *w/b* of 0.18. Such substitution reduced the HRWRA demand and plastic viscosity and secured a 28-day compressive strength (f_c') of 170 MPa (24.65 ksi).

Proper use of SCM can reduce autogenous shrinkage. For example, replacing cement with 50 wt% slag cement in UHPC, compared to a mixture containing cement and 25 wt% SF, reduced autogenous shrinkage from 750 to 250 $\mu\varepsilon$.[8] Despite the positive effect of SCM on autogenous shrinkage, UHPC can still be vulnerable to self-desiccation, which induces internal tensile stresses and can cause microcracking due to high cementitious content, low *w/b*, and high matrix density.[9,10] The incorporation of nanomaterials and fibers in UHPC reinforcement can significantly enhance its mechanical performance and durability. Using nanoalumina fibers, nanocellulose fibers, and graphite nanoplatelets provide nucleation sites for further hydration, improving the microstructure while enabling a reduction in silica fume and steel fiber content. This optimization contributes to improved mechanical properties and durability.[11] Although the aforementioned steps enhance UHPC's characteristics, it is crucial to upgrade it into a more sustainable material.

Recently, an alternative design for UHPC using alkali-activated materials, also known as geopolymer precursors, has been proposed. This approach employs natural and industrial by-products to create ultra-high-performance geopolymer concrete (UHP-GPC), which has shown promise in enhancing early-age strength, impermeability, thermal performance, fire resistance, and overall environmental sustainability.[12-17] Alkali-activated materials can reduce unit energy consumption and CO_2 emission by 70% compared to portland cement.[18,19] An alkali-activated binder, or a so-called geopolymer, with minimal calcium content can be synthesized from aluminosilicate precursors such as metakaolin (MK), FA, and slag.[20,21] High-alkali activators such as sodium/potassium hydroxide and sodium/potassium silicate facilitate both dissolution and geopolymerization processes. Alkali-based geopolymerization includes six steps: alkalination, depolymerization of silicate, gel formation of oligo-sialates, polycondensation, reticulation, and solidification.[22] In the alkaline environment, aluminosilicate minerals dissolve, forming a three-dimensional sialate network (Si–O–Al–O) with noncrystalline polymeric bonds, which serves as a fundamental geopolymer structure or geopolymer blocks.[23,24] The geopolymer blocks react with sodium and calcium compounds and form sodium

---

ACI Materials Journal, V. 122, No. 5, September 2025.
MS No. M-2024-346.R3, doi: 10.14359/51747873, received March 16, 2025, and reviewed under Institute publication policies. Pertinent discussion including author's closure, if any, will be published ten months from this journal's date if the discussion is received within four months of the paper's print publication.

alumina silicate hydrate (N-A-S-H) (using low-calcium precursor) and calcium alumina silicate hydrate (C-A-S-H) (using high-calcium precursor) gels, which act as nucleation sites. This, along with the formation of calcium silicate hydrate (C-S-H) in high-calcium precursor systems, causes hybrid binding, thus accelerating strength development and enhancing mechanical and durability characteristics.[25,26] Because the specified binding products are gel phases susceptible to leaching, it is debatable whether the system can be classified as fully geopolymeric. However, stabilizing these products with materials such as MK-750 can prevent leaching and promote genuine polymerization.[27,28]

Based on the literature, hot-pressed UHP-GPC made with volcanic ash and low alkali activator content of approximately 20 wt% (alkali activator-to-solid mass ratio 1:5) with f_c' of up to 160 MPa (23.21 ksi) can be produced.[29] It was reported that using simultaneous heating and pressing techniques at up to 350°C (662°F) and 41 MPa (5.95 ksi) can accelerate the dissolution of the aluminosilicate precursors and their polycondensation, resulting in reduced pore volume and a disconnected small pore network.[29] Therefore, the enhanced mechanical properties were ascribed to the denser microstructure of the UHP-GPC due to the advanced geopolymerization during the hot-pressing process.[16] Findings by Ambily et al.[23] indicated the production of slag-based UHP-GPC that can achieve a high f_c' of 175 MPa (25.38 ksi) through the incorporation of up to 2% steel fibers under ambient temperature curing. The concept of strain-hardening UHP-GPC was proposed by Lao et al.[13,30] for producing UHP-GPC with superior mechanical properties and ductility. The authors reported that by adjusting the slag-FA ratio (20% FA and 80% slag) and steel fiber volume (4%), a significantly dense microstructure of UHP-GPC with f_c' up to 222 MPa (32.20 ksi) and tensile strain capacity up to 0.55% can be produced. According to reported results, the UHP-GPC exhibited a significantly low residual crack width (up to 20 μm) after tensile testing, indicating the enhanced microstructure of the concrete by superior bonding between fibers and matrix. To further enhance the sustainability of UHP-GPC, recycled aggregate or carbonated recycled aggregate with superior properties can be employed. Liang et al.[31] used waste nickel slag as recycled fine aggregate to produce UHP-GPC. The synergistic effect of several precursors including slag, FA, and rice husk ash (RHA) can significantly enhance the quality of microstructure and aggregate/fiber-matrix interfacial transition zone in geopolymer concrete. This synergy resulted in compressive strengths of up to 145 MPa (21.03 ksi) and significantly improved the durability of UHP-GPC. Additionally, after 300 freezing-and-thawing cycles, the loss of f_c' and mass was limited to 6% and 1%, respectively.[31]

Despite the effective development of UHP-GPC through alkali-activation technology, tailoring the UHP-GPC to achieve adequate mechanical properties and matrix density is challenging as many factors contribute to the successful production and strength development of UHP-GPC. These factors include the type and combination of SCM and fillers, the aggregate volume and characteristics, the type and content of fibers, as well as the type and ratio of alkali activators. Therefore, this study is carried out to shed light on the effect of these parameters on f_c' of UHP-GPC. A data set was compiled from previous studies and a hybrid approach of employing statistical modeling (multiple linear regression) using JMP software and machine learning (ML) techniques was adopted to estimate the 28-day f_c' of UHP-GPC. In the ML analysis, advanced ensemble modeling using random forest (RF), gradient boosting (GB), extreme gradient boosting (XGB), and stacking ensemble learning techniques were used. By estimating f_c' and smart design of UHP-GPC, this research seeks to contribute to the continued advancement and integration of this alternative UHPC material in modern and sustainable construction.

RESEARCH SIGNIFICANCE

Cement production contributes to at least 8% of human-induced global carbon emission, and approximately 0.9 kg of CO_2 is released with the production of each kg of cement through the carbonate decomposition and fossil fuel combustion.[32,33] The exceptional performance of UHPC is primarily attributed to its high cement content; however, its excessive cement use raises environmental concerns. Developing alternative designs for UHPC by replacing traditional cement-based binders with SCMs and alkali-activated materials has become imperative. Given the importance of the mechanical properties of UHPC, accurately predicting the strength of UHP-GPC is crucial to justify its use as a sustainable alternative to conventional UHPC.

ANALYTICAL INVESTIGATION

Factors affecting UHP-GPC performance

The principals of producing UHP-GPC predominantly include: 1) implementing either heat curing or pressurized environment curing[29]; 2) using binary or ternary combinations of SF/MK, FA, and slag for enhanced alkali-activation potential and flowability at low *w/b*[34]; 3) decreasing the particle size and increasing the constituents' specific surface area[13]; and 4) employing an activator such as sodium- or potassium-based alkaline solutions.[35] Geopolymer binder, aggregate, alkali activators, and fibers are used as main constituents in the production of UHP-GPC, which can offer unique benefits to the mechanical properties, durability, and environmental impacts of the concrete. A brief review of the aforementioned constituents is presented as follows.

Binder—A variety of natural and industrial by-products can serve as geopolymer binder. This study focuses on the most commonly used materials, for which extensive data sets are available. Pozzolans and SCMs such as slag, FA, MK, and SF, and limestone powder (LP)[36]; natural by-products such as RHA; and recyclable waste materials[12,31,37] such as granite powder,[38] ground glass powder (GGP),[39] and dehydrated cementitious powder[40] have been used to produce UHP-GPC. These materials can contribute to geopolymeric, hydraulic, and pozzolanic reactions depending on their chemical composition, leading to the formation of strong binding phases such as C-A-S-H (in high-calcium precursors), N-A-S-H (in low-calcium precursors), and C-S-H. Moreover, binders with fine particles, such as LP and GGP, can improve particle packing density, resulting in lower water demand and enhanced flowability. Fine particles fill voids and serve as nucleation sites, promoting hydration, refining the microstructure, and improving overall performance.

Aggregate—Quartz sand is often used as the primary aggregate in UHPC. However, such sand is a limited nonrenewable resource that requires mining and manufacturing operations.[41] The substitution of quartz sand with industrial by-products in the preparation of UHP-GPC can enhance the sustainability of the material. Industrial by-products include waste nickel slag,[31] waste glass sand,[39] recycled concrete aggregate and carbonated recycled concrete aggregate,[42] and ceramic waste aggregate.[43] Recycling waste materials as aggregate can avoid accumulation of waste and effectively resolve the scarcity of natural aggregate. Coal bottom ash, coal FA, steel slag, blast-furnace slag, plastic wastes, and natural aggregate such as those generated from dates palm kernel are other refused sources of aggregate that can be employed as partial replacement of quartz sand.[44-46]

Alkali activator—Several types of alkali activators are used for geopolymerization of alkali-activated concrete. The most common ones are sodium/potassium silicate (Na_2SiO_3/K_2SiO_3) and sodium/potassium hydroxide (NaOH/KOH).[47,48] Alkali activators can impact the fresh and mechanical properties of UHP-GPC. The combination of potassium hydroxide (KOH) and sodium silicate (Na_2SiO_3) alkali activators can enhance mechanical properties of the concrete. The chemical activators contribute to enhancing the microstructure, strength, and durability of UHP-GPC, particularly at temperatures exceeding 600°C (1112°F).[49] The concentration of alkali activators also can affect the mechanical properties of alkali-activated concrete.

Fiber—A drawback of UHP-GPC is brittleness, which can be addressed by adding appropriate fibers.[50] In addition to a variety of steel fibers,[50,51] synthetic, natural, and nano fibers have been employed to reinforce UHP-GPC.[30,52-54] Although a higher fiber content can enhance UHP-GPC's performance, there would be an optimum limit. The fiber aspect ratio plays a critical role in the mechanical properties. Relatively high-aspect-ratio straight fibers can be used in UHP-GPC proportioning due to their extensive distribution and superior performance.[50] The use of corrugated fibers with a higher deformation ratio in UHP-GPC can result in lower strengthening and toughening efficiency compared to that of similar straight and hooked-end fibers.[50,55] The combined use of polypropylene and steel fibers can improve the mechanical properties of UHP-GPC. However, substituting polypropylene with steel fibers can decrease mechanical strength while enhancing durability due to the lower vulnerability of polypropylene fibers to corrosive agents compared to steel fibers.[56]

Nano materials—Nano materials as fillers, binders, pozzolans, and fibers can play a significant role in improving the quality and performance of UHP-GPC, leading to substantial mechanical properties and durability enhancement.[53,57,58] The incorporation of nano materials such as nano-SiO_2, nano-MK, nano-TiO_2, nano-Al_2O_3, carbon nanotubes, and nano clay can enhance packing density, reduce sorptivity, water absorption, and provide nucleation sites due to higher surface area, thus facilitating the aluminosilicate network formation.[53,59] Nanomaterials can reduce microcrack development by improving interfacial bonding, refining pores, enhancing the homogeneity of the UHP-GPC microstructure, and modifying stress-transfer mechanisms within the matrix, thereby minimizing the risk of spalling.

Predicting UHP-GPC's compressive strength

Selecting the optimum combination of constituents at adequate contents can result in the production of UHP-GPC with superior performance. As f_c' is one of the most important indicators of UHP-GPC performance, it has been measured more frequently than other properties of UHP-GPC. In this study, statistical and ensemble ML modeling were employed to predict the effect of constituents such as SCM, sand, fiber, w/b, and alkali activators on the 28-day f_c' of UHP-GPC. Although the source and chemical composition of alkali-activated materials significantly influence UHP-GPC's strength development, their exclusion from the analysis was due to insufficient data and the complexity involved. In this study, the general relative richness of compounds is assumed as follows: for silica, SF > FA > slag; for alumina, FA > slag > SF; and for calcium, slag > FA > SF.

Due to intricacies and nonlinear relationships among features, statistical modeling and a spectrum of ML techniques were employed to develop predictive models. Statistical modeling using JMP software typically relies on linear relationships between dependent and independent variables, often overlooking nonlinear interactions among features and offering limited capabilities for fine-tuning model parameters.[60] These characteristics can limit its performance when having intricate data sets with potential outliers. Therefore, ML techniques were employed as a complementary approach, not only for comparison but also to improve the flexibility, sensitivity, and accuracy of the analysis.

Ensemble learning methods can be divided into three main categories of bagging, boosting, and stacking, as illustrated in Fig. 1. In this study, the strengths of these three categories of ensemble modeling were leveraged. The bagging category was represented by RF, whereas boosting models included GB and XGB. Additionally, the stacking ensemble model was employed as a powerful technique to combine the strengths of bagging and boosting methods for achieving a trade-off between variance and bias. These strategies were employed to further improve the models' predictive power in forecasting the 28-day f_c' of UHP-GPC.[61-63]

A data set including 120 entries related to the effect of various factors, discussed in the previous section, on the 28-day f_c' of UHP-GPC was compiled. Table 1 summarizes UHP-GPC characteristics made with diverse alkali-activated materials, sand, fiber, w/b, and alkali activators at various proportions.

Statistical data analysis

Multiple linear regression—Multiple linear regression analysis of variance was performed to assess the significance of features (alkali-activated material, sand, fiber, w/b, and alkali activator, typically sodium silicate-sodium hydroxide ratio [SS/SH]), on the 28-day f_c' of UHP-GPC. The recognized statistically significant features are shown in the effect

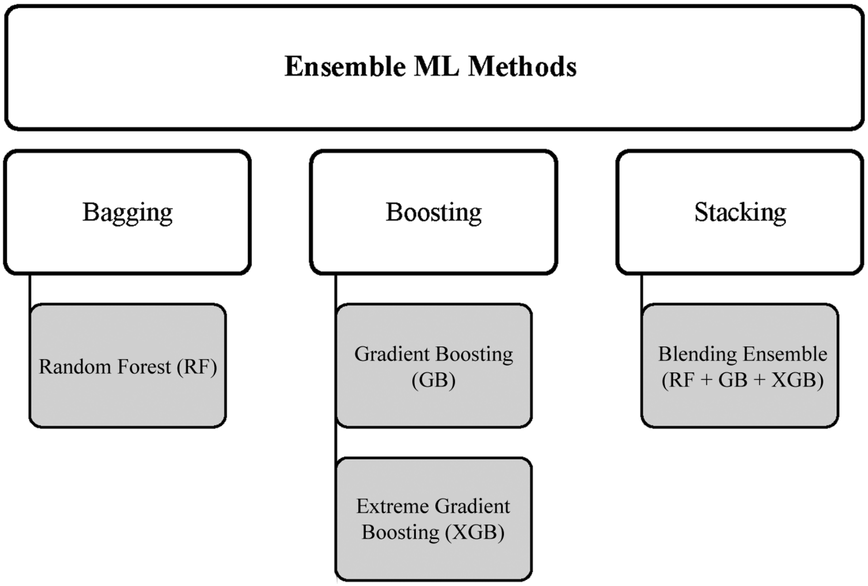

Fig. 1—Flowchart of ensemble ML methods and associated algorithms employed in this study.

tests table (Table 2). The statistical significance level of 0.05 represents the probability that a given random sample is not a true reflection of the overall population. Table 2 results imply the importance of fiber, sand, *w*/*b*, slag, *SS*/*SH*, FA, and SF, respectively, on the 28-day f_c' of UHP-GPC.

The predicted versus actual 28-day f_c' of UHP-GPC based on the training data set is presented in Fig. 2 ($R^2 = 0.79$).

Linear prediction equation and significant factors—Using multiple linear regression, the statistical model developed the following equation to predict the f_c' of UHP-GPC based on the five significant features listed in Table 2. This equation applies within the specific range of features analyzed in this study.

$$f_c' = 338.64 + 0.14\ \text{Fiber} - 0.12\ \text{Sand} - 234.30\ w/b - 0.10\ \text{Slag} + 6.01\ \text{SS/SH}$$

The main constituents considered in the analysis (fiber, sand, slag, FA, and SF) are expressed as unit mass values added to the mixture (kg/m^3), while the *SS*/*SH* and *w*/*b* denote alkali activator and water-geopolymer binder ratios, respectively.

The effect of the two most significant factors (fiber and sand) on the 28-day f_c' of UHP-GPC can be further discussed by the surface plot shown in Fig. 3. As can be seen, based on the compiled database, for a UHP-GPC made with 0.3 *w*/*b*, 665 kg/m^3 (41.5 lb/ft^3) slag, and 1.5 *SS*/*SH*, increasing the fiber dosage and decreasing sand content increase the 28-day f_c'. The positive effect of fiber on the mechanical properties of UHP-GPC has been documented in previous studies.[13,30,50,51] Less sand allows for higher alkali-activated binder use, which can enhance the 28-day f_c' of UHP-GPC. Although individual use of SCM except for slag was not identified among the most significant factors, the synergy and combination of alkali-activated materials at the presence of alkali activators can play a significant role in strength development of UHP-GPC.

In this study, the 28-day f_c' values of 24 mixtures obtained from previous studies[50,69] were employed for testing the statistical model. These mixtures were not used to establish or train the model. As shown in Fig. 4, the statistical modeling offers an adequate prediction of the 28-day f_c' of UHP-GPC, with R^2 of 0.75 on the testing data set.

ML—As a complement to statistical modeling, ML algorithms were employed to forecast the f_c' of UHP-GPC. These algorithms, which are considered ensemble learning methods, were applied on the similar data set including 120 data points (shown in Table 1), of which 80% was employed for training and 20% for testing the models. The training subset was used to develop the ML models through various ensemble techniques to uncover relationships among input features such as slag, FA, SF, sand, fiber, *w*/*b*, *SS*/*SH*, and the 28-day f_c' of UHP-GPC. The test subset, which was reserved during the training phase, was subsequently used to evaluate the models' performance.

In this study, ensemble learning techniques using various bagging and boosting algorithms such as RF, GB, and XGB, along with stacking ensemble technique were employed to enhance the predictive power. Stacking combined the predictions of these models using a decision tree regressor meta-model. The hyperparameters of the ML algorithms—including number and depth of trees, learning rate, maximum features per split, and minimum samples per split/leaf—were fine-tuned to enhance the predictive performance of the models.

RF—RF constructs decision trees using bootstrap aggregation, creating multiple training data sets through sampling with replacement from the original data. It introduces randomness by selecting a subset of features at each split rather than evaluating all features, which enhances model diversity. The final prediction is obtained by averaging the outputs of all trees, thereby reducing variance through ensemble averaging. RF performs nonlinear regression with relatively few hyperparameters (primarily the number of trees and the number of features sampled at each split) and is generally insensitive to feature scaling. It also enables rapid training and evaluation by leveraging parallel computation of multiple decision trees. As a representative of bagging

Table 1—Effect of various factors on 28-day f_c' of UHP-GPC

Reference	Slag, kg/m^3	FA, kg/m^3	SF, kg/m^3	Sand, c	Fiber, kg/m^3	*w*/*b*	*SS*/*SH*	28-day f_c', MPa
Kim et al.[12]	1175	—	176	216	—	0.3	3	139
	1062		159	391				142
	971		146	536				146
	895		134	659				147
	831		125	764				161
Liu et al.[50]	688	172	45	905	0	0.32	7	102
					78			142
					156			159
					234			169
					78			146
					156			162
					234			170
					78			132
					156			142
					234			151
Liu et al.[51]	688	172	45	905	0	0.32	7	101
	688	172	45		78			109
	688	172	45		156			128
	688	172	45		234			155
	652	163	90		156			104
	580	145	180		156			137
	508	127	270		156			150
Mousavinejad and Sammak[64]	850.23	—	283.4	846.65	0	0.168	3	113
					78.5			138
					118			142
					157			151
					78.5			135
					118			140
					157			146
					66			134
					153			145
Kathirvel and Sreekumaran[65]	950	—	0	912	0	0.3	1.5	85
	950		0	912	78.5			90
	950		0	912	157			100
	950		0	798	0			83
	950		0	798	78.5			90
	950		0	798	157			100
	950		0	684	0			98
	950		0	684	78.5			105
	950		0	684	157			113
	807.5		142.5	912	0			85
	807.5		142.5	912	78.5			90
	807.5		142.5	912	157			100
	807.5		142.5	798	0			90

Table 1 (cont.)—Effect of various factors on 28-day f_c' of UHP-GPC

Reference	Slag, kg/m^3	FA, kg/m^3	SF, kg/m^3	Sand, c	Fiber, kg/m^3	w/b	SS/SH	28-day f_c', MPa
Kathirvel and Sreekumaran[65]	807.5	—	142.5	798	78.5	0.3	1.5	105
	807.5		142.5	798	157			115
	807.5		142.5	684	0			107
	807.5		142.5	684	78.5			121
	807.5		142.5	684	157			130
	665		285	912	0			93
	665		285	912	78.5			110
	665		285	912	157			117
	665		285	798	0			107
	665		285	798	78.5			120
	665		285	798	157			132
	665		285	684	0			123
	665		285	684	78.5			134
	665		285	684	157			150
Aisheh et al.[56]	860	—	285	850	0	0.168	3.5	115
					78.5			140
					98			147
					118			144
					137			152
					157			150
					177			162
					78.5			145
					118			153
					157			154
Rakesh et al.[66]	690	180	0	905	0	0.3	6.3	125
	690	180	0		9			132
	690	180	0		18			140
	690	180	0		27			147
	690	180	45		0			117
	690	180	45		9			127
	690	180	45		18			132
	690	180	45		27			140
	650	165	90		0			100
	650	165	90		9			113
	650	165	90		18			123
	650	165	90		27			135
	580	145	180		0			134
	580	145	180		9			139
	580	145	180		18			152
	580	145	180		27			158
	510	125	270		0			149
	510	125	270		9			156
	510	125	270		18			160
	510	125	270		27			167

Table 1 (cont.)—Effect of various factors on 28-day f_c' of UHP-GPC

Reference	Slag, kg/m^3	FA, kg/m^3	SF, kg/m^3	Sand, c	Fiber, kg/m^3	w/b	SS/SH	28-day f_c', MPa
Liu et al.[67]	790	130	80	830	0	0.3	6	94
					157			102
					157			110
					157			141
					202			151
Midhin et al.[68]	850.23	—	283.4	930.4	—	0.175	1	105
				940.9		0.165	2	111
				945.9		0.16	3	116
				945.9		0.153	3	122
				945.9		0.146	3	130
Liu et al.[50]	688	172	45	905	78	0.32	7	140
	688	172	45	905	156	0.32	7	149
	688	172	45	905	234	0.32	7	157
	688	172	45	905	78	0.32	7	126
	688	172	45	905	156	0.32	7	134
	688	172	45	905	234	0.32	7	144
	688	172	45	905	156	0.32	7	132
Althoey et al.[69]	685	0	207.5	1105	39	0.20	0.5	115
	685	0	207.5	1105	78	0.20	0.5	122
	685	0	207.5	1105	117	0.20	0.5	118
	685	0	250	1105	39	0.19	0.5	120
	685	0	250	1105	117	0.19	0.5	121
	685	0	292.5	1105	39	0.18	0.5	118
	685	0	292.5	1105	78	0.18	0.5	127
	685	0	292.5	1105	117	0.18	0.5	118
Liang et al.[31]	688	172	45	905	0	0.3	7	104
	688	172	45		78			122
	688	172	45		156			140
	688	172	45		234			146
	652	163	90		156			145
	616	154	135		156			146
	580	145	180		156			132

Note: 1 MPa = 0.145 ksi; 1 kg/m^3 = 0.0624 lb/ft^3.

algorithms, RF effectively reduces the high variance typically associated with individual decision trees.[70]

GB—GB is a powerful ML algorithm that combines shallow decision trees (typically with low variance and high bias) and refines iteratively to create a low bias ensemble. Each successive tree is trained to minimize the residual errors of the combined previous learners. GB optimizes model performance using gradient descent, relying on the negative gradient of a specified loss function to update the ensemble. The process begins with a weak initial model and incrementally improves prediction accuracy by reducing residuals in each iteration until a convergence criterion is met. GB is computationally efficient, requires relatively few hyperparameters (for example, tree depth, number of iterations, and learning rate), and is generally insensitive to feature scaling.[71]

XGB—XGB is a highly efficient and scalable implementation of GB, known for its superior performance and optimization capabilities. XGB uses an innovative tree algorithm that enables handling scattered data with parallel and distributed computing. It incorporates regularization techniques, and tree pruning strategies to enhance efficiency. XGB builds asymmetric ensemble trees sequentially, with each new tree learning from the residuals of the previous one. It uses a depth-wise learning approach, focusing on splits that produce the greatest reduction in loss at each leaf. This method can reduce the risk of overfitting while enhancing computational efficiency.[72]

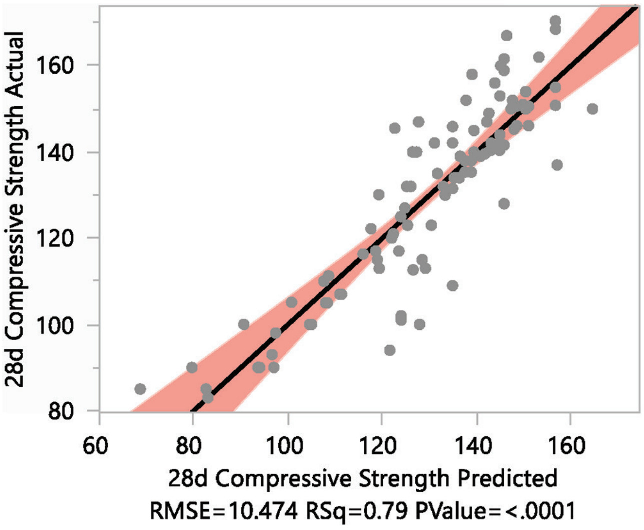

Fig. 2—Comparison between actual and predicted 28-day f_c' of UHP-GPC based on training data set. (Note: 1 MPa = 0.145 ksi.)

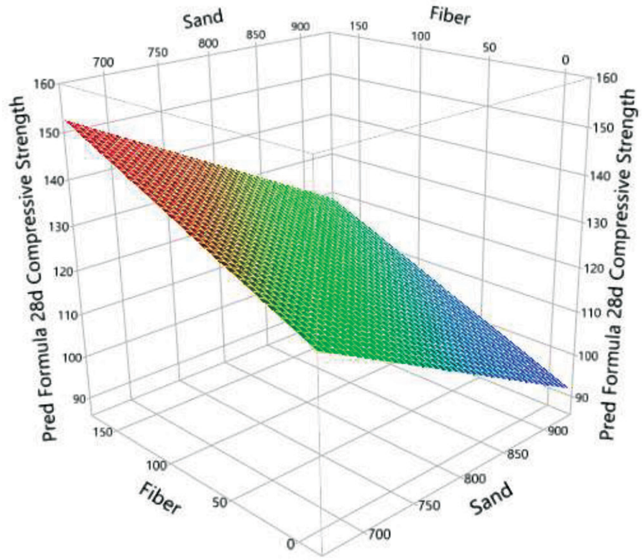

Fig. 3—Surface plot showing contribution of fiber and sand to 28-day f_c' of UHP-GPC. (Note: w/b = 0.3; slag = 665 kg/m^3 [41.5 lb/ft^3]; SS/SH = 1.5; 1 MPa = 0.145 ksi.)

Stacking—Stacking is an ensemble learning technique that integrates multiple regressors generated by different ML algorithms on the same data set. It leverages the complementary strengths of diverse models—such as those based on bagging and boosting—to achieve a more balanced trade-off between bias and variance. In this approach, a set of base-level regressors is first trained independently, and their predictions are then used as inputs for a meta-learner, which synthesizes the outputs to generate the final prediction. Due to its flexibility and potential to enhance predictive accuracy, stacking was employed in this study to construct a robust and efficient ensemble model.[73] In this study, a decision tree regressor was employed as the meta-learner to integrate the predictions of diverse base-level algorithms. Figure 5 illustrates the schematic representation of the stacking procedure used.

Table 2—Effect test table for 28-day f_c' of UHP-GPC

Source	Nparm	DF	Sum of squares	*F*-ratio	Prob > *F*
Slag	1	1	986.502	8.992	0.0035*
FA	1	1	10.612	0.097	0.7565
SF	1	1	5.278	0.048	0.8269
Sand	1	1	4773.345	43.510	<0.0001*
Fiber	1	1	8781.506	80.046	<0.0001*
w/*b*	1	1	1970.936	17.966	<0.0001*
SS/*SH*	1	1	731.148	6.665	0.0114*

*Denotes statistically significant factors.

Note: Nparm is number of parameters; DF is degree of freedom.

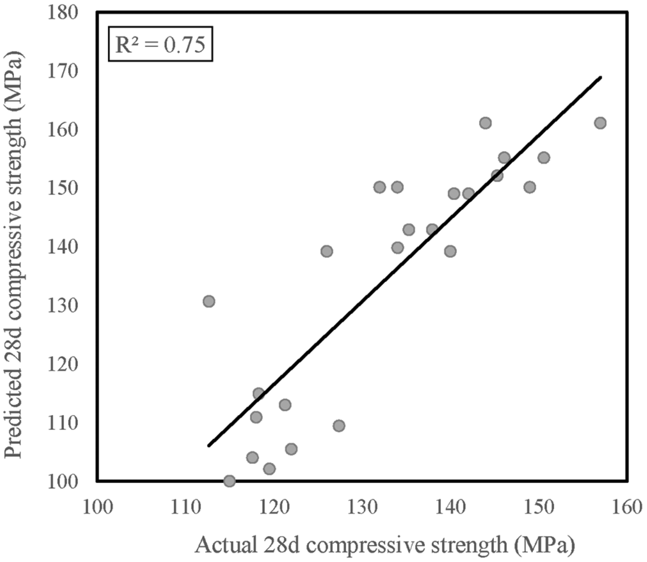

Fig. 4—Predicted versus actual 28-day f_c' values of UHP-GPC for testing data set. (Note: 1 MPa = 0.145 ksi.)

DISCUSSION, COMPARISON, AND EVALUATION OF ML MODELS

The descriptive statistics including mean, standard deviation (SD), minimum, and maximum values of the input and output variables are shown in Table 3.

Pair plot and heatmap correlation—shown in Fig. 6 and 7, respectively—were employed to visually represent the data distribution. Figure 6 shows the pairwise relationship between the features and indicates that the relationship among most pairs of features except for slag-SF, SF-sand, and *SS*/*SH*-*w*/*b* is nonlinear.

The Pearson correlation coefficients on the heatmap shown in Fig. 7, which range between –0.72 and +0.94, indicate the extent of relationship between the features. Positive numbers imply a direct relationship, while negative ones indicate the inverse relationship between the features. As it can be observed, the strongest direct and inverse pairwise relationships are associated with FA-*SS*/*SH* and SF-*w*/*b*.

For assessing the accuracy of the ML models, three widely recognized performance indicators, including R^2, mean absolute error (MAE), and mean squared error (MSE) values were employed. The R^2 or coefficient of determination indicates how effectively independent variables (slag,

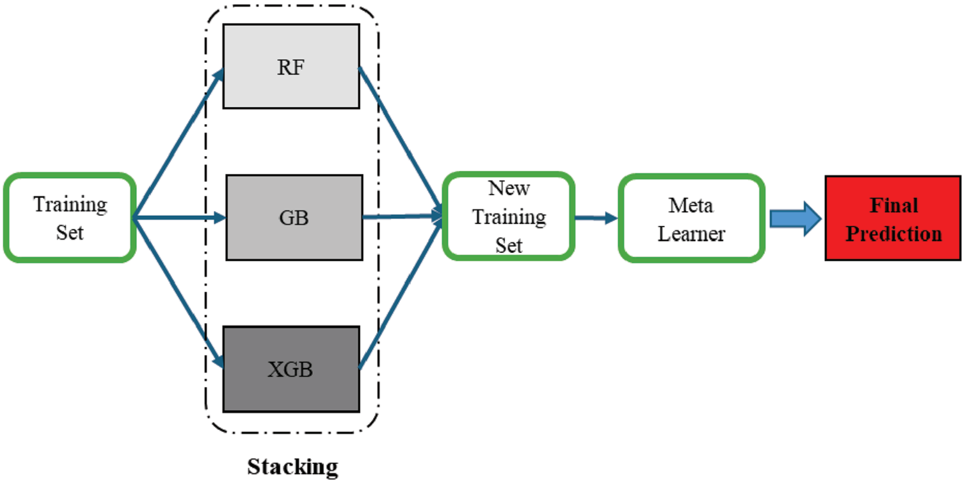

Fig. 5—Schematic view of stacking ensemble technique procedure.

Table 3—Statistical properties of variables

ID	Data	Unit	Mean	SD	Minimum	Maximum
1	28-day f_c'	MPa	129.5	21.1	83.0	170.4
2	Slag	kg/m^3	761.5	121.4	508.0	1175.0
3	FA	kg/m^3	65.1	80.2	0.0	180.0
4	SF	kg/m^3	164.4	111.5	0.0	292.0
5	Sand	kg/m^3	863.8	120.3	216.0	1105.0
6	Fiber	kg/m^3	83.1	71.7	0.0	234.0
7	*w*/*b*	—	0.257	0.071	0.120	0.320
8	*SS*/*SH*	—	4.0	2.3	0.5	7.0

FA, SF, sand, fiber, *w*/*b*, and *SS*/*SH*) explain the variability in a dependent variable (28-day f_c' of UHP-GPC). MAE calculates the average of the absolute differences between actual and predicted values, reflecting the typical magnitude of prediction errors regardless of direction. MSE measures the average squared differences between actual and predicted values, offering an overall assessment of prediction accuracy. As shown in Fig. 8 and Table 4, the XGB and stacking models stand out for their high accuracy in predicting the 28-day f_c' of UHP-GPC, achieving R^2 values of up to 0.85. Among the other algorithms, GB outperformed RF on the testing set. The R^2 values on the training set for RF, GB, and XGB were 0.91, 0.90, and 0.93, respectively. These results suggest that RF exhibited the highest and GB the lowest degree of overfitting. The superior performance of the boosting algorithms can be associated with their efficiency in sequential correction and incremental improvement while learning the complex and nonlinear relationships between the 28-day f_c' of UHP-GPC and features. These algorithms learn from previous errors and adjustments, progressively building models with improved accuracy. The lower values of MAE and MSE achieved by the stacking and XGB models further highlight their adequacy. Abdellatief et al.[74] conducted a similar study to predict the compressive strength of UHP-GPC using random forest, support vector regression (SVR), and XGB algorithms. The authors indicated the efficiency of the boosting algorithm compared to SVR and RF algorithms. The adequacy of boosting algorithms and stacking ensemble learning techniques in effective prediction of concrete materials behavior was reported in other studies.[75,76]

The feature importance, which implies the impact of each feature on the 28-day f_c' of UHP-GPC, was obtained using various ML algorithms, and the most dominant trend is illustrated in Fig. 9. The *SS*/*SH*, fiber, and slag were identified as the three most important features influencing the 28-day f_c' of UHP-GPC. According to both statistical and ML modeling, the fiber content presents a significant role in the 28-day f_c' of UHP-GPC. Abdellatief et al.[74] recognized the effect of steel fiber as the most significant feature affecting UHP-GPC's compressive strength.

The results obtained indicate that statistical modeling can be efficient with acceptable accuracy. The software performs simple analysis using multiple linear regression and finds the best-fit line (or hyperplane in higher dimensions) that minimizes the error between the predicted and actual values. On the other hand, ML algorithms demonstrate superior performance in managing complex data that present a nonlinear relationship with the target variable and deliver commendable prediction when meticulous hyperparameter fine-tuning is applied. The algorithms demonstrate adaptive and scalable capabilities, benefiting from both intrinsic linear and nonlinear modeling capacities. They enable dynamic modification and precise analysis of small (with a reasonable number of features) and large, complex data sets—without being constrained by the assumptions of conventional statistical analysis. The studied ensemble techniques can benefit

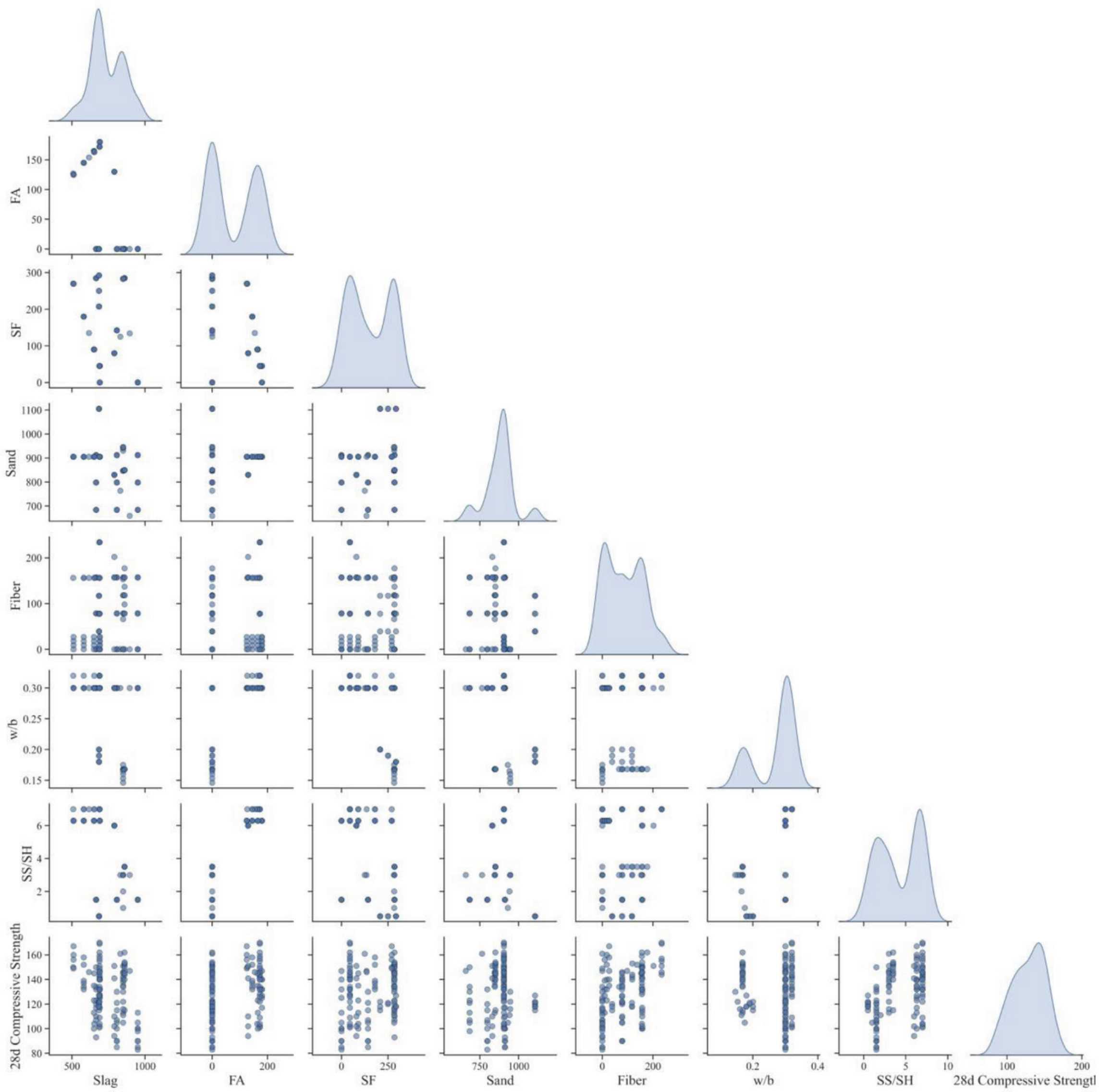

Fig. 6—Pair plot showing relationships among data set variables.

from sequential correction and incremental improvement of the model (boosting), and the integration of multiple models (stacking) for enhanced predictions.

CONCLUSIONS

This study explored the effect of various factors including alkali-activated materials, aggregate, fiber, water-binder ratio (*w*/*b*), and alkali activators on the 28-day compressive strength (f_c') of ultra-high-performance geopolymer concrete (UHP-GPC). Statistical modeling using JMP software and machine learning (ML) including several ensemble techniques were employed to predict the 28-day f_c' of UHP-GPC based on the mentioned factors. The study offered a comparison between the various statistical and ensemble ML models. According to the analyses carried out, the following conclusions can be drawn:

1. UHP-GPC proportioned with the appropriate combination of alkali-activated materials, alkali activators, and fibers can exhibit comparable mechanical properties to ultra-high-performance concrete (UHPC).

Table 4—Average performance metrics of ML models on test data set

Algorithm	R^2	MAE	MSE
RF	0.78	7.48	75.22
GB	0.82	6.36	61.02
XGB	0.84	5.83	55.06
Stacking	0.85	5.87	51.88

2. Based on statistical and ML modeling, the significance of fiber, slag, and sand as the top three most important features affecting the 28-day f_c' of UHP-GPC were identified.

3. The comparison between statistical and ensemble ML modeling revealed that ML models, with R^2 of ranging from 0.78 to 0.85, outperform statistical modeling ($R^2 = 0.75$).

4. While statistical modeling exhibited significant efficiency in predicting the UHP-GPC's 28-day f_c', ML modeling especially using boosting and stacking techniques showed superior performance.

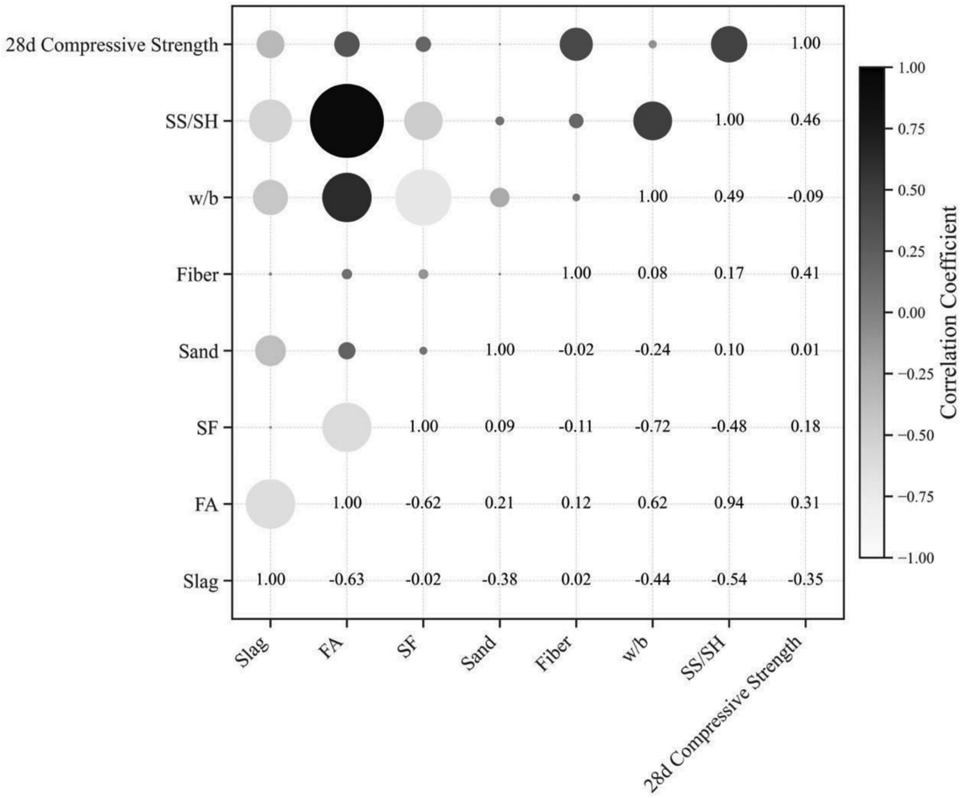

Fig. 7—Heatmap illustrating Pearson correlation coefficients among data set variables.

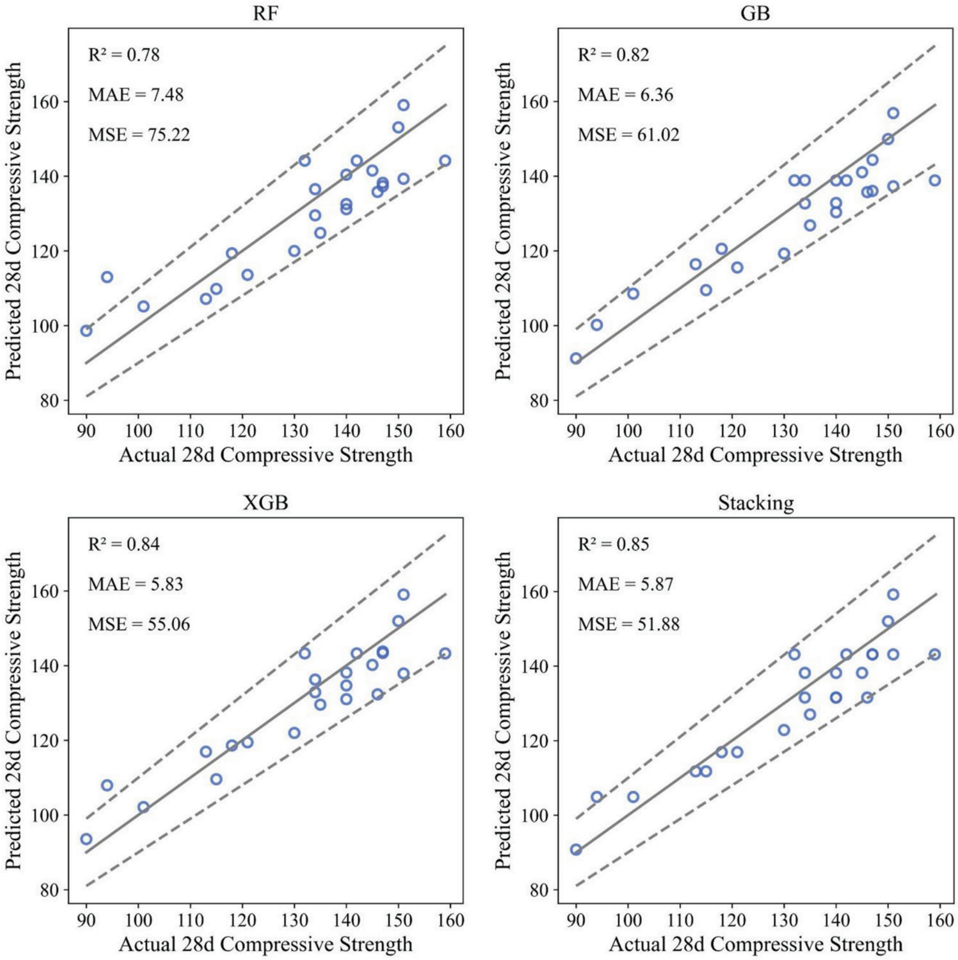

Fig. 8—Predicted versus actual values of 28-day f_c' of UHP-GPC. (Note: 1 MPa = 0.145 ksi.)

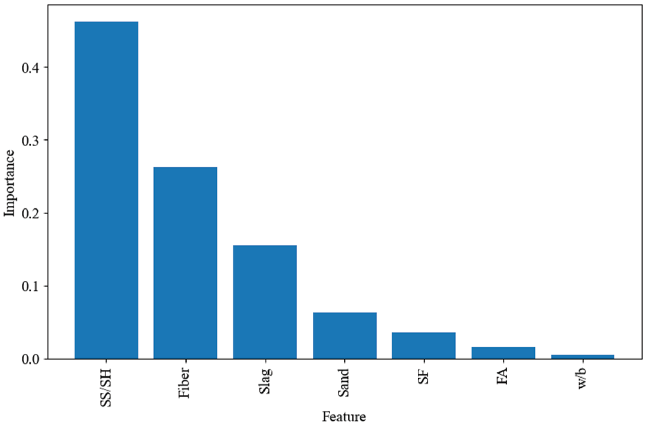

Fig. 9—Significance of features in 28-day f_c' *of UHP-GPC.*

5. The enhanced capability of the ensemble ML algorithms in learning intricate and nonlinear relationships is associated with the sequential correction and incremental improvement of the model and the integration of multiple models. Additionally, the ability to perform meticulous hyperparameter fine-tuning contributed to their superior performance compared to statistical modeling.

6. The linear equation derived from statistical and the complex ML models can enable precise prediction of the 28-day f_c' of UHP-GPC based on the features. The findings of this study provide insights into designing UHP-GPC with enhanced performance for further sustainability.

AUTHOR BIOS

ACI member **Kamran Aghaee** *is an Assistant Professor at West Virginia State University, Institute, WV. He received his MS in civil structural engineering from the University of Kansas, Lawrence, KS, in 2019, and his PhD in civil materials engineering from Missouri University of Science and Technology (Missouri S&T), Rolla, MO, in 2022. He is a member of ACI Committees 223, Shrinkage-Compensating Concrete, and 544, Fiber Reinforced Concrete. His research interests include high-strength and sustainable concrete composites,* CO_2 *mineralization, three-dimensional (3-D) printing, and machine learning applications in concrete materials.*

Kamal H. Khayat, *FACI, is Professor and Vice Chancellor for Research and Innovation at Missouri S&T. He is a member of several ACI committees and received the ACI Wason Medal for the Most Meritorious Paper published by the institute in 2016. His research interests include self-consolidating concrete, rheology of cement-based materials, ultra-high-performance concrete, 3-D printing, and repair.*

REFERENCES

1. Du, J.; Meng, W.; Khayat, K. H.; Bao, Y.; Guo, P.; Lyu, Z.; Abu-obeidah, A.; Nassif, H.; and Wang, H., "New Development of Ultra-High-Performance Concrete (UHPC)," *Composites Part B: Engineering*, V. 224, 2021, p. 109220. doi: 10.1016/j.compositesb.2021.109220

2. Shah, H. A.; Yuan, Q.; and Photwichai, N., "Use of Materials to Lower the Cost of Ultra-High-Performance Concrete – A Review," *Construction and Building Materials*, V. 327, 2022, p. 127045. doi: 10.1016/j.conbuildmat.2022.127045

3. Glanz, D.; Sameer, H.; Göbel, D.; Wetzel, A.; Middendorf, B.; Mostert, C.; and Bringezu, S., "Comparative Environmental Footprint Analysis of Ultra-High-Performance Concrete Using Portland Cement and Alkali-Activated Materials," *Frontiers in Built Environment*, V. 9, 2023.

4. Zhu, Y.; Hussein, H.; Kumar, A.; and Chen, G., "A Review: Material and Structural Properties of UHPC at Elevated Temperatures or Fire Conditions," *Cement and Concrete Composites*, V. 123, 2021, p. 104212. doi: 10.1016/j.cemconcomp.2021.104212

5. Wang, R.; Gao, X.; Huang, H.; and Han, G., "Influence of Rheological Properties of Cement Mortar on Steel Fiber Distribution in UHPC," *Construction and Building Materials*, V. 144, 2017, pp. 65-73. doi: 10.1016/j.conbuildmat.2017.03.173

6. Wang, X.; Yu, R.; Song, Q.; Shui, Z.; Liu, Z.; Wu, S.; and Hou, D., "Optimized Design of Ultra-High Performance Concrete (UHPC) with a High Wet Packing Density," *Cement and Concrete Research*, V. 126, 2019, p. 105921. doi: 10.1016/j.cemconres.2019.105921

7. Vance, K.; Kumar, A.; Sant, G.; and Neithalath, N., "The Rheological Properties of Ternary Binders Containing Portland Cement, Limestone, and Metakaolin or Fly Ash," *Cement and Concrete Research*, V. 52, 2013, pp. 196-207. doi: 10.1016/j.cemconres.2013.07.007

8. Meng, W.; Valipour, M.; and Khayat, K. H., "Optimization and Performance of Cost-Effective Ultra-High Performance Concrete," *Materials and Structures*, V. 50, No. 1, 2017, p. 29. doi: 10.1617/s11527-016-0896-3

9. Kang, S.-H.; Hong, S.-G.; and Moon, J., "Shrinkage Characteristics of Heat-Treated Ultra-High Performance Concrete and its Mitigation Using Superabsorbent Polymer Based Internal Curing Method," *Cement and Concrete Composites*, V. 89, 2018, pp. 130-138. doi: 10.1016/j.cemconcomp.2018.03.003

10. Zhang, X.; Liu, Z.; and Wang, F., "Autogenous Shrinkage Behavior of Ultra-High Performance Concrete," *Construction and Building Materials*, V. 226, 2019, pp. 459-468. doi: 10.1016/j.conbuildmat.2019.07.177

11. Alsalami, Z. H. A., and Abbas, F. H., "Ultra-High-Performance Concrete with Micro- to Nanoscale Reinforcement," *ACI Materials Journal*, V. 121, No. 2, Mar. 2024, pp. 73-92. doi: 10.14359/51740369

12. Kim, G. W.; Oh, T.; Lee, S. K.; Banthia, N.; and Yoo, D.-Y., "Development of Ca-Rich Slag-Based Ultra-High-Performance Fiber-Reinforced Geopolymer Concrete (UHP-FRGC): Effect of Sand-to-Binder Ratio," *Construction and Building Materials*, V. 370, 2023, p. 130630. doi: 10.1016/j.conbuildmat.2023.130630

13. Lao, J.-C.; Xu, L.-Y.; Huang, B.-T.; Dai, J.-G.; and Shah, S. P., "Strain-Hardening Ultra-High-Performance Geopolymer Concrete (UHPGC): Matrix Design and Effect of Steel Fibers," *Composites Communications*, V. 30, 2022, p. 101081. doi: 10.1016/j.coco.2022.101081

14. Wongsa, A.; Wongkvanklom, A.; Tanangteerapong, D.; and Chindaprasirt, P., "Comparative Study of Fire-Resistant Behaviors of High-Calcium Fly Ash Geopolymer Mortar Containing Zeolite and Mullite," *Journal of Sustainable Cement-Based Materials*, V. 9, No. 5, 2020, pp. 307-321. doi: 10.1080/21650373.2020.1748741

15. Tahwia, A. M.; Heniegal, A. M.; Abdellatief, M.; Tayeh, B. A.; and Elrahman, M. A., "Properties of Ultra-High Performance Geopolymer Concrete Incorporating Recycled Waste Glass," *Case Studies in Construction Materials*, V. 17, 2022, p. e01393. doi: 10.1016/j.cscm.2022.e01393

16. Ranjbar, N.; Mehrali, M.; Maheri, M. R.; and Mehrali, M., "Hot-Pressed Geopolymer," *Cement and Concrete Research*, V. 100, 2017, pp. 14-22. doi: 10.1016/j.cemconres.2017.05.010

17. Nishikawa, K.; Hashimoto, S.; Imai, H.; and Rossignol, S., "Cold Reaction Sintering for Preparation of Ultra-Dense Geopolymer Products," *Construction and Building Materials*, V. 328, 2022, p. 127101. doi: 10.1016/j.conbuildmat.2022.127101

18. Yoo, D.-Y.; Banthia, N.; You, I.; and Lee, S.-J., "Recent Advances in Cementless Ultra-High-Performance Concrete Using Alkali-Activated Materials and Industrial Byproducts: A Review," *Cement and Concrete Composites*, V. 148, 2024, p. 105470. doi: 10.1016/j.cemconcomp.2024.105470

19. Alsalman, A.; Assi, L. N.; Kareem, R. S.; Carter, K.; and Ziehl, P., "Energy and CO_2 Emission Assessments of Alkali-Activated Concrete and Ordinary Portland Cement Concrete: A Comparative Analysis of Different Grades of Concrete," *Cleaner Environmental Systems*, V. 3, 2021, p. 100047. doi: 10.1016/j.cesys.2021.100047

20. Nilimaa, J., "Smart Materials and Technologies for Sustainable Concrete Construction," *Developments in the Built Environment*, V. 15, 2023, p. 100177. doi: 10.1016/j.dibe.2023.100177

21. Danish, A.; Öz, A.; Bayrak, B.; Kaplan, G.; Aydın, A. C.; and Ozbakkaloglu, T., "Performance Evaluation and Cost Analysis of Prepacked Geopolymers Containing Waste Marble Powder under Different Curing Temperatures for Sustainable Built Environment," *Resources, Conservation and Recycling*, V. 192, 2023, p. 106910. doi: 10.1016/j.resconrec.2023.106910

22. Davidovits, J., *Geopolymer Chemistry and Applications*, fifth edition, Geopolymer Institute, Saint-Quentin, France, 2020.

23. Ambily, P. S.; Ravisankar, K.; Umarani, C.; Dattatreya, J. K.; and Iyer, N. R., "Development of Ultra-High-Performance Geopolymer Concrete," *Magazine of Concrete Research*, V. 66, No. 2, 2014, pp. 82-89. doi: 10.1680/macr.13.00057

24. Shi, C.; Jiménez, A. F.; and Palomo, A., "New Cements for the 21st Century: The Pursuit of an Alternative to Portland Cement," *Cement and Concrete Research*, V. 41, No. 7, 2011, pp. 750-763. doi: 10.1016/j.cemconres.2011.03.016

25. Xie, T.; Visintin, P.; Zhao, X.; and Gravina, R., "Mix Design and Mechanical Properties of Geopolymer and Alkali Activated Concrete: Review of the State-of-the-Art and the Development of a New Unified

Approach,” *Construction and Building Materials*, V. 256, 2020, p. 119380. doi: 10.1016/j.conbuildmat.2020.119380

26. Chen, X.; Sutrisno, A.; and Struble, L. J., “Effects of Calcium on Setting Mechanism of Metakaolin-Based Geopolymer,” *Journal of the American Ceramic Society*, V. 101, No. 2, 2018, pp. 957-968. doi: 10.1111/jace.15249

27. Davidovits, J., “High-Alkali Cements for 21st Century Concretes,” *Concrete Technology: Past, Present, and Future*, SP-144, P. K. Mehta, ed., American Concrete Institute, Farmington Hills, MI, 1994, pp. 383-398.

28. Davidovits, J., “Why Alkali-Activated Materials (AAM) are Not Geopolymers,” Technical Paper #25, Geopolymer Institute, Saint-Quentin, France. doi: 10.13140/RG.2.2.34337.25441

29. Ranjbar, N.; Kashefi, A.; Ye, G.; and Mehrali, M., “Effects of Heat and Pressure on Hot-Pressed Geopolymer,” *Construction and Building Materials*, V. 231, 2020, p. 117106. doi: 10.1016/j.conbuildmat.2019.117106

30. Lao, J.-C.; Huang, B.-T.; Fang, Y.; Xu, L.-Y.; Dai, J.-G.; and Shah, S. P., “Strain-Hardening Alkali-Activated Fly Ash/Slag Composites with Ultra-High Compressive Strength and Ultra-High Tensile Ductility,” *Cement and Concrete Research*, V. 165, 2023, p. 107075. doi: 10.1016/j.cemconres.2022.107075

31. Liang, G.; Yao, W.; and Wei, Y., “A Green Ultra-High Performance Geopolymer Concrete Containing Recycled Fine Aggregate: Mechanical Properties, Freeze-Thaw Resistance and Microstructure,” *The Science of the Total Environment*, V. 895, 2023, p. 165090. doi: 10.1016/j.scitotenv.2023.165090

32. Cheng, D.; Reiner, D. M.; Yang, F.; Cui, C.; Meng, J.; Shan, Y.; Liu, Y.; Tao, S.; and Guan, D., “Projecting Future Carbon Emissions from Cement Production in Developing Countries,” *Nature Communications*, V. 14, No. 1, 2023, p. 8213. doi: 10.1038/s41467-023-43660-x

33. Mahasenan, N.; Smith, S.; and Humphreys, K., “The Cement Industry and Global Climate Change: Current and Potential Future Cement Industry CO2 Emissions,” *Greenhouse Gas Control Technologies - 6th International Conference*, J. Gale and Y. Kaya, eds., Pergamon, Oxford, UK, 2003, pp. 995-1000. doi: 10.1016/B978-008044276-1/50157-4

34. Wetzel, A., and Middendorf, B., “Influence of Silica Fume on Properties of Fresh and Hardened Ultra-High Performance Concrete Based on Alkali-Activated Slag,” *Cement and Concrete Composites*, V. 100, 2019, pp. 53-59. doi: 10.1016/j.cemconcomp.2019.03.023

35. Hosan, A.; Haque, S.; and Shaikh, F., “Compressive Behaviour of Sodium and Potassium Activators Synthetized Fly Ash Geopolymer at Elevated Temperatures: A Comparative Study,” *Journal of Building Engineering*, V. 8, 2016, pp. 123-130. doi: 10.1016/j.jobe.2016.10.005

36. Li, P. P.; Brouwers, H. J. H.; Chen, W.; and Yu, Q., “Optimization and Characterization of High-Volume Limestone Powder in Sustainable Ultra-High Performance Concrete,” *Construction and Building Materials*, V. 242, 2020, p. 118112. doi: 10.1016/j.conbuildmat.2020.118112

37. Bahmani, H., and Mostofinejad, D., “A Review of Engineering Properties of Ultra-High-Performance Geopolymer Concrete,” *Developments in the Built Environment*, V. 14, 2023, p. 100126. doi: 10.1016/j.dibe.2023.100126

38. Zhang, H.; Ji, T.; He, B.; and He, L., “Performance of Ultra-High Performance Concrete (UHPC) with Cement Partially Replaced by Ground Granite Powder (GGP) under Different Curing Conditions,” *Construction and Building Materials*, V. 213, 2019, pp. 469-482. doi: 10.1016/j.conbuildmat.2019.04.058

39. Soliman, N.; Omran, A.; Aghaee, K.; Ozbulut, O.; and Tagnit-Hamou, A., “Synergistic Effect of Nano-to-Macro Waste Glass of Various Particle Sizes on Ultra-High-Performance Concrete: Tradeoff between Mix Design Parameters and Performance through a Statistical Design Approach,” *Journal of Building Engineering*, V. 95, 2024, p. 110129. doi: 10.1016/j.jobe.2024.110129

40. Shohan, A. A. A.; Zaid, O.; Arbili, M. M.; Alsulamy, S. H.; and Ibrahim, W. M., “Development of Novel Ultra-High-Performance Lightweight Concrete Modified with Dehydrated Cement Powder and Aerogel,” *Journal of Sustainable Cement-Based Materials*, V. 13, No. 3, 2024, pp. 1-24. doi: 10.1080/21650373.2023.2278134

41. Zhang, L.; Shen, H.; Xu, K.; Huang, W.; Wang, Y.; Chen, M.; and Han, B., “Effect of Ceramic Waste Tile as a Fine Aggregate on the Mechanical Properties of Low-Carbon Ultrahigh Performance Concrete,” *Construction and Building Materials*, V. 370, 2023, p. 130595. doi: 10.1016/j.conbuildmat.2023.130595

42. Leng, Y.; Rui, Y.; Zhonghe, S.; Dingqiang, F.; Jinnan, W.; Yonghuan, Y.; Qiqing, L.; and Xiang, H., “Development of an Environmental Ultra-High Performance Concrete (UHPC) Incorporating Carbonated Recycled Coarse Aggregate,” *Construction and Building Materials*, V. 362, 2023, p. 129657. doi: 10.1016/j.conbuildmat.2022.129657

43. Liu, J.; Wu, C.; Liu, Z.; Li, J.; Xu, S.; Liu, K.; Su, Y.; and Chen, G., “Investigations on the Response of Ceramic Ball Aggregated and Steel Fibre Reinforced Geopolymer-Based Ultra-High Performance Concrete (G-UHPC) to Projectile Penetration,” *Composite Structures*, V. 255, 2021, p. 112983. doi: 10.1016/j.compstruct.2020.112983

44. Alsalami, Z. H. A.; Harith, I. K.; and Dhahir, M. K., “Utilization of Dates Palm Kernel in High Performance Concrete,” *Journal of Building Engineering*, V. 20, 2018, pp. 166-172. doi: 10.1016/j.jobe.2018.07.015

45. Tamanna, K.; Raman, S. N.; Jamil, M.; and Hamid, R., “Coal Bottom Ash as Supplementary Material for Sustainable Construction: A Comprehensive Review,” *Construction and Building Materials*, V. 389, 2023, p. 131679. doi: 10.1016/j.conbuildmat.2023.131679

46. Panda, S.; Nanda, A.; and Panigrahi, S. K., “Potential Utilization of Waste Plastic in Sustainable Geopolymer Concrete Production: A Review,” *Journal of Environmental Management*, V. 366, 2024, p. 121705. doi: 10.1016/j.jenvman.2024.121705

47. Ryu, G. S.; Lee, Y. B.; Koh, K. T.; and Chung, Y. S., “The Mechanical Properties of Fly Ash-Based Geopolymer Concrete with Alkaline Activators,” *Construction and Building Materials*, V. 47, 2013, pp. 409-418. doi: 10.1016/j.conbuildmat.2013.05.069

48. Payá, J.; Agrela, F.; Rosales, J.; Morales, M. M.; and Borrachero, M. V., “13 - Application of Alkali-Activated Industrial Waste,” *New Trends in Eco-Efficient and Recycled Concrete*, J. de Brito and F. Agrela, eds., Woodhead Publishing, Sawston, UK, 2019, pp. 357-424. doi: 10.1016/B978-0-08-102480-5.00013-0

49. Cai, R., and Ye, H., “Clinkerless Ultra-High Strength Concrete Based on Alkali-Activated Slag at High Temperatures,” *Cement and Concrete Research*, V. 145, 2021, p. 106465. doi: 10.1016/j.cemconres.2021.106465

50. Liu, Y.; Zhang, Z.; Shi, C.; Zhu, D.; Li, N.; and Deng, Y., “Development of Ultra-High Performance Geopolymer Concrete (UHPGC): Influence of Steel Fiber on Mechanical Properties,” *Cement and Concrete Composites*, V. 112, 2020, p. 103670. doi: 10.1016/j.cemconcomp.2020.103670

51. Liu, Y.; Shi, C.; Zhang, Z.; Li, N.; and Shi, D., “Mechanical and Fracture Properties of Ultra-High Performance Geopolymer Concrete: Effects of Steel Fiber and Silica Fume,” *Cement and Concrete Composites*, V. 112, 2020, p. 103665. doi: 10.1016/j.cemconcomp.2020.103665

52. Ghasemzadeh Mousavinejad, S. H., and Sammak, M., “An Assessment of the Fracture Parameters of Ultra-High-Performance Fiber-Reinforced Geopolymer Concrete (UHPFRGC): The Application of Work of Fracture and Size Effect Methods,” *Theoretical and Applied Fracture Mechanics*, V. 117, 2022, p. 103157. doi: 10.1016/j.tafmec.2021.103157

53. Paruthi, S.; Rahman, I.; Husain, A.; Khan, A. H.; Manea-Saghin, A.-M.; and Sabi, E., “A Comprehensive Review of Nano Materials in Geopolymer Concrete: Impact on Properties and Performance,” *Developments in the Built Environment*, V. 16, 2023, p. 100287. doi: 10.1016/j.dibe.2023.100287

54. Moujoud, Z.; Sair, S.; Ait Ousaleh, H.; Ayouch, I.; El Bouari, A.; and Tanane, O., “Geopolymer Composites Reinforced with Natural Fibers: A Review of Recent Advances in Processing and Properties,” *Construction and Building Materials*, V. 388, 2023, p. 131666. doi: 10.1016/j.conbuildmat.2023.131666

55. Bhutta, A.; Borges, P. H. R.; Zanotti, C.; Farooq, M.; and Banthia, N., “Flexural Behavior of Geopolymer Composites Reinforced with Steel and Polypropylene Macro Fibers,” *Cement and Concrete Composites*, V. 80, 2017, pp. 31-40. doi: 10.1016/j.cemconcomp.2016.11.014

56. Aisheh, Y. I. A.; Atrushi, D. S.; Akeed, M. H.; Qaidi, S.; and Tayeh, B. A., “Influence of Polypropylene and Steel Fibers on the Mechanical Properties of Ultra-High-Performance Fiber-Reinforced Geopolymer Concrete,” *Case Studies in Construction Materials*, V. 17, 2022, p. e01234. doi: 10.1016/j.cscm.2022.e01234

57. Rabiaa, E.; Mohamed, R. S.; Sofi, W. H.; and Tawfik, T. A., “Developing Geopolymer Concrete Properties by Using Nanomaterials and Steel Fibers,” *Advances in Materials Science and Engineering*, V. 2020, No. 1, 2020, p. 5186091. doi: 10.1155/2020/5186091

58. Çevik, A.; Alzeebaree, R.; Humur, G.; Niş, A.; and Gülşan, M. E., “Effect of Nano-Silica on the Chemical Durability and Mechanical Performance of Fly Ash Based Geopolymer Concrete,” *Ceramics International*, V. 44, No. 11, 2018, pp. 12253-12264. doi: 10.1016/j.ceramint.2018.04.009

59. Yoo, D.-Y.; Oh, T.; and Banthia, N., “Nanomaterials in Ultra-High-Performance Concrete (UHPC) – A Review,” *Cement and Concrete Composites*, V. 134, 2022, p. 104730. doi: 10.1016/j.cemconcomp.2022.104730

60. SAS Institute, Inc., “JMP 9 Design of Experiments Guide,” Cary, NC, 2010.

61. Polikar, R., “Ensemble Learning,” *Ensemble Machine Learning: Methods and Applications*, C. Zhang and Y. Ma, eds., Springer, New York, 2012, pp. 1-34. doi: 10.1007/978-1-4419-9326-7_1

62. Kumar, A.; Arora, H. C.; Kapoor, N. R.; Kumar, K.; Hadzima-Nyarko, M.; and Radu, D., “Machine Learning Intelligence to Assess the Shear Capacity of Corroded Reinforced Concrete Beams,” *Scientific Reports*, V. 13, No. 1, 2023, p. 2857. doi: 10.1038/s41598-023-30037-9

63. Song, H.; Ahmad, A.; Farooq, F.; Ostrowski, K. A.; Maślak, M.; Czarnecki, S.; and Aslam, F., “Predicting the Compressive Strength of

Concrete with Fly Ash Admixture Using Machine Learning Algorithms," *Construction and Building Materials*, V. 308, 2021, p. 125021. doi: 10.1016/j.conbuildmat.2021.125021

64. Mousavinejad, S. H. G., and Sammak, M., "Strength and Chloride Ion Penetration Resistance of Ultra-High-Performance Fiber Reinforced Geopolymer Concrete," *Structures*, V. 32, 2021, pp. 1420-1427. doi: 10.1016/j.istruc.2021.03.112

65. Kathirvel, P., and Sreekumaran, S., "Sustainable Development of Ultra High Performance Concrete Using Geopolymer Technology," *Journal of Building Engineering*, V. 39, 2021, p. 102267. doi: 10.1016/j.jobe.2021.102267

66. Rakesh, P.; Rao, S. V.; Kumar, P. R.; and De Brito, J., "A Study on the Strength and Microstructure Properties of High Strength Geopolymer Concrete (HSGPC)," *Innovative Infrastructure Solutions*, V. 10, No. 6, 2025, p. 240. doi: 10.1007/s41062-025-02012-y

67. Liu, J.; Wu, C.; Li, J.; Liu, Z.; Xu, S.; Liu, K.; Su, Y.; Fang, J.; and Chen, G., "Projectile Impact Resistance of Fibre-Reinforced Geopolymer-Based Ultra-High Performance Concrete (G-UHPC)," *Construction and Building Materials*, V. 290, 2021, p. 123189. doi: 10.1016/j.conbuildmat.2021.123189

68. Midhin, M. A. K.; Wong, L. S.; Ahmed, A. N.; Jasim, A. M. D. A.; and Paul, S. C., "Strength and Chemical Characterization of Ultra High-Performance Geopolymer Concrete: A Coherent Evaluation," *Civil Engineering Journal*, V. 9, No. 12, 2023, pp. 3254-3277. doi: 10.28991/CEJ-2023-09-12-020

69. Althoey, F.; Zaid, O.; Alsulamy, S.; Martínez-García, R.; de Prado-Gil, J.; and Arbili, M. M., "Experimental Study on the Properties of Ultra-High-Strength Geopolymer Concrete with Polypropylene Fibers and Nano-Silica," *PLoS One*, V. 18, No. 4, 2023, p. e0282435. doi: 10.1371/journal.pone.0282435

70. Breiman, L., "Random Forests," *Machine Learning*, V. 45, No. 1, 2001, pp. 5-32. doi: 10.1023/A:1010933404324

71. Schapire, R. E., "A Brief Introduction to Boosting," *Proceedings of the 16th International Joint Conference on Artificial Intelligence - Volume 2*, Morgan Kaufmann Publishers Inc., San Francisco, CA, 1999, pp. 1401-1406.

72. Chen, T., and Guestrin, C., "XGBoost: A Scalable Tree Boosting System," *Proceedings of the 22nd ACM SIGKDD International Conference on Knowledge Discovery and Data Mining*, Association for Computing Machinery, New York, 2016, pp. 785-794. doi: 10.1145/2939672.2939785

73. Džeroski, S., and Ženko, B., "Is Combining Classifiers with Stacking Better than Selecting the Best One?" *Machine Learning*, V. 54, No. 3, 2004, pp. 255-273. doi: 10.1023/B:MACH.0000015881.36452.6e

74. Abdellatief, M.; Hassan, Y. M.; Elnabwy, M. T.; Wong, L. S.; Chin, R. J.; and Mo, K. H., "Investigation of Machine Learning Models in Predicting Compressive Strength for Ultra-High-Performance Geopolymer Concrete: A Comparative Study," *Construction and Building Materials*, V. 436, 2024, p. 136884. doi: 10.1016/j.conbuildmat.2024.136884

75. Aghaee, K., and Roshan, A., "Predicting Time to Cracking of Concrete Composites under Restrained Shrinkage: A Review with Insights from Statistical Analysis and Ensemble Machine Learning Approaches," *Journal of Building Engineering*, V. 97, 2024, p. 110856. doi: 10.1016/j.jobe.2024.110856

76. Kazemi, F.; Shafighfard, T.; Jankowski, R.; and Yoo, D.-Y., "Active Learning on Stacked Machine Learning Techniques for Predicting Compressive Strength of Alkali-Activated Ultra-High-Performance Concrete," *Archives of Civil and Mechanical Engineering*, V. 25, No. 1, 2024, p. 24. doi: 10.1007/s43452-024-01067-5

ACI MATERIALS JOURNAL TECHNICAL PAPER

Title No. 122-M37

Impact of Under-Sulfated Cement on Concrete Performance: Detection and Mitigation Using Real-Time Slump Monitoring

by Justin Dickey, Kevin J. Folliard, and Thanos Drimalas

This study investigates the impact of under-sulfated cement combined with high-calcium fly ash and lignosulfonate-based admixtures in ready mixed concrete, leading to rapid stiffening and delayed setting. Using an on-board slump-monitoring system (SMS) installed on a ready mixed concrete truck, significant increases in water demand were recorded to maintain target slumps, with mixtures showing minimal slump response to water additions. Laboratory tests, including isothermal calorimetry and mortar trials, confirmed the under-sulfated cement's inadequate sulfate levels as the cause. Optimal sulfate addition was determined through calorimetry, and adjustments with gypsum effectively remedied rapid stiffening and delayed setting. This research demonstrates that an SMS can detect undesirable combinations of cement, fly ash, and admixtures in concrete, allowing real-time corrections. It underscores the importance of optimized sulfate levels in cement, particularly when using high-calcium fly ash combined with some high-range water reducers, to achieve desired concrete performance under varying field conditions.

Keywords: flash setting; fly ash (FA); high-range water reducer; incompatibility issues; on-board slump-monitoring system (SMS); setting time.

INTRODUCTION

The role of sulfate in portland cement hydration has been thoroughly researched and documented. The seminal research on this topic took place in 1946 (Lerch 1946). Early research used 1-day compressive strength to determine optimum sulfate levels for portland cement per ASTM C563-20 (2020) or variations of that standard. Experience has shown that even if determined in standard conditions, this optimal sulfate content will typically ensure the control of flash setting, false setting, delayed setting, and delayed strength gain for a broad range of use conditions (for example, different ambient temperatures, combinations with supplementary cementitious materials [SCMs], chemical admixtures, and so on).

The increased use of high-calcium fly ash (FA) with certain admixtures has created an environment where the 1-day compressive strength based on cement only (no SCMs or admixtures) may not predict undesirable outcomes. Slow setting and slow strength gain rates have been linked to inadequate sulfate levels in systems with high-calcium FA and certain types of admixtures (Meyer 1976; Khalil and Ward 1978; Johnson 1987; Helmuth et al. 1995; Ramachandran 1995; Roberts 1995; Hills and Tang 2004; Detwiler and Shkolnik 2005; Sandberg and Roberts 2005; Cost 2006; Taylor et al. 2006; Wang et al. 2006; Roberts and Taylor 2007; Lashley 2009; Taylor 2007).

This research examines an instance where an under-sulfated cement was paired with a high-calcium FA and a lignosulfonate (LS)-based admixture during daily ready mixed concrete operations and placed in the field. The resulting rapid stiffening was recorded by an on-board slump-monitoring and management system (SMS), and water additions were recorded along with the slump response of the concrete. The SMS uses an algorithm that combines hydraulic pressure and drum speed sensors with load size and mixture properties to measure slump. The algorithm is powered by machine learning using data from millions of loads of concrete to create a robust measuring system. Once a slump is predicted, the system uses adaptive algorithms to "learn" how much water or admixture is needed to reach the target slump.

Once the concrete was in place, delayed setting times were reported. Samples of the cement and Class C FA were collected from the ready mixed concrete plant and chemically evaluated, including the determination of the sulfate content of the cement and the calcium oxide content of the FA. Isothermal calorimetry was used to assess heat generation, and mortar mixtures were used to evaluate compressive strength, slump loss, lack of slump response to water additions, delayed setting time, and delayed strength gain. Using isothermal calorimetry, an optimal sulfate addition was determined and confirmed with the setting time and strength gain of mortar mixtures.

RESEARCH SIGNIFICANCE

This research confirms through laboratory mortar trials that the use of an SMS can help identify when an undesirable combination of cement, FA, and admixture is present in a concrete mixture. An SMS could potentially use an algorithm to detect this reaction and alert the concrete truck driver and quality control representatives so that either an admixture could be added to the concrete, or the load can be aborted and returned to the batch plant if the problem cannot be addressed with on-board monitoring and additions

---

ACI Materials Journal, V. 122, No. 5, September 2025.

MS No. M-2024-434.R1, doi: 10.14359/51749036, received May 24, 2025, and reviewed under Institute publication policies. Pertinent discussion including author's closure, if any, will be published ten months from this journal's date if the discussion is received within four months of the paper's print publication.

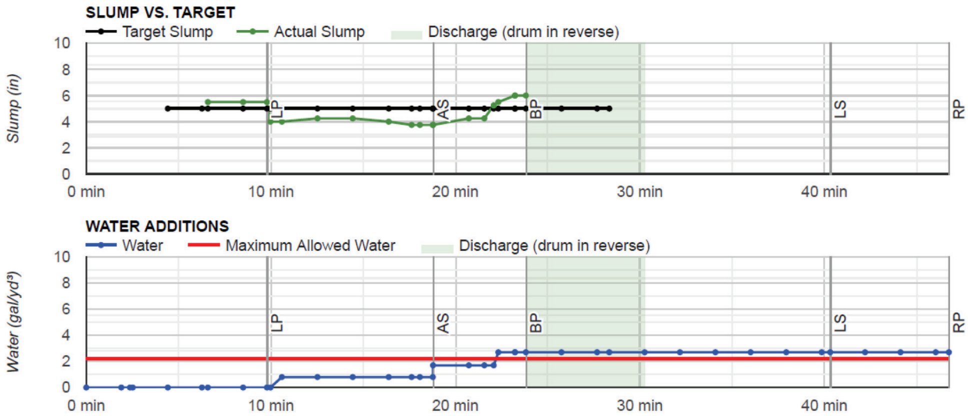

Fig. 1—Concrete Load 1A. (Note: 1 in. = 25.4 mm; 1 gal./yd^3 = 4.95 L/m^3.)

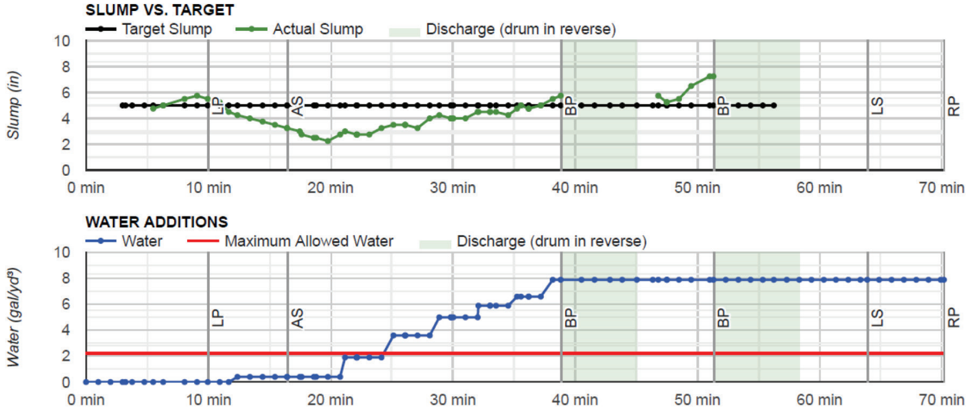

Fig. 2—Concrete Load 1B. (Note: 1 in. = 25.4 mm; 1 gal./yd^3 = 4.95 L/m^3.)

of water and/or chemical admixtures. Furthermore, this research reconfirms that an increase in cement sulfate will remedy rapid stiffening and delayed setting of mortar mixtures containing the previously described materials.

EXPERIMENTAL INVESTIGATION AND PROCEDURES

Field investigation

In early November 2022, an unknown number of cement tankers delivered under-sulfated cement to multiple ready mixed concrete plants. This cement, when combined with high-calcium FA, an LS-based admixture, or a combination of both, caused rapid stiffening of the concrete, followed by delayed setting. Figure 1 shows the typical slump life and water demand of a 10 yd^3 (7.6 m^3) load of concrete with properly sulfated cement, high-calcium FA, and an LS admixture. These data were provided by an on-board slump-monitoring and adjustment system. This concrete load required 1.7 gal./yd^3 (8.4 L/m^3) of water to achieve and hold a 5 in. (127 mm) slump. Each graph shows two plots. The top plot shows slump versus time, with the status of “leave plant,” “arrive site,” and “begin placement” indicated with the vertical axes LP, AS, and BP, respectively. The lower plot shows the volume of water added versus time. For this load of concrete, the beginning water-cementitious materials ratio (*w*/*cm*) was 0.58, and the as-placed *w*/*cm* was 0.62.

Figure 2 shows the rapid slump loss and increased water demand that occurred due to the under-sulfated cement being incorporated into the mixture. The mixture design is the same as the previous concrete load shown in Fig. 1. This load required 6.6 gal./yd^3 (32.7 L/m^3) to keep and hold a 5 in. (127 mm) slump. This is a 296% increase in water demand over the normal concrete load. For this load of concrete, the beginning *w*/*cm* was 0.58, and the as-placed *w*/*cm* was 0.72.

Note that the time from LP to BP for Loads 1A and 1B was different. However, water additions needed to hold the slump for all loads started at approximately the same time, based on the time from when the concrete was batched. Load 1A water additions began at the 11-minute mark, while Load 1B water additions began at 12 and 13 minutes from batching. Load 1B would have still been below the target slump upon arrival at the project site had it needed to discharge concrete at the same concrete age as Load 1A.

Figure 3 shows the typical slump life and water demand of a 10 yd^3 (7.6 m^3) load of concrete with properly sulfated cement combined with an LS admixture. There was no high-calcium FA present in this load. This load required 1.5 gal./yd^3 (7.4 L/m^3) to achieve and hold a 5 in. (127 mm) slump. For this load of concrete, the beginning *w*/*cm* was 0.58, and the as-placed *w*/*cm* was 0.61.

Figure 4 shows the rapid slump loss and increased water demand that occurred due to the under-sulfated cement being incorporated into the mixture. The mixture design was the same as Load 2A. This load required 6.0 gal./yd^3 (29.7 L/m^3) to keep and hold a 5 in. (127 mm) slump. This is a 377% increase in water demand compared to Load 2A. For

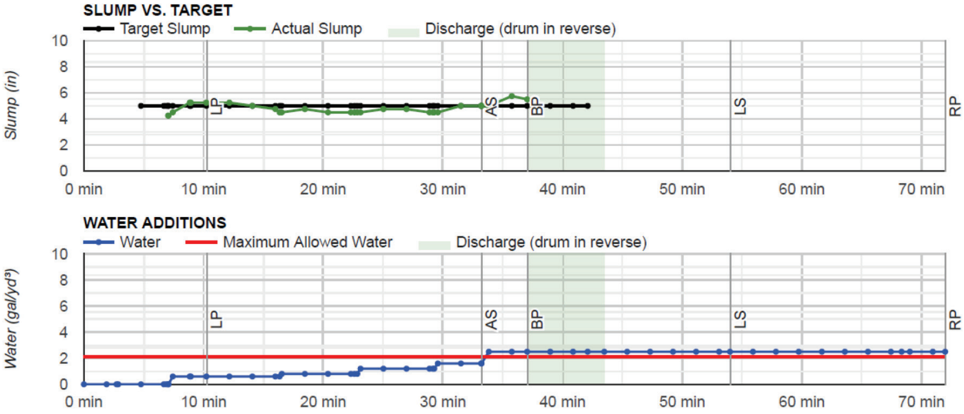

Fig. 3—Concrete Load 2A. (Note: 1 in. = 25.4 mm; 1 gal./yd^3 = 4.95 L/m^3.)

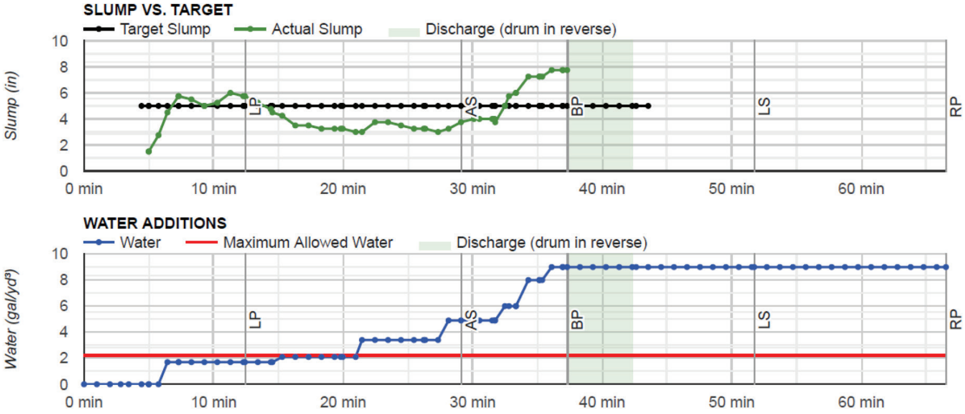

Fig. 4—Concrete Load 2B. (Note: 1 in. = 25.4 mm; 1 gal./yd^3 = 4.95 L/m^3.)

this load of concrete, the beginning *w*/*cm* was 0.58, and the as-placed *w*/*cm* was 0.70.

The LP to BP times for Loads 2A and 2B were similar. Similar to Loads 1A and 1B, the water additions for 2A and 2B all started at approximately the same time from batching, which in this case was approximately 7 minutes.

Figure 5 shows the normal slump and water demand after the under-sulfated cement had been depleted from the plant. This load responded to a 4.0 gal./yd^3 (19.8 L/m^3) water addition, with the slump increasing by 4 in. (101.6 mm), which was to be expected. The final *w*/*cm* for Load 3A was 0.66.

This unique data set showed, in real time, the adverse effects of under-sulfated cement on hydration. The effect was similar for concrete with and without Class C FA. Water additions were initiated to try to meet the target slump, but the mixtures with the under-sulfated cement minimally responded to water additions, leading to excessive water additions. These mixtures also rapidly stiffened and were very slow to set, based on feedback from the field. When the under-sulfated cement made its way through the cement silo and was replaced with a properly sulfated cement, the problems went away.

Laboratory investigation and procedures

Under-sulfated cement was collected from a ready mixed concrete plant silo, along with an ASTM C618-23 (2023) high-calcium FA. Both an ASTM C494/C494M-19 (2019) LS-based and polycarboxylate-based admixture were also collected from a ready mixed concrete plant. An ASTM C150/C150M-22 (2022) control cement, with normal sulfate levels, was acquired from the same manufacturer as the under-sulfated cement. Gypsum and ASTM C778-21 (2021) standard graded sand were obtained from commercial sources. Table 1 identifies each material with an ID that is used as a material identification code throughout this research and within this paper. Table 2 shows the chemical analysis of the cementitious materials, which was calculated using X-ray diffraction (XRD) and Rietveld analysis. XRD was performed with an X-ray diffractometer, and Rietveld analysis was performed using analysis software. X-ray fluorescence (XRF) was also performed, and the chemical analysis is shown in Table 3; potential compounds per the Bogue equation are listed in Table 4. Low sulfate was confirmed for cement U based on the low content of gypsum present through XRD and the reduced SO_3 result found through XRF.

Table 5 shows the particle-size distribution of each cementitious material, which was performed using a particle-size analyzer. While cement U had a larger median particle size than cement C, it was not sufficiently different to drastically impact the fresh and hardened properties of mortar compared to the overwhelming impact of the cement sulfate content.

Table 6 shows the isothermal calorimetry (as per ASTM C1702-23e1 [2023]) for various paste mixture combinations using an eight-channel calorimeter. The calorimeter was set at 73.4°F (23°C) for 7 days. The cementitious materials

Table 1—Materials for calorimetry and mortar mixtures

ID	Material
U	Under-sulfated ASTM C150/C150M-22 Type I
C	Normal-sulfated ASTM C150/C150M-22 Type I
FA	ASTM C618-23 Class C fly ash
LS	ASTM C494/C494M-19 Type A and F lignosulfonate-based admixture
PC	ASTM C494/C494M-19 Type A and F polycarboxylate-based admixture
G	Terra alba No. 1 gypsum
Sand	ASTM C778-21 standard graded sand

and admixtures that were used can be determined using the material IDs found in Table 1.

Figures 6 to 9 show the first 48 hours of heat flow for the combinations listed in Table 6. It was decided, for this research, to focus on the initial 48 hours of hydration due to the undesirable interaction of the cementitious materials observed at an early age in ready mixed concrete loads. Figure 10 is a bar graph that places similar mixtures side-by-side to more easily show the difference in cumulative heat, with the variable being cement.

Based on the isothermal calorimetry results listed previously, a new set of mixtures was evaluated that included only cement, gypsum, and water. This was done to determine the amount of gypsum needed to produce a cumulative heat

Table 2—X-ray diffraction analysis of cement and fly ash

	Percent by mass						
ID	C_3S	C_2S	C_4AF	C_3A cubic	C_3A orthorhombic	K_2SO_4	Gypsum
U	51.6	29.5	5.8	8.1	2.2	1.9	0.8
C	50.0	27.63	7.48	5.29	1.1	1.8	4.3
FA	0.0	37.76	0.0	1.97	8.72	0.0	6.73

Table 3—X-ray fluorescence analysis of cement and fly ash

	Percent by mass									
ID	SiO_2	Al_2O_3	Fe_2O_3	CaO	MgO	SO_3	Na_2O	K_2O	LOI	Alk
U	21.8	5.5	2.1	62.3	1.3	2.4	0.15	0.91	4.22	0.75
C	21.0	4.7	3.0	61.2	1.2	2.9	0.14	0.84	1.43	0.69
FA	37.0	21.3	5.57	22.89	4.21	2.26	1.63	0.56	0.79	2.0

Note: LOI is loss on ignition; Alk is alkalies.

Table 4—Potential cement compounds per Bogue equation

	Percent by mass			
ID	C_3S	C_2S	C_4AF	C_3A
U	41.5	31	6.3	11
C	45.9	25.6	9.2	7.2

Table 5—Particle-size distribution of cement, fly ash, and gypsum

ID	$d(0.1)$	$d(0.5)$	$d(0.9)$
U	3.77	16.52	47.87
C	2.16	13.40	39.72
FA	1.33	9.74	40.36
G	0.62	9.04	28.85

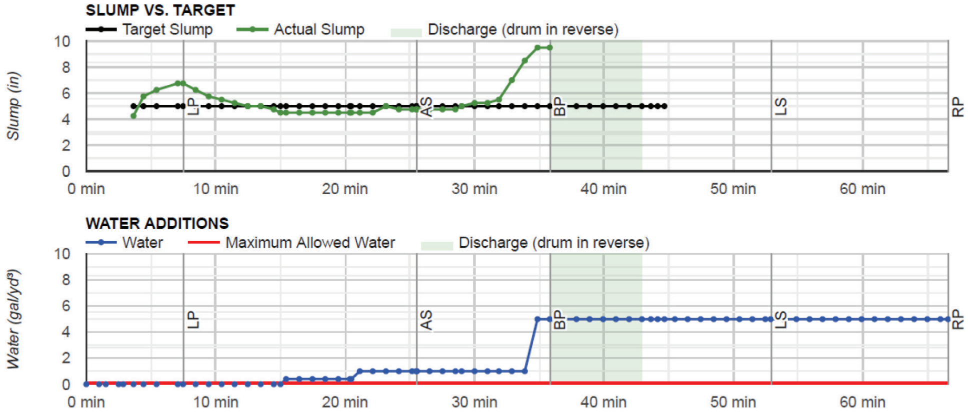

Fig. 5—Concrete Load 3A. (Note: 1 in. = 25.4 mm; 1 gal./yd^3 = 4.95 L/m^3.)

similar to the mixture C-O. These new mixtures are found in Table 7. The number found within the mixture ID indicates, in percent by mass of cement, the amount of gypsum added. The same mixing procedure and isothermal calorimetry settings used previously were also used for these mixtures.

Figure 11 shows normalized heat flow for the gypsum-modified mixtures and also includes mixtures C-0.0 and U-0.0, which contained no gypsum. Figure 12 shows the cumulative heat for these same mixtures. Based on cumulative heat at 48 hours, it was determined that mixture U-1.0, with a 1% gypsum addition, would be the basis for correcting the under-sulfated cement interaction issue. A comparison of cumulative heat at 48 hours between mixtures C-0.0 and U-1.0 is shown in Fig. 13.

To reproduce in the laboratory what happened in the field, the concrete mixture design that was batched by the ready mixed plant was reproduced as a mortar mixture. The mortar mixtures are listed in Table 8. The letter M at the end of each design ID indicates that they were mortar mixtures. The other design ID components can be identified using Table 1. An 8 qt. (7.57 L) mixer was used, and materials were added to the mixing bowl in the same sequence that they were batched at the ready mixed concrete plant. The sequencing was as follows: 80% of the batch water, 80% of the sand,

Table 6—Isothermal calorimetry paste mixtures

Mixture ID	Cement, lb (g)	Fly ash, lb (g)	Water reducer, oz. (g)	Water, lb (g)
C-0	0.11 (50)	0	0	0.04 (20)
C-LS	0.11 (50)	0	0.005 (0.15)	0.04 (20)
C-FA	0.07 (30)	0.04 (20)	0	0.04 (20)
C-LS-FA	0.07 (30)	0.04 (20)	0.005 (0.15)	0.04 (20)
U-0	0.11 (50)	0	0	0.04 (20)
U-LS	0.11 (50)	0	0.005 (0.15)	0.04 (20)
U-FA	0.07 (30)	0.04 (20)	0	0.04 (20)
U-LS-FA	0.07 (30)	0.04 (20)	0.005 (0.15)	0.04 (20)

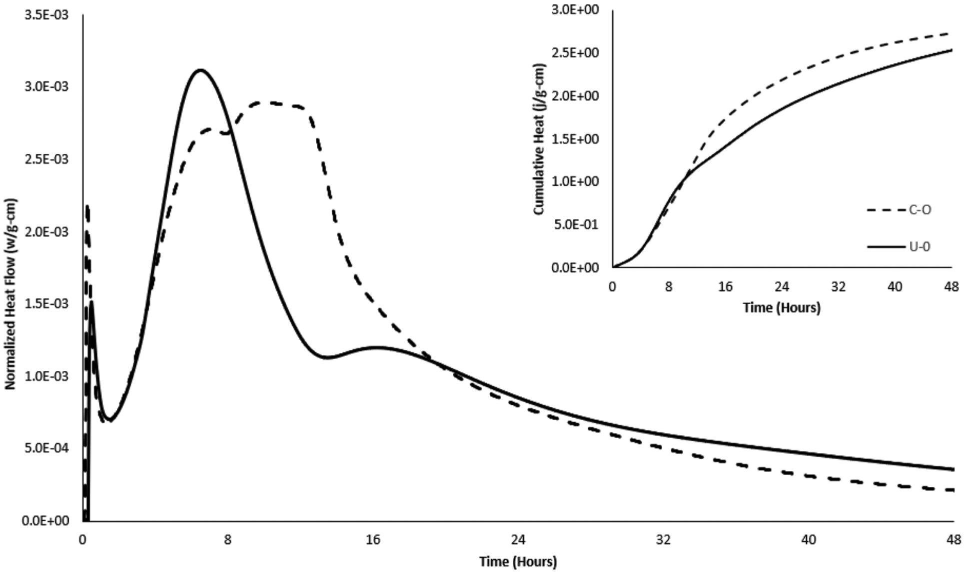

Fig. 6—Heat flow and cumulative heat (upper right corner) of cements C and U at 48 hours.

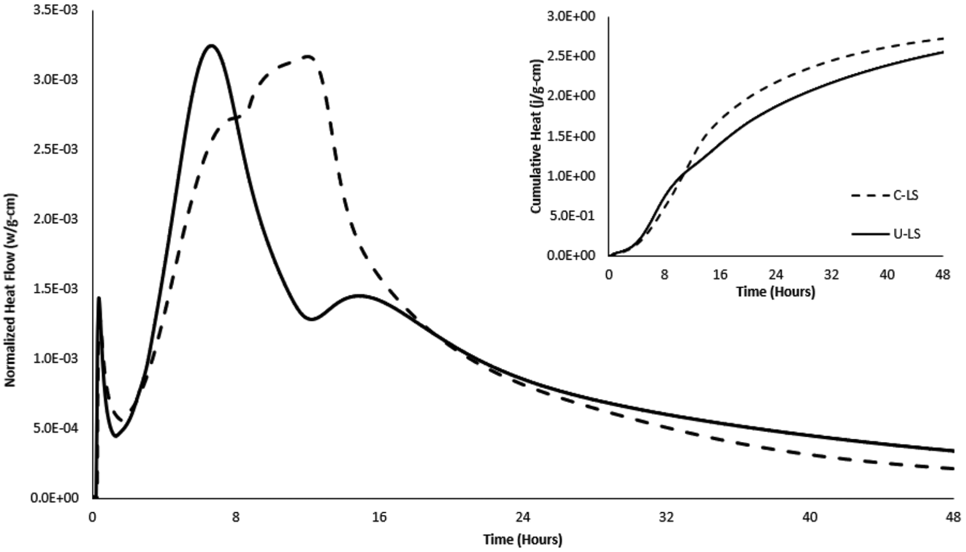

Fig. 7—Heat flow and cumulative heat (upper right corner) of cements C and U with LS admixture at 48 hours.

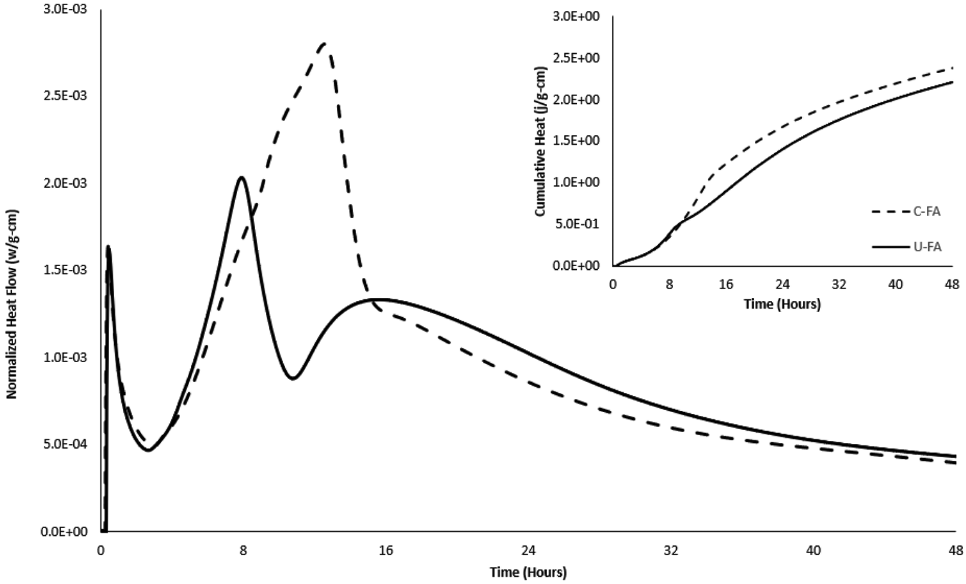

Fig. 8—Heat flow and cumulative heat (upper right corner) of cements C and U with FA at 48 hours.

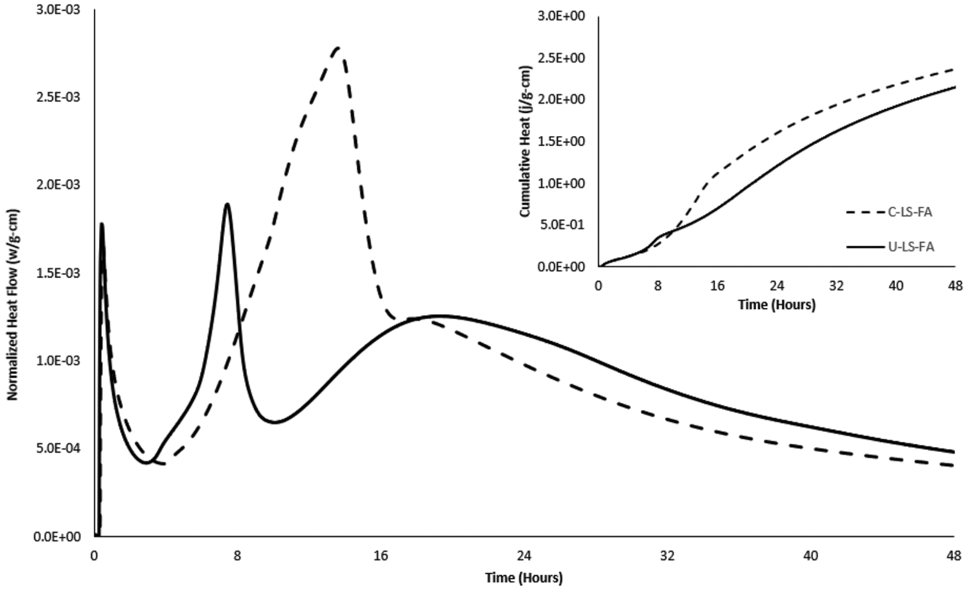

Fig. 9—Heat flow and cumulative heat (upper right corner) of cements C and U with LS and FA at 48 hours.

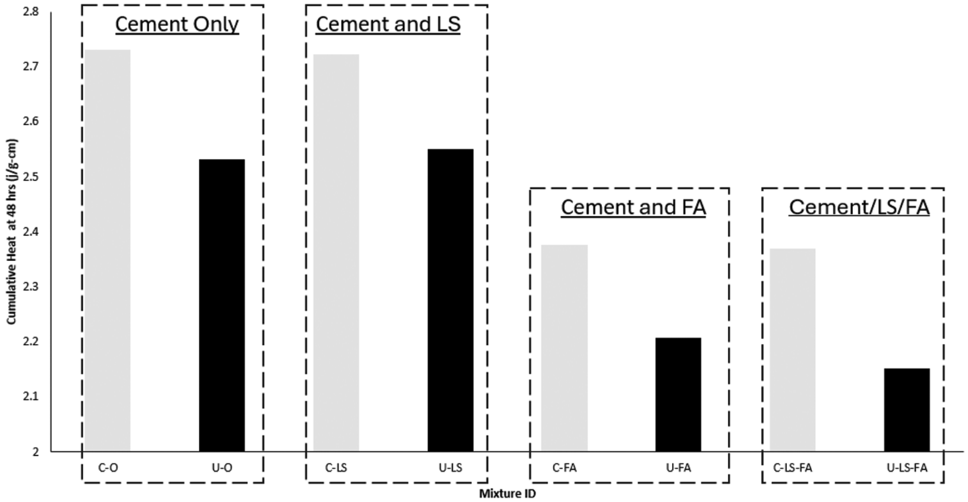

Fig. 10—Comparisons of cumulative heat at 48 hours.

Table 7—Isothermal calorimetry mixtures with gypsum additions

Mixture ID	Cement, oz. (g)	Gypsum, oz. (g)	Water, oz. (g)
C-0.0	1.76 (50)	0	0.71 (20)
U-0.0	1.76 (50)	0	0.71 (20)
U-0.5	1.75 (49.75)	0.0088 (0.25)	0.71 (20)
U-1.0	1.74 (49.5)	0.017 (0.5)	0.71 (20)
U-1.5	1.73 (49.25)	0.026 (0.75)	0.71 (20)
U-2.0	1.72 (49)	0.035 (1)	0.71 (20)
U-2.5	1.725 (48.75)	0.044 (1.25)	0.71 (20)
U-3.0	1.71 (48.5)	0.053 (1.5)	0.71 (20)

100% of cementitious materials, the remaining 20% of sand, and the remaining 20% of batch water with 100% of admixture mixed with this final portion of water. The mortar was mixed for 2 minutes on the low-speed setting, and an initial slump measurement was taken.

Along with the concrete mixture that was batched, the water additions that took place through the on-board slump-monitoring and adjustment system were reproduced, and water was added to the mortar mixture at the same ages that water was added to the concrete mixture in the truck. After each water addition, the mortar continued to mix for 1 minute. The mixer was stopped, and the slump was measured with a mini slump cone. The procedure for slump testing was as follows: The mold is placed in the center of a 12 x 12 in. (305 x 305 mm) poly(methyl methacrylate)

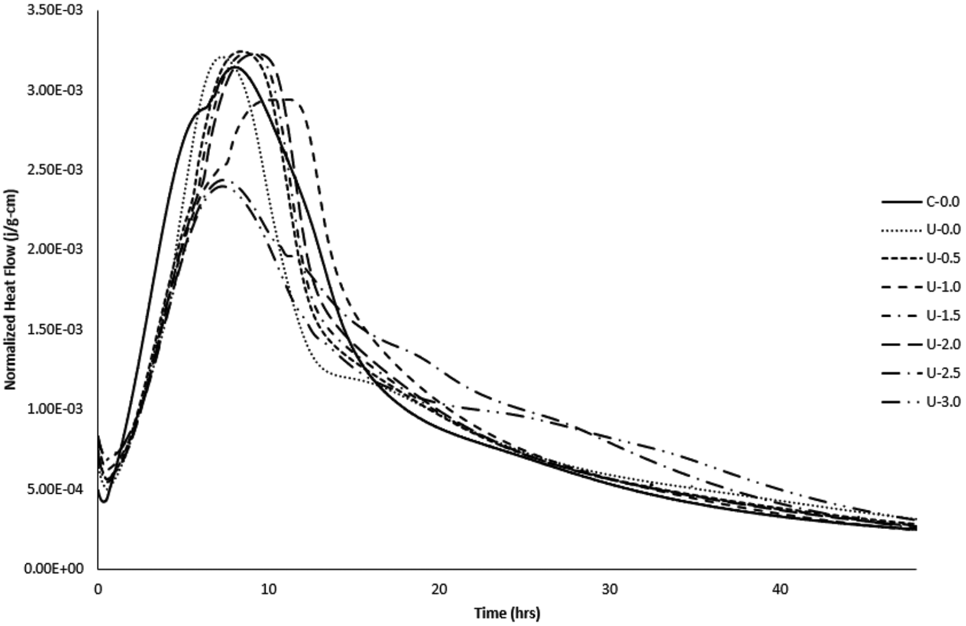

Fig. 11—Heat flow for control and paste mixtures with gypsum addition.

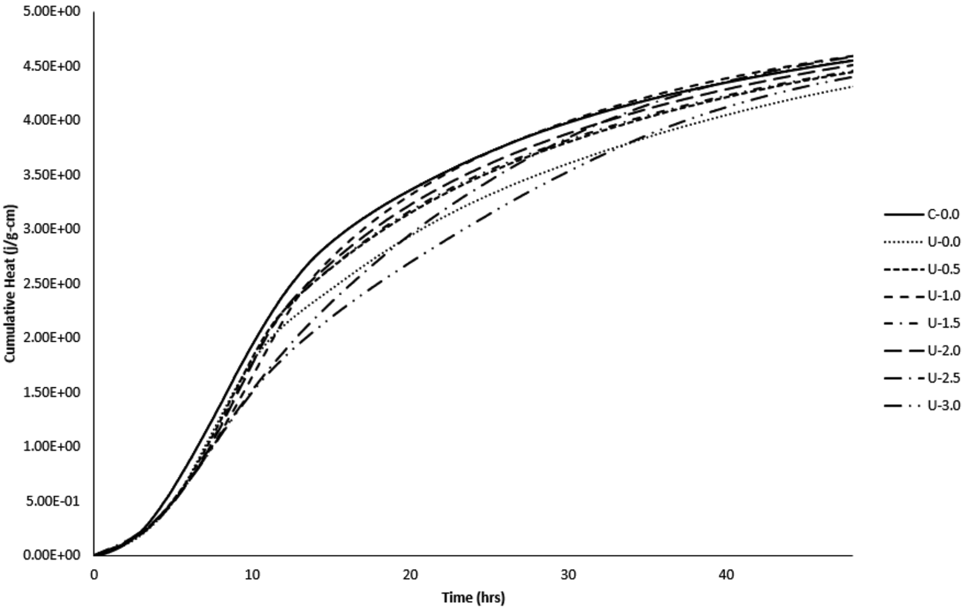

Fig. 12—Cumulative heat for control and paste mixtures with gypsum addition.

Table 8—Mortar mixture components variables

Mixture ID	Cement, lb (g)	Fly ash, lb (g)	Water, lb (g)	Graded sand, lb (g)	Water reducer, oz. (mL)	Gypsum, lb (g)
U-LS-FA-M	1.5 (678)	0.644 (292)	1.25 (566)	7.56 (3429)	0.113 (3.2)	0
C-LS-FA-M	1.5 (678)	0.644 (292)	1.25 (566)	7.56 (3429)	0.113 (3.2)	0
U-LS-FA-G-M	1.5 (678)	0.644 (292)	1.25 (566)	7.56 (3429)	0.113 (3.2)	0.015 (6.78)
U-PC-FA-M	1.5 (678)	0.644 (292)	1.25 (566)	7.56 (3429)	0.458 (1.3)	0

Table 9—Mortar mixture water additions

Time from beginning batch, minutes							
0	12	21	25	29	32	35	38
Water, oz. (g)							
0.00	0.274 (7.78)	1.03 (29.2)	1.164 (33)	0.960 (27.2)	0.617 (17.5)	0.480 (13.6)	0.892 (25.3)
Cumulative *w*/*cm*							
0.584	0.591	0.622	0.656	0.684	0.702	0.716	0.742

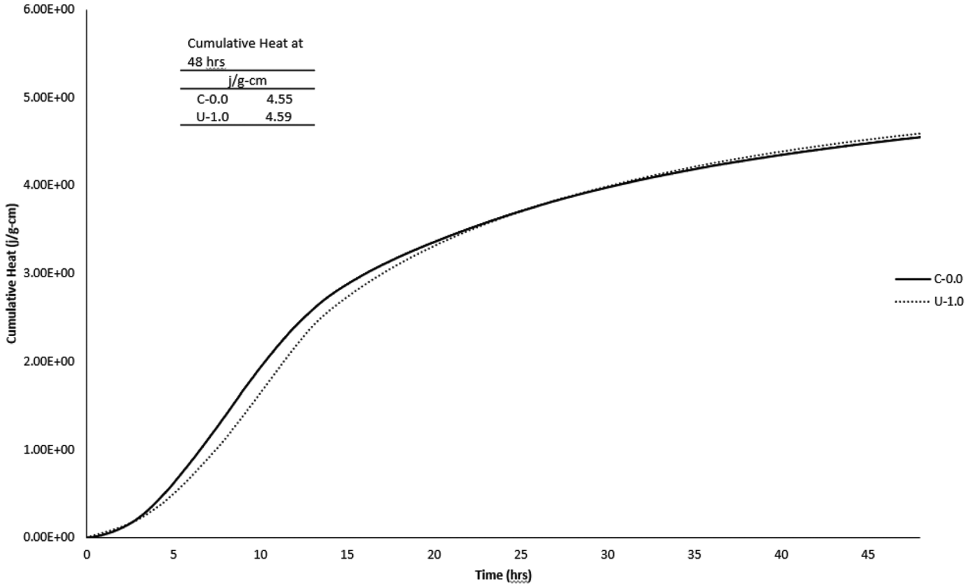

Fig. 13—Cumulative heat curve for cement C and paste mixtures with 1% gypsum addition (cumulative heat at 48 hours in upper left).

square and filled halfway to the top with mortar. A rubber tamping rod was used to tamp the mortar 25 times, penetrating halfway down. Then the mold was filled to the top with mortar, and the tamping rod was used in the same manner as the first layer. The top was struck-off even with the top of the cone, and the cone was pulled straight up as quickly as possible. Slump was measured to the displaced center of the top of the mortar. Table 9 shows the mass of water added at each time interval from the batch, along with the cumulative *w*/*cm* at each time interval. Figure 14 shows slump versus time for each mixture.

A sample was taken from each mortar mixture at the completion of all water additions and placed in an isothermal calorimeter. Temperature settings were the same as the isothermal calorimetry settings used earlier in this research. Heat flow and cumulative heat calorimetry results are found in Fig. 15 to 17. In addition, compressive strength (ASTM C109/C109M-23 [2023]) and time of setting (ASTM C403/C403M-23 [2023]) testing were conducted for each mixture. Compressive strength results are shown in Table 10, and time of setting is shown in Fig. 18. Per ASTM C403/C403M-23, initial setting of concrete is generally accepted to take place at 500 psi (3.45 MPa) and is when initial finishing operations can commence. Research has shown that initial finishing operations for concrete begin well before a 500 psi (3.45 MPa) value is reached through a mortar sample (Lee and Hover 2016); however, this value was used simply as a reference point to show the difference in setting when comparing the different mortar mixtures.

DISCUSSION

Rapid slump loss and delayed setting in the field were initially attributed to low sulfate content of the cement and were confirmed by chemical analysis by other parties prior to the commencement of this research. This research confirmed the low sulfate nature of the cement through additional XRF and XRD analysis. While ASTM C150/C150M-22 sets a maximum SO_3 limit of 3% by mass, many cement producers

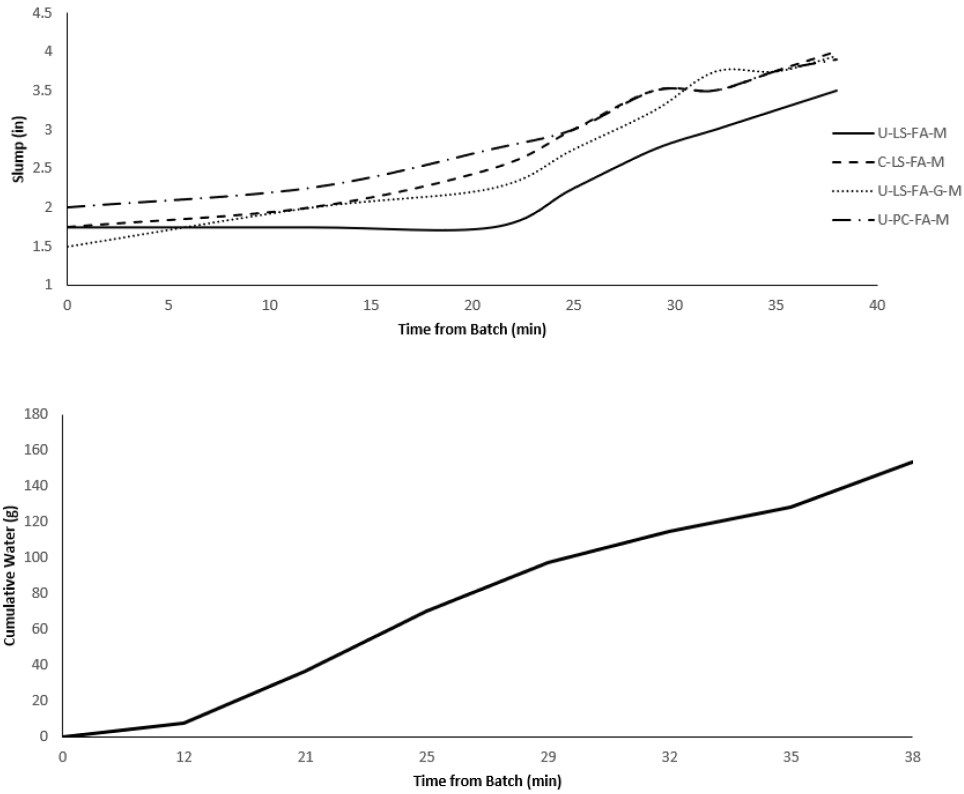

Fig. 14—(Top plot) Slump versus time for mortar mixtures; and (bottom plot) cumulative added water versus time. (Note: 1 in. = 25.4 mm; 1 g = 0.035 oz.)

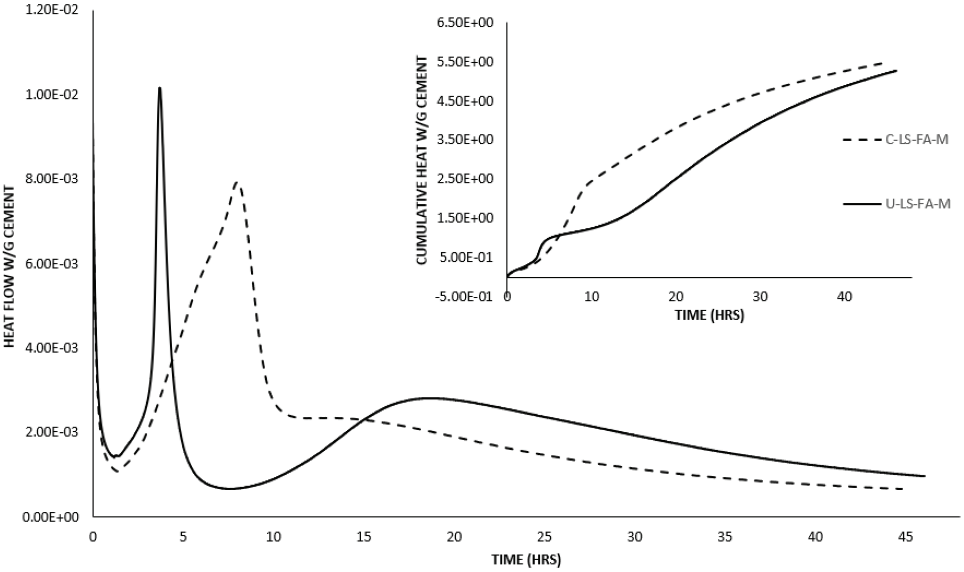

Fig. 15—Heat flow and cumulative heat (upper right corner) of mortar mixtures at 48 hours.

have identified the need to optimize and sometimes exceed this limit for their cement to perform satisfactorily when combined with high-calcium oxide FA or certain chemical admixtures (Niemuth 2012). XRF analysis showed the SO_3 content of the under-sulfated cement to be only 0.5% lower than the control cement. While this does not appear to be drastically lower, and is also within the specification, it was enough to create an under-sulfated system.

Calorimetry results revealed that the under-sulfated combinations created an earlier and higher initial heat flow peak; however, cumulative heat was lower than that of combinations with the control cement. Previous research (Roberts and Taylor 2007) indicates that the addition of gypsum can remedy the reduced heat experienced with an under-sulfated cement; this was confirmed by laboratory testing of mortar mixtures and through isothermal and adiabatic calorimetry. Lack of strength development, shown in Table 10, indicates a roughly 50% reduction in 1-day strength for mixtures that include cement U, except for the mixture with 1% gypsum addition. This can be attributed to the lower cumulative heat generated by these mixtures.

To help confirm the physical properties of rapid slump loss and delayed setting observed in the field, a mini-mortar mixture similar to the concrete mixture was created, and the slump and time of setting tests were performed in the laboratory. These tests reflected what was initially seen in the field and show that an SMS can be used to identify a chemical imbalance of a concrete mixture transported by a ready mixed concrete truck. The lack of slump increase with water additions for the under-sulfated cement combinations is most likely due to uncontrolled aluminate hydration, rapid dissolution of SO_3 combined with aluminates to form ettringite, or a combination of both. Lack of SO_3 in the system also leads to delayed setting and reduced early strength, which was seen in the field and confirmed in the laboratory. The use of a polycarboxylate admixture instead of LS can remedy the slump issue but does not completely cure the delayed

Table 10—Mortar mixture cube strengths

Age	C-LS-FA-M, psi (MPa)	U-LS-FA-M, psi (MPa)	U-LS-FA-G-M, psi (MPa)	U-PC-FA-M, psi (MPa)
1 day	530 (3.65)	210 (1.45)	500 (3.45)	210 (1.45)
3 days	1250 (8.62)	1100 (7.58)	1400 (9.65)	1290 (8.89)
7 days	1590 (10.96)	1660 (11.45)	1830 (12.62)	1780 (12.27)
28 days	2840 (19.58)	2620 (10.06)	2910 (20.06)	3050 (21.03)

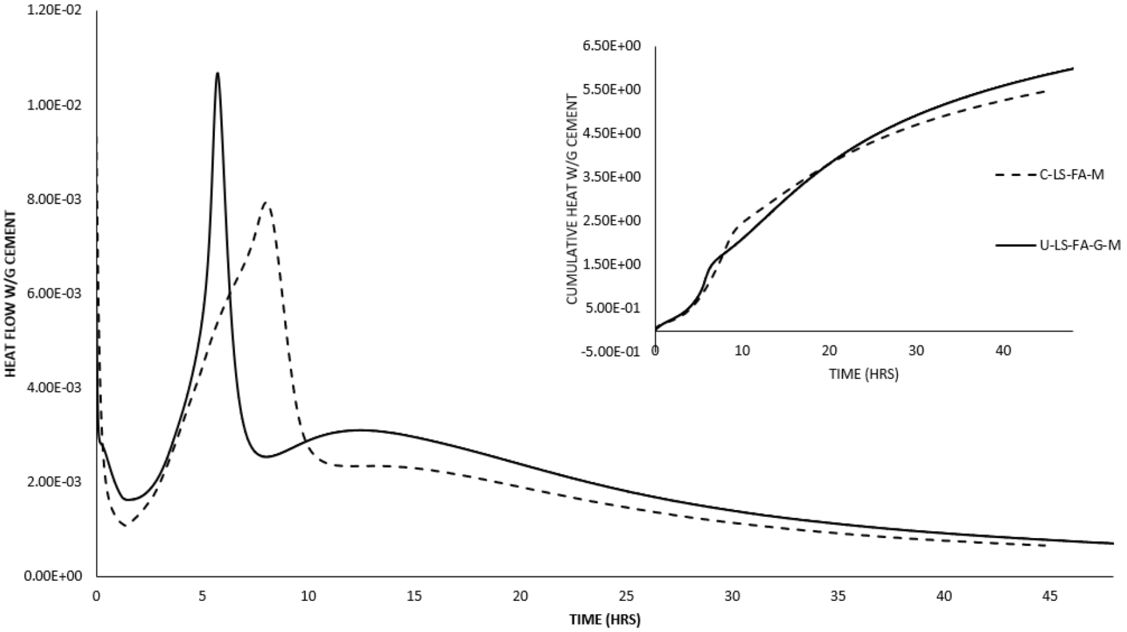

Fig. 16—Heat flow and cumulative heat (upper right corner) of mortar mixtures with gypsum addition at 48 hours.

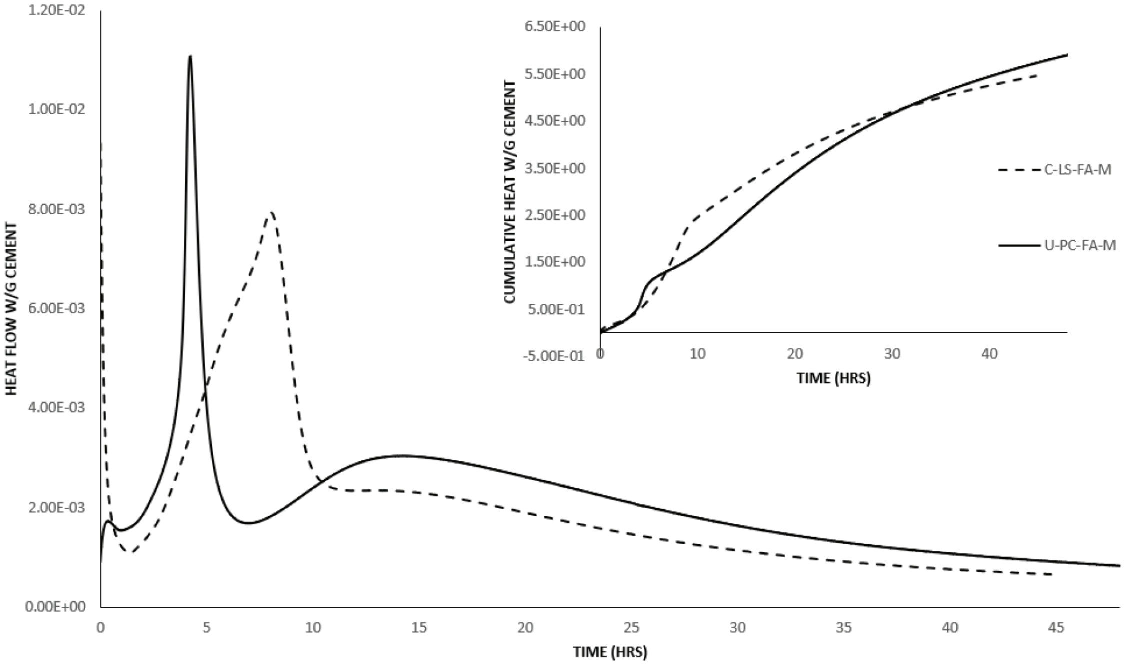

Fig. 17—Heat flow and cumulative heat (upper right corner) of mortar mixtures with polycarboxylate admixture at 48 hours.

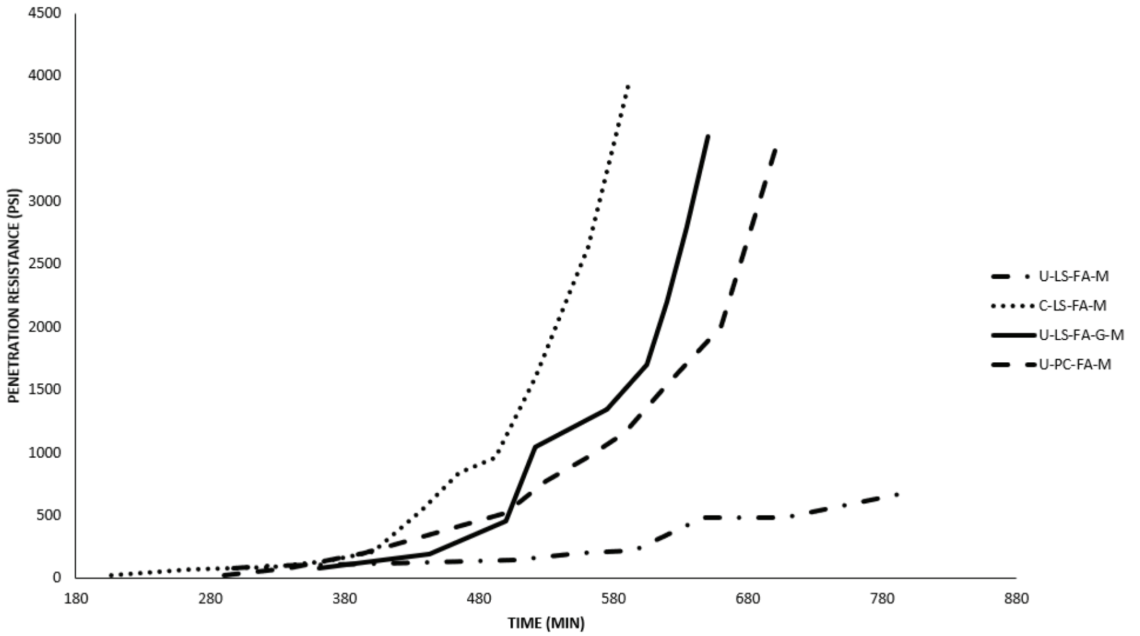

Fig. 18—Mortar mixture time of setting. (Note: 1 psi = 0.0069 MPa.)

setting issue in this instance. The proper addition of gypsum corrects both the slump and setting issues.

CONCLUSIONS AND FURTHER RESEARCH

This study highlights the critical role of sulfate content in portland cement, especially when combined with high-calcium fly ash (FA) and specific admixtures. The findings demonstrate how real-time monitoring tools, like the on-board slump-monitoring system (SMS), can effectively identify and mitigate issues caused by chemical imbalances in concrete mixtures. The research confirms that adjusting sulfate levels through gypsum addition can address problems of rapid stiffening and delayed setting. However, further investigation is needed to refine the detection of chemical imbalances in concrete and optimize sulfate adjustment methods. The following points summarize key conclusions and suggest areas for additional research.

- Incompatibility of materials within a concrete mixture can be identified in the field by an SMS installed on a ready mixed concrete truck. A chemical imbalance such as this may be present when a mixture experiences rapid slump loss and a lower-than-expected slump response to additional water.
- Chemical imbalances identified in the field can be reproduced in the laboratory, on a small scale, as long as material samples are available.
- Low-SO_3 cement can be remedied with the addition of gypsum.
- More research is needed to refine the process of identifying and quantifying crystalline phases present in hydrated paste samples containing various cementitious materials and chemical admixtures. This process was conducted for this research; however, results were somewhat inconclusive and did not provide a quantifiable basis for linking hydration product formation with mortar heat of hydration, setting time, or strength development.
- More research is also needed to determine a laboratory gypsum addition method that more closely mimics the process used for commercial cement production.

AUTHOR BIOS

ACI member **Justin Dickey** *is Director of Technical Services – Ready-Mix Concrete for Cemex USA in Houston, TX, and a Doctoral Student in the Infrastructure Materials Engineering program at The University of Texas at Austin, Austin, TX. He received his Master of Science in Technology from Texas State University, San Marcos, TX. He is a Past President of the ACI Texas State University Student Chapter and was a Board member of the ACI Central Texas Chapter.*

Kevin J. Folliard*, FACI, is the Warren S. Bellows Centennial Professor in Civil Engineering at The University of Texas at Austin. He received the ACI Young Member Award for Professional Achievement in 2002 and the ACI Wason Medal for Materials Research in 2011 and 2015. His research interests include the durability of portland cement concrete, issues related to alkali-silica reaction (ASR), delayed ettringite formation (DEF), and external sulfate attack.*

Thanos Drimalas*, FACI, is a Research Associate in the Fariborz Maseeh Department of Civil, Architectural and Environmental Engineering at The University of Texas at Austin. He is a member of ACI Committees 201, Durability of Concrete; 301, Specifications for Concrete Construction; 321, Concrete Durability Code; and 350, Environmental Engineering Concrete Structures. He received the ACI Wason Medal for Materials Research in 2015.*

ACKNOWLEDGMENTS

The authors would like to thank Tex-Mix Concrete, Texas Materials (a CRH Company), Cemex USA, and Verifi (a Saint-Gobain company). The authors would also like to acknowledge the efforts of P. Sandberg in reviewing the manuscript and interpreting the calorimetry results.

REFERENCES

ASTM C109/C109M-23, 2023, “Standard Test Method for Compressive Strength of Hydraulic Cement Mortars (Using 50 mm [2 in.] Cube Specimens),” ASTM International, West Conshohocken, PA, 11 pp.

ASTM C150/C150M-22, 2022, “Standard Specification for Portland Cement,” ASTM International, West Conshohocken, PA, 9 pp.

ASTM C403/C403M-23, 2023, “Standard Test Method for Time of Setting of Concrete Mixtures by Penetration Resistance,” ASTM International, West Conshohocken, PA, 6 pp.

ASTM C494/C494M-19, 2019, “Standard Specification for Chemical Admixtures for Concrete,” ASTM International, West Conshohocken, PA, 15 pp.

ASTM C563-20, 2020, "Standard Guide for Approximation of Optimum SO3 in Hydraulic Cement," ASTM International, West Conshohocken, PA, 8 pp.

ASTM C618-23, 2023, "Standard Specification for Coal Ash and Raw or Calcined Natural Pozzolan for Use in Concrete," ASTM International, West Conshohocken, PA, 5 pp.

ASTM C778-21, 2021, "Standard Specification for Standard Sand," ASTM International, West Conshohocken, PA, 3 pp.

ASTM C1702-23e1, 2023, "Standard Test Method for Measurement of Heat of Hydration of Hydraulic Cementitious Materials Using Isothermal Conduction Calorimetry," ASTM International, West Conshohocken, PA, 9 pp.

Cost, V. T., 2006, "Incompatibility of Common Concrete Materials – Influential Factors, Effects, and Prevention," *HPC: Build Fast, Build to Last: The 2006 Concrete Bridge Conference*, Reno, NV, 24 pp.

Detwiler, R. J., and Shkolnik, E., 2005, "Something Uncommon: New Admixtures, Supplementary Materials Lead to One Problem – Incompatibility," *Roads and Bridges*, V. 43, No. 1, Jan., pp. 30-32.

Helmuth, R.; Hills, L. M.; Whiting, D. A.; and Bhattacharja, S., 1995, "Abnormal Concrete Performance in the Presence of Admixtures," PCA R&D Serial No. RP333, American Cement Association, Washington, DC, 94 pp.

Hills, L., and Tang, F., 2004, "Manufacturing Solutions for Concrete Performance," *IEEE-IAS/PCA 2004 Cement Industry Technical Conference*, Chattanooga, TN, Apr., pp. 121-130.

Johnson, C. D., 1987, "Admixture-Cement Incompatibility: A Case History," *Concrete International*, V. 9, No. 4, Apr., pp. 51-60.

Khalil, S. M., and Ward, M. A., 1978, "Influence of SO_3 and C_3A on the Early Reaction Rates of Portland Cement in the Presence of Calcium Lignosulfonate," *American Ceramic Society Bulletin*, V. 57, No. 12, Dec., pp. 1116-1122.

Lashley, L., 2009, "The Compatibility and Performance of Cementitious Materials and Chemical Admixtures," MASc thesis, Department of Civil Engineering, University of Toronto, Toronto, ON, Canada, 185 pp.

Lee, C. H., and Hover, K. C., 2016, "Early-Age Stiffening of Paste, Mortar, and Concrete in Lab and Field," *ACI Materials Journal*, V. 113, No. 1, Jan.-Feb., pp. 83-93. doi: 10.14359/51687917

Lerch, W., 1946, "The Influence of Gypsum on the Hydration and Properties of Portland Cement Pastes," *Proceedings of the American Society for Testing Materials*, V. 46, pp. 1252-1292.

Meyer, L. M., 1976, "Effect of Admixtures on Cement Performance in Concrete," *1976 Cement Chemists' Seminar*, American Cement Association, Washington, DC, 11 pp.

Niemuth, M. D., 2012, "Effect of Fly Ash on the Optimum Sulfate of Portland Cement," PhD dissertation, Purdue University, West Lafayette, IN, 506 pp.

Ramachandran, V. S., ed., 1995, *Concrete Admixtures Handbook: Properties, Science, and Technology*, second edition, Noyes Publications, Park Ridge, NJ.

Roberts, L. R., 1995, "Dealing with Cement-Admixture Interactions," *23rd Annual Convention of the Institute of Concrete Technology*, Institute of Concrete Technology, Sandhurst, Berkshire, UK, 15 pp.

Roberts, L. R., and Taylor, P. C., 2007, "Understanding Cement-SCM-Admixture Interaction Issues," *Concrete International*, V. 29, No. 1, Jan., pp. 33-41.

Sandberg, P. J., and Roberts, L. R., 2005, "Cement-Admixture Interactions Related to Aluminate Control," *Journal of ASTM International*, V. 2, No. 6, June, pp. 1-14. doi: 10.1520/JAI12296

Taylor, P. C.; Graf, L. A.; Zemajtis, J. Z.; Johansen, V.; and Kozikowski, R. L., 2006, "Identfiying Incompatible Combinations of Concrete Materials: Volume I-Final Report," Federal Highway Administration and Portland Cement Association, Skokie, IL, 159 pp.

Taylor, P. C., 2007, "Concrete Material Incompatibility-Predicting and Preventing Pavement Mix Problems," *The Construction Specifier*, V. 60, No. 1, pp. 46-53.

Wang, H.; Qi, C.; Farzam, H.; and Turici, J., 2006, "Interaction of Materials Used in Concrete," *Concrete International*, V. 28, No. 4, Apr., pp. 47-52.

JOIN AN ACI Chapter!

The American Concrete Institute has Chapters and Student Chapters located throughout the world. Participation in a local chapter can be extremely rewarding in terms of gaining greater technical knowledge and networking with leaders in the concrete community.

Because chapters are distinct and independent legal entities, membership includes both ACI members and non-ACI members and is made up of a diverse blend of architects, engineers, consultants, contractors, educators, material suppliers, equipment suppliers, owners, and students—basically anyone interested in concrete. Many active ACI members initially became involved in ACI through their local chapter. In addition to technical programs and publications, many chapters sponsor ACI Certification programs, ACI educational seminars, project award recognition programs, and social events with the goal of advancing concrete knowledge.

To find a chapter near you, go to: https://www.concrete.org/getinvolved/chapters.aspx

---

Student Chapters

Join or form an ACI Student Chapter to maximize your influence, knowledge sharing, and camaraderie! ACI has 240+ student chapters located throughout the world, each providing opportunities for students to:

- Connect with their peers and participate in concrete-related activities such as: student competitions, ACI Conventions, ACI Certification Programs, ACI Educational Seminars, local chapter meetings, social events, and community service projects;
- Network with members of local chapters, many of whom have been in the industry for decades and can help to develop professional relationships and offer career advice;
- Win recognition for their universities through the University Award; and
- Learn about the many scholarships and fellowships offered by the ACI Foundation and by ACI's local chapters.

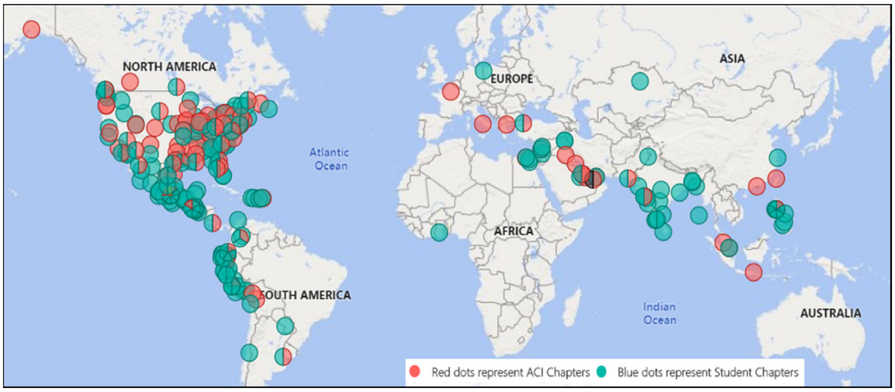

American Concrete Institute

www.concrete.org/getinvolved/chapters.aspx aci Foundation

Building the Future

We're Building the Future

OUR MISSION

We make strategic investments in ideas, research, and people to create the future of the concrete industry.

Through its councils and programs, the ACI Foundation helps to keep the concrete industry at the forefront of advances in material composition, design, and construction.

OUR FOCUS

- Identifying technologies and innovations which provide needed solutions for the concrete industry
- Seeking concrete research projects that further the knowledge and sustainability of concrete materials, construction, and structures
- Supporting our future concrete innovators and leaders by administering fellowships and scholarships
- Helping honorably discharged veterans with our Veterans Rebate for ACI Certification program

www.acifoundation.org

CALL FOR ACTION

ACI Invites You To...

Share your expertise

Do you have EXPERTISE in any of these areas?

- BIM
- Chimneys
- Circular Concrete Structures Prestressed by Wrapping with Wire and Strand
- Circular Concrete Structures Prestressed with Circumferential Tendons
- Concrete Properties
- Demolition
- Deterioration of Concrete in Hydraulic Structures
- Electronic Data Exchange
- Insulating Concrete Forms, Design, and Construction
- Nuclear Reactors, Concrete Components
- Pedestal Water Towers
- Pipe, Cast-in-Place
- Strengthening of Concrete Members
- Sustainability

Then become a REVIEWER for the *ACI Structural Journal* or the *ACI Materials Journal*.

Become a Reviewer for the ACI Journals

How to become a Reviewer:

1. Go to: **http://mc.manuscriptcentral.com/aci**;
2. Click on "Create Account" in the upper right-hand corner; and
3. Enter your E-mail/Name, Address, User ID and Password, and Area(s) of Expertise.

Update your Manuscript Central user account information

Did you know that the database for MANUSCRIPT CENTRAL, our manuscript submission program, is separate from the ACI membership database?

How to update your user account:

1. Go to **http://mc.manuscriptcentral.com/aci**;
2. Log in with your current User ID & Password; and
3. Update your E-mail/Name, Address, User ID and Password, and Area(s) of Expertise.

QUESTIONS?

E-mail any questions to Journals.Manuscripts@concrete.org.

American Concrete Institute
Always advancing

ARE YOU A RESEARCHER?

SIGN UP FOR ORCID TODAY!

1. Register
2. Use your ORCID ID
3. Share

ORCID provides a digital identifier that distinguishes you from every other researcher and, through integration in key research workflows such as manuscript and grant submission, supports automated linkages between you and your professional activities, ensuring that your work is recognized.

ORCID services are FREE and it's as easy as **1-2-3**.

WWW.ORCID.ORG

aci® in Your Classroom

Integrate aci® into your classroom!

To support future leaders, ACI has launched several initiatives to engage students in the Institute's activities and programs – select programs that may be of interest to Educators are:

- **Free student membership –** encourage students to sign up
- **Special student discounts on *ACI 318 Building Code Requirements for Structural Concrete*, *ACI 530 Building Code Requirements and Specification for Masonry Structure*, & *Formwork for Concrete* manual.**
- **Access to *Concrete International* –** free to all ACI student members
- **Access to *ACI Structural Journal* and *ACI Materials Journal* –** free to all ACI student members
- **Free sustainability resources –** free copies of Sustainable Concrete Guides provided to universities for use in the classroom
- **Student competitions –** participate in ACI's written and/or team-based competitions
- **Scholarships and fellowships –** students who win awards are provided up to $15,000 and may be offered internships and paid travel to attend ACI's conventions
- **ACI Award for University Student Activities –** receive local and international recognition for your University's participation in concrete-related activities
- **Free access to the *ACI Collection of Concrete Codes, Specifications, and Practices* –** in conjunction with ACI's chapters, students are provided free access to the online ACI Collection
- **ACI online recorded web sessions and continuing education programs –** online learning tools ideal for use as quizzes or in-class study material

https://www.concrete.org/educatorsandresearchers/aciinyourclassroom.aspx

NEW Symposium Publications from ACI

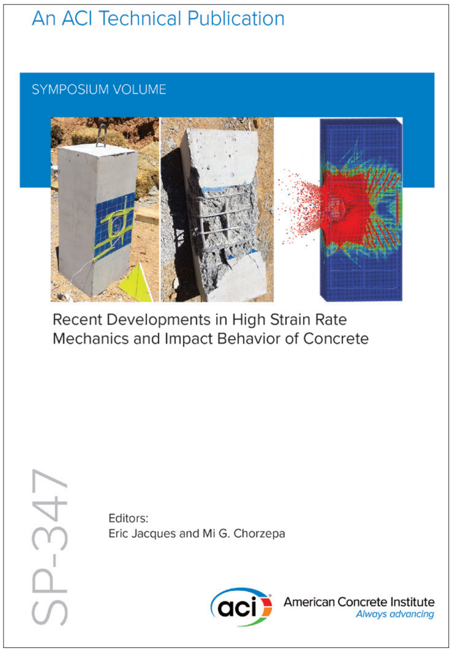

An ACI Technical Publication

SYMPOSIUM VOLUME

Recent Developments in High Strain Rate Mechanics and Impact Behavior of Concrete

SP-347

Editors:
Eric Jacques and Mi G. Chorzepa

American Concrete Institute
Always advancing

SP-347: Recent Developments in High Strain Rate Mechanics and Impact Behavior of Concrete

This Symposium Volume reports on the latest developments in the field of high-strain-rate mechanics and behavior of concrete subject to impact loads. This effort supports the mission of ACI Committee 370, Blast and Impact Load Effects, to develop and disseminate information on the design of concrete structures subjected to impact, as well as blast and other short-duration dynamic loads.

Available in PDF format: $69.50
(ACI members: $39.00) ($30.50 savings)

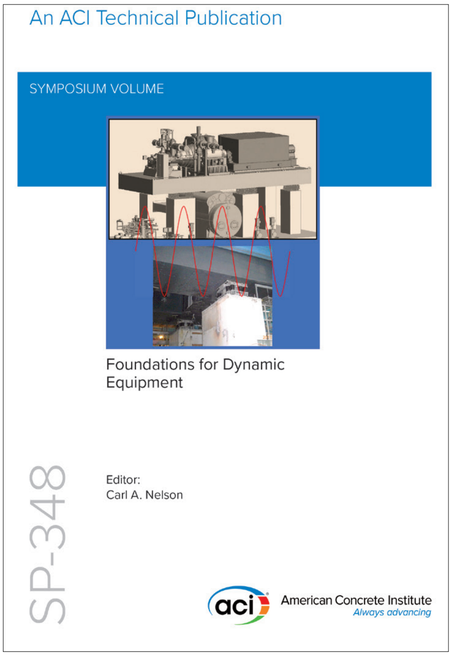

An ACI Technical Publication

SYMPOSIUM VOLUME

Foundations for Dynamic Equipment

SP-348

Editor:
Carl A. Nelson

American Concrete Institute
Always advancing

SP-348: Foundations for Dynamic Equipment

This special publication grew out of the Technical Session titled “Application of ACI 351-C Report on Dynamic Foundations,” held at the ACI Spring 2019 Convention in Québec City, Québec. Following this event, ACI Committee 351 decided to undertake a special publication with contributions from those session participants willing to develop their presentations into full-length papers. Three papers included in the current publication were contributed by these presenters and their coauthors, with six additional papers provided by others.

Available in PDF format: $69.50
(ACI members: $39.00) ($30.50 savings)

American Concrete Institute
+1.248.848.3700 • www.concrete.org

ACI MATERIALS JOURNAL

American Concrete Institute